Lecture Notes in Physics

Volume 865

For further volumes:
www.springer.com/series/5304

The Lecture Notes in Physics

The series Lecture Notes in Physics (LNP), founded in 1969, reports new developments in physics research and teaching—quickly and informally, but with a high quality and the explicit aim to summarize and communicate current knowledge in an accessible way. Books published in this series are conceived as bridging material between advanced graduate textbooks and the forefront of research and to serve three purposes:

- to be a compact and modern up-to-date source of reference on a well-defined topic
- to serve as an accessible introduction to the field to postgraduate students and nonspecialist researchers from related areas
- to be a source of advanced teaching material for specialized seminars, courses and schools

Both monographs and multi-author volumes will be considered for publication. Edited volumes should, however, consist of a very limited number of contributions only. Proceedings will not be considered for LNP.

Volumes published in LNP are disseminated both in print and in electronic formats, the electronic archive being available at springerlink.com. The series content is indexed, abstracted and referenced by many abstracting and information services, bibliographic networks, subscription agencies, library networks, and consortia.

Proposals should be sent to a member of the Editorial Board, or directly to the managing editor at Springer:

Christian Caron
Springer Heidelberg
Physics Editorial Department I
Tiergartenstrasse 17
69121 Heidelberg/Germany
christian.caron@springer.com

Mariejo Goupil • Kévin Belkacem •
Coralie Neiner • Francois Lignières •
John J. Green
Editors

Studying Stellar Rotation and Convection

Theoretical Background and Seismic Diagnostics

Springer

Editors
Mariejo Goupil
LESIA
Observatoire de Paris-Meudon
Meudon Cedex, France

Kévin Belkacem
LESIA
Observatoire de Paris-Meudon
Meudon Cedex, France

Coralie Neiner
LESIA
Observatoire de Paris-Meudon
Meudon Cedex, France

Francois Lignières
Institut de Recherche en Astrophysique,
et Planétologie
Observatoire Midi-Pyrénées
Toulouse, France

John J. Green
LESIA
Observatoire de Paris-Meudon
Meudon Cedex, France

ISSN 0075-8450
Lecture Notes in Physics
ISBN 978-3-642-33379-8
DOI 10.1007/978-3-642-33380-4
Springer Heidelberg New York Dordrecht London

ISSN 1616-6361 (electronic)

ISBN 978-3-642-33380-4 (eBook)

Library of Congress Control Number: 2012955403

Printed on acid-free paper

Springer is part of Springer Science+Business Media (www.springer.com)

Preface

This volume synthesizes the work carried out by several French teams and their international collaborators during SIROCO (SeIsmology for ROtation and COnvection), a project funded by the French *Agence Nationale de la Recherche* (ANR), from 2007 to 2010. This work was driven by the need for theoretical insight into the huge quantity of high-quality observational data recently provided by space experiments such as CoRoT and Kepler.

Ultra-high precision photometry is now available for thousands of stars, from main-sequence to red-giant stars and spanning the Hertzsprung–Russell diagram with an unprecedented completeness. As the SoHo mission unveiled the solar interior, the CoRoT and Kepler missions constitute a new dawn for asteroseismology, allowing a detailed probing of stellar interiors. This enables our understanding and modeling of stellar structure and evolution to be tested as never before. In particular, stellar masses, radii, and ages can be derived with an unprecedented accuracy.

It has long been known that the main uncertainties in stellar structure and evolution are those related to hydrodynamical processes, in particular to those of stellar rotation and the transport of energy by turbulent convection. In the context of CoRoT and Kepler this project came at a propitious time, since the convergent efforts in developing theories and numerical models for rotating stars and their oscillations provide a crucial step in the progress of our knowledge of stellar interiors.

For instance, rotation is known to have significant impact on the structure of stars and their evolution. Many issues regarding the modeling of such an impact needs to be investigated. Centrifugal distortion of fast rotating stars requires fully two-dimensional studies to properly infer the effect of rotation on oscillations, and this was one of the SIROCO objectives. This is particularly important for massive stars such as O and B stars, many of which are fast rotators, in particular the very rapidly rotating Be stars, and for intermediate-mass rapidly rotating stars such as the delta Scuti stars. Both exhibit complex and puzzling features in their oscillation frequency spectra that call for a solid theoretical background to aid their interpretation.

The second SIROCO topic was related to turbulent convection, a cornerstone of any realistic stellar model, but which up to now had been lacking tight observational constraints. Mode frequencies can be used for this purpose, but mode ampli-

tudes provide more powerful seismic diagnostics since they depend on the dynamical properties of turbulent convection. It is only the recent space observations that have provided data with sufficient precision for such theories to bear fruits.

The focus of the SIROCO project on these two fundamental problems, with the aim of providing a solid theoretical background, has enabled the development of adapted seismic diagnostics. This is a crucial step toward a complete and fruitful exploitation of the wealth of data provided by the CoRoT and Kepler spacecrafts.

The first part of the book concentrates on rotation and associated seismology. The first four chapters present the modeling of rotating stars; in particular, they examine the impact of rotation on massive-star evolution, the different transport processes in stellar interiors, the 2D modeling of rotating stars, and the influence of initial conditions on the rotation history. Then, four chapters present models for the oscillation of rotating stars. The first two consider the properties of the oscillation modes through 2D numerical calculations and asymptotic theory, and the next two discuss low-frequency oscillations and prospects for asteroseismology in rapidly rotating stars.

The second part of the book deals with convection and associated seismology. First, the connections between stellar oscillations and turbulent convection are examined; next, a chapter investigates semi-convection; finally, experimental and numerical investigations of internal gravity waves excited by turbulent penetrative convection are presented.

The audience targeted by this book consists of researchers, PhD students, and postdocs. This book is based on tutorials and discussions held at the SIROCO workshop in Paris (France) in May 2011, which has allowed us to give a progress report on the very latest asteroseismological developments in stellar rotation and convection. It is our hope that this book will stimulate further research in this fascinating field.

The editors sincerely thank the authors for the high quality of their contributions.

Paris, France

M.J. Goupil
K. Belkacem
C. Neiner
F. Lignières
J.J. Green

Contents

Part I Rotation and Associated Seismology

1 Models of Rotating Massive Stars: Impacts of Various Prescriptions 3
Georges Meynet, Sylvia Ekstrom, André Maeder, Patrick Eggenberger, Hideyuki Saio, Vincent Chomienne, and Lionel Haemmerlé
1.1 Rotation in Stellar Models 4
1.2 The Models Computed 6
1.3 Evolutionary Tracks and Lifetimes During the Main-Sequence Phase 7
1.4 Changes of the Surface Composition During the MS Phase 11
1.5 Changes of the Surface Velocity During the MS Phase 13
1.6 The Distribution of the Core Helium Lifetime in the Blue and Red Parts of the HR Diagram 13
1.7 The Extensions of the Blue Loops 15
1.8 The Angular Momentum of the Core 15
1.9 The Synthesis of Primary Nitrogen in Fast-Rotating Metal-Poor Massive Stars 17
1.10 Conclusions 20
References 21

2 Transport Processes in Stellar Interiors 23
Stéphane Mathis
2.1 Introduction 23
2.2 Modeling 25
2.2.1 Preliminary Definitions 25
2.2.2 Transport Equation System 26
2.2.3 The Spectral Method 27
2.3 Dynamical Processes in Stellar Convection Zones 29
2.3.1 Convection, Differential Rotation, and Meridional Flows . . 29
2.3.2 Dynamo Action 30
2.4 Dynamical Processes in Stellar Radiation Zones 31
2.4.1 Meridional Circulation 32

2.4.2 Shear-Induced Turbulence . . . 34
2.4.3 The Fossil Magnetic Field Dynamics . . . 34
2.4.4 Internal Waves . . . 37
2.5 Conclusion . . . 41
References . . . 42

3 Ab Initio Modelling of Steady Rotating Stars . . . 49
Michel Rieutord and Francisco Espinosa Lara
3.1 Introduction . . . 49
3.1.1 The Astrophysical Context . . . 49
3.1.2 The 1D Models . . . 50
3.1.3 The History of 2D Models of Rotating Stars . . . 51
3.2 The Route to Ideal Models . . . 52
3.3 Setting the Problem . . . 53
3.3.1 Equations for a Steady Rotating Star . . . 53
3.3.2 Boundary Conditions—Angular Momentum Condition . . . 54
3.3.3 Scalings . . . 55
3.3.4 Dimensionless Equations and Numbers . . . 56
3.3.5 Global Parameters ρ_c, T_c, R of the Star Model . . . 56
3.3.6 Numerical Method . . . 57
3.3.7 Tests of the Results . . . 62
3.4 Some Results . . . 64
3.5 Conclusions . . . 68
References . . . 72

4 The Influence of Initial Conditions on Stellar Rotation History . . . 75
J.P. Marques and M.J. Goupil
4.1 Introduction . . . 75
4.2 Transport of Angular Momentum . . . 76
4.2.1 Evolution of the Chemical Composition . . . 78
4.2.2 Turbulent Coefficients of Diffusivity . . . 78
4.3 Magnetic Braking . . . 79
4.4 Initial Conditions . . . 81
4.5 Solar-Type Stars . . . 82
4.5.1 Evolution of the Rotation Rate . . . 83
4.5.2 Evolution of the Surface Lithium Abundance . . . 85
4.6 Intermediate Mass Stars . . . 86
4.7 Conclusions . . . 88
References . . . 88

5 Numerical Exploration of Oscillation Modes in Rapidly Rotating Stars . . . 91
Jérôme Ballot, François Lignières, and Daniel R. Reese
5.1 Introduction . . . 91
5.2 The Construction of an Oscillation Code for Rotating Stars . . . 93
5.2.1 The Governing Equations . . . 94

5.2.2 Discussion on the Mathematical and Numerical Options . . 94
5.2.3 Development and Validation of the TOP Code 96
5.3 Exploring Spectra 98
5.3.1 Following Modes 98
5.3.2 Scanning the Spectrum 100
5.3.3 Mode Labeling 100
5.4 Results 101
5.4.1 Testing Perturbative Methods 101
5.4.2 Structure of p-Mode Spectra 103
5.4.3 Structure of g-Mode Spectra 105
5.5 Conclusion 109
References 110

6 Regular and Irregular Pressure Modes in Rapidly Rotating Stars . . 115
Michael Pasek and Bertrand Georgeot
6.1 Introduction 115
6.2 The Ray Limit of Acoustic Waves 116
6.2.1 Waves in Their Short-Wavelength Limit 116
6.2.2 Hamiltonian Systems 116
6.2.3 Integrable and Chaotic Hamiltonian Systems 117
6.2.4 Ray Dynamics in Rotating Stars 119
6.3 Construction of Modes from the Ray Limit 120
6.3.1 Modes Associated to the Different Types of Rays 120
6.3.2 The Different Subspectra 122
6.3.3 Visibility of the Modes 122
6.4 Asymptotic Theory of Island Modes 123
6.4.1 Regularities in Numerical Computations of Oscillation Spectra 123
6.4.2 Asymptotic Formula for the Island Mode Spectrum 125
6.4.3 Comparison with Numerical Modes 127
6.5 Chaotic Spectrum 128
6.6 Conclusion 130
References 130

7 Low-Frequency Oscillations in Rotating Stars 133
Umin Lee
7.1 Introduction 133
7.2 Perturbation Analysis 134
7.3 Low-Frequency Oscillations 136
7.4 Traditional Approximation 138
7.5 Linear Mode Coupling 140
7.6 Series Expansion Method 144
7.7 Stability of g-Modes and r-Modes in Rotating SPB Stars 146
7.8 Parametric Instability: Weakly Nonlinear Oscillation 151
7.9 Conclusion 154
References 155

8 Prospects for Asteroseismology of Rapidly Rotating B-Type Stars . . 159
Hideyuki Saio
8.1 Oscillations in Main-Sequence B-Stars 159
8.2 Oscillations in Rotating Stars 162
8.2.1 Coriolis and Centrifugal Force Effects 162
8.2.2 r-Modes 165
8.2.3 Latitudinal Amplitude Distributions 165
8.2.4 Expected Frequency Ranges of g- and r-Modes 168
8.3 Comparisons with Frequency Groups of Be Stars 170
8.3.1 HD 50209 170
8.3.2 Rotation Rates of Be Stars 172
8.4 Conclusion 173
References 174

Part II Convection and Associated Seismology

9 Connections Between Stellar Oscillations and Turbulent Convection 179
K. Belkacem and R. Samadi
9.1 Introduction 179
9.1.1 A Brief History on the Energetical Aspects of Solar-Like Oscillations 180
9.1.2 Mode Damping and Driving in Solar-Like Pulsators: A Difficult Problem 181
9.2 Mode Driving and Damping by Turbulent Convection 182
9.2.1 Modelling Mode Driving ($\mathcal{P}$) 183
9.2.2 Mode Damping (η) 188
9.3 Scaling Relations as the Result of the Connections Between Pulsations and Convection 191
9.3.1 Relation Between Mode Line-Width with Effective Temperature 192
9.3.2 Relation Between $\nu_{\max}$ and ν_c 195
9.3.3 Mode Amplitudes Across the HR Diagram 198
9.4 Concluding Remarks 203
References 204

10 Semi-convection: What Is the Underlying Physical Context? 209
A. Noels
10.1 Introduction 209
10.2 A Few Basic Points 210
10.3 Semi-convection in Low-Mass Stars 212
10.4 Semi-convection in Massive Stars 214
10.5 Semi-convection in Helium-Burning Stars 215
10.6 Discussion in Terms of Vibrational Stability 216
References 218

11 Semi-convection 219
F. Zaussinger, F. Kupka, and H.J. Muthsam
11.1 Introduction 219
11.2 The Meaning of Semi-convection for Stellar Evolution 220
11.3 The Double-Diffusive Mixing Process 223
11.4 Models, Experiments and Numerical Simulations 228
11.4.1 Models 228
11.4.2 Experiments 230
11.4.3 Numerical Simulations 230
11.5 Conclusions 233
References 235

12 Experimental and Numerical Investigation of Internal Gravity Waves Excited by Turbulent Penetrative Convection in Water Around Its Density Maximum 239
Stéphane Perrard, Michaël Le Bars, and Patrice Le Gal
12.1 Introduction 240
12.2 Experimental Setup and Measurement Techniques for Penetrative Convection in Water Around 4 °C 242
12.3 Turbulent Penetrative Convection 244
12.3.1 Classical Rayleigh Bénard Convection Between Two Horizontal Plates 244
12.3.2 Penetrative Convection in Water Around 4 °C 245
12.4 The Buffer Zone Between the Convective and Stratified Layers . . 248
12.5 The Stratified Layer 250
12.6 Numerical Simulation: To Go Further into the Analysis 252
12.7 Conclusion 256
References 256

Index 259

Part I
Rotation and Associated Seismology

Chapter 1
Models of Rotating Massive Stars: Impacts of Various Prescriptions

Georges Meynet, Sylvia Ekstrom, André Maeder, Patrick Eggenberger, Hideyuki Saio, Vincent Chomienne, and Lionel Haemmerlé

Abstract The rotation of stars has many interesting and important consequences for the photometric and chemical evolution of galaxies. Many of the predictions of models of stellar rotation are now compared with observations of surface abundances and velocities, with interferometric studies of fast rotating stars, with internal rotation profiles as they can be deduced by asteroseismology, to cite just a few observational constraints. In this paper, we investigate how the outputs of models depend on the prescriptions used for the diffusion coefficients included in the shellular rotating models. After recalling the various prescriptions found in the literature, we discuss their impacts on the evolutionary tracks and lifetimes of the Main-Sequence (MS) phase, the changes of the surface composition and velocities during the MS phase, the distribution of the core helium lifetime in the blue and red parts of the HR diagram, the extensions of the blue loops, the evolution of the angular momentum of the core, and the synthesis of primary nitrogen in fast-rotating metal-poor massive stars. While some of these outputs depend only slightly on the prescriptions used (for instance, the evolution of the surface velocities), most of them show a significant dependence. The models which best fit the changes of the surface abundances

G. Meynet (✉) · S. Ekstrom · A. Maeder · P. Eggenberger · V. Chomienne · L. Haemmerlé
Geneva Observatory, Geneva University, 1290 Versoix, Switzerland
e-mail: georges.meynet@unige.ch

S. Ekstrom
e-mail: Sylvia.Ekstrom@unige.ch

A. Maeder
e-mail: Andre.Maeder@unige.ch

P. Eggenberger
e-mail: Patrick.Eggenberger@unige.ch

V. Chomienne
e-mail: Vincent.Chomienne@unige.ch

L. Haemmerlé
e-mail: Lionel.Haemmerle@unige.ch

H. Saio
Astronomical Institute, Graduate School of Science, Tohoku University, Sendai 980-8578, Japan
e-mail: saio@astr.tohoku.ac.jp

M. Goupil et al. (eds.), *Studying Stellar Rotation and Convection*,
Lecture Notes in Physics 865, DOI 10.1007/978-3-642-33380-4_1,

are those computed with the vertical shear diffusion coefficient of Maeder (Astron. Astrophys. 321:134–144, 1997) and the horizontal shear diffusion coefficient by Zahn (Astron. Astrophys. 265:115–132, 1992).

1.1 Rotation in Stellar Models

In recent years, many effects of axial rotation on the structure and the evolution of massive stars have been studied (see, e.g., the recent review [17]). Among the most important effects, there are those linked to the transport of angular momentum and of chemical species in the interior of stars. These may strongly affect many outputs of stellar models such as the variation with the age of the surface abundances and velocities, the evolutionary tracks and lifetimes, the nature of the supernova events and of the stellar remnants, and the nature and the amount of new synthesized species. As a consequence, when results of rotating models are used in population synthesis models or in models for the chemical evolution of galaxies, quite different results are obtained with respect to results obtained from nonrotating models.

Most, if not all, of the recent grids of rotating models have been computed in the framework of the theory proposed by [31], with further improvements by [18]. This was named the theory of shellular rotation, since it is based on the assumption that on an isobaric surface, the angular velocity, Ω, is nearly constant, which means that any variations can be considered as a small perturbation. This nearly constant value of Ω on an isobaric surface is due to the fact that along those directions, there are neither stable temperature nor density gradients which counteract shear turbulence. This implies the existence of strong "horizontal" (i.e., along an isobaric surface) diffusion coefficient called $D_{\rm h}$ hereafter. In the following, when we speak about rotating models, we implicitly assume that we consider models with shellular rotation. The present models do not include the effects of the dynamo theory suggested by [29].[1]

In the framework of the shellular theory of rotation, the equation describing the transport of chemical species is a pure diffusive equation [2],

$$\rho \left.\frac{\partial X_i}{\partial t}\right|_{M_r} = \frac{1}{r^2}\frac{\partial}{\partial r}\left(\rho r^2 D_{\rm chem}\frac{\partial X_i}{\partial r}\right), \tag{1.1}$$

where X_i is the abundance in mass fraction of particles i, and $D_{\rm chem}$ is the appropriate diffusion coefficient for chemical elements (see below).

In a differentially rotating star, the evolution of the angular velocity Ω has to be followed at each level r (for shellular rotation), so that a full description of $\Omega(r,t)$ is available. The values of $\Omega(r,t)$ influence the mixing of elements, and in turn the evolution of $\Omega(r,t)$ also depends on the mixing processes and on the distribution

[1] Numerical simulations by [32] have studied MHD instabilities arising in the radiation zone of a differentially rotating star, in which a poloidal field of fossil origin is sheared into a toroidal field. Their simulations show no sign of dynamo action.

of the elements. The derivation of the equation for the transport of angular momentum is not straightforward. In the case of shellular rotation, the equation in the Lagrangian form becomes [15, 31]

$$\rho \frac{\partial}{\partial t}\left(r^2 \bar{\Omega}\right)_{M_r} = \frac{1}{5r^2}\frac{\partial}{\partial r}\left(\rho r^4 \bar{\Omega} U_2(r)\right) + \frac{1}{r^2}\frac{\partial}{\partial r}\left(\rho D_{\text{ang}} r^4 \frac{\partial \bar{\Omega}}{\partial r}\right). \tag{1.2}$$

Here, $\bar{\Omega}$ is the average value of Ω on an isobar. U_2 is the radial component of the meridional circulation velocity, and D_{ang} is the appropriate diffusion coefficient for angular momentum. The second term on the right is a diffusion term, similar in its form to (1.1), while the first term on the right is *an advective term*, i.e., modeling the transport by a velocity current. We notice that Eq. (1.1) does not contain such an advective term. It could contain a term of that kind; however, it can be shown [2] that the combined effect of turbulence and circulation currents is equivalent to a diffusion *for the element transport* (see Eq. (1.1)).

In the equation for the transport of chemical species in radiative zones, the diffusion coefficient, D_{chem}, is made up of two terms. These are the vertical shear diffusion coefficient D_{shear} and the effective diffusion coefficient, D_{eff}, which account for the resultant effect of the strong horizontal shear diffusion, D_{h} (i.e., the shear on an isobaric surface) and of the meridional currents.

In the equation for the transport of angular momentum, the diffusion coefficient, D_{ang}, is made up of only one term, the shear diffusion coefficient D_{shear}.

For the coefficients D_{shear}, we can find two different expressions in the literature:

D_{shear} from [13, M97],

$$D_{\text{shear}} = f_{\text{energ}} \frac{H_P}{g\delta} \frac{K}{\left[\frac{\varphi}{\delta}\nabla_\mu + (\nabla_{\text{ad}} - \nabla_{\text{rad}})\right]} \left(\frac{9\pi}{32}\Omega \frac{\mathrm{d}\ln\Omega}{\mathrm{d}\ln r}\right)^2, \tag{1.3}$$

where $K = \frac{4ac}{3\kappa}\frac{T^4\nabla_{\text{ad}}}{\rho P \delta}$, and with $f_{\text{energ}} = 1$, and $\varphi = (\frac{\mathrm{d}\ln\rho}{\mathrm{d}\ln\mu})_{P,T} = 1$;
D_{shear} from [30, TZ97],

$$D_{\text{shear}} = f_{\text{energ}} \frac{H_P}{g\delta} \frac{(K + D_{\text{h}})}{\left[\frac{\varphi}{\delta}\nabla_\mu (1 + \frac{K}{D_{\text{h}}}) + (\nabla_{\text{ad}} - \nabla_{\text{rad}})\right]} \left(\frac{9\pi}{32}\Omega \frac{\mathrm{d}\ln\Omega}{\mathrm{d}\ln r}\right)^2 \tag{1.4}$$

with K, f_{energ}, and φ as in (1.1).

For the coefficients D_{h}, we can find three different expressions in the literature:

D_{h} from [31, Z92],

$$D_{\text{h}} = \frac{1}{c_{\text{h}}} r \left|2V(r) - \alpha U(r)\right|, \tag{1.5}$$

where $\alpha = \frac{1}{2}\frac{\mathrm{d}\ln(r^2\bar{\Omega})}{\mathrm{d}\ln r}$ and $c_{\text{h}} = 1$;

$D_{\rm h}$ from [14, M03],

$$D_{\rm h} = Ar\left(r\bar{\Omega}(r)V|2V - \alpha U|\right)^{1/3} \tag{1.6}$$

with α as in Eq. (5) and $A = 0.002$;
$D_{\rm h}$ from [20, MZ04],

$$D_{\rm h} = \left(\frac{\beta}{10}\right)^{1/2}\left(r^2\bar{\Omega}\right)^{1/2}\left(r|2V - \alpha U|\right)^{1/2} \tag{1.7}$$

with α as in Eq. (5) and $\beta = 1.5 \times 10^{-6}$.

All prescriptions use the same effective mixing coefficient for the chemical species:

$$D_{\rm eff} = \frac{1}{30}\frac{|r\ U(r)|^2}{D_{\rm h}}. \tag{1.8}$$

There are therefore six different combinations of the two shear diffusion coefficients and of the three horizontal diffusion coefficients. The physics sustaining the different expressions for these various diffusion coefficients is described in details in the papers indicated above, and we shall not recall them in the present work. We just summarize below a few facts which are useful to keep in mind in order to understand their different impacts in stellar models.

- Since the angular momentum is transported mainly by the meridional currents, one can expect that changing the expressions for the diffusion coefficients will have only a weak impact on the angular momentum distribution in stars. We shall see that this is well verified by the numerical models.
- The diffusion coefficient $D_{\rm eff}$ is the key quantity determining the efficiency of mixing in regions where there is a strong μ-gradient, for instance, at the border of the H-convective core.
- The larger $D_{\rm h}$, the smaller $D_{\rm eff}$, and thus less mixing will occur in regions of strong μ-gradients. The expressions of M03 and MZ04 for $D_{\rm h}$ are larger than the expression given by Z92.
- The diffusion coefficient $D_{\rm shear}$ is the key quantity determining the efficiency of mixing in regions with weak or no μ-gradients, typically in the radiative envelope of massive stars above the H-convective core.
- The two expressions of $D_{\rm shear}$ are strictly equivalent in zones with no μ-gradients.
- The ratio $D_{\rm shear}({\rm M97})/D_{\rm shear}({\rm TZ97}) \sim K/D_{\rm h}$ in regions where $\frac{\varphi}{\delta}\nabla_\mu$ is significantly larger than the difference $\nabla_{\rm ad} - \nabla_{\rm rad}$. Since $D_{\rm h}$ is inferior to K, one has that $D_{\rm shear}({\rm M97}) > D_{\rm shear}({\rm TZ97})$.

1.2 The Models Computed

In the present work, we study the implications of these different choices on the following model outputs:

- Evolutionary tracks and lifetimes during the Main-Sequence (MS) phase.
- Changes of the surface composition during the MS phase.
- Changes of the surface velocities during the MS phase.
- The distribution of the core helium lifetime in the blue and red parts of the HR diagram.
- The extensions of the blue loops.
- The evolution of the angular momentum of the core.
- The synthesis of primary nitrogen in fast rotating metal poor massive stars.

For that purpose, we have computed models for different initial masses, metallicities, and rotations, with each one of the six possible combinations of values for ($D_{\rm shear}$, $D_{\rm h}$) (see Table 1.1). For each mass and metallicity, the models are labeled by one digit and one letter: 1 is for models computed with the shear diffusion coefficient of [13], and 2 for models computed with the shear diffusion coefficient of [30]; the letters A, B, and C are respectively for the horizontal diffusion coefficient from [14, 20, 31].

In Table 1.1, the first column gives the prescription used. The time-averaged equatorial velocity during the MS phase is given in column 2, the MS lifetime is given in column 3, and the difference between the surface helium abundance in mass fraction at the end of the MS phase and on the ZAMS is given in column 4. Column 5 presents the N/H ratio obtained at the surface, at the end of the MS phase, and normalized to the initial N/H value. The core He-burning lifetime and the analogs of columns 4 and 5 but at the end of the core He-burning phase are indicated in columns 6, 7, and 8, respectively. The duration of the core He-burning phase spent in the red ($\log T_{\rm eff} < 3.68$), blue ($\log T_{\rm eff} > 3.87$), and yellow ($3.68 < \log T_{\rm eff} < 3.87$) parts of the HR diagram are given in columns 9, 10, and 11, respectively. The ratio of the time spent in the blue to that spent in the red is shown in column 12, and the masses of the helium cores, of the carbon-oxygen cores, and of the remnants are given in columns 13, 14, and 15. The mass of nitrogen produced divided by the mass of CNO elements initially present is given in column 16.

1.3 Evolutionary Tracks and Lifetimes During the Main-Sequence Phase

Figure 1.1 presents the tracks in the Hertzsprung–Russell diagram (left panel) and the variation of the mass fraction of hydrogen as a function of the Lagrangian mass coordinate (right panel) for the $15 M_{\odot}$ at $Z = 0.002$ and with $\Omega_{\rm ini}/\Omega_{\rm crit} = 0.5$. One can classify the models in three categories:

1. The models which present very little differences with respect to the nonrotating model. These are the models 2B (not shown in Fig. 1.1) and 2C.
2. The models which become overluminous with respect to the nonrotating model but present no significant extension toward lower effective temperatures. These are the models 1A, 1B (not shown), and 1C.

Table 1.1 Models computed in the present work

	$\overline{v}_{eq}$ km s^{-1}	t_H My	ΔY_s	$\frac{(N/H)}{(N/H)_{ini}}$	t_{He} My	ΔY_s	$\frac{(N/H)}{(N/H)_{ini}}$	t_{blue} My	t_{red} My	t_{yel} My	$\frac{t_{blue}}{t_{red}}$	M_{He} $M_\odot$	M_{CO} $M_\odot$	M_{rem} $M_\odot$	$\frac{M(^{14}N)}{M(CNO_{ini})}$
$9M_\odot$, $Z = 0.002$, $v_{ini}/v_{crit} = 0.5$															
1A	177	30.065	+0.0149	4.9	2.966	0.0157	4.9	3.0964	0.0970	0.0104	31.9	2.9	1.5	1.3	0.5
1B	−0.6 %	−11.8 %	+0.0051	3.8	+37.6 %	0.0055	3.8	+37.5 %	+21.0 %	+27.9 %	36.3	2.7	1.5	1.3	0.5
1C	+0.6 %	−13.3 %	+0.0024	3.1	+28.9 %	0.0064	3.8	+28.6 %	+63.1 %	× 2	25.2	2.5	1.4	1.2	0.5
2A	−1.1 %	+0.3 %	+0.0004	2.2	−11.7 %	0.0123	3.5	−52.4 %	× 11.1	× 27.3	1.4	2.9	1.5	1.3	0.4
2B	−2.2 %	−11.7 %	+0.0003	3.0	+17.4 %	0.0040	4.2	−10.4 %	× 9.6	× 8.7	3	2.6	1.4	1.2	0.9
2C	+0.6 %	−13.3 %	+0.0017	3.4	+37.1 %	0.0099	4.8	+27.7 %	× 3.8	× 3.3	10.8	2.5	1.6	1.3	0.4
$9M_\odot$, $Z = 0.014$, $v_{ini}/v_{crit} = 0.5$															
1A	163	31.423	+0.0050	2.5	3.291	0.0620	5.8	1.3982	2.0974	0.0997	0.7	2.5	1.4	1.2	0.4
1B	−1.2 %	−13.0 %	+0.0009	1.8	+47.6 %	0.0363	4.9	+64.0 %	+35.1 %	−14.0 %	0.8	1.6	1.4	1.2	0.3
1C	−0.6 %	−14.7 %	+0.0003	1.6	+36.1 %	0.0314	4.7	+53.8 %	+27.2 %	−18.7 %	0.8	1.4	1.2	1.1	0.4
2A	−0.6 %	−0.2 %	+0.0001	1.3	−5.3 %	0.0495	4.5	−42.9 %	+12.5 %	× 2.1	0.3	2.5	1.4	1.2	0.3
2B	−1.8 %	−12.9 %	+0.0000	1.6	+17.5 %	0.0240	4.2	$\times \frac{1}{9.2}$	× 2.0	0.0	0.04	1.7	1.1	1.1	0.4
2C	−0.6 %	−14.7 %	+0.0002	1.7	+36.8 %	0.0242	4.7	$\times \frac{1}{8.8}$	× 2.3	$\times \frac{1}{14.4}$	0.03	1.5	1.3	1.2	0.3

Table 1.1 (Continued)

	$\overline{\upsilon}_{\rm eq}$ km s^{-1}	$t_{\rm H}$ My	ΔY_s	$\frac{(N/H)}{(N/H)_{\rm ini}}$	$t_{\rm He}$ My	ΔY_s	$\frac{(N/H)}{(N/H)_{\rm ini}}$	$t_{\rm blue}$ My	$t_{\rm red}$ My	$t_{\rm yel}$ My	$\frac{t_{\rm blue}}{t_{\rm red}}$	$M_{\rm He}$ $M_\odot$	$M_{\rm CO}$ $M_\odot$	$M_{\rm rem}$ $M_\odot$	$\frac{M(^{14}N)}{M(CNO_{\rm ini})}$
$15M_\odot$, $Z = 0.002$, $\upsilon_{\rm ini}/\upsilon_{\rm crit} = 0.5$															
1A	197	13.173	+0.0248	5.4	1.323	0.0612	6.9	1.2622	0.0749	0.0416	16.9	5.3	3.0	1.7	0.4
1B	−3.0 %	−2.2 %	+0.0215	5.1	+8.8 %	0.0237	7.1	+18.6 %	0.0	$\times\frac{1}{3.5}$	–	4.8	2.8	1.6	0.5
1C	−2.5 %	−5.3 %	+0.0105	4.2	+12.9 %	0.0496	5.9	+24.6 %	0.0	0.0	–	4.5	2.6	1.6	0.5
2A	−0.5 %	−0.4 %	+0.0012	2.4	−17.5 %	0.0549	5.8	$\times\frac{1}{34.2}$	× 4.5	$\times\frac{1}{2.7}$	0.03	5.8	3.6	1.8	0.4
2B	−3.0 %	−11.5 %	+0.0006	3.1	+1.8 %	0.0110	4.3	+6.3 %	−35.1 %	$\times\frac{1}{2.0}$	27.6	4.9	2.8	1.6	0.4
2C	−1.5 %	−13.5 %	+0.0039	3.9	+43.9 %	0.0047	4.0	+53.9 %	$\times\frac{1}{8.6}$	$\times\frac{1}{3.6}$	167.5	4.6	3.4	1.8	0.4
$40M_\odot$, $Z = 0.00001$, $\upsilon_{\rm ini}/\upsilon_{\rm crit} = 0.75$															
1A	702	5.559	+0.0949	47.9	0.409	0.0964	48.2	0.4161	0.0	0.0	–	17.1	14.0	4.3	1.1
1B	−2.4 %	−2.6 %	+0.0743	44.2	+5.7 %	0.0753	44.4	+6.0 %	0.0	0.0	–	16.7	12.8	4.1	15.3
2A	−2.8 %	+1.4 %	+0.0459	30.7	−2.5 %	0.2006	50.9	−20.8 %	0.0	0.0748	–	23.9	17.3	5.3	8.2
2B	−5.3 %	−7.4 %	+0.0162	27.1	>5.2 %	0.0164	27.2	+4.8 %	0.0	0.0	–	20.9:	12.9:	4.1:	105.8:

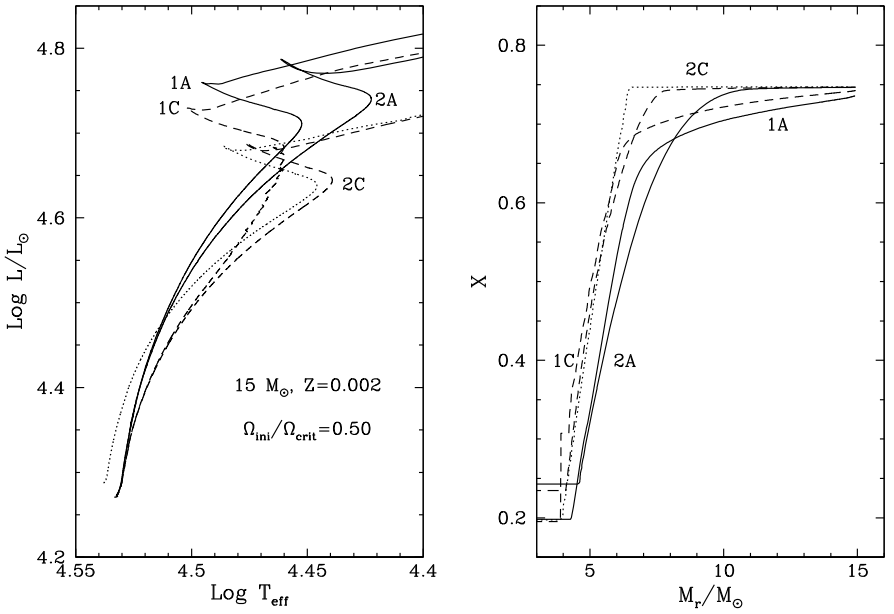

Fig. 1.1 Evolutionary tracks in the Hertzsprung–Russell diagram (*left panel*) and the variation of the mass fraction of hydrogen as a function of the Lagrangian mass coordinate (*right panel*) for the $15M_{\odot}$ at $Z = 0.002$ and with $\Omega_{\rm ini}/\Omega_{\rm crit} = 0.5$. The *dotted line* corresponds to the nonrotating model, and the other models are labeled as indicated in Table 1.1. The models used in the *right panel* have all a $\log T_{\rm eff}$ equal to 4.48. The central hydrogen mass fraction is equal to 0.1973 (nonrotating model), 0.1982 (*1A*), 0.2068 (*1C*), 0.2427 (*2A*), 0.2244 (*2C*). The models *1B* and *2B* are not shown since they present many similarities with the models *1C* and *2C*

3. Only one model, the model 2A, becomes overluminous and reaches lower effective temperatures at the end of the MS phase.

This behavior reflects differences in the efficiency of mixing in different regions of the stars. The models which are of the less efficiently mixed stars (2B and 2C, due to large $D_{\rm h}$ and thus small $D_{\rm eff}$) show indeed very little difference in their nonrotating tracks (compare lines for the model 2C and the nonrotating model in Fig. 1.1). The model 2A presents a situation where there is an efficient mixing at the border of the convective core but where the shear is not so efficient in the radiative envelope. Thus, the surface abundances are not yet modified at the stage represented in Fig. 1.1 (right panel). The larger core increases the luminosity and also is responsible for the extension toward lower temperature of the MS band in the HR diagram (an effect similar to an extension of the core produced by an overshoot). Finally, the model which presents the greatest efficiency of mixing both at the border of the core and in the radiative zone is the model 1A. This mixing keeps this model in bluer positions in the HR diagram compared to model 2.

One notes that in model 1A, the μ-gradient (with respect to mass) is steeper than in the model 2A, while both models have the same expression for $D_{\rm eff}$ (since they

have the same expression for $D_{\rm h}$). This is because in model 1A, which has $D_{\rm shear}$ larger than in 2A, hydrogen flows more efficiently inwards and helium outwards. This replenishes hydrogen at the border of the core. The net effect of these diffusions of hydrogen and helium is to make the star more luminous and bluer. The same occurs in the 1C model, although the effect is less marked because of the smaller value for $D_{\rm eff}$.

In Table 1.1, the MS lifetimes are indicated in column 3. The first row for each model gives the value of the MS lifetime in million years for the model 1A. The rows for the other models show the differences in percentage with respect to the value obtained for the model 1A. We see that the impact on the MS lifetimes remains modest (at most 13.5 % for the $15M_{\odot}$ models considered here) with respect to the precision with which an age estimated can be made through the fitting of an isochrone in this mass domain. On the other hand, the scatter is not negligible with respect to the amplitude of the effect of the increase of the MS lifetime due to rotation. Indeed, the increase of the MS lifetime with respect to the nonrotating case amounts to 18.5 % for the $15M_{\odot}$ model.

All the models computed here account for the same overshoot, but Fig. 1.1 shows that the track will present quite different extensions due to the various prescriptions. One sees also that the models 1A and 2A (those computed with the smaller $D_{\rm h}$ and thus greater $D_{\rm eff}$) are the only ones presenting an extension of the core with respect to the nonrotating model. Therefore, only the use of these two prescriptions can attribute part of the extension of the convective core to an effect of rotational mixing. Let us note that the recent determination of the extension of the mixed core in fast rotating stars by [27] seem to support the view that rotation enlarges the convective core. This would support prescriptions 1A or 2A. In that case, one should use slowly rotating stars in order to constrain the extension of the core due to the process of convective penetration alone as is done, for instance, in [7].

1.4 Changes of the Surface Composition During the MS Phase

The changes of the surface composition during the MS phases can be seen in Table 1.1 and in Fig. 1.2 for the $15M_{\odot}$ at $Z = 0.002$ and $\Omega_{\rm ini}/\Omega_{\rm crit} = 0.5$ cases. Columns 3 and 4 of Table 1.1 give, at the end of the MS phase, the excesses of helium at the surface of the star (in mass fraction and with respect to the initial value) and the ratio of nitrogen to hydrogen normalized to the initial value, respectively.

Independent of the prescriptions used, one notes, as was already obtained in previous works (see [16]), that the surface enrichment in nitrogen increases in increasing initial stellar masses and that it also increases for decreasing metallicity, in both cases keeping the initial rotation the same and comparing stars at similar evolutionary stages.

One sees also that the surface enrichments are higher when $D_{\rm shear}$ is higher (compare models of series 1 with models of series 2). This is quite logical since $D_{\rm shear}$ is the parameter which governs the transport of chemical elements in the region extending from the vicinity of the core up to the surface.

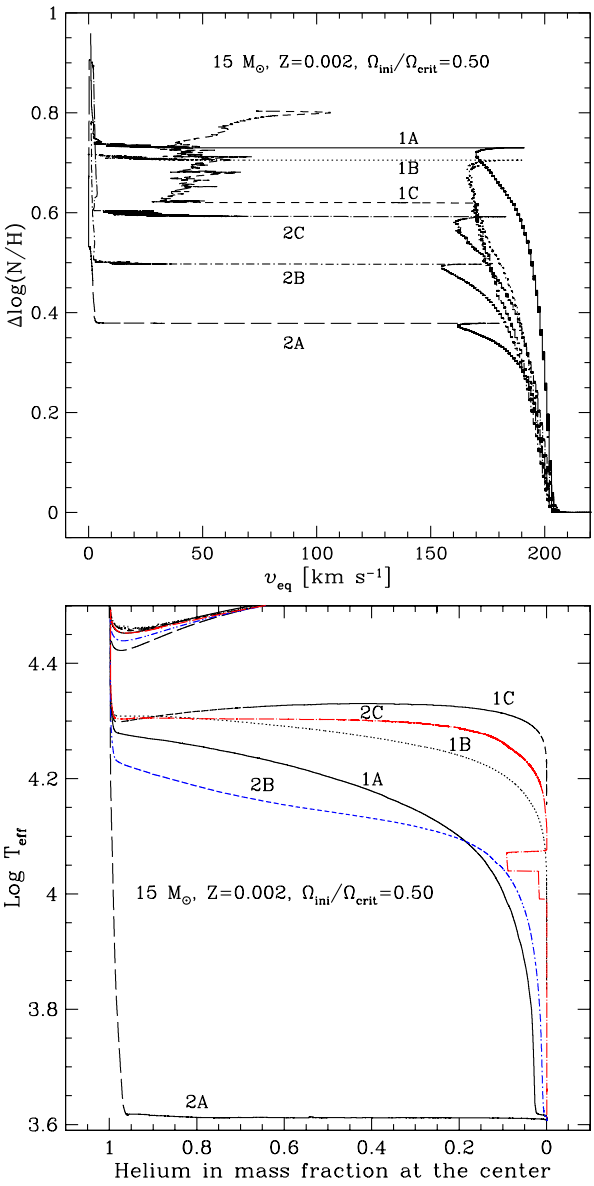

Fig. 1.2 *Upper panel*: Evolution of the N/H ratio at the surface of stellar models computed with various diffusive coefficients as a function of the equatorial velocity. *Lower panel*: Evolution of the effective temperature during the core He-burning phases for different prescriptions of the diffusive coefficients

The greatest surface enrichments are always obtained for the model 1A, the smallest for the model 2A (except for the very metal poor $40M_{\odot}$ model, but the difference between models 2A and 2B is quite small). For a given model, the variation of the prescriptions used produces a scatter of the N/H value obtained at the end of the MS phase of around a factor of 2. For the excesses in helium, the factors are

greater, however, except for the $40M_{\odot}$ at $Z = 0.00001$ case, the enhancements are very modest and well below those which could be estimated from observed spectra.

1.5 Changes of the Surface Velocity During the MS Phase

Column 2 in Table 1.1 compares the time-averaged equatorial velocity during the MS phase. The first row of the table indicates the equatorial surface velocity for model 1A in $\mathrm{km\,s^{-1}}$. The other lines indicate the difference in percentage with respect to model 1A. One sees that the differences are always less than 5.3 %, which is small. This is due to the fact that changing the prescriptions for the diffusion coefficients has only a very weak impact on the velocity of the meridional currents. Thus, the transport of the angular moment which is mainly driven by these currents is almost unaffected by changes of the diffusion coefficients.

This can also be seen in Fig. 1.2 (lower panel), which shows the variation of the nitrogen enhancement with respect to the surface equatorial velocity (tracks on this diagram go from right to left as time proceeds). One sees that during the MS phase, all of the models span the same interval in equatorial velocities. What changes is the surface nitrogen enrichment obtained at the end of the MS phase. In the plane N/H versus υ_{eq}, model 1A will produce a steeper relation than model 2A.

If one considers mean values of the ratio N/H for B dwarfs in the Galaxy and in the SMC, one obtains enhancement factors between 1.6 and 2.5 for the Galaxy and 3.2 and 6.3 for the SMC (see Table 2 in [17] and references therein). These mean values should be obtained for stars with an average rotation during the MS phase of around $200\ \mathrm{km\,s^{-1}}$.

At solar metallicity, the $15M_{\odot}$ model 1A well reproduces the observed enrichments [7]. This is not a surprise, since the value of the parameter f_{energ} in D_{shear}, chosen equal to one, has been selected in order to fit these observed enrichments. With the same value of f_{energ}, the $15M_{\odot}$ at $Z = 0.002$ with an average rotation of $200\ \mathrm{km\,s^{-1}}$ and prescriptions 1A predicts an enhancement factor between 3 and 5.3 in the last third of its MS lifetime, which is in the range of the observed values. In that case, no calibration has been made, and the good fit supports this kind of model. The other prescriptions gives too low surface enrichments keeping f_{energ} equal to 1.

We note that a value equal to 1 for f_{energ} implies that we really account for the physics involved into the expression for D_{shear}, which would not be the case if one would have to multiply the expression by a constant much greater or much smaller than one!

1.6 The Distribution of the Core Helium Lifetime in the Blue and Red Parts of the HR Diagram

The observed number of blue to red supergiants in clusters at different metallicities is an important feature that stellar models should be able to reproduce. This is

important for many reasons, for instance, to predict the correct photometric evolution of young starburst regions or the nature of the progenitors of the core collapse supernovae. It happens that observation shows that the blue-to-red ratio in clusters with masses at the turn off between $9M_{\odot}$ and $30M_{\odot}$ increases when the metallicity increases, while standard stellar models predict that the blue-to-red supergiant ratio decreases when the metallicity increases [6, 12, 21, 25]. The blue-to-red supergiant ratio has also been discussed in the context of field stellar populations in [5, 9].

At the moment, there is no explanation for this general trend. On the other hand, many works could reproduce the blue-to-red supergiant ratios observed at one given metallicity by changing the mass loss rates (see, e.g., [28]) or mixing [12, 16]. In this paper we shall not discuss all the aspects of this question but focus on the importance of mixing.

Looking at the right panel of Fig. 1.2, which shows the evolution of the effective temperature during the core Helium burning phase, we see that only one set of diffusion coefficients (the one using the $D_{\rm shear}$ of Talon and Zahn 1997 and the $D_{\rm h}$ of Zahn 1992) makes the $15M_{\odot}$ at $Z = 0.002$ evolve rapidly to the red part of the HR diagram after the MS phase. This is the prescription that we used in [16], where we suggested that rotational mixing could help a lot in reproducing the observed blue-to-red supergiant ratio in the Small Magellanic Cloud. In view of the present results, we see that, while this conclusion might always be correct, it is however quite dependent on the prescriptions used for the diffusion coefficients.

It is interesting to identify from the numerical experiments performed in this work the conditions which favor a rapid redward evolution at low metallicity. It does appear that two conditions have to be satisfied: (1) The mixing at the border of the convective cores (both during the H- and He-burning phases) have to be sufficiently efficient. Indeed, we see that any very strong values for $D_{\rm h}$ that prevent any strong mixing in regions with strong molecular weight gradient (μ-gradient) also prevent the star evolving to the red phase. (2) The mixing in the zones where the μ-gradients are weak, namely the outer part of the radiative envelope, should not be too strong, because any strong mixing there would make the star be more "homogeneous" and thus maintain a bluer position in the HR diagram. As very often noticed in the literature, we see that this red-to-blue evolution is a feature which is very sensitive to many physical ingredients of the models. The fact that it depends on subtle changes of the efficiency of mixing in different regions of the star is just one illustration of this.

Taken at face value, the set of diffusion coefficients $D_{\rm shear}$ from [30], and the $D_{\rm h}$ of [31] appear as the most favored to explain the blue-to-red supergiant ratio at low metallicity. However, other parameters—for instance, the changes of the surface abundances expected for an averaged rotational velocity—are better fitted with the prescription 1A (keeping $f_{\rm energ} = 1$). Moreover, since mass loss, both during the MS phase and at the red supergiant phase, plays a key role in shaping the blue-to-red supergiant ratio (see, e.g., the discussion in [25]), it may be premature to use the observed variation of the blue-to-red supergiant ratio to constrain the prescription to be used. Probably in order to make progress in this area of research, two important points have first to be settled: (1) to distinguish, using observations of the surface

abundances and/or of the vibrational properties, those blue supergiants which are direct successors of MS stars from those which are on a blue loop after a red supergiant stage; the ability to distinguish, at different metallicities, between those blue supergiants coming from the MS phase from those coming from the red supergiant phase would improve considerably our understanding of the blue supergiant formation process; (2) to obtain more reliable mass loss rates especially during the red and blue supergiant phases.

1.7 The Extensions of the Blue Loops

Another feature which is sensitive to the form of the diffusion coefficients is the extension of the blue loops for stars with masses between about $3M_{\odot}$ to $12M_{\odot}$. This is important in order to predict the populations of Cepheids, and also for the blue-to-red supergiant ratio discussed above, since the presence of a blue loop (when compared with the same model without blue loop) will reduce the lifetime of red supergiant but increase that of the blue supergiant.

Looking at Fig. 1.3, we can see the following features: at $Z = 0.002$, the duration of the blue loops increases more and more passing from models 2A to 2B, and then to 2C. When the D_{shear} is changed (model 1), the "loop" (if we can still speak of a loop in this case) even begins in the blue part of the HR diagram.

At $Z = 0.014$, the situation is quite different. First, the loops in all models are significantly reduced, which is a well-known effect when the metallicity increases. Second, models 2B and 2C do not show any loops. If such prescriptions were to be adopted, then only slow rotators could show blue loops and thus explain the existence of Cepheids.

We can note also that in the first set of models (labels beginning with one, i.e., D_{shear} from Maeder 1997), the impact of changing D_{h} on blue loops is quite modest in both metallicities. In the second set of models, changing D_{h} has a strong effect.

At low metallicity, models 2A for $9M_{\odot}$ would be the more helpful to reconcile the theoretical predictions with the observations as was suggested from previous section which focused on $15M_{\odot}$ stellar models. At solar metallicity, whatever model is considered, the blue-to-red supergiant ratios do appear too low (at most 1 while it is observed at around 3). At this metallicity, the problem may be at least partially cured by enhancing the mass loss rate during the red supergiant phase.

1.8 The Angular Momentum of the Core

During the evolution of a star, the core loses some angular momentum, mainly due to the effect of meridional currents. It happens that, in shellular rotating models without interior magnetic field, these losses are not sufficient to explain the relatively long observed rotation periods of young pulsars [10]. This is the reason why some authors have considered much stronger coupling between the core and the

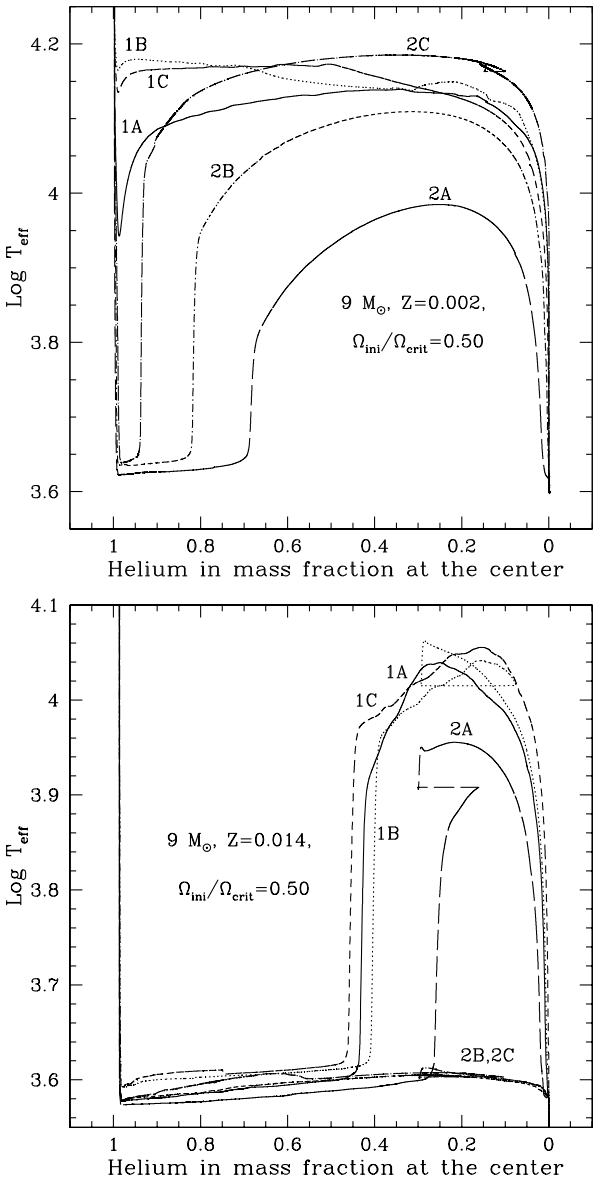

Fig. 1.3 *Upper panel*: Evolution of the effective temperature during the core He-burning phases for different prescriptions of the diffusive coefficients in a rotating $9M_{\odot}$ stellar model at $Z = 0.002$. *Lower panel*: Same as *upper panel* at $Z = 0.014$

envelope by introducing a magnetic field which forces solid body rotation or near solid body rotation during the MS phase [11]. Here, we have not accounted for such a strong coupling. A question however that we may ask is the extent to which this loss of angular momentum depends on the prescription used. Are there any of these prescriptions which would significantly change the angular momentum contained in the core at the end of its evolution?

A priori, one would expect that the loss of angular momentum by the core due to the transport processes should be only slightly dependent on the various prescriptions because, as already stressed, during most of the stellar lifetime, angular momentum is transported by the meridional currents whose velocities are only weakly dependent on the choice of $D_{\rm h}$. Let us, however, check this point in the numerical models that we have. Since we have not pursued the computation beyond the end of the core He-burning phase, we compare here the angular momentum of the core obtained at the end of the core helium burning phase. The masses of the remnant of the different $15M_{\odot}$ $Z = 0.002$ models are between $1.6M_{\odot}$ and $1.8M_{\odot}$. The angular momentum which would be locked into the $1.6M_{\odot}$ remnant supposing that no change does occur in the advanced phases of the evolution, would be between 0.93 and 1.14×10^{50} g cm^{-2} s^{-1} depending on the prescription used. The analog values in the case that the remnant is $1.8M_{\odot}$ would be between 1.19 and 1.44×10^{50} g cm^{-2} s^{-1}. So we see that these quantities present a scatter around their mean values of at most 20 %.

Is such a scatter important? As it concerns the missing angular momentum loss of the core, the answer is clearly no. To illustrate this, let us derive the following numerical estimate: if we lock an angular momentum content of 1×10^{50} g cm^{-2} s^{-1} in a neutron star, it would show a rotation period of about 0.1 ms, smaller by a factor between 4 and 7 than the critical periods for neutron stars, which are between 0.44 and 0.65 ms as given by [8]. The period is also smaller by two to three orders of magnitude than the observed periods of young pulsars which are between 20 and 100 ms [19, 26]. We can at least conclude that the missing transport mechanism cannot be due to a particular choice of the diffusion coefficients for $D_{\rm shear}$ and $D_{\rm h}$, since whatever choice is made, the angular momentum content of the core is more or less the same at the end of the core He-burning phase.

The angular momentum losses of the core may be underestimated either during the H and He-burning phases of the star and/or in the advanced phases and/or at the time of the supernova explosion and/or during the early years of the evolution of the new born neutron star. It may be that magnetic braking may play a role in this context [24].

1.9 The Synthesis of Primary Nitrogen in Fast-Rotating Metal-Poor Massive Stars

Fast-rotating massive stars may be the sources of primary nitrogen in the early phases of the evolution of galaxies [3, 4]. Therefore, it is important to assess the extent to which the primary nitrogen production depends on the prescriptions used. In the last column of Table 1.1, we have indicated the mass of nitrogen (in solar masses) present in the region outside the stellar remnant normalized by the mass of CNO elements that were initially present in the same region of the star. We call this quantity M(^{14}N)/M(CNO). When nitrogen is produced by the transformation of the carbon and oxygen initially present in the star (secondary nitrogen production

channel), then the quantity shown in Table 1.1 can at most be equal to one. It would be one if all the carbon and oxygen initially present in that region were to have been transformed into nitrogen. Actually it is less than one because, in the regions inside the H-burning shell, the nitrogen which has been produced by the CNO burning will then have been further transformed into ^{22}Ne.

We see that M(^{14}N)/M(CNO) is inferior to one except in the fast-rotating very metal-poor $40M_{\odot}$ stellar models. This illustrates the results already discussed by [22, 23] that rotational mixing, by bringing carbon and oxygen (freshly synthesized in the helium-burning core) into the H-burning shell, enhances significantly the quantities of nitrogen produced. The quantities produced are no longer limited by the initial metallicity of the star, since the carbon and oxygen transformed into nitrogen are synthesized by the star itself through helium transformation (primary nitrogen production channel).

We see, however, that the enhancements of primary nitrogen production present great variations depending on the prescriptions used for $D_{\rm shear}$ and $D_{\rm h}$. Before we analyze these results in more detail, let us recall a few general facts:

1. Primary nitrogen production depends on the efficiency of transport mechanisms in the region between the He-burning core and the H-burning shell;
2. The diffusion coefficient which dominates the transport in that region is $D_{\rm shear}$. A careful reader may be puzzled by such a statement since we mentioned above that $D_{\rm shear}$ operates mainly in weak μ-gradient regions while the appropriate diffusion coefficient in strong μ-gradient regions would be $D_{\rm eff}$. Does it mean that the μ-gradients are not so strong at the border of the He-burning core? The answer is yes. Indeed, in the core-shell intermediate region, most of the time, the gradients of μ are not very strong since the connected regions are all helium rich; moreover, the gradient of Ω which enters into the expression for $D_{\rm shear}$ is important.
3. Since $D_{\rm shear}$ is the dominant diffusion coefficient, the gradient of Ω becomes the key factor for primary nitrogen production, a small gradient producing less efficient shear mixing than a steep gradient.

In Fig. 1.4, we can see the variations of Ω as a function of the radius in the $40M_{\odot}$ stellar models when the mass fraction of helium in the core is equal to 0.45 (that means models at the middle of the core He-burning phase). We see that models using the prescription by [13] have a smooth gradient immediately above the convective core and show in outer zones a succession of regions with very steep and flat gradients. We shall call this zone the cliff. The cliff corresponds to the transition between the envelope and the core. The H-burning shell is more or less at its base (see Fig. 1.4).

The smooth gradient results, at least in part, from the activity of the shear transport having occurred during the core He-burning phase. The flat Ω regions in the cliff are produced by intermediate convective zones that are no longer present at the stage shown in the figure but have appeared in previous stages of the evolution of the star. In the present models, we assume that convective regions rotate as solid bodies, hence the flattening of Ω in these zones. The flat regions present a very low $D_{\rm shear}$

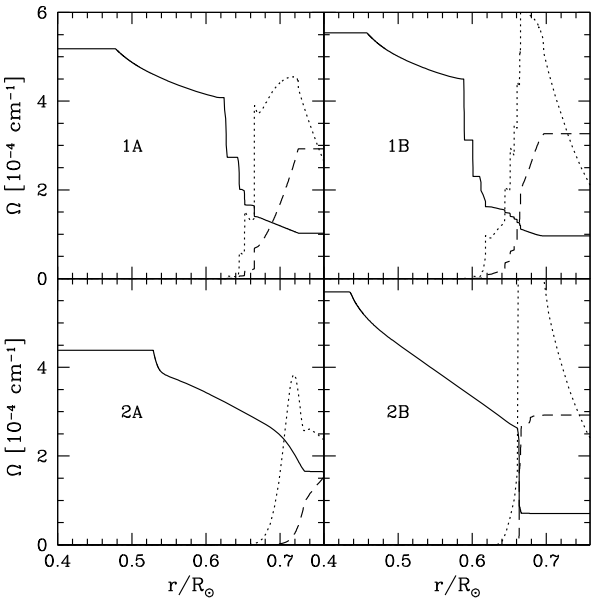

Fig. 1.4 Variation of the angular velocity as a function of the radius inside the $40M_{\odot}$ stellar models when the mass fraction of helium at the center is equal to 0.45. The *dotted lines* show, in each model, the variation as a function of the radius of the rate of production of energy by H-burning, ε_{H}, in units of 10^5 erg g^{-1} s^{-1}. The *long-dashed line* shows the mass fraction of hydrogen

coefficient since the Ω-gradients are very small. The part of the Ω profile which is important for primary nitrogen production is the portion with a smooth gradient just above the He-burning core.

In the model 1B (higher D_{h} and thus smaller D_{eff}), we note that the smooth gradient zone is more compact, making the gradient of Ω in that region steeper. This results from the less efficient chemical mixing at the border of the H-burning core. As a result, the helium core will be smaller, and the transition zone between the core and the shell will be in a deeper part of the star. Since model 1B presents a steeper gradient of Ω in the smooth gradient zone, it produces more primary nitrogen than model 1A (see Table 1.1).

The configurations presented in the bottom panels, resulting from prescriptions 2A and 2B, show different characteristics with respect to models 1A and 1B in upper panels: (1) just above the core the gradient of Ω is steeper; (2) the region with a succession of strong Ω-gradients and flat portions no longer exists. These two features result from less efficient shear transport at the border of the burning cores. Again, as in model 1, we see that when high values of D_{h} are used, stronger gradients are obtained.

We can see from Table 1.1 that, actually, the primary nitrogen production is larger in the models 1B, 2A, and 2B than in model 1A as can be expected from the line of reasoning above. An interesting conclusion of this discussion is that primary nitrogen production depends mainly of the gradient of Ω just above the helium burning core.

1.10 Conclusions

We have studied the impact of various prescriptions on important outputs of rotating massive star models. The main conclusions are the following:

- The outputs of stellar models which show marginal dependence on the prescriptions used for $D_{\rm shear}$ and $D_{\rm h}$ are the MS lifetimes, the evolution of the surface velocities, and the evolution of the angular momentum of the core.
- The outputs of stellar models that show significant dependence on the prescriptions used for $D_{\rm shear}$ and $D_{\rm h}$ are the shape of the evolutionary tracks, the surface enrichments predicted for a given initial rotation, the blue-to-red evolution, and the extensions of blue loops and the amount of primary nitrogen produced.
- The general trends of the increase of the mixing efficiency with the increase of the initial mass of the star, of its initial rotation, and with the decrease of the initial metallicity remain the same whatever the prescriptions used for $D_{\rm shear}$ and $D_{\rm h}$.

The hope would be, of course, to identify the most realistic diffusion coefficients on the basis of physical considerations. From an analytic point of view, the difficulty is mainly in how to treat turbulence. This is reflected by the fact that in each of these expressions, a free parameter is present ($f_{\rm energ}$ in $D_{\rm shear}$ for instance). At the moment, this free parameter is chosen so as to allow models to reproduce one well-identified observed feature (for instance, the surface enrichments observed at the surface of MS B-type stars at solar metallicity). Thus, a good fit with the observed feature which has been used to calibrate the models is not a test of the models. The tests of the models are comparisons with other observed features such as comparisons with surface enrichments for other velocities, metallicities, or initial mass ranges. We show above that prescription 1A can account for the observed enrichments in the SMC, while the prescription has been calibrated on solar metallicity stars. Thus, this can be viewed as a support of this kind of model.

We see also that one set of prescriptions cannot give satisfactory fit to all the observed features discussed here. This is expected since these observed features are not all governed only by the way mixing is treated. As indicated in the paper, the blue-to-red supergiant ratio, for instance, also depends a lot on the way in which the mass loss due to stellar winds is implemented in the models. Moreover, other effects, not accounted for here, such as close binary evolution or magnetic braking, may also contribute to some of the observed features.

The key to progress on the theoretical front would seem to be the ability to treat turbulence in a more rigorous way. Probably multidimensional hydrodynamical simulations can provide important hints on this topic [1].

Another complementary approach is to use well-observed stars to constrain the models. Stellar models that can account for many observed features have a great chance to provide a realistic description of the structure of stars. It may be sometimes for wrong reasons, in the sense that the physical process invoked may not be exactly the one operating in nature, but the effect of the physical process actually occurring in nature, whatever it is, has some chance to produce the structure as obtained in the model which best fits the observations.

We are confident that improvements in the two directions of hydrodynamical simulations and comparisons of evolutionary models with observed stars will allow us to constrain the possibilities for the physics occurring in stellar interiors.

Acknowledgements The authors thank Dr. J.J. Green and Dr. Kévin Belkacem for the careful copy editing of the manuscript.

References

1. Arnett, W.D., Meakin, C.: Turbulent cells in stars: fluctuations in kinetic energy and luminosity. Astrophys. J. **741**, 33 (2011)
2. Chaboyer, B., Zahn, J.P.: Effect of horizontal turbulent diffusion on transport by meridional circulation. Astron. Astrophys. **253**, 173–177 (1992)
3. Chiappini, C., Hirschi, R., Meynet, G., Ekström, S., Maeder, A., Matteucci, F.: A strong case for fast stellar rotation at very low metallicities. Astron. Astrophys. **449**, L27–L30 (2006)
4. Chiappini, C., Ekström, S., Meynet, G., Hirschi, R., Maeder, A., Charbonnel, C.: A new imprint of fast rotators: low $^{12}C/^{13}C$ ratios in extremely metal-poor halo stars. Astron. Astrophys. **479**, L9–L12 (2008)
5. Dohm-Palmer, R.C., Skillman, E.D.: The ratio of blue to red supergiants in Sextans A from Hubble Space Telescope imaging. Astron. J. **123**, 1433–1437 (2002)
6. Eggenberger, P., Meynet, G., Maeder, A.: The blue to red supergiant ratio in young clusters at various metallicities. Astron. Astrophys. **386**, 576–582 (2002)
7. Ekström, S., Georgy, C., Eggenberger, P., Meynet, G., Mowlavi, N., Wyttenbach, A., Granada, A., Decressin, T., Hirschi, R., Frischknecht, U., Charbonnel, C., Maeder, A.: Grids of stellar models with rotation. I. Models from 0.8 to $120M_{\odot}$ at solar metallicity ($Z = 0.014$). Astron. Astrophys. **537**, A146 (2012)
8. Georgy, C., Ekström, S., Meynet, G., Massey, P., Levesque, E.M., Hirschi, R., Eggenberger, P., Maeder, A.: Grids of stellar models with rotation. II. WR populations and supernovae/GRB progenitors at $Z = 0.014$. Astron. Astrophys. **542**, A29 (2012)
9. Hartwick, F.D.A.: Radial variation in the ratio of blue to red supergiants in the galaxy. Astrophys. J. Lett. **7**, 151 (1970)
10. Heger, A., Woosley, S.E., Langer, N., Spruit, H.C.: Presupernova evolution of rotating massive stars and the rotation rate of pulsars (invited review). In: Maeder, A., Eenens, P. (eds.) Stellar Rotation. IAU Symposium, vol. 215, p. 591 (2004)
11. Heger, A., Woosley, S.E., Spruit, H.C.: Presupernova evolution of differentially rotating massive stars including magnetic fields. Astrophys. J. **626**, 350–363 (2005)
12. Langer, N., Maeder, A.: The problem of the blue-to-red supergiant ratio in galaxies. Astron. Astrophys. **295**, 685 (1995)
13. Maeder, A.: Stellar evolution with rotation II. A new approach for shear mixing. Astron. Astrophys. **321**, 134–144 (1997)
14. Maeder, A.: Stellar rotation: evidence for a large horizontal turbulence and its effects on evolution. Astron. Astrophys. **399**, 263–269 (2003)
15. Maeder, A.: Physics, Formation and Evolution of Rotating Stars. Springer, Berlin (2009)
16. Maeder, A., Meynet, G.: Stellar evolution with rotation. VII. Low metallicity models and the blue to red supergiant ratio in the SMC. Astron. Astrophys. **373**, 555–571 (2001)
17. Maeder, A., Meynet, G.: Rotating massive stars: from first stars to gamma ray bursts. Rev. Mod. Phys. **84**, 25–63 (2012)
18. Maeder, A., Zahn, J.P.: Stellar evolution with rotation. III. Meridional circulation with μ-gradients and non-stationarity. Astron. Astrophys. **334**, 1000–1006 (1998)
19. Marshall, F.E., Gotthelf, E.V., Zhang, W., Middleditch, J., Wang, Q.D.: Discovery of an ultrafast X-ray pulsar in the supernova remnant N157B. Astrophys. J. Lett. **499**, L179 (1998)

20. Mathis, S., et al.: On shear-induced turbulence in rotating stars. Astron. Astrophys. **425**, 243–247 (2004)
21. Meylan, G., Maeder, A.: Comparisons of the HR diagrams of the youngest clusters in the Galaxy, the LMC and SMC—evidence for a large MS widening. Astron. Astrophys. **108**, 148–156 (1982)
22. Meynet, G., Maeder, A.: Stellar evolution with rotation. VIII. Models at $Z = 10^{-5}$ and CNO yields for early galactic evolution. Astron. Astrophys. **390**, 561–583 (2002)
23. Meynet, G., Ekström, S., Maeder, A.: The early star generations: the dominant effect of rotation on the CNO yields. Astron. Astrophys. **447**, 623–639 (2006)
24. Meynet, G., Eggenberger, P., Maeder, A.: Massive star models with magnetic braking. Astron. Astrophys. **525**, L11 (2011)
25. Meynet, G., Georgy, C., Hirschi, R., Maeder, A., Massey, P., Przybilla, N., Nieva, M.F.: Red supergiants, luminous blue variables and Wolf–Rayet stars: the single massive star perspective. Bull. Soc. R. Sci. Liège **80**, 266–278 (2011)
26. Muslimov, A., Page, D.: Magnetic and spin history of very young pulsars. Astrophys. J. **458**, 347 (1996)
27. Neiner, C., Mathis, S., Saio, H., Lovekin, C., Eggenberger, P., Lee, U.: Seismic modelling of the late Be stars HD 181231 and HD 175869 observed with CoRoT: a laboratory for mixing processes. Astron. Astrophys. **539**, A90 (2012)
28. Salasnich, B., Bressan, A., Chiosi, C.: Evolution of massive stars under new mass-loss rates for RSG: is the mystery of the missing blue gap solved? Astron. Astrophys. **342**, 131–152 (1999)
29. Spruit, H.C.: Dynamo action by differential rotation in a stably stratified stellar interior. Astron. Astrophys. **381**, 923–932 (2002)
30. Talon, S., Zahn, J.-P.: Anisotropic diffusion and shear instabilities. Astron. Astrophys. **317**, 749–751 (1997)
31. Zahn, J.P.: Circulation and turbulence in rotating stars. Astron. Astrophys. **265**, 115–132 (1992)
32. Zahn, J.P., Brun, A.S., Mathis, S.: On magnetic instabilities and dynamo action in stellar radiation zones. Astron. Astrophys. **474**, 145–154 (2007)

Chapter 2
Transport Processes in Stellar Interiors

Stéphane Mathis

Abstract Stars are rotating and magnetic bodies. Moreover, more and more constraints are obtained on such dynamical processes using, for example, seismology and spectropolarimetry. Therefore, it is now necessary to get a complete and coherent picture of dynamical processes in stellar interiors. However, to simulate such processes in a star in full details would require treating length scales and time scales spanning many orders of magnitude. This is clearly not feasible, even with the most powerful computers available today. This is the reason why it is nowadays necessary to use and couple 1-D, 2-D, and 3-D modelings to get a global picture of macroscopic MHD transport processes in stellar interiors. In this review, we report the state of the art of the modeling of transport processes in stellar interiors (both in radiation and in convection zones) aimed to study the stars angular momentum history, the related profile of differential rotation, and their magnetism.

2.1 Introduction

Stars are rotating and magnetic bodies. Moreover, more and more constraints are obtained on such dynamical processes, for example, using helioseismology (see, for example, [47]), asteroseismology [10, 34, 43, 82], and spectropolarimetry [38]. Therefore, it is now necessary to get a complete and coherent picture of dynamical processes in stellar interiors. However, to simulate such processes in a star in full details would require treating length scales and time scales spanning many orders of magnitude. This is clearly not feasible, even with the most powerful computers available today. Therefore, either one chooses to describe what occurs on a dynamical time scale (such as a convective turnover time), or one focuses on the long-time

S. Mathis (✉)
Laboratoire AIM Paris-Saclay, CEA/DSM–Université Paris Diderot–CNRS, IRFU/SAp, CEA, 91191 Gif-sur-Yvette, France
e-mail: stephane.mathis@cea.fr

S. Mathis
LESIA, Observatoire de Paris–CNRS–Université Paris Diderot–Université Pierre et Marie Curie, Observatoire de Paris, 5 place Jules Janssen, 92195 Meudon, France

M. Goupil et al. (eds.), *Studying Stellar Rotation and Convection*,
Lecture Notes in Physics 865, DOI 10.1007/978-3-642-33380-4_2,

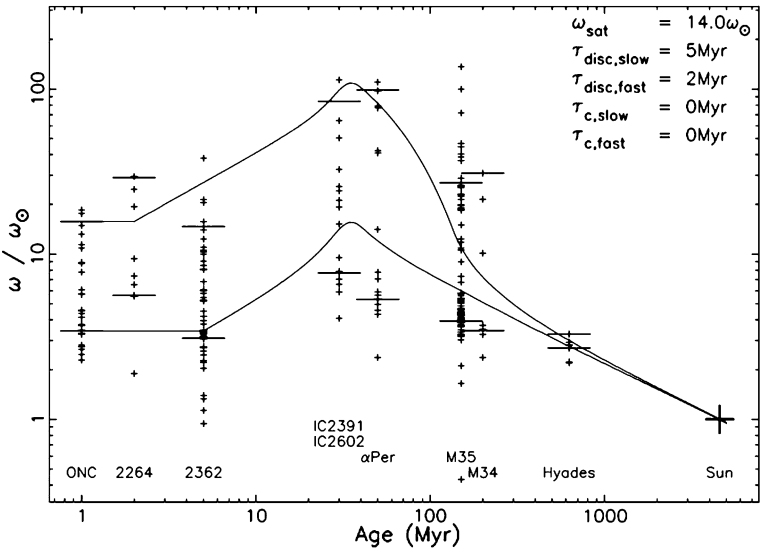

Fig. 2.1 Rotational angular velocity ω plotted as a function of time for stars with masses $0.9 < M/M_\odot < 1.1$. *Crosses* show the open cluster rotation period data such that each cluster collapses into a vertical stripe on the diagram, and *short horizontal lines* show the 25th and 90th percentiles of ω, used to characterize the slow and fast rotators, respectively. The *lines* show rotational evolution models for $1.0M_\odot$ stars, fitted to the percentiles for each cluster using a simple unweighted least squares method. For this plot, we have assumed that the stars rotate as solid bodies (i.e., constant ω as a function of radius inside the star). Plotted are the ONC, NGC 2264, NGC 2362, IC 2391, IC 2602, α Per, M35, M34, the Hyades, and the Sun. (Taken from [50], courtesy Cambridge University Press)

evolution where the typical time is either the Kelvin–Helmholtz time or that characterizing the dominant nuclear reactions. The same is true for the length scales. First, in the vertical direction, we have to choose the resolution that adequately represents the steepest gradients that develop during the evolution. Furthermore, in the horizontal direction, the resolution that allows one to describe convective structures, possible instabilities and turbulence has to be chosen. This is the reason why it is nowadays necessary to use and couple 1-D, 2-D, and 3-D modelings to get a global picture of macroscopic MHD transport processes in stellar interiors.

In this review, we report the state of the art of the modeling of transport processes in stellar interiors (both in radiation and in convection zones) aimed to study the star's angular momentum history (see [13, 50], Fig. 2.1), the related profile of differential rotation ([47], Fig. 2.2), and their magnetism. First, we recall the common methods used both on dynamical and secular time scales, namely the spectral expansion of MHD equations. Next, we focus on the behavior of convective regions and describe couplings between differential rotation, meridional circulation, turbulence, and magnetic field and the related dynamo processes. Then, we give a global picture of transport and mixing processes operating in stellar radiation zones. Finally, we conclude on the necessity of obtaining integrated models of stars from

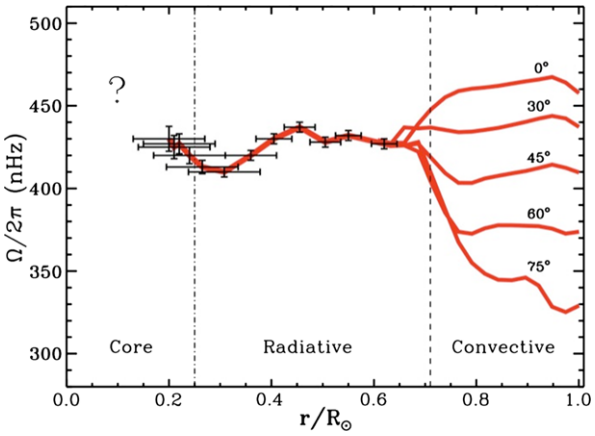

Fig. 2.2 Internal angular velocity in the Sun revealed by helioseismology ($R_\odot$ is the solar radius). It is conical in the convective envelope ($0.02M_\odot$, $M_\odot$ being the solar mass), uniform in the radiative core ($0.98M_\odot$), the transition layer, the tachocline being very thin (less than $0.04R_\odot$). (Taken from [47], courtesy Science)

their cores to their surfaces and to take into account in such models the action of the stellar environment.

2.2 Modeling

2.2.1 Preliminary Definitions

Here, we describe the method which is used to treat MHD equations in stellar interiors both in convective and in radiative regions.

First, the macroscopic velocity field is expanded

$$\mathbf{V}(\mathbf{r},t) = r\sin\theta\Omega(r,\theta,t)\hat{\mathbf{e}}_\varphi + \dot{r}\hat{\mathbf{e}}_r + \mathscr{U}_M(r,\theta,t) + \mathbf{u}(r,\theta,\varphi,t), \qquad (2.1)$$

where $\mathbf{r} = \{r,\theta,\varphi\}$ are the classical spherical coordinates with their associated orthonormal basis $\{\hat{\mathbf{e}}_j\}_{j=\{r,\theta,\varphi\}}$, with t being the time. The first term, where Ω is the internal angular velocity, is the azimuthal velocity field associated with the differential rotation. The second is the radial Lagrangian velocity due to the contractions and the dilatations of the star during its evolution. The third term is the large-scale meridional circulation velocity field ($\mathscr{U}_M$). Finally, $\mathbf{u}$ is the fluctuating velocity associated with turbulence or waves.

Next, the anelastic approximation is adopted to treat macroscopic large-scale transport processes. The continuity equation, $\partial_t\rho + \boldsymbol{\nabla}\cdot(\rho\mathbf{V}) = 0$, ρ being the density, thus becomes $\boldsymbol{\nabla}\cdot(\rho\mathbf{V}) = 0$, and acoustic waves are filtered.

Then, using the divergence-free property of the magnetic field, we expand it

$$\mathbf{B}(\mathbf{r},t) = \boldsymbol{\nabla}\wedge\boldsymbol{\nabla}\wedge\left[\xi_P(\mathbf{r},t)\hat{\mathbf{e}}_r\right] + \boldsymbol{\nabla}\wedge\left[\xi_T(\mathbf{r},t)\hat{\mathbf{e}}_r\right], \qquad (2.2)$$

where ξ_P and ξ_T are the poloidal and the toroidal magnetic stream functions.

For an axisymmetric magnetic field, the poloidal field $\mathbf{B}_P(r,\theta,t)$ is in the meridional plane $(\hat{\mathbf{e}}_r, \hat{\mathbf{e}}_\theta)$, while the toroidal one $\mathbf{B}_T(r,\theta,t)$ is purely azimuthal along $\hat{\mathbf{e}}_\varphi$.

The different fields being now defined, we have to consider the transport equations that have to be solved in stellar interiors.

2.2.2 Transport Equation System

The first transport equation we consider is the one related to the transport of magnetic field, namely the induction equation

$$\partial_t \mathbf{B} = \boldsymbol{\nabla} \wedge (\mathbf{V} \wedge \mathbf{B}) - \boldsymbol{\nabla} \wedge (\eta \boldsymbol{\nabla} \wedge \mathbf{B}), \tag{2.3}$$

η being the magnetic diffusivity. Two equations, for ξ_P and ξ_T respectively, are then obtained when the expansion given in Eq. (2.2) is introduced. First, they describe the advection of both poloidal and toroidal components of the field by the large-scale meridional currents, both in radiation and convection zones. Then, we get the creation of toroidal magnetic field by shearing the poloidal through differential rotation (the so-called Ω effect). Next, they give the Ohmic diffusion of each component. Finally, they describe the action of the turbulent magnetic field fluctuations, which will be possible in the case where the dynamo threshold is reached, to generate and sustain magnetic energy; this is the so-called α-effect in the mean-field formalism. Furthermore, in the case where secular time-scales are studied we take into account the Lagrangian variation of magnetic field due to the contractions and dilatations of the star during its evolution. This is the reason why we have introduced the time-Lagrangian derivative $\mathrm{d}/\mathrm{d}t = \partial_t + \dot{r}\partial_r$.

The second transport equation which has to be treated is the momentum equation, i.e., the Navier–Stokes equation

$$\rho\left[\partial_t \mathbf{V} + (\mathbf{V}\cdot\boldsymbol{\nabla})\mathbf{V}\right] = -\boldsymbol{\nabla} P - \rho\mathbf{g} + \boldsymbol{\nabla}\cdot\mathsf{T} + \left[\frac{1}{\mu_0}(\boldsymbol{\nabla}\wedge\mathbf{B})\right]\wedge\mathbf{B}. \tag{2.4}$$

Here P and $\mathbf{g}$ are respectively the pressure and the gravity, T is the viscous stress tensor, and the last term is the Lorentz force, where μ_0 is the magnetic permeability of vacuum. Taking its azimuthal component and averaging over φ, the 2-D equation (in r and θ) for the transport of angular momentum is obtained (see [27, 69]). In the case of both radiation and convection zones, it describes the advection of angular momentum by meridional flows and the actions of the viscous diffusion, of Reynolds stresses, of large-scale magnetic torque, and of Maxwell stresses. Furthermore, taking the curl of this equation and focusing on the azimuthal component gives the so-called thermal wind equation, which describes the baroclinicity of flows inside the star and which links the differential rotation to entropy fluctuations along isobars. In the convective regions the study of this equation allows one to study the behavior of the differential rotation, while in the radiation zones it allows one to close the transport loop.

The last transport equation that has to be solved is the heat transport equation for the macroscopic entropy (S):

$$\rho T\big[\partial_t S + (\mathbf{V}\cdot\boldsymbol{\nabla})S\big] = \boldsymbol{\nabla}\cdot(\chi\boldsymbol{\nabla}T) + \rho\varepsilon + \mathscr{Q}. \tag{2.5}$$

It describes the transport of entropy by advection, the thermal diffusion (χ is the thermal conductivity), the production of energy associated to nuclear reactions (ε is the nuclear energy production rate per unit mass), and the heating due to turbulence and Ohmic effects.

One should note that assuming hydrostatic and thermal equilibrium hypotheses in Eqs. (2.4) and (2.5) returns us to the standard stellar evolution equations.

Finally, the equation for the transport of chemicals

$$\rho\big[\partial_t c_i + (\mathbf{V}\cdot\boldsymbol{\nabla})c_i\big] = \boldsymbol{\nabla}\cdot\big[\rho(D_{\text{mic}} + \mathsf{D})\otimes\boldsymbol{\nabla}c_i\big] + \rho\dot{c}_i \tag{2.6}$$

has to be solved to study elements mixing. Here c_i is the concentration of the considered ith element, $\dot{c}_i$ its creation (destruction) rate, D_{mic} the microscopic diffusivity, and D the diffusivity tensor, which can be anisotropic, for example, in radiative regions that are highly stable stratified zones. Since turbulent movements in the convection zone are vigorous, chemicals are assumed to be instantaneously mixed there. In the radiation zone, the situation is different, and the secular action of transport processes in this region induces extra-mixing, which is necessary to explain observed surface chemical element abundances.

2.2.3 The Spectral Method

Once the system of MHD dynamical equations has been established, we solve it applying spectral methods in the horizontal direction. Then, because of the spherical geometry of the star, we describe both scalar quantities and vectorial fields using spherical harmonics.

Indeed, scalar quantities (X) are expanded as

$$X(\mathbf{r},t) = \overline{X}(r) + X'(r,\theta,\varphi,t) = \overline{X}(r) + \sum_{l=0}^{N}\sum_{m=-l}^{l}\big\{X_m^l(r,t)Y_l^m(\theta,\varphi)\big\}, \tag{2.7}$$

$\overline{X}$ being the hydrostatic value, and X' the fluctuation induced by transport processes.

Likewise, we expand the poloidal and toroidal magnetic stream functions:

$$\begin{aligned}\xi_P(\mathbf{r},t) &= \sum_{l=1}^{N_{\text{mag}}}\sum_{m=-l}^{l}\big\{\xi_{l,m}^P(r,t)Y_l^m(\theta,\varphi)\big\},\\ \xi_T(\mathbf{r},t) &= \sum_{l=1}^{N_{\text{mag}}}\sum_{m=-l}^{l}\big\{\xi_{l,m}^T(r,t)Y_l^m(\theta,\varphi)\big\}.\end{aligned} \tag{2.8}$$

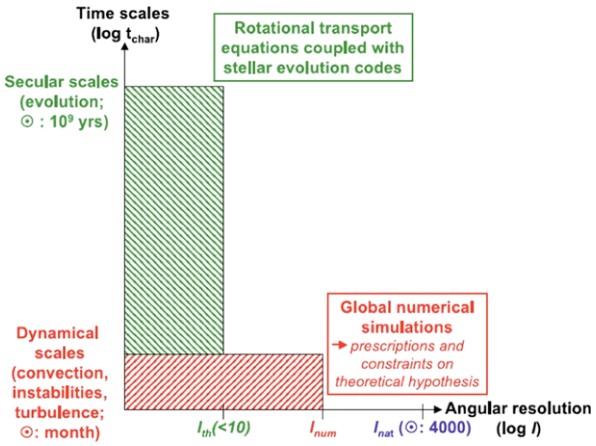

Fig. 2.3 Modeling strategy to study dynamical stellar evolution. The diagram presents time scales of the typical physical processes as functions of the angular resolution needed to properly describe these processes. The angular resolution is expressed in terms of the l index of the spherical harmonics $Y_l^m(\theta,\varphi)$. $l_{\rm num} \approx 600$ indicates the maximum angular resolution (in terms of spherical harmonics modes) presently achieved in global numerical simulations. (Adapted from [33], courtesy Astronomy & Astrophysics)

The expansion degree N (and $N_{\rm mag}$) on spherical harmonics depends on the problem which is treated (cf. Fig. 2.3). On the one hand, in a convection zone or if we study highly nonaxisymmetric and nonlinear processes in a radiative region such as shear-induced instabilities or fossil field MHD ones, we will use an expansion involving high-degree spherical harmonics. On the other hand, if transport processes in a radiation zone are studied on secular time scales, we will use only low-degree spherical harmonics but with an high radial accuracy to capture the strongest gradients which develop during the star evolution. This approach has allowed us to study, across the various scales of time and space, the problems of dynamical stellar evolution which cannot yet be modeled with direct numerical simulations.

Then, since transport equations such as the induction equation for the magnetic field and the momentum equation are three-dimensional vector equations, we expand vector fields (magnetic field and macroscopic velocity) in vectorial spherical harmonics as in stellar oscillations theory

$$\mathbf{u}(r,\theta,\varphi,t) = \sum_{l=0}^{N}\sum_{m=-l}^{l}\left\{u_m^l(r,t)\mathbf{R}_l^m(\theta,\varphi) + v_m^l(r,t)\mathbf{S}_l^m(\theta,\varphi) + w_m^l(r,t)\mathbf{T}_l^m(\theta,\varphi)\right\}, \tag{2.9}$$

where we have defined $\mathbf{R}_l^m(\theta,\varphi) = Y_l^m(\theta,\varphi)\hat{\mathbf{e}}_r$, $\mathbf{S}_l^m(\theta,\varphi) = \boldsymbol{\nabla}_{\rm H} Y_l^m(\theta,\varphi)$, and $\mathbf{T}_l^m(\theta,\varphi) = \boldsymbol{\nabla}_{\rm H} \wedge [Y_l^m(\theta,\varphi)\hat{\mathbf{e}}_r]$, while $\boldsymbol{\nabla}_{\rm H} = \hat{\mathbf{e}}_\theta \partial_\theta + \hat{\mathbf{e}}_\varphi \frac{1}{\sin\theta}\partial_\varphi$. These expansions (Eqs. (2.7) and (2.9)) allow us to separate variables in transport equations. Thus,

modal equations in r and t are solved in MHD spectral codes and in dynamical stellar evolution ones.

2.3 Dynamical Processes in Stellar Convection Zones

2.3.1 Convection, Differential Rotation, and Meridional Flows

First, in the case of the Sun, the most recent studies of global rotating convection in the external envelope have been achieved by the ASH group [25, 78, 80]. For the first time, the solar convection is now examined using global models with a strong density contrast of 150 from top to bottom. This leads to significant results on the turbulent convection spectra from large-scale (giant cell-like) down to supergranular-like convection patterns and their correlation with temperature fluctuations. Then, large-scale flows such as differential rotation and meridional circulation are associated with the turbulent convection action. Indeed, [24] discussed the respective role of Reynolds stresses, baroclinic effects, and latitudinal heat transport in establishing the conical differential rotation profile observed by Helioseismology (see, for example, Fig. 2.2). In fact, the so-called Taylor–Proudman constraint for rotating fluids implies that the differential rotation should be invariant along the rotation axis, thus leading to a cylindrical rotation profile. Since this is not observed, it is necessary to understand the source of the breaking of these constraint. First, [79] have shown that baroclinic effects are, in part, associated with temperature latitudinal variations because of the poleward heat transport. Moreover, using helioseismic inversions of the temperature, of the entropy fluctuations, and angular velocity profiles, [29] show that the Sun is not in strict thermal-wind balance and that departure from baroclinic forcing by Reynolds stresses are likely. Thus, assessing the meridional circulation pattern in the convective envelope is very important. In fact, if this flow contributes little to the heat transport and to the kinetic energy budget, it plays a pivotal role in the angular momentum transport by opposing and balancing the equatorial transport by Reynolds stresses [25]. In most simulations, meridional flows are found to be multicellular and fluctuate significantly over a solar rotation. Moreover, if temporal average are performed, it is possible to find solution exhibiting a large-single shell per hemisphere. Finally, the first complete 3-D hydrodynamical models of the Sun from the top of the convective envelope to the radiative core have been computed [30] showing the consistent establishment of the tachocline and the profile of the large-scale flows, i.e., the differential rotation that matches with helioseismic inversions and the meridional circulation.

Next, such studies have been extended to other stars. Indeed, the convection properties and the associated differential rotation have been examined in young solar-type stars as a function of their rotation rate [6, 18], in T-Tauri [12], in G & K stars [73], in F stars [3], in red giant stars [23], and in the convective cores of more massive stars [4, 21]. These works have allowed us to study scaling laws for the differential rotation, its properties (pro- or retrograde at the equator) and the associated

thermal imbalance, the meridional flow properties, etc., in the whole Hertzsprung–Russell diagram. Finally, the properties of convective penetration, which is important for chemicals mixing, have been examined both at the base of a convective envelope in the case of the Sun [30] and at the top of a convective core [21].

2.3.2 Dynamo Action

Using such powerful 3-D global numerical simulations, it is now possible to study in detail the nonlinear interactions between turbulence, rotation, and the magnetic field in the Sun. Then, if an initial weak magnetic field is introduced in global solar turbulent convection simulations, the magnetic energy grows by many orders of magnitude through dynamo action if a critical value of the magnetic Reynolds number ($R_m = V_f L_f/\eta$, where V_f and L_f are characteristic velocity and length of the flow) is reached [27]. After a linear phase of exponential growth, magnetic energy saturates, because of the nonlinear feed-back of the Lorentz force, to a fraction of its kinetic energy retaining that level over many Ohmic decay times. Then, when saturation is reached, the kinetic energy is reduced when compared to the initial hydrodynamical value because of the reduction of the energy contained in the differential rotation. Moreover, the kinetic energy contained in the convective motions is less modified, and the nonaxisymmetric contribution to the kinetic energy is increased. The radial magnetic field is concentrated in the cold downflows. There, the Lorentz force modifies the flow, influencing the evolution of the strong downflows through magnetic tension that reduces the vorticity creation and inhibits the shear. The magnetic field and radial velocity are highly intermittent both in space and in time. The poloidal field is found to reverse in simulations, but it is not yet possible to get the observed 11-year solar cycle. To solve this problem, [22] have introduced in such simulations a shallow stably stratified tachocline at the bottom of the computed domain (Fig. 2.4). They show in this work that this stable layer plays a crucial role in organizing the irregular field produced in the convective zone into axisymmetric toroidal structures. The presence of such a large-scale mean field in the tachocline seems to influence the behavior of the model with much less frequent magnetic reversals. This is the reason why it is now clear that the presence of the tachocline is one of the key factors in generating large-scale magnetic structures and associated magnetic cycles. From now on, butterfly diagrams are only reproduced using 2-D mean field kinematic dynamo models with prescribed differential rotation, meridional circulation, magnetic diffusivity, and α-effect (see, for example, [51]).

This work has now been extended to solar-like stars. In the series of papers [19, 20] magnetic wreaths (coherent toroidal magnetic structures) have been identified and shown to survive within turbulent convective zones. This is a major result as it was thought until then that this was not possible because of magnetic flux expulsion. These results are also in accord with current spectropolarimetric observations of fast-rotating suns, which exhibit a dominant toroidal field topology. Activity cycles have also been obtained with regular reversals of field polarity found to exist in

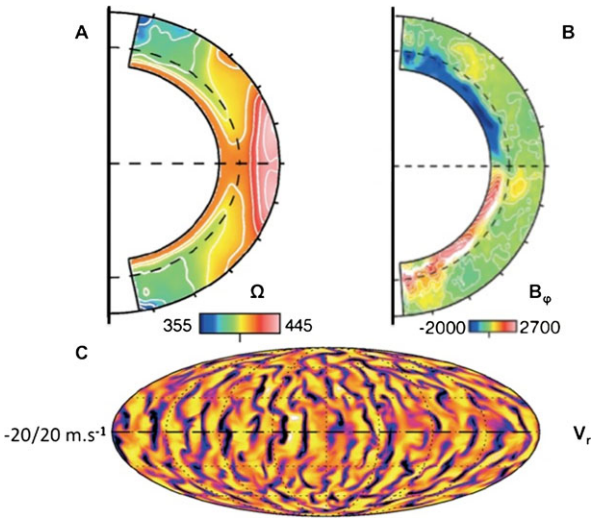

Fig. 2.4 *Top-left* (**A**): Angular velocity profile, *top-right* (**B**): azimuthal mean toroidal magnetic field, and *bottom* (**C**): convective radial velocities obtained using integrated ASH 3-D numerical simulations of the solar convective envelope and the tachocline. (Adapted from [22], courtesy The Astrophysical Journal)

turbulent conditions. In the same time, as in the Solar case, 2-D mean field dynamo models have been developed in order to study the impact of various physical processes on stellar magnetic cycles guided by 3-D numerical simulations. It has been shown that multicelled meridional flows and turbulent pumping have a significant impact on the cycle period and the butterfly diagram that are used to interpret the observed scaling law linking the star's cycle period to its rotation rate [37, 52].

Finally, the dynamo action due to turbulent convection has been undertaken in convective cores of more massive stars [4, 28]. In [44], the interaction of a convective core dynamo with various fossil fields in its surrounding radiative envelope (see Sect. 2.4.3) has been studied. It has demonstrated that such interaction (if the external field possesses a poloidal component) can lead to a strong dynamo branch in the core with magnetic field strength reaching the mega-Gauss level.

2.4 Dynamical Processes in Stellar Radiation Zones

In the classical approach, stellar radiation zones are supposed to be motionless. However, they are the seat of dynamical processes that act on secular time scales to transport angular momentum and chemicals. Four main processes are then identified (see, for example, [106, 121]): the meridional circulation, turbulence, fossil magnetic fields, and internal waves. These mechanisms form what is called the rotational transport (cf. Fig. 2.5). We will now describe each of them and the state of the art of their modeling.

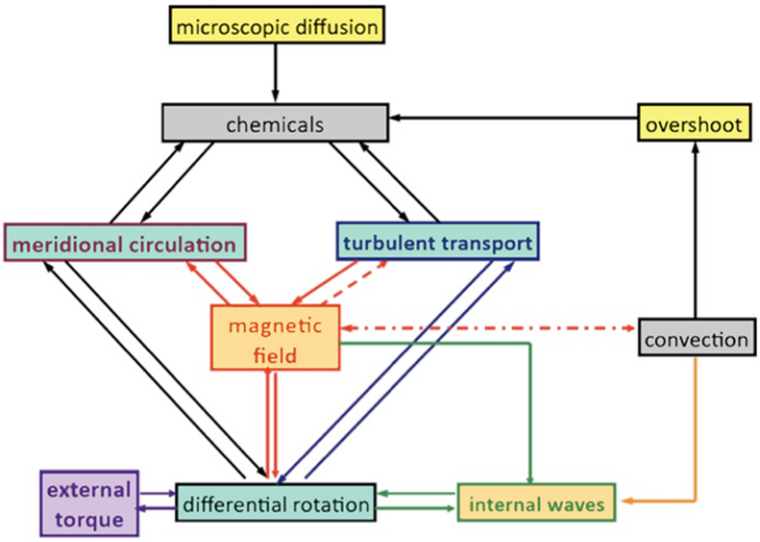

Fig. 2.5 The highly nonlinear rotational transport in the solar radiative core. Meridional circulation, shear-induced turbulence, fossil magnetic field, and internal waves act together to transport angular momentum and chemicals. In the solar case, the two latter processes are necessary to explain the observed angular velocity profile

2.4.1 Meridional Circulation

In a first step, the large-scale meridional circulation, which occurs in stellar radiation zones, was ascribed to the deformation of the isothermal surfaces by the centrifugal acceleration (and by the Lorentz force if there is a magnetic field and the tidal force if there is a close companion). Then, the radiative flux is no longer divergence-free [113] and must be balanced by heat advection. Therefore, in the original treatment [42, 105, 112] the meridional circulation velocity (and the induced mixing) was linked to the ratio of the centrifugal acceleration (and other perturbing forces) to the gravity. The characteristic time was derived by Sweet and named the Eddington–Sweet time $t_{\rm ES} = t_{\rm KH}\frac{GM}{\Omega^2 R^3}$, $t_{\rm KH} = \frac{GM^2}{RL}$ being the Kelvin–Helmholtz time (R, M, and L are respectively the stellar radius, mass, and luminosity). These results indicated that rapid rotators should be well mixed due to this circulation that should modify their evolution to the giant branch. This was then corrected by [75] who invoked the effects of μ-gradients (i.e., the chemical composition) to cancel such circulation effects.

However, the fact that meridional circulation advects angular momentum was ignored. Then, after a transient phase which lasts about an Eddington–Sweet time, the star settles into an asymptotic regime where the circulation is mainly driven by the torques applied to the star and internal stresses as those related to the shear-induced turbulence (if we do not take into account fossil magnetic fields and internal waves); their cases will be discussed respectively in Sects. 2.4.3 and 2.4.4. On one hand, if

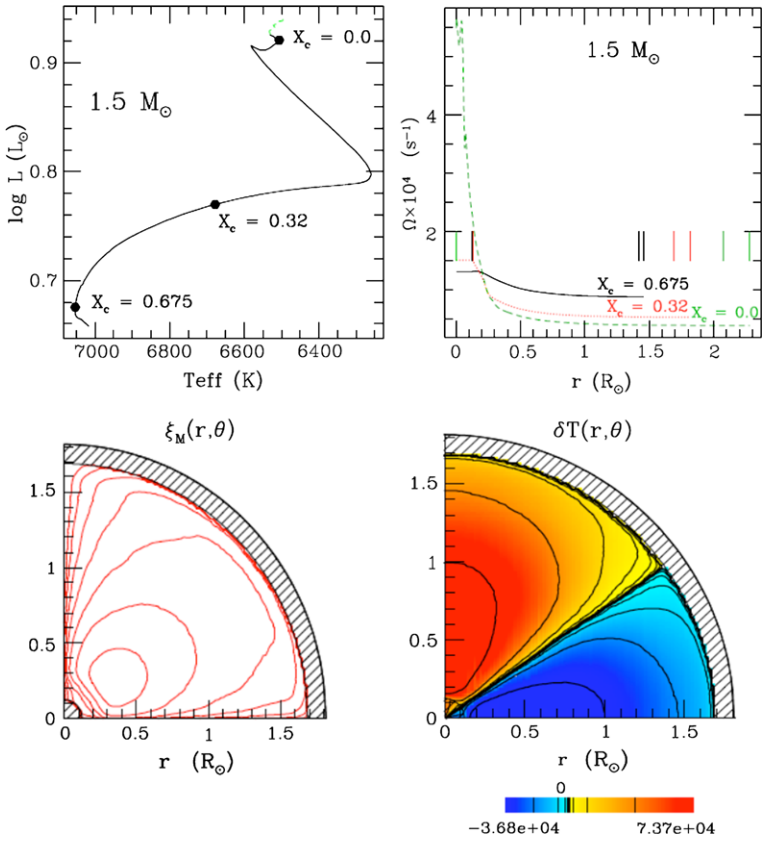

Fig. 2.6 Highly nonlinear interactions between the differential rotation (*upper-right panel*), the meridional circulation (*bottom-left panel*, where we represent the iso-contours of the stream meridional function (ξ); the meridional circulation is tangent to these lines), and the related thermal imbalance (δT) (*bottom-right panel*) during the evolution on the main sequence of a $1.5 M_{\odot}$ star with a solar metallicity and an initial equatorial velocity $V_{\rm ini} = 100$ km s^{-1}. The rotation profile is represented for three positions in the Hertzsprung–Russell diagram (*upper-left corner*): $X_{\rm c} = \{0.675, 0.32, 0.0\}$, where $X_{\rm c}$ is the central fraction in mass in hydrogen. The meridional currents, which are driven here by the torque of the wind that slows down the surface, and the related temperature fluctuation are represented for $X_{\rm c} = 0.32$. (Adapted from [33], courtesy Astronomy & Astrophysics)

the star losses angular momentum through a wind, the circulation adjusts to transport angular momentum to the surface [33, 62, 68, 120]. The induced rotation, resulting from the angular momentum advection, is then nonuniform and a baroclinic state sets in where the temperature varies with latitude along the isobar. On the other hand, if the star does not exchange angular momentum, the advection by the circulation balances the turbulent transport induced by the shear of the differential rotation; in the case of a uniform rotation without any turbulent transport the circulation thus dies [31]. In the case of solar-type stars (cf. Fig. 2.6) it is thus the loss or the gain of

angular momentum which drives the circulation and not the amplitude of the angular velocity. Note also that the circulation can be driven by star's structural adjustments during their evolution. Therefore, the loop of the transport in stellar radiation zones in the case where we treat the highly nonlinear interactions between the differential rotation, the related shear-induced turbulence, and the meridional circulation is identified (see [33, 88]): first, meridional currents are sustained by the torques applied at the stellar surface, by internal stresses such as the viscous ones related to turbulence and by structural adjustments; next, the temperature relaxes to balance the advection of entropy by the meridional circulation; finally, because of the baroclinic torque induced by the latitudinal distribution of temperature fluctuations on the isobar, a new differential rotation profile is established because of the so-called thermal-wind balance that may again generate turbulence, and the loop is closed.

2.4.2 Shear-Induced Turbulence

Stellar radiation zones are stably stratified. In such regions, hydrodynamical turbulence is thus strongly influenced by the buoyancy force, which inhibits vertical displacements. The vertical and horizontal shear instabilities thus give birth to a supposed strongly anisotropic turbulent transport much efficient in the horizontal direction, as in oceans [99, 120]. Vertical turbulent diffusion of angular velocity and chemicals is thus weaker than the horizontal and horizontal gradients of all quantities are thus strongly damped allowing reduced expansion in few spherical harmonics in Eq. (2.7). A review of prescriptions used for describing shear-induced turbulent transport in stellar radiation zones is given in [70]. Other instabilities such as baroclinic and double diffusive instabilities can also develop (see, for example, [118] and [49]).

Secular modeling has shown that combined action of such turbulent transport and meridional circulation advection are successful, for example, in explaining properties of massive stars [77]. However, since such mechanisms are unable to explain the observed solar radiation zone angular velocity profile (see, for example, [84, 111]) and the rotation of the core of subgiants and red giant stars [10, 34], fossil magnetic fields that are detected, for example, at the surface of the radiative envelope of some of the massive stars [114] and internal waves that are excited by convective regions must be studied.

2.4.3 The Fossil Magnetic Field Dynamics

The core of solar-type stars and the envelopes of massive ones are supposed to be the seat of a fossil magnetic field, which has been trapped during the star's birth and is a remnant of the stellar formation and of the PMS dynamo. The possible configurations of this field are now understood as resulting from an MHD turbulent

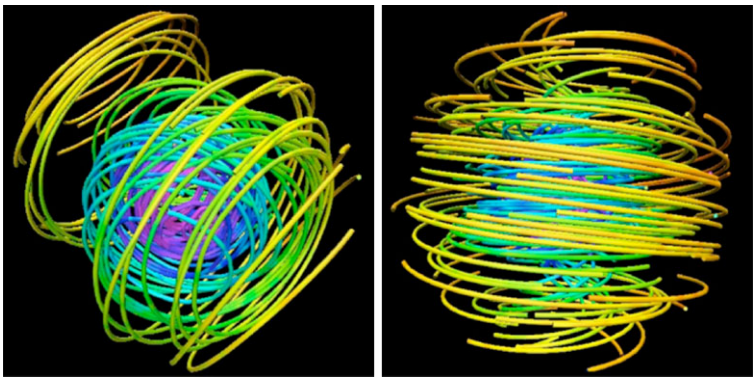

Fig. 2.7 *Left*: Unstable purely toroidal fossil magnetic field, once the Tayler instability has reached its saturation (the colorscale is a function of the density). *Right*: Mixed stable fossil field configuration resulting from an initial MHD turbulent relaxation. (Taken from [41], courtesy The Astrophysical Journal)

relaxation process, in which the magnetic energy has decreased while conserving the global magnetic helicity of the initial field. Numerical simulations [15–17, 39] and semi-analytical work [40, 41] have been devoted to study such initial conditions for fossil fields. They conclude that it must be, to a first approximation, in a non-force-free stable relaxed equilibrium with a mixed configuration, both poloidal and toroidal (cf. the right panel of Fig. 2.7) because purely toroidal and poloidal fields are unstable in stellar radiation zones (see respectively [110] and [63] and the left panel of Fig. 2.7).

Once the initial non-force-free magnetic configuration (axisymmetric or nonaxisymmetric) has been established by the initial MHD turbulent relaxation processes, it interacts with differential rotation. Then, two cases are possible as described by [100]. In the first case, if the field is strong, the rotation becomes uniform on magnetic surfaces due to Alfvén wave phase mixing, which damps the differential rotation; in the axisymmetric case this leads to the Ferraro's state where the rotation is frozen along the poloidal field lines (see, for example, [98]) and to a uniform rotation in the nonaxisymmetric case (the oblique rotators case for example; see, for example, [81]). Then, the field can only be modified by structural adjustments, and the mixing is frozen. In the second case, if the field is weak, it could first become axisymmetric if it is nonaxisymmetric because of rotational smoothing, and then, because of phase mixing, this leads to the Ferraro's state. However, this picture could be strongly modified by MHD magnetic instabilities if during the first step of the phase mixing, the residual differential rotation on each magnetic surface is able to generate a strong toroidal component of the field that becomes unstable and if this instability becomes able to trigger a dynamo action through an α-effect; this question still remains open [2, 14, 93, 101, 123]. The critical value of the field that gives the limit between the weak and the strong field regimes has been given in [5]. A summary is given in Fig. 2.8.

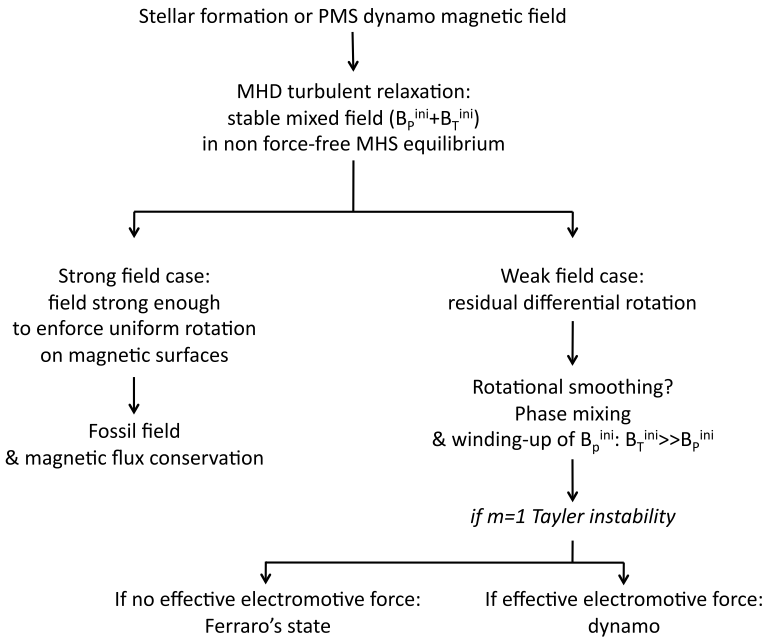

Fig. 2.8 Interaction of fossil magnetic field and differential rotation (see also [65, 102])

Let us now take into account the meridional circulation. To understand its interaction with the other dynamical processes (the differential rotation and the shear induced turbulence) in presence of a fossil magnetic field, we shall adopt the picture of rotational transport as described in Sect. 2.4.1 in the purely hydrodynamical case and generalize it to the magnetized case. As described previously, meridional circulation in radiation zones are driven by applied torques (internal, like the Lorentz torque or external, like those induced by stellar winds), structural adjustments during stellar evolution and turbulent transport. In the case where all these sources vanish, the meridional circulation dies after an Eddington–Sweet time, and the star settles in a baroclinic state described by the MHD thermal wind equation. If we apply this picture to the case of radiation zones with a fossil magnetic field, we thus understand that the meridional circulation (if we consider a star without structural adjustments and external torques) will be mainly driven by the residual magnetic torque until the phase mixing leads the star to a torque-free state. Then, the meridional circulation advection of angular momentum balances the residual Lorentz torque (see [76] and [69] and Fig. 2.9).

However, this global picture is only respected if the poloidal field lines are entirely confined in a radiation zone. If the poloidal field connects with the differentially convective envelope in the case of solar-type stars, the differential rotation is then transmitted along the field lines to their radiative core (see, for example, [32]). To resolve this problem, [48] (see also [92]) proposed a scenario in which the Ohmic diffusion of the fossil field into the convective envelope is prevented by its advection

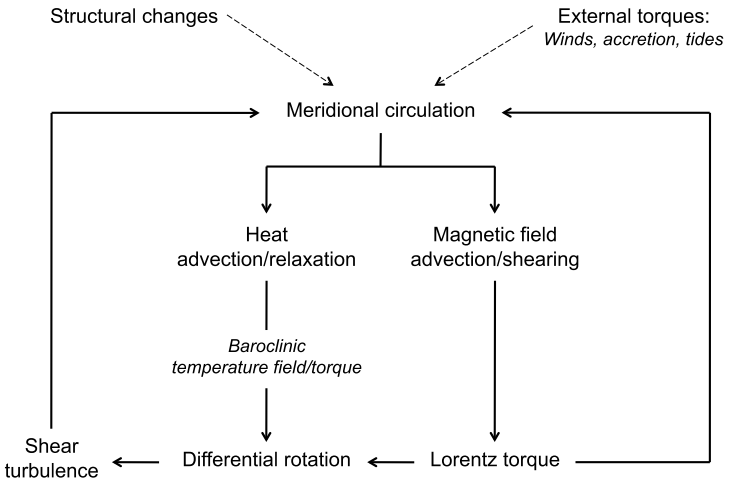

Fig. 2.9 The transport loop in a differentially rotating magnetized stellar radiation zone (see also [65])

by the down-flow part of the thermally driven circulation in the tachocline. However, this circulation has also an up-flow component, which would advect the field into the convection zone that would then imprint a small differential rotation in the radiation zone. The first detailed calculations to settle the question were achieved in [45, 46] (see also [56, 115]), who considered 2-D stationary solutions for various parameters. This work showed that the field lines would penetrate into the convection zone over a broad region at high latitudes, thus imprinting differential rotation to the radiation zone. This behavior is now confirmed by 3-D consistent calculations ([26, 103, 104], Fig. 2.10) where authors showed that even a deeply buried magnetic field will eventually connect with the convection zone, inducing differential rotation in the radiative core both in the case of axi- and nonaxisymmetric configurations. Therefore, another transport process seems to be responsible for the uniform rotation in the radiative core of solar-type stars.

2.4.4 Internal Waves

Since the fossil magnetic field seems unable to enforce the observed uniform rotation in the radiative core of the Sun, we must examine the last possible mechanism: the transport of angular momentum by the internal waves excited by the turbulent motions at convection/radiation transitions in stellar interiors, namely the bases of convective envelopes in low-mass stars and the tops of convective cores in intermediate-mass and massive ones. The importance of these processes was first anticipated by [86, 96, 122] (see also [97]).

Let us first discuss the case where modifications of gravity waves by rotation and magnetic field are not taken into account. In this simplest case, the restoring

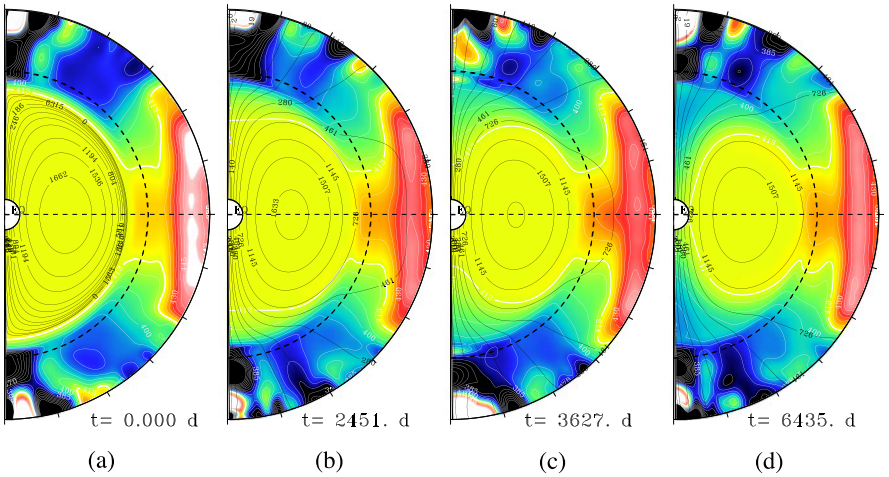

Fig. 2.10 Interaction of a deeply buried axisymmetric fossil magnetic field in the Solar radiative core with the surrounding convective envelope. During its evolution, the fossil field connects with the convection zone transmitting its differential rotation to the radiation zone. (Taken from [104], courtesy Astronomy & Astrophysics)

force operating on waves is the buoyancy force. They thus propagate only in stably stratified regions, i.e., in the radiative core of low-mass stars. After an excitation of a whole spectrum of such waves at the base of the convective envelope, they penetrate into the radiation zone, transporting angular momentum which is deposited where they are dissipated mainly through thermal diffusion as first described by [117].

Waves that are of short wavelength are first dissipated close to the convection zone. Prograde waves carry positive angular momentum, and retrograde waves negative angular momentum. If they propagate in a radiative region, which is rotating faster than the excitation region, their frequency is Doppler-shifted, leading to higher dissipation for the prograde waves than for the retrograde waves. This is the reason why the angular velocity first increases where it was already high, and its slope with depth steepens until the shear becomes unstable. The induced turbulent layer then merges with the convective envelope. In the same time, retrograde waves extract angular momentum at a deeper layer, thus building there a "negative" shear layer, which takes the place of the former and the cycle repeats. This phenomenon, which depends on the waves turbulent excitation, is called the Shear Layer Oscillation [107] and is similar to the quasi-biennial oscillation observed in the Earth's atmosphere. The question, which must then be answered, is how this thin shear layer modifies the propagation of waves of lowest frequencies, which are less damped. If there is no slope in angular velocity, the shear layer is symmetric, and the effect is the same on the prograde as on the retograde waves. However, if the angular velocity increases with depth, the prograde waves will be more dissipated, which allows the retrograde waves to extract angular momentum from the deep interior. This picture was first studied by [109] using a first approach where only gravity waves and shear-induced turbulence are taken into account. This was confirmed using complete

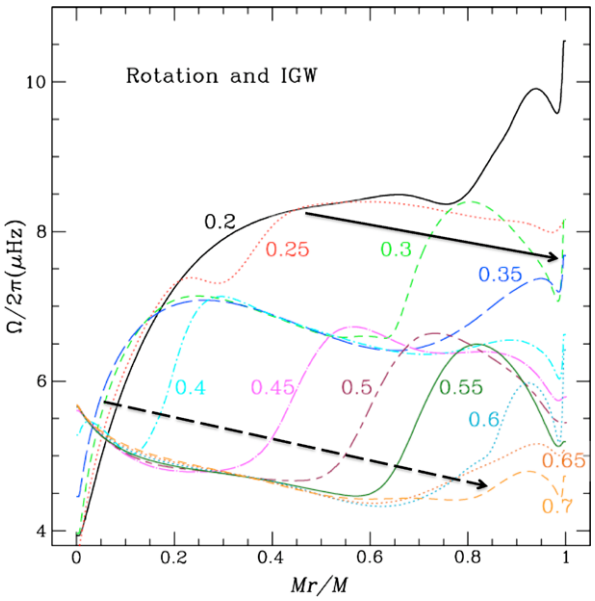

Fig. 2.11 Evolution of the (differential) rotation profile (averaged on latitudes) in a $1.2M_{\odot}$ star (its metallicity is $Z = 0.02$) with an initial rotation velocity of 50 km s^{-1}. This is obtained making simulations using the STAREVOL code, where the transport of angular momentum by the meridional circulation, the shear vertical turbulence, and the internal gravity waves are taken into account. The *black arrows* show the successive angular momentum extraction fronts (the first is represented by the *continuous line*, and the second one by the *dashed line*), which are mainly driven by the angular momentum extraction at the surface by the wind. The *curves* are labeled according to the corresponding ages in Gyrs. (Adapted from [107], courtesy Astronomy & Astrophysics)

calculation including also meridional circulation [107]. In this modeling, where horizontal differential rotation is damped by the strong horizontal turbulence, internal gravity waves succeed in achieving nearly uniform rotation in solar-type stars at the solar age with successive angular momentum extraction fronts (cf. Fig. 2.11).

These fronts are mainly driven by wave-damping and the meridional circulation, while the shear-induced turbulence acts only in regions of strong differential rotation. Furthermore, efficiency of this transport is strongly correlated with the external extraction of angular momentum by magnetic wind, which creates a differential rotation between the convective envelope and the radiative core, which feeds the transport by waves. Moreover, as in Sects. 2.4.1 and 2.4.3, the transport loop can be identified: first, external torques and internal stresses (i.e., viscous ones related to the shear-induced turbulence and waves Reynolds stresses) sustain the large-scale meridional circulation that advects entropy leading to a new temperature distribution and thus to a new differential rotation profile (see Fig. 2.12). Furthermore, models including waves predict the observed Li abundance, which is a strong constraint for stellar modeling.

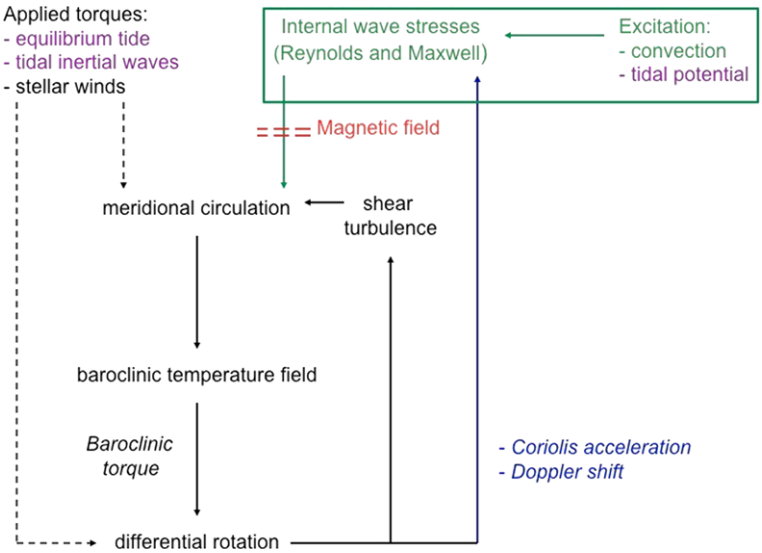

Fig. 2.12 Hydrodynamical transport loop in stellar radiation zones when taking into account internal waves. The different applied torques (winds and tides) are shown. (Adapted from [67], courtesy Astronomy & Astrophysics)

Now, work has been undertaken to obtain a more complete picture of this promising mechanism in the whole Hertzsprung–Russell diagram [108].

Firstly, theoretical studies [11, 94] and numerical simulations aim to determine the wave spectrum excited by convective envelopes and cores. For numerical simulations, results in Cartesian simulations [36, 54, 55] show a broad spectrum with an overevaluated energy flux in 2-D. More recently, integrated simulation of the Sun, first in 2-D in the solar equatorial plane [89] and then in 3-D [30], show a complex excited spectrum, which we should aim to understand.

Secondly, in the case of waves that have frequencies close to the inertial (2Ω) or to the Alfvén (ω_A) frequencies, the Coriolis acceleration and the Lorentz force, which modifies their propagation, their damping, and thus the related transport, must be taken into account. First, in the purely hydrodynamical case, waves become gravito-inertial waves [7, 8, 35, 60]. Two main wave families are then identified: the super-inertial gravito-inertial waves ($\sigma > 2\Omega$), which propagate in the whole sphere, and the sub-inertial ($\sigma \leq 2\Omega$), which are trapped in an equatorial belt (see Fig. 2.13). In this context, transport by gravito-inertial waves has been studied both in the case of a weak [71] and of a general differential rotation [58, 59, 64]. Then, the Coriolis acceleration's main action is to reduce the efficiency of the transport. Next, the effect of a toroidal magnetic field at the bottom of the tachocline and in the radiative core has been studied [57, 61, 66, 67, 90, 91, 95], and latitudinal trapping phenomena such as in the gravito-inertial wave case have been isolated. Furthermore, the azimuthal field acts, depending on the considered frequency, as a vertical filter. However, when taking simultaneously the action of the Coriolis acceleration

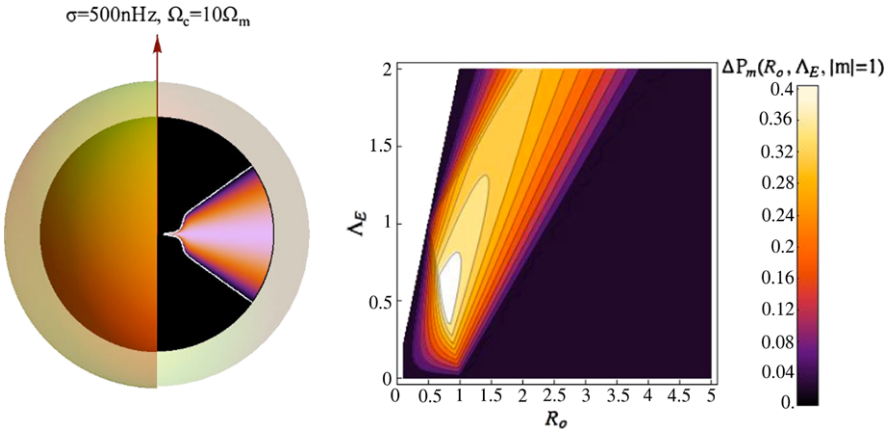

Fig. 2.13 Impact of (differential) rotation and magnetic fields on internal waves propagation and the related transport of angular momentum. *Left*: Equatorial trapping of a sub-inertial gravito-inertial wave (with a frequency $\sigma = 500$ n Hz) in the differentially rotating radiation zone of a $1M_\odot$ star, which has a given uniform rotation $\Omega_\mathrm{m} = 430$ n Hz from 0.2 to $0.7R_\odot$ and a core that rotates 10 times faster [64]. The colored region is the one where waves are propagative, while the black one is the "dead-region" for such propagation. *Right*: Net bias in the convection's energy transmission to prograde and retrograde waves (here for an azimuthal number $m = 1$) as a function of the wave Rossby ($R_\mathrm{o} = \sigma/2\Omega$) and Elsasser ($\Lambda_\mathrm{E} = \omega_\mathrm{A}^2/\Omega\sigma$) numbers; because of the stronger equatorial trapping of prograde waves, the retrograde are favored as well as the related net extraction of angular momentum. (Taken from [67], courtesy Astronomy & Astrophysics)

and of the Lorentz force related to a toroidal field into account, even if the efficiency of the transport can be strongly affected by trappings both in the horizontal and in the vertical directions, the results obtained by [107] of a net extraction of angular momentum because of a net bias in favor of retrograde waves is conserved in low-mass stars (see Fig. 2.13).

Finally, nonlinear effects such as wave braking at the center of the star are now studied [1]; some signs appear of a possible acceleration of the central rotation by this mechanism [9].

2.5 Conclusion

Work to go beyond the classical static picture of stars to get a global understanding of their dynamics is thus in a golden age. From dynamical to secular time scales 1-D, 2-D, and 3-D stellar models, including macroscopic transport processes, now allow us to enter into the details of the highly nonlinear couplings between differential rotation, meridional circulations, turbulence, dynamo and fossil magnetic fields, and waves. Moreover, we feel now how the impact of the star's environment is a key actor for internal transport processes. Therefore, as physical modeling becomes more and more complex and refined, it is clear that integrated models that take into account all the known internal processes and external constraints such as winds or

accretion [53, 72, 74, 85] and tides [83, 87, 116, 119] must be built. In order to guide such construction, constraints obtained by helioseismology, asteroseismology, and spectropolarimetry will be crucial.

Acknowledgements We thank the Programme National de Physique Stellaire (CNRS/INSU), the CNES/GOLF grant at the Service d'Astrophysique (CEA–Saclay), the CNRS Physique théorique et ses interfaces program and the ANR SIROCO for their support.

References

1. Alvan, L., Mathis, S.: Critical layers for internal waves in stellar radiation zones. In: Alecian, G., Belkacem, K., Samadi, R., Valls-Gabaud, D. (eds.) SF2A-2011: Proceedings of the Annual Meeting of the French Society of Astronomy and Astrophysics, pp. 443–447 (2011)
2. Arlt, R., Rüdiger, G.: Amplification and stability of magnetic fields and dynamo effect in young A stars. Mon. Not. R. Astron. Soc. **412**, 107–119 (2011)
3. Augustson, K., Brown, B.P., Brun, A.S., Toomre, J.: Dynamo action, magnetic activity, and rotation in F stars. Bull. Am. Astron. Soc. **39**, 117 (2007)
4. Augustson, K.C., Brun, A.S., Toomre, J.: Convection and dynamo action in B stars. In: Brummell, N.H., Brun, A.S., Miesch, M.S., Ponty, Y. (eds.) Astrophysical Dynamics: From Stars to Galaxies. IAU Symposium, vol. 271, pp. 361–362 (2011)
5. Aurière, M., Wade, G.A., Silvester, J., Lignières, F., Bagnulo, S., Bale, K., Dintrans, B., Donati, J.F., Folsom, C.P., Gruberbauer, M., Hui Bon Hoa, A., Jeffers, S., Johnson, N., Landstreet, J.D., Lèbre, A., Lueftinger, T., Marsden, S., Mouillet, D., Naseri, S., Paletou, F., Petit, P., Power, J., Rincon, F., Strasser, S., Toqué, N.: Weak magnetic fields in Ap/Bp stars. Evidence for a dipole field lower limit and a tentative interpretation of the magnetic dichotomy. Astron. Astrophys. **475**, 1053–1065 (2007)
6. Ballot, J., Brun, A.S., Turck-Chièze, S.: Simulations of turbulent convection in rotating young solarlike stars: differential rotation and meridional circulation. Astrophys. J. **669**, 1190–1208 (2007)
7. Ballot, J., Lignières, F., Reese, D.R., Rieutord, M.: Gravity modes in rapidly rotating stars. Limits of perturbative methods. Astron. Astrophys. **518**, A30 (2010)
8. Ballot, J., Lignières, F., Prat, V., Reese, D.R., Rieutord, M.: 2D computations of g modes. arXiv:1109.6856 [astro-ph]
9. Barker, A.J., Ogilvie, G.I.: On internal wave breaking and tidal dissipation near the centre of a solar-type star. Mon. Not. R. Astron. Soc. **404**, 1849–1868 (2010)
10. Beck, P.G., Montalban, J., Kallinger, T., De Ridder, J., Aerts, C., García, R.A., Hekker, S., Dupret, M.A., Mosser, B., Eggenberger, P., Stello, D., Elsworth, Y., Frandsen, S., Carrier, F., Hillen, M., Gruberbauer, M., Christensen-Dalsgaard, J., Miglio, A., Valentini, M., Bedding, T.R., Kjeldsen, H., Girouard, F.R., Hall, J.R., Ibrahim, K.A.: Fast core rotation in red-giant stars as revealed by gravity-dominated mixed modes. Nature **481**, 55–57 (2012)
11. Belkacem, K., Samadi, R., Goupil, M.J., Dupret, M.A., Brun, A.S., Baudin, F.: Stochastic excitation of nonradial modes. II. Are solar asymptotic gravity modes detectable? Astron. Astrophys. **494**, 191–204 (2009)
12. Bessolaz, N., Brun, A.S.: Hunting for giant cells in deep stellar convective zones using wavelet analysis. Astrophys. J. **728**, 115 (2011)
13. Bouvier, J.: Lithium depletion and the rotational history of exoplanet host stars. Astron. Astrophys. **489**, L53–L56 (2008)
14. Braithwaite, J.: A differential rotation driven dynamo in a stably stratified star. Astron. Astrophys. **449**, 451–460 (2006)
15. Braithwaite, J.: On non-axisymmetric magnetic equilibria in stars. Mon. Not. R. Astron. Soc. **386**, 1947–1958 (2008)

16. Braithwaite, J., Nordlund, Å.: Stable magnetic fields in stellar interiors. Astron. Astrophys. **450**, 1077–1095 (2006)
17. Braithwaite, J., Spruit, H.C.: A fossil origin for the magnetic field in A stars and white dwarfs. Nature **431**, 819–821 (2004)
18. Brown, B.P., Browning, M.K., Brun, A.S., Miesch, M.S., Toomre, J.: Rapidly rotating suns and active nests of convection. Astrophys. J. **689**, 1354–1372 (2008)
19. Brown, B.P., Browning, M.K., Brun, A.S., Miesch, M.S., Toomre, J.: Persistent magnetic wreaths in a rapidly rotating sun. Astrophys. J. **711**, 424–438 (2010)
20. Brown, B.P., Miesch, M.S., Browning, M.K., Brun, A.S., Toomre, J.: Magnetic cycles in a convective dynamo simulation of a young solar-type star. Astrophys. J. **731**, 69 (2011)
21. Browning, M.K., Brun, A.S., Toomre, J.: Simulations of core convection in rotating A-type stars: differential rotation and overshooting. Astrophys. J. **601**, 512–529 (2004)
22. Browning, M.K., Miesch, M.S., Brun, A.S., Toomre, J.: Dynamo action in the solar convection zone and tachocline: pumping and organization of toroidal fields. Astrophys. J. Lett. **648**, L157–L160 (2006)
23. Brun, A.S., Palacios, A.: Numerical simulations of a rotating red giant star. I. Three-dimensional models of turbulent convection and associated mean flows. Astrophys. J. **702**, 1078–1097 (2009)
24. Brun, A.S., Rempel, M.: Large scale flows in the solar convection zone. Space Sci. Rev. **144**, 151–173 (2009)
25. Brun, A.S., Toomre, J.: Turbulent convection under the influence of rotation: sustaining a strong differential rotation. Astrophys. J. **570**, 865–885 (2002)
26. Brun, A.S., Zahn, J.P.: Magnetic confinement of the solar tachocline. Astron. Astrophys. **457**, 665–674 (2006)
27. Brun, A.S., Miesch, M.S., Toomre, J.: Global-scale turbulent convection and magnetic dynamo action in the solar envelope. Astrophys. J. **614**, 1073–1098 (2004)
28. Brun, A.S., Browning, M.K., Toomre, J.: Simulations of core convection in rotating A-type stars: magnetic dynamo action. Astrophys. J. **629**, 461–481 (2005)
29. Brun, A.S., Antia, H.M., Chitre, S.M.: Is the solar convection zone in strict thermal wind balance? Astron. Astrophys. **510**, A33 (2010)
30. Brun, A.S., Miesch, M.S., Toomre, J.: Modeling the dynamical coupling of solar convection with the radiative interior. Astrophys. J. **742**, 79 (2011)
31. Busse, F.H.: On the problem of stellar rotation. Astrophys. J. **259**, 759–766 (1982)
32. Charbonneau, P., MacGregor, K.B.: Angular momentum transport in magnetized stellar radiative zones. II. The solar spin-down. Astrophys. J. **417**, 762 (1993)
33. Decressin, T., Mathis, S., Palacios, A., Siess, L., Talon, S., Charbonnel, C., Zahn, J.P.: Diagnoses to unravel secular hydrodynamical processes in rotating main sequence stars. Astron. Astrophys. **495**, 271–286 (2009)
34. Deheuvels, S., Garcia, R.A., Chaplin, W.J., Basu, S., Antia, H.M., Appourchaux, T., Benomar, O., Davies, G.R., Elsworth, Y., Gizon, L., Goupil, M.J., Reese, D.R., Regulo, C., Schou, J., Stahn, T., Casagrande, L., Christensen-Dalsgaard, J., Fischer, D., Hekker, S., Kjeldsen, H., Mathur, S., Mosser, B., Pinsonneault, M., Valenti, J., Christiansen, J.L., Kinemuchi, K., Mullally, F.: Seismic evidence for a rapidly rotating core in a lower-giant-branch star observed with Kepler. arXiv:1206.3312 [astro-ph]
35. Dintrans, B., Rieutord, M.: Oscillations of a rotating star: a non-perturbative theory. Astron. Astrophys. **354**, 86–98 (2000)
36. Dintrans, B., Brandenburg, A., Nordlund, Å., Stein, R.F.: Spectrum and amplitudes of internal gravity waves excited by penetrative convection in solar-type stars. Astron. Astrophys. **438**, 365–376 (2005)
37. Do Cao, O., Brun, A.S.: Effects of turbulent pumping on stellar activity cycles. Astron. Nachr. **332**, 907 (2011)
38. Donati, J.F., Landstreet, J.D.: Magnetic fields of nondegenerate stars. Astron. Astrophys. Rev. **47**, 333–370 (2009)

39. Duez, V.: Numerical simulations of magnetic relaxation in rotating stellar radiation zones. Astron. Nachr. **332**, 983 (2011)
40. Duez, V., Mathis, S.: Relaxed equilibrium configurations to model fossil fields. I. A first family. Astron. Astrophys. **517**, A58 (2010)
41. Duez, V., Braithwaite, J., Mathis, S.: On the stability of non-force-free magnetic equilibria in stars. Astrophys. J. Lett. **724**, L34–L38 (2010)
42. Eddington, A.S.: Circulating currents in rotating stars. Observatory **48**, 73–75 (1925)
43. Eggenberger, P., Meynet, G., Maeder, A., Miglio, A., Montalban, J., Carrier, F., Mathis, S., Charbonnel, C., Talon, S.: Effects of rotational mixing on the asteroseismic properties of solar-type stars. Astron. Astrophys. **519**, A116 (2010)
44. Featherstone, N.A., Browning, M.K., Brun, A.S., Toomre, J.: Effects of fossil magnetic fields on convective core dynamos in A-type stars. Astrophys. J. **705**, 1000–1018 (2009)
45. Garaud, P.: Dynamics of the solar tachocline—I. An incompressible study. Mon. Not. R. Astron. Soc. **329**, 1–17 (2002)
46. Garaud, P., Garaud, J.D.: Dynamics of the solar tachocline—II. The stratified case. Mon. Not. R. Astron. Soc. **391**, 1239–1258 (2008)
47. García, R.A., Turck-Chièze, S., Jiménez-Reyes, S.J., Ballot, J., Pallé, P.L., Eff-Darwich, A., Mathur, S., Provost, J.: Tracking solar gravity modes: the dynamics of the solar core. Science **316**, 1591 (2007)
48. Gough, D.O., McIntyre, M.E.: Inevitability of a magnetic field in the Sun's radiative interior. Nature **394**, 755–757 (1998)
49. Hirschi, R., Maeder, A.: The GSF instability and turbulence do not account for the relatively low rotation rate of pulsars. Astron. Astrophys. **519**, A16 (2010)
50. Irwin, J., Bouvier, J.: The rotational evolution of low-mass stars. In: Mamajek, E.E., Soderblom, D.R., Wyse, R.F.G. (eds.) The Ages of Stars. IAU Symposium, vol. 258, pp. 363–374 (2009)
51. Jouve, L., Brun, A.S.: On the role of meridional flows in flux transport dynamo models. Astron. Astrophys. **474**, 239–250 (2007)
52. Jouve, L., Brown, B.P., Brun, A.S.: Exploring the $P_{\rm cyc}$ vs. $P_{\rm rot}$ relation with flux transport dynamo models of solar-like stars. Astron. Astrophys. **509**, A32 (2010)
53. Kawaler, S.D.: Angular momentum loss in low-mass stars. Astrophys. J. **333**, 236–247 (1988)
54. Kiraga, M., Jahn, K., Stępień, K., Zahn, J.P.: Direct numerisimulations of penetrative convection and generation of internal gravity waves. Acta Astron. **53**, 321–339 (2003)
55. Kiraga, M., Stepien, K., Jahn, K.: Generation and propagation of internal gravity waves: Comparison between two- and three-dimensional models at low resolution. Acta Astron. **55**, 205–217 (2005)
56. Kitchatinov, L.L., Rüdiger, G.: Magnetic field confinement by meridional flow and the solar tachocline. Astron. Astrophys. **453**, 329–333 (2006)
57. Kumar, P., Talon, S., Zahn, J.P.: Angular momentum redistribution by waves in the sun. Astrophys. J. **520**, 859–870 (1999)
58. Lee, U.: R modes of slowly pulsating B stars. Mon. Not. R. Astron. Soc. **365**, 677–687 (2006)
59. Lee, U., Saio, H.: Angular momentum transfer by non-radial oscillations in massive main-sequence stars. Mon. Not. R. Astron. Soc. **261**, 415–424 (1993)
60. Lee, U., Saio, H.: Low-frequency nonradial oscillations in rotating stars. I. Angular dependence. Astrophys. J. **491**, 839 (1997)
61. MacGregor, K.B., Rogers, T.M.: Reflection and ducting of gravity waves inside the sun. Sol. Phys. **270**, 417–436 (2011)
62. Maeder, A., Zahn, J.P.: Stellar evolution with rotation. III. Meridional circulation with μ-gradients and non-stationarity. Astron. Astrophys. **334**, 1000–1006 (1998)
63. Markey, P., Tayler, R.J.: The adiabatic stability of stars containing magneticfields—II. Poloidal fields. Mon. Not. R. Astron. Soc. **163**, 77 (1973)
64. Mathis, S.: Transport by gravito-inertial waves in differentially rotating stellar radiation zones. I—Theoretical formulation. Astron. Astrophys. **506**, 811–828 (2009)

65. Mathis, S.: Dynamics of fossil magnetic fields in massive star interiors. In: Neiner, C., Wade, G., Meynet, G., Peters, G. (eds.) Active OB Stars: Structure, Evolution, Mass Loss, and Critical Limits. IAU Symposium, vol. 272, pp. 160–165 (2011)
66. Mathis, S., de Brye, N.: Low-frequency internal waves in magnetized rotating stellar radiation zones. I. Wave structure modification by a toroidal field. Astron. Astrophys. **526**, A65 (2011)
67. Mathis, S., de Brye, N: Low-frequency internal waves in magnetized rotating stellar radiation zones. II. Angular momentum transport with a toroidal field. Astron. Astrophys. **540**, A37 (2012)
68. Mathis, S., Zahn, J.P.: Transport and mixing in the radiation zones of rotating stars. I. Hydrodynamical processes. Astron. Astrophys. **425**, 229–242 (2004)
69. Mathis, S., Zahn, J.P.: Transport and mixing in the radiation zones of rotating stars. II. Axisymmetric magnetic field. Astron. Astrophys. **440**, 653–666 (2005)
70. Mathis, S., Palacios, A., Zahn, J.P.: On shear-induced turbulence in rotating stars. Astron. Astrophys. **425**, 243–247 (2004)
71. Mathis, S., Talon, S., Pantillon, F.P., Zahn, J.P.: Angular momentum transport in the sun's radiative zone by gravito-inertial waves. Sol. Phys. **251**, 101–118 (2008)
72. Matt, S., Pudritz, R.E.: The spin of accreting stars: dependence on magnetic coupling to the disc. Mon. Not. R. Astron. Soc. **356**, 167–182 (2005)
73. Matt, S.P., Do Cao, O., Brown, B.P., Brun, A.S.: Convection and differential rotation properties of G and K stars computed with the ASH code. Astron. Nachr. **332**, 897 (2011)
74. Matt, S.P., MacGregor, K.B., Pinsonneault, M.H., Greene, T.P.: Magnetic braking formulation for sun-like stars: dependence on dipole field strength and rotation rate. arXiv:1206.2354 [astro-ph]
75. Mestel, L.: Rotation and stellar evolution. Mon. Not. R. Astron. Soc. **113**, 716 (1953)
76. Mestel, L., Tayler, R.J., Moss, D.L.: The mutual interaction of magnetism, rotation and meridian circulation in stellar radiative zones. Mon. Not. R. Astron. Soc. **231**, 873–885 (1988)
77. Meynet, G., Maeder, A.: Stellar evolution with rotation. V. Changes in all the outputs of massive star models. Astron. Astrophys. **361**, 101–120 (2000)
78. Miesch, M.S., Elliott, J.R., Toomre, J., Clune, T.L., Glatzmaier, G.A., Gilman, P.A.: Three-dimensional spherical simulations of solar convection. I. Differential rotation and pattern evolution achieved with laminar and turbulent states. Astrophys. J. **532**, 593–615 (2000)
79. Miesch, M.S., Brun, A.S., Toomre, J.: Solar differential rotation influenced by latitudinal entropy variations in the tachocline. Astrophys. J. **641**, 618–625 (2006)
80. Miesch, M.S., Brun, A.S., De Rosa, M.L., Toomre, J.: Structure and evolution of giant cells in global models of solar convection. Astrophys. J. **673**, 557–575 (2008)
81. Moss, D.: Magnetic fields and differential rotation in stars. Mon. Not. R. Astron. Soc. **257**, 593–601 (1992)
82. Neiner, C., Mathis, S., Saio, H., Lovekin, C., Eggenberger, P., Lee, U.: Seismic modelling of the late Be stars HD 181231 and HD 175869 observed with CoRoT: a laboratory for mixing processes. Astron. Astrophys. **539**, A90 (2012)
83. Ogilvie, G.I., Lin, D.N.C.: Tidal dissipation in rotating solar-type stars. Astrophys. J. **661**, 1180–1191 (2007)
84. Pinsonneault, M.H., Kawaler, S.D., Sofia, S., Demarque, P.: Evolutionary models of the rotating sun. Astrophys. J. **338**, 424–452 (1989)
85. Pinto, R.F., Brun, A.S., Jouve, L., Grappin, R.: Coupling the solar dynamo and the corona: Wind properties, mass, and momentum losses during an activity cycle. Astrophys. J. **737**, 72 (2011)
86. Press, W.H.: Radiative and other effects from internal waves in solar and stellar interiors. Astrophys. J. **245**, 286–303 (1981)
87. Remus, F., Mathis, S., Zahn, J.P.: The equilibrium tide in stars and giant planets: I—the coplanar case. arXiv:1205.3536 [astro-ph]

88. Rieutord, M.: The dynamics of the radiative envelope of rapidly rotating stars. I. A spherical Boussinesq model. Astron. Astrophys. **451**, 1025–1036 (2006)
89. Rogers, T.M., Glatzmaier, G.A.: Gravity waves in the sun. Mon. Not. R. Astron. Soc. **364**, 1135–1146 (2005)
90. Rogers, T.M., MacGregor, K.B.: On the interaction of internal gravity waves with a magnetic field—I. Artificial wave forcing. Mon. Not. R. Astron. Soc. **401**, 191–196 (2010)
91. Rogers, T.M., MacGregor, K.B.: On the interaction of internal gravity waves with a magnetic field—II. Convective forcing. Mon. Not. R. Astron. Soc. **410**, 946–962 (2011)
92. Rudiger, G., Kitchatinov, L.L.: The slender solar tachocline: a magnetic model. Astron. Nachr. **318**, 273 (1997)
93. Ruediger, G., Kitchatinov, L.L., Elstner, D.: Helicity and dynamo action in magnetized stellar radiation zones. arXiv:1107.2548 [astro-ph]
94. Samadi, R., Belkacem, K., Goupil, M.J., Dupret, M.A., Brun, A.S., Noels, A.: Stochastic excitation of gravity modes in massive main-sequence stars. Astrophys. Space Sci. **328**, 253–258 (2010)
95. Schatzman, E.: Filtering of gravity waves. Astron. Astrophys. **271**, L29 (1993)
96. Schatzman, E.: Transport of angular momentum and diffusion by the action of internal waves. Astron. Astrophys. **279**, 431–446 (1993)
97. Schatzman, E.: Diffusion process produced by random internal waves. J. Fluid Mech. **322**, 355–382 (1996)
98. Spada, F., Lanzafame, A.C., Lanza, A.F.: A semi-analytic approach to angular momentum transport in stellar radiative interiors. Mon. Not. R. Astron. Soc. **404**, 641–660 (2010)
99. Spiegel, E.A., Zahn, J.P.: The solar tachocline. Astron. Astrophys. **265**, 106–114 (1992)
100. Spruit, H.C.: Differential rotation and magnetic fields in stellar interiors. Astron. Astrophys. **349**, 189–202 (1999)
101. Spruit, H.C.: Dynamo action by differential rotation in a stably stratified stellar interior. Astron. Astrophys. **381**, 923–932 (2002)
102. Spruit, H.C.: Angular momentum transport and mixing by magnetic fields (invited review). In: Maeder, A., Eenens, P. (eds.) Stellar Rotation. IAU Symposium, vol. 215, p. 356 (2004)
103. Strugarek, A., Brun, A.S., Zahn, J.P.: Magnetic confinement of the solar tachocline: the oblique dipole. Astron. Nachr. **332**, 891 (2011)
104. Strugarek, A., Brun, A.S., Zahn, J.P.: Magnetic confinement of the solar tachocline: II. Coupling to a convection zone. Astron. Astrophys. **532**, A34 (2011)
105. Sweet, P.A.: The importance of rotation in stellar evolution. Mon. Not. R. Astron. Soc. **110**, 548 (1950)
106. Talon, S.: Transport processes in stars: Diffusion, rotation, magnetic fields and internal waves. In: Charbonnel, C., Zahn, J.P. (eds.) Stellar Nucleosynthesis: 50 Years After B^2FH, Aussois, France. EAS Publications Series, vol. 32, pp. 81–130 (2008)
107. Talon, S., Charbonnel, C.: Hydrodynamical stellar models including rotation, internal gravity waves, and atomic diffusion. I. Formalism and tests on Pop I dwarfs. Astron. Astrophys. **440**, 981–994 (2005)
108. Talon, S., Charbonnel, C.: Angular momentum transport by internal gravity waves. IV. Wave generation by surface convection zone, from the pre-main sequence to the early-AGB in intermediate mass stars. Astron. Astrophys. **482**, 597–605 (2008)
109. Talon, S., Kumar, P., Zahn, J.P.: Angular momentum extraction by gravity waves in the sun. Astrophys. J. Lett. **574**, L175–L178 (2002)
110. Tayler, R.J.: The adiabatic stability of stars containing magnetic fields—I. Toroidal fields. Mon. Not. R. Astron. Soc. **161**, 365 (1973)
111. Turck-Chièze, S., Palacios, A., Marques, J.P., Nghiem, P.A.P.: Seismic and dynamical solar models. I. The impact of the solar rotation history on neutrinos and seismic indicators. Astrophys. J. **715**, 1539–1555 (2010)
112. Vogt, H.: Zum Strahlungsgleichgewicht der Sterne. Astron. Nachr. **223**, 229 (1925)
113. Von Zeipel, H.: The radiative equilibrium of a rotating system of gaseous masses. Mon. Not. R. Astron. Soc. **84**, 665–683 (1924)

114. Wade, G.A., Alecian, E., Bohlender, D.A., Bouret, J.C., Cohen, D.H., Duez, V., Gagné, M., Grunhut, J.H., Henrichs, H.F., Hill, N.R., Kochukhov, O., Mathis, S., Neiner, C., Oksala, M.E., Owocki, S., Petit, V., Shultz, M., Rivinius, T., Townsend, R.H.D., Vink, J.S.: The MiMeS project: overview and current status. In: Neiner, C., Wade, G., Meynet, G., Peters, G. (eds.) Active OB Stars: Structure, Evolution, Mass Loss, and Critical Limits. IAU Symposium, vol. 272, pp. 118–123 (2011)
115. Wood, T.S., McCaslin, J.O., Garaud, P.: The sun's meridional circulation and interior magnetic field. Astrophys. J. **738**, 47 (2011)
116. Zahn, J.P.: Les marées dans une étoile double serrée (suite). Ann. Astrophys. **29**, 489 (1966)
117. Zahn, J.P.: The dynamical tide in close binaries. Astron. Astrophys. **41**, 329–344 (1975)
118. Zahn, J.P.: Instability and mixing processes in upper main sequence stars. In: Cox, A.N., Vauclair, S., Zahn, J.P. (eds.) Astrophysical Processes in Upper Main Sequence Stars. Saas-Fee Advanced Courses, vol. 13, p. 253 (1983)
119. Zahn, J.P.: Tidal evolution of close binary stars. I—Revisiting the theory of the equilibrium tide. Astron. Astrophys. **220**, 112–116 (1989)
120. Zahn, J.P.: Circulation and turbulence in rotating stars. Astron. Astrophys. **265**, 115–132 (1992)
121. Zahn, J.P.: Modeling stellar interiors with rotational mixing. In: Straka, C.W., Lebreton, Y., Monteiro, M.J.P.F.G. (eds.) Proceedings of the Joint HELAS and CoRoT/ESTA Workshop. EAS Publications Series, vol. 26, pp. 49–64 (2007)
122. Zahn, J.P., Talon, S., Matias, J.: Angular momentum transport by internal waves in the solar interior. Astron. Astrophys. **322**, 320–328 (1997)
123. Zahn, J.P., Brun, A.S., Mathis, S.: On magnetic instabilities and dynamo action in stellar radiation zones. Astron. Astrophys. **474**, 145–154 (2007)

Chapter 3
Ab Initio Modelling of Steady Rotating Stars

Michel Rieutord and Francisco Espinosa Lara

Abstract Modelling isolated rotating stars at any rotation rate is a challenge for the next generation of stellar models. These models will couple dynamical aspects of rotating stars, like angular momentum and chemicals transport, with classical chemical evolution, gravitational contraction or mass-loss. Such modelling needs to be achieved in two dimensions, combining the calculation of the structure of the star, its mean flows and the time-evolution of the whole. We present here a first step in this challenging programme. It leads to the first self-consistent two-dimensional models of rotating stars in a steady state generated by the ESTER code. In these models the structure (pressure, density and temperature) and the flow fields are computed in a self-consistent way allowing the prediction of the differential rotation and the associated meridian circulation of the stars. After a presentation of the physical properties of such models and the numerical methods at work, we give the first grid of such models describing massive and intermediate-mass stars for a selection of rotation rates up to 90 % of the breakup angular velocity.

3.1 Introduction

3.1.1 The Astrophysical Context

In the last ten years rotation has become an essential part of stellar models. It influences all stages of stellar evolution. For instance, during the formation process, a drastic reduction of the specific angular momentum, by a factor of order 10^5, is observed when matter passes from the initial molecular cloud to the newly born

M. Rieutord (✉) · F. Espinosa Lara
UPS-OMP, IRAP, Université de Toulouse, Toulouse, France
e-mail: Michel.Rieutord@irap.omp.eu

F. Espinosa Lara
e-mail: Francisco.Espinosa@irap.omp.eu

M. Rieutord · F. Espinosa Lara
IRAP, CNRS, 14 avenue E. Belin, 31400 Toulouse, France

M. Goupil et al. (eds.), *Studying Stellar Rotation and Convection*,
Lecture Notes in Physics 865, DOI 10.1007/978-3-642-33380-4_3,

main-sequence star. Later, during the evolution of the star on the main sequence, many hydrodynamical instabilities, along with meridian circulations, drive some mixing in the radiative zones. The effects of this mixing are actually observed on the surface of many stars, which show elements obviously synthesized in their core region. In addition, recent work by [19] shows that rotation plays a role in the nucleosynthesis of s-elements in massive stars. Effects of rotation are also thought to be important in understanding the evolution and "yields" of the first generation of stars. Lacking in metals, these stars were more compact than present stars and had also weaker winds. Thus, their rotation was certainly faster than that of present day stars. It is therefore crucial to master rotational effects in order to reconstruct the history of metal enrichment in galaxies and to understand how the observed stars have been influenced by the first generation. Lastly, we may mention an example of the importance of rotation in the end of the life of stars: recent works on the gravitational collapse of massive stars (e.g., [29]) insist on the importance of the combined effect of rotation and magnetic fields to model the explosion of supernovae and the associated production of a gamma-ray burst. The few foregoing examples are just illustrative, since rotation influences many other aspects of stellar physics like the oscillation spectrum, mass-loss etc.

3.1.2 The 1D Models

Presently, rotation is included in spherically symmetric stellar models through the approach proposed by [43]. Since these models are one-dimensional, all of the effects of rotation are averaged on spheres. Thus differential rotation is only in the radial direction (said to be shellular), and no meridian flow appears explicitly. Because only the first terms of the spherical harmonic expansion of fields are included, this modelling is valid at small rotation rates. An equally important part of the models is that they assume the existence of some small-scale turbulence in the radiative regions that efficiently transport momentum horizontally (i.e. on isobars), erasing latitudinal gradients of angular velocity.

Although limited to slow rotation and needing some ad hoc constants (like turbulent diffusivities), this approach has the great merit of allowing the use of 1D models, which are now very precise as far as microphysics is concerned. It thus allowed investigators to reproduce many observed features of stars: surface abundance of lithium as a function mass (e.g., [6]), the (relative) high number of red super-giants in low-metallicity galaxies (e.g., [27]), or the ratio of type Ibc to type II supernovae (e.g., [30]), etc.

Although these examples reflect a truly successful modelling, the understanding of the effects of rotation is still incomplete because in many circumstances rotation is fast. Stellar conditions thus do not meet the requirements of the models, and the use of Zahn's approach becomes dubious. Clearly, we are missing a more detailed view of reality. For instance, no one knows the rotation rates that are allowed in the foregoing 1D models.

3.1.3 The History of 2D Models of Rotating Stars

The solution to the deficiencies of 1D models about rotation will come from the use of multidimensional models (two-dimensional at least), which include the mean-field hydrodynamics along with the centrifugal distortion of the star. Unfortunately, building such models turned out to be a very difficult challenge. The story of this modelling is illuminating, and we briefly summarize it below, following the more detailed account of [37].

The first step dates back to polytropic hydrostatic models of [25]. An important step forward was made by a US group around Bodenheimer and Ostriker [1–3, 22, 28, 31–33]. Their works are based on the Self-Consistent Field method which solves Poisson's equation for the gravitational potential, $\Delta\phi = 4\pi G\rho$, with the Green function, namely

$$\phi(\mathbf{x}) = -G \int \frac{\rho(\mathbf{x}')}{|\mathbf{x} - \mathbf{x}'|} d^3\mathbf{x}'.$$

This solution readily includes the boundary conditions at infinity for the gravitational field.

Making general stellar models was impeded by many numerical difficulties. The codes could not deal with stellar masses less than $9M_\odot$ nor with very rapid rotation. An indication of the precision reached by these models is given by the virial test (see below). Reference [22] found it to be around 4×10^{-3}.

Soon after, M. Clement took up the challenge and solved directly the Poisson equation with a finite difference discretization [7]. Results improved as testified by a better virial test at 2×10^{-4}.

Another series of work aimed at the construction of 2D models was published by the Japanese school led by Eriguchi (see [11, 14]). These works led to the first attempts to account for the baroclinicity of radiative zones [41, 42], but the neglecting of viscosity imposed the prescription of some ad hoc constraints. The series ended with the work of [40], who improved the microphysics but relaxed the dynamics, considering only barotropic models.

To be complete, we need to mention the work of [12, 13] who attacked the problem in a different way, using a mapping of the star. The grid points are indeed mapped to the sphere through the relation

$$r_i(\theta_k) = \zeta_i R_s(\theta_k)$$

where ζ is a new radial variable spanning $[0, 1]$. Finite differences are used for both variables ζ and θ. The ensuing code was quite robust, being able to compute configurations quite far from the pure sphere, but the precision of calculation as monitored by the virial test remained around 5×10^{-4}.

The more recent efforts on 2D modelling not related to the ESTER project have been those of [39], motivated by the need of models of rapidly rotating stars for asteroseismology, and those of [23, 24], motivated by the discovery of the extreme

flattening of the Be star Achernar (e.g., [10]). These two works use barotropic models with an imposed rotation law. We note that [23] used a new version of the Self-Consistent Field technique which leads to a much more robust code, not restricted to a given mass range. These models have also been used to investigate the acoustic oscillation spectrum of rapidly rotating stars by [34, 35]. Lastly, [8] worked out a series of 2D models with uniform rotation for masses between 1.625 and $8M_\odot$.

3.2 The Route to Ideal Models

As may be observed, the weakest point of the foregoing models is their lack of dynamics as well as of time evolution. We recall that any radiative region of a rotating star is pervaded by baroclinic flows that appear in the first place as a differential rotation and a meridian circulation (e.g., [36]). These flows control some turbulence there and affect the whole star, playing an important role in the transport of elements and momentum.

We may now wonder what would be the ideal model of an isolated rapidly rotating star. This question was addressed in [37], and we reproduce here his discussion, which is still fully relevant:

Such a model should describe the mean state of a star at any time of its life and especially the new quantity specific to these stars, angular momentum.

Unlike a non-rotating star, which is a one-dimensional object (in a large-scale description) which needs only scalar fields ([we] forget magnetic fields), a rotating star is, at least, a two-dimensional object with, at least, one vector field in addition to all scalar fields. Hence, complexity increases not only by the multidimensional nature of the model but also by the number of physical quantities to be determined. This implies that the ideal model deals consistently with angular momentum and especially the losses and gains through stellar winds and accretion. Such a model should also take into account the baroclinicity of radiative zones and there, the anisotropic turbulence which appears through shear instabilities; it should also include a mean-field theory of convection to forecast Reynolds stresses and heat flux. Of course, observers would like to know the emissivity of the atmosphere as a function of latitude (if they use interferometry) or as a function of wavelength if they do spectroscopy. But if they do asteroseismology, they surely wish to know the eigenspectra of these objects.

"The foregoing points show that progress in the understanding of rotating stars needs also some advances in the following questions of stellar physics:

- How angular momentum is distributed in a star and how is it input or output with what consequences?
- The immediately following question concerns the nature of the Reynolds stresses in the convective and radiative zones.
- Then, what is the baroclinic state of the radiative regions?
- Similarly, the atmosphere is in a baroclinic state and cannot be at rest: how strong are the differential rotation and the meridional currents? Does the atmosphere develop strong azimuthal winds streaming around the star like Jupiter's winds?

- Gravity darkening can be so efficient that equatorial regions are cool enough to develop convection; this raises the question of the latitude dependence of emissivity of the atmosphere beyond the von Zeipel model (see the attempt of [26]).
- [we] did not mention magnetic fields. Clearly, they multiply the number of problems, and first steps should ignore them if possible."

3.3 Setting the Problem

Many of the foregoing questions can be answered by steady rotating stars, which evolve neither dynamically by losing mass and angular momentum, nor by gravitationally contracting, nor by nuclear evolution. As a first step towards the general models, we concentrate on this simpler problem.

3.3.1 Equations for a Steady Rotating Star

We consider a lonely rotating star in a steady state. The star is governed by the following equations for macroscopic quantities:

$$\begin{cases} \Delta\phi = 4\pi G\rho, \\ \rho T\,\mathbf{v}\cdot\boldsymbol{\nabla} s = -\operatorname{div}\mathbf{F} + \varepsilon_*, \\ \rho(2\boldsymbol{\Omega}_*\wedge\mathbf{v} + \mathbf{v}\cdot\boldsymbol{\nabla}\mathbf{v}) = -\boldsymbol{\nabla} P - \rho\boldsymbol{\nabla}(\phi - \frac{1}{2}\Omega_*^2 s^2) + \mathbf{F}_v, \\ \operatorname{div}(\rho\mathbf{v}) = 0. \end{cases} \tag{3.1}$$

The first equation is Poisson's equation, which relates the mass distribution (ρ is the density) and the gravitational potential ϕ (G is the gravitation constant). The second equation is the heat equation, which relates the advection of entropy s by the velocity field $\mathbf{v}$ when nuclear heat sources ε_* are present, with the heat flux $\mathbf{F}$. The third equation is the momentum equation written in a frame rotating at angular velocity $\boldsymbol{\Omega}_*$. P is the pressure field, and $\mathbf{F}_v$ the viscous force. Finally the last equation ensures mass conservation.

These equations need to be completed by those describing the microphysics and the transport properties of stellar matter. We propose to describe the heat flux with

$$\mathbf{F} = -\chi_r\boldsymbol{\nabla} T - \frac{\chi_{\text{turb}} T}{\mathscr{R}_M}\boldsymbol{\nabla} s,$$

where χ_r is the radiative conductivity, and χ_{turb} a turbulent heat conductivity. In this expression the second term is assumed to represent the convective heat flux, which is supposed to be controlled by the entropy gradient. $\mathscr{R}_M = \mathscr{R}/\mathscr{M}$ where $\mathscr{R}$ is the ideal gas constant and $\mathscr{M}$ the mean molecular mass of the fluid.

A realistic modelling of the viscous force would be derived from the turbulent Reynolds stresses; however, before reaching this long term goal, we assume the simple model of a constant dynamical viscosity μ, namely:

$$\mathbf{F}_v = \mu\left(\Delta\mathbf{v} + \frac{1}{3}\boldsymbol{\nabla}\,\mathrm{div}\,\mathbf{v}\right).$$

The microphysics is completed by the three expressions

$$\begin{cases} P \equiv P(\rho, T), \\ \kappa \equiv \kappa(\rho, T), \\ \varepsilon_* \equiv \varepsilon_*(\rho, T), \end{cases} \tag{3.2}$$

which respectively give the equation of state, the opacities and the nuclear heat generation. We recall that in radiative diffusive equilibrium, heat conductivity is related to opacity by

$$\chi_r = \frac{16\sigma T^3}{3\kappa\rho},$$

where σ is the Stefan–Boltzmann constant.

3.3.2 Boundary Conditions—Angular Momentum Condition

The previous system of partial differential equations needs to be completed by boundary conditions that affect the gravitational potential, the velocity field, the pressure and temperature.

At the star centre these conditions are simply that all functions should be regular. At the surface things are more difficult. First because the surface of a star is ill-defined. To simplify, we shall assume that the surface is an isobar or an equipotential. If the properties of the model are independent of the chosen surface, then we may say that the choice of the bounding surface is not crucial. On this surface we have to:

- Match the gravitational potential to that in the vacuum, which vanishes at infinity;
- Impose stress-free conditions on the velocity field, namely that

$$\mathbf{v}\cdot\mathbf{n} = 0 \quad \text{and} \quad \big([\sigma]\mathbf{n}\big) \wedge \mathbf{n} = \mathbf{0},$$

  where $[\sigma]$ is the stress tensor. The fluid is assumed to not flow outside the star and to feel no horizontal stress ($\mathbf{n}$ is the outer normal of the star);
- Specify the pressure on the surface. A simple choice is $P_s = \frac{2}{3}\frac{\overline{g}}{\overline{\kappa}}$, where $\overline{\kappa}$ and $\overline{g}$ are the averaged opacity and gravity on this surface;

- Impose the temperature boundary conditions. To simplify, we assume that the star radiates locally as a black body. Therefore we ask

$$\mathbf{n} \cdot \nabla T + T/L_T = 0,$$

where L_T is specifying the scale of temperature variations near the surface. We note that if the diffusion approximation is used, then $L_T = 16/(3\rho\kappa)$, κ being the opacity.

We note that this problem, as formulated by Eqs. (3.1), is not fully constrained because the total angular momentum is not specified. We have specified the rotation rate of the frame where the solution is computed, but this is not specifying the rotation rate of matter, which is the combination of both $\mathbf{v}$ and the solid body rotation of the frame. To remove this degeneracy, we may either specify the total angular momentum of the matter or specify the equatorial velocity of the star. In the first case we may write

$$\int_{(V)} r \sin\theta \rho u_\varphi \, dV = 0$$

and, in the second case,

$$v_\varphi(r = R, \theta = \pi/2) = 0.$$

The first condition just specifies that all the angular momentum of the star is in the solid body rotation of the frame, while the second just says that the frame is rotating at the equatorial angular velocity.

3.3.3 Scalings

As formulated by (3.1), the problem is that of the steady flow of a self-gravitating compressible gas subject to some heat sources. As all fluid mechanics problem we first need to choose the various relevant scales that feature the physical quantities. These scales are used to rewrite the set of equations with dimensionless variables. We converged to the following set:

Length scale: equatorial radius	R
Time scale	$(R^2/\mathscr{R}_M T_c)^{1/2}$
Velocity scale	$V = \sqrt{\mathscr{R}_M T_c}$
Density scale: central density	ρ_c
Temperature scale: central temperature	T_c
Pressure scale	$\mathscr{R}_M \rho_c T_c$
Entropy scale	$\mathscr{R}_M$
Potential scale	$4\pi G R^2 \rho_c$

This scaling uses the sound travel time as the time scale, and as a consequence the velocity field is scaled by a central sound velocity. Accordingly, the potential scale would be V^2, but we prefer to use $4\pi G R^2 \rho_c$, which comes from the free-fall time scale.

3.3.4 Dimensionless Equations and Numbers

Using the foregoing scaling leads to the following dimensionless equations:

$$\begin{cases} \rho(2\Omega\mathbf{e}_z \wedge \mathbf{u} + (\mathbf{u}\cdot\boldsymbol{\nabla})\mathbf{u}) \\ \quad = -\boldsymbol{\nabla} p - \rho\boldsymbol{\nabla}(\Lambda_p\psi - \frac{1}{2}\Omega^2 s^2) + E(\Delta\mathbf{u} + \frac{1}{3}\boldsymbol{\nabla}\,\mathrm{div}\,\mathbf{u}), \\ \rho T\mathbf{u}\cdot\boldsymbol{\nabla} s = \mathrm{div}(\chi\boldsymbol{\nabla} T + \chi_t T\boldsymbol{\nabla} s) + \varepsilon, \\ \mathrm{div}\,\rho\mathbf{u} = 0, \\ \Delta\psi = \rho, \end{cases} \tag{3.3}$$

with the numbers

$$\Omega = \frac{\Omega_* R}{\sqrt{\mathscr{R}_M T_c}}, \qquad E = \frac{\mu}{\rho_c R\sqrt{\mathscr{R}_M T_c}}, \qquad \Lambda_p = \frac{4\pi G R^2\rho_c}{\mathscr{R}_M T_c}$$

and the dimensionless functions

$$\psi = \frac{\phi_*}{4\pi G R^2\rho_c}, \qquad \chi = \frac{\chi_r(\rho, T)}{\mathscr{R}_M\rho_c R\sqrt{\mathscr{R}_M T_c}}, \qquad \varepsilon = \frac{R\varepsilon_*(\rho, T)}{\rho_c(\mathscr{R}_M T_c)^{3/2}}.$$

Although the critical angular velocity can only be computed after the completion of the calculation, it is useful to define the pseudo-critical angular velocity $\Omega_c = \sqrt{4\pi G\rho_c}$,

$$\frac{\Omega_*}{\Omega_c} = \frac{\Omega}{\sqrt{\Lambda_p}},$$

and introduce other dimensionless functions, namely

$$\overline{\varepsilon} = \varepsilon/\varepsilon(0), \qquad \overline{\chi} = \chi/\chi(0), \qquad \Lambda_T = \frac{\varepsilon(0)}{\chi(0)} = \frac{R^2\varepsilon_*(\rho_c, T_c)}{T_c\chi_r(\rho_c, T_c)}.$$

3.3.5 Global Parameters ρ_c, T_c, R of the Star Model

Let us suppose that we know the mass of the star M. How can the foregoing equations be used to determine the stellar quantities, especially ρ_c, T_c and R?

If we have solved the problem, we observe that Λ_p is known, which gives a first relation between ρ_c, T_c and R^2. In the same manner, the central value of ε gives a relation between ρ_c and T_c:

$$\varepsilon(0) = \frac{R\varepsilon_*(\rho_c, T_c)}{\rho_c(\mathscr{R}_M T_c)^{3/2}}.$$

Thus, taking into account that the mass of the star expresses as a function of R and ρ_c, namely

$$M = \rho_c R^3 \int_{(V)} \rho \, dV,$$

the expressions of Λ_p and $\varepsilon(0)$ completely determine the parameters of the stars, i.e. the radius, the central temperature and central density.

3.3.6 Numerical Method

The resolution of the set of Eqs. (3.3) imposes some numerical challenges. First, the shape of a rotating star is spheroidal and not known a priori. We thus use a mapping of coordinates adapted to this geometry and modify it during the calculation. Secondly, as the problem is two-dimensional, its size quickly grows with the resolution, thus imposing the use of an efficient numerical method that should be, at the same time, precise enough to deal with velocity fields. Finally, as the problem is nonlinear, we solve it using an iterative procedure.

3.3.6.1 Computational Domain and Mapping of Coordinates

Following [4], we use a mapping of the coordinates $r(\zeta, \theta)$ adapted to the geometry of the star. The new spheroidal coordinates (ζ, θ) are defined in such a way that $\zeta = 1$ represents the surface of the star, θ being the colatitude. In so doing, the surface of the star is a surface of coordinate, a property that very much simplifies the implementation of boundary conditions.

The star can be subdivided in several domains, and in each domain the relation between spherical and spheroidal coordinates is given by the general expression

$$r = a_i \zeta + A_i(\zeta)\big[R_{i+1}(\theta) - a_i \eta_{i+1}\big] + B_i(\zeta)\big[R_i(\theta) - a_i \eta_i\big], \quad \eta_i \le \zeta \le \eta_{i+1}, \tag{3.4}$$

where $B_i(\zeta) = 1 - A_i(\zeta)$. Here $R_i(\theta)$ and $R_{i+1}(\theta)$ represent the internal and external boundary of the domain respectively, and a_i, $A_i(\zeta)$ are chosen to satisfy some properties at the boundaries between the different domains. In particular, we want

$$r(\zeta = \eta_i, \theta) = R_i(\theta) \quad \text{and} \quad r(\zeta = \eta_{i+1}, \theta) = R_{i+1}(\theta);$$

then it should be that $A_i(\eta_i) = 0$ and $A_i(\eta_{i+1}) = 1$. The values of the parameters a_i should be such that r is monotonically increasing with ζ.

A nice property of this mapping is that it reduces to the spherical coordinates near the centre. The use of a spherical harmonic expansion of the unknowns is therefore possible, and the asymptotic properties of the solutions near the centre are well known. The decomposition of the stellar domain into multi-subdomains improves

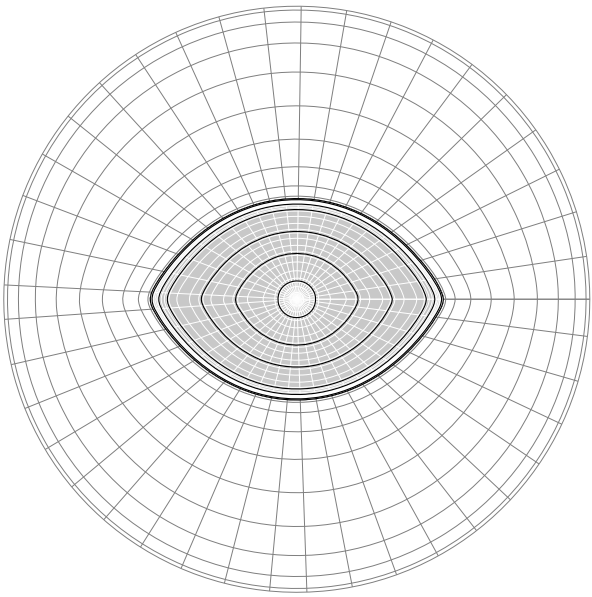

Fig. 3.1 The computational domain: the star at the centre is divided into sub-domains (layers) that ease the computations. It is surrounded by a vacuum domain limited by a sphere that allows an easy implementation of the boundary conditions on the gravitational potential

the efficiency of the spectral methods to be used, especially in dealing with discontinuities (interface between a convective and radiative region) and in dealing with the large pressure and density variations.

As we have already mentioned, at the stellar surface, the gravitational potential must match the vacuum solution vanishing at infinity. There is no easy way of imposing this condition on a surface with arbitrary shape. To circumvent this difficulty, we follow [4], who use an additional domain such that $1 \leq \zeta \leq 2$, and whose outer boundary is a sphere as shown in Fig. 3.1. On this sphere bounding the computational domain, the gravitational potential can meet simple boundary conditions for each of its spherical harmonics, namely

$$\frac{\partial \phi_\ell}{\partial r} + \frac{(\ell+1)\phi_\ell}{r} = 0,$$

which ensure the matching with a field vanishing at infinity. Figure 3.1 shows the full computational domain along with the key surfaces of the mapping.

To write down Eqs. (3.3), the operators should be written with the spheroidal coordinates. Let us first recall that the relation between these coordinates and the classical spherical coordinates is

$$r \equiv r\big(\zeta, \theta'\big), \qquad \theta = \theta', \qquad \varphi = \varphi'. \tag{3.5}$$

In order to manipulate these new coordinates, and especially the vectors, we use the natural basis defined by

$$\mathbf{E}_\zeta = \frac{\partial \mathbf{r}}{\partial \zeta}, \qquad \mathbf{E}_\theta = \frac{\partial \mathbf{r}}{\partial \theta}, \qquad \mathbf{E}_\varphi = \frac{\partial \mathbf{r}}{\partial \varphi}.$$

Making explicit these definitions, we can express the covariant and contravariant vectors, namely

$$\mathbf{E}_\zeta = r_\zeta \mathbf{e}_r, \qquad \mathbf{E}_\theta = r_\theta \mathbf{e}_r + r\mathbf{e}_\theta, \qquad \mathbf{E}_\varphi = r\sin\theta \mathbf{e}_\varphi,$$
$$\mathbf{E}^\zeta = \frac{\mathbf{e}_r}{r_\zeta} - \frac{r_\theta}{r r_\zeta}\mathbf{e}_\theta, \qquad \mathbf{E}^\theta = \frac{\mathbf{e}_\theta}{r}, \qquad \mathbf{E}^\varphi = \frac{\mathbf{e}_\varphi}{r\sin\theta},$$

as functions of the usual unit vectors associated with spherical coordinates $(\mathbf{e}_r, \mathbf{e}_\theta, \mathbf{e}_\varphi)$. We set:

$$r_\zeta = \frac{\partial r}{\partial \zeta}, \qquad r_\theta = \frac{\partial r}{\partial \theta}.$$

Passing from the spherical to the spheroidal coordinates may be done using the following relations:

$$\frac{\partial f}{\partial r} = \frac{1}{r_\zeta}\frac{\partial f}{\partial \zeta}, \qquad \frac{\partial f}{\partial \theta} = \frac{\partial f}{\partial \theta'} - \frac{r_\theta}{r_\zeta}\frac{\partial f}{\partial \zeta}, \qquad \frac{\partial f}{\partial \varphi} = \frac{\partial f}{\partial \varphi'}. \tag{3.6}$$

These expressions give the metric tensor whose covariant ($g_{ij} = \mathbf{E}_i \cdot \mathbf{E}_j$) and contravariant ($g^{ij} = \mathbf{E}^i \cdot \mathbf{E}^j$) components are:

$$g_{\zeta\zeta} = r_\zeta^2, \qquad g_{\zeta\theta} = r_\zeta r_\theta, \qquad g_{\theta\theta} = r^2 + r_\theta^2, \qquad g_{\varphi\varphi} = r^2\sin^2\theta, \tag{3.7}$$

$$g^{\zeta\zeta} = \frac{r^2 + r_\theta^2}{r^2 r_\zeta^2}, \qquad g^{\zeta\theta} = -\frac{r_\theta}{r^2 r_\zeta}, \qquad g^{\theta\theta} = \frac{1}{r^2}, \qquad g^{\varphi\varphi} = \frac{1}{r^2\sin^2\theta}, \tag{3.8}$$

and $g_{\zeta\varphi} = g_{\theta\varphi} = g^{\zeta\varphi} = g^{\theta\varphi} = 0$. At $r = 0$, $g^{\theta\theta}$ and $g^{\varphi\varphi}$ are singular. The metric determinant is such that

$$\sqrt{|g|} = r^2 r_\zeta \sin\theta \quad \text{and} \quad \left|\varepsilon^{ijk}\right| = \frac{1}{\sqrt{|g|}}.$$

The volume element is given by

$$dV = \sqrt{|g|}\, d\zeta\, d\theta\, d\varphi = r^2 r_\zeta \sin\theta\, d\zeta\, d\theta\, d\varphi = r^2 r_\zeta\, d\zeta\, d\Omega.$$

As an example, the Poisson equation for the gravitational potential takes the form

$$\begin{aligned}\Delta\psi = {} & g^{\zeta\zeta}\frac{\partial^2\psi}{\partial\zeta^2} + \left[\frac{2}{r r_\zeta}\left(1 + \frac{r_\theta r_{\zeta\theta}}{r r_\zeta}\right) - g^{\zeta\zeta}\frac{r_{\zeta\zeta}}{r_\zeta} - \frac{r_{\theta\theta} + r_\theta\cot\theta}{r^2 r_\zeta}\right]\frac{\partial\psi}{\partial\zeta} \\ & - \frac{2r_\theta}{r^2 r_\zeta}\frac{\partial^2\psi}{\partial\zeta\,\partial\theta} + \frac{1}{r^2}\left[\frac{1}{\sin\theta}\frac{\partial}{\partial\theta}\left(\sin\theta\frac{\partial\psi}{\partial\theta}\right) + \frac{1}{\sin^2\theta}\frac{\partial^2\psi}{\partial\varphi^2}\right] \\ = {} & \rho,\end{aligned}$$

where $r_{\zeta\zeta} = \frac{\partial^2 r}{\partial\zeta^2}$, $r_{\theta\theta} = \frac{\partial^2 r}{\partial\theta^2}$ and $r_{\zeta\theta} = \frac{\partial^2 r}{\partial\zeta\,\partial\theta}$.

3.3.6.2 Numerical Method

As we have mentioned earlier, due to the 2D nature of the problem, the size of the calculation will increase very quickly with the number of grid points. This motivates the use of a high-order method that can achieve high precision with low-resolution grids, optimizing computation time and memory requirements.

An additional difficulty comes from the fact that the overall structure of the star (profile of pressure, temperature, etc.) and its dynamics (rotation, meridional circulation) must be computed simultaneously. This requires a great precision and the ability to calculate higher-order derivatives of some variables.

Spectral methods are specially well suited for this kind of problem [5, 20]. These methods expand the solutions on a basis of orthogonal functions. The approximation of the solution using n basis functions will be

$$\phi^{(n)}(x) = \sum_{l=0}^{n-1} a_l P_l(x). \tag{3.9}$$

The basis functions $P_l(x)$ used are usually a set of orthogonal polynomials, such as the Legendre or Chebyshev polynomials. In our case it can be shown that if $\phi(x)$ is infinitely differentiable, the approximate function $\phi^{(n)}(x)$ will converge to the exact solution $\phi(x)$ faster than any power of the grid resolution h. This expresses the fact that, in spectral methods, the error decreases exponentially with the number of basis functions n [18]. The ith derivative of a function is approximated by

$$\left(\frac{d^i \phi}{dx^i}\right)^{(n)} = \sum_{l=0}^{n-1} a_l \frac{d^i P_l}{dx^i}. \tag{3.10}$$

Due to the nonlinearity of the equations that we have to solve, we have to calculate the product of two variables of the model in an efficient way. Unfortunately, multiplication cannot be easily performed using the spectral coefficients, as it involves a convolution in the transformed space. This can be solved by using an alternate approach of spectral methods, with the same properties, called pseudospectral collocation methods. In a pseudospectral method the variables are not represented by their spectral coefficients, but by their values at certain points x_i called the *collocation points*. Then, all the calculations can be performed in the real space.

The basis functions are orthogonal against some scalar product

$$\langle P_l, P_m \rangle = \delta_{lm}.$$

Then, we can get the spectral coefficients a_l by

$$a_l = \langle \phi(x), P_l(x) \rangle.$$

The scalar product (usually a weighted integral over the interval) can be calculated using the Gaussian quadrature formula associated with the family of orthogonal

polynomials P_l,

$$a_l = \sum_{j=0}^{n-1} w_j P_l(x_j)\phi(x_j),$$

where x_j and w_j are the nodes and weights of the Gaussian quadrature. Note that x_j are the collocation points. Then, the first derivative at the collocation points can be obtained as

$$\begin{aligned}\phi'(x_i) &= \sum_{l=0}^{n-1}\left(\sum_{j=0}^{n-1} w_j P_l(x_j)\phi(x_j)\right)P_l'(x_i)\\ &= \sum_{j=0}^{n-1}\left(\sum_{l=0}^{n-1} w_j P_l(x_j)P_l'(x_i)\right)\phi(x_j) = \sum_{j=0}^{n-1} D_{ij}\phi(x_j),\end{aligned}$$

where D_{ij} is the differentiation matrix.

We use this procedure in the radial and latitudinal directions to transform the original system of nonlinear partial differential equations into a system of nonlinear algebraic equations. For the latitudinal direction, we use Legendre polynomials as the basis functions, while for the radial direction, we use Chebyshev polynomials associated with the Gauss–Lobatto collocation points. This grid includes the points at the extrema in order to deal with boundary conditions.

The nice convergence properties of spectral and pseudospectral methods are only valid for smooth functions that are infinitely differentiable. However, it is known that inside a star there will be some discontinuities, as for example, at the boundary between a convective core and a radiative envelope. This difficulty is solved by using a multi-domain approach, in a way that the variables are continuous and differentiable within each domain but not necessarily at the boundaries between different domains.

3.3.6.3 Iterative Procedure

The system of algebraic equations resulting from the discretization of the problem is nonlinear and is solved using an iterative method. For that, we either use the well-known Newton's method or a relaxation method. For Newton's method, we write the problem in the form

$$\mathbf{F}(\mathbf{x}) = \mathbf{0}, \tag{3.11}$$

where the vector function $\mathbf{F}$ represents the equations that we want to solve, and $\mathbf{x}$ is the vector containing all the independent variables of the problem (pressure, temperature, etc.) including the shape of the surface, which is not known a priori. The equations are linearized using the Jacobian matrix of $\mathbf{F}(\mathbf{x})$ defined as

$$\delta\mathbf{F}(\mathbf{x}) = \mathrm{J}(\mathbf{x})\delta\mathbf{x}. \tag{3.12}$$

Then the correction to the solution in the kth iteration will be calculated solving the linear system

$$\mathsf{J}\big(\mathbf{x}^{(k)}\big)\delta\mathbf{x}^{(k)} = -\delta\mathbf{F}\big(\mathbf{x}^{(k)}\big), \tag{3.13}$$

and we set $\mathbf{x}^{(k+1)} = \mathbf{x}^{(k)} + \delta\mathbf{x}^{(k)}$.

With an appropriate initial approximation $\mathbf{x}^{(0)}$, Newton's method has quadratic convergence. In practice, a rotating stellar model can be calculated in approximately 10 iterations starting with the corresponding non-rotating model.

3.3.6.4 The Case of Flow Fields

The computation of the flow field is certainly the most delicate part of the solution. Its computation needs to circumvent two difficulties: first, the flow faces very large variations of the density (typically eight orders of magnitude), and second, the low viscosity of the stellar fluid. Indeed, this latter complication implies that the flows need to be computed within the asymptotic regime of low Ekman numbers while the zero viscosity solution is degenerate for the linear part of the velocity operator (any geostrophic flow may be added to a solution; see [36] for detailed explanations). We shall present this rather technical point in a separate work [17].

3.3.7 Tests of the Results

We checked the results with two global tests: the virial theorem and the global balance of energy.

3.3.7.1 The Virial Test

Let us first present the virial test. For this, we recall that the equations of a steady flow in a rotating frame are:

$$\begin{aligned} 2\boldsymbol{\Omega}\wedge\rho\mathbf{u} + \rho\mathbf{u}\cdot\boldsymbol{\nabla}\mathbf{u} &= -\rho\boldsymbol{\nabla}\phi + \rho\Omega^2 s\mathbf{e}_s + \mathbf{Div}[\sigma], \\ \operatorname{div}\rho\mathbf{u} &= 0, \end{aligned}$$

with the boundary conditions on the velocity field $\mathbf{u}\cdot\mathbf{n} = 0$ and $\mathbf{n}\wedge[\sigma]\mathbf{n} = \mathbf{0}$. The virial equality is obtained by integrating the scalar product of $\mathbf{r}$ with the momentum equation over the fluid's volume. Hence, we have to evaluate the following integrals:

- The z-component of the relative angular momentum

$$\int_{(V)} \mathbf{r}\cdot 2\boldsymbol{\Omega}\wedge\rho\mathbf{u}\,dV = -2\boldsymbol{\Omega}\cdot\int_{(V)}\mathbf{r}\wedge\rho\mathbf{u}\,dV = -2\Omega L_z.$$

- The gravitational energy

$$-\int_{(V)} \mathbf{r}\cdot\rho\nabla\phi\,dV = \frac{1}{2}\int_{(V)} \rho\phi\,d^3\mathbf{r} = W.$$

- The kinetic energy due to bulk rotation as measured by the frame rotation

$$\int_{(V)} \mathbf{r}\cdot\rho\Omega^2 s\mathbf{e}_s\,dV = \int_{(V)} \rho s^2\,dV = I\Omega^2,$$

  where I is the moment of inertia.
- The relative kinetic energy

$$\int_{(V)} \mathbf{r}\cdot\rho\mathbf{u}\cdot\nabla\mathbf{u}\,dV = -\int_{(V)} \rho u^2\,dV = -2T_{\mathrm{rel}}.$$

- The stress integral

$$\int_{(V)} \mathbf{r}\cdot\mathbf{Div}[\sigma]\,dV = \int_{(S)} r_i\sigma_{ij}\,dS_j - \int_{(V)} \sigma_{ii}\,dV.$$

  Stellar gas is assumed to be a Newtonian fluid without volume viscosity, and hence the stress tensor is

$$\sigma_{ij} = \mu c_{ij} - p\delta_{ij},$$

  where $[c]$ is the shear tensor ($c_{ij} = \partial_i v_j + \partial_j v_i - 2(\partial_k v_k)\delta_{ij}/3$), so that $\sigma_{ii} = -3p$.

Thus the virial equality may be written

$$2T_{\mathrm{rel}} + I\Omega_*^2 + W + 3P + I_s + 2\Omega_* L_z = 0$$

or, with non-dimensional quantities,

$$2T_{\mathrm{rel}} + I\Omega^2 + \Lambda_p W + 3P + I_s + 2\Omega L_z = 0, \tag{3.14}$$

where I_s is the surface integral that appears in the stress integral. In the case of a steady configuration like the one under consideration, the surface integral is estimated as follows:

$$I_s = \int_{(S)} \mu r_i c_{ij}\,dS_j - \int_{(S)} p\mathbf{r}\cdot d\mathbf{S}$$

with

$$\mathbf{n} = \mathbf{E}^\zeta \big/ \|\mathbf{E}^\zeta\|, \qquad \mathbf{r}\cdot\mathbf{n} = \frac{r}{r_\zeta\sqrt{g^{\zeta\zeta}}}, \qquad dS = r\sqrt{r^2 + r_\theta^2}\,d\Omega.$$

Using non-dimensional quantities, this leads to

$$I_s = \int_{4\pi}\left[E\left(2\partial_r u_r - \frac{2}{3}\operatorname{div}\mathbf{u} - \frac{r_\theta}{r}\left(\frac{1}{r}\frac{\partial u_r}{\partial\theta} + \frac{\partial u_\theta}{\partial r} - \frac{u_\theta}{r}\right)\right) - p(\theta)\right] r^3\,d\Omega.$$

3.3.7.2 The Energy Test

Another test of internal coherence of the solutions is provided by the energy balance between sources and losses. The integral of the entropy equation over the fluid's volume gives

$$\int_{(V)} \rho T \mathbf{u} \cdot \boldsymbol{\nabla} s \, dV = \int_{(S)} (\chi \boldsymbol{\nabla} T + \chi_t T \boldsymbol{\nabla} s) \cdot d\mathbf{S} + \int_{(V)} \varepsilon \, dV.$$

In the case of radiative envelopes at zero Prandtl number, this equation can be simplified to

$$\int_{(S)} (\chi \boldsymbol{\nabla} T) \cdot d\mathbf{S} + \int_{(V)} \varepsilon \, dV = 0.$$

3.4 Some Results

The foregoing algorithm has been used to compute models of rotating stars in a steady state. For these models, we use an analytic expression for the energy generation rate, namely

$$\varepsilon_*(\rho, T, X, Z) = \varepsilon_0(X, Z) \rho^2 T^{-2/3} \exp\left(A/T^{1/3}\right)$$

as in [15]. It is completed by the use of OPAL tables for the computation of the opacity and the derivation of the density from the equation of state ($X = 0.7$ and $Z = 0.02$ with solar composition of [21]).

We computed a few models of stars with a convective core, assumed to be an isentropic region, and with a radiative envelope. Presently, no convective envelope can be included in the models, which are therefore limited to stars with masses above $1.5 M_\odot$.

Numerical difficulties come both from the high density and pressure contrast between centre and from high rotation rates. At the time of writing (April 2012) the most extreme models deal with

$$p_{\rm surf}/p_{\rm centre} = 10^{-14} \quad \text{and} \quad \Omega/\Omega_K = 0.9.$$

The latter rotation corresponds to a flattening of 0.3. For these models, the spatial resolution uses a spherical harmonics series truncated at $L = 64$ and $N = 400$ collocation points on the radial grid, which are distributed over eight domains.

As far as the velocity field is concerned, we recall that the baroclinic flows that pervade the radiative region are computed in the asymptotic limit of vanishing Ekman numbers. Thus, the Prandtl number is also set to zero and heat advection by meridional flows is neglected. Figures 3.2 and 3.3 illustrate the differential rotation that is forced by the baroclinic torque. As also observed in previous (simpler) models of [15] and [38], the core is rotating faster than the envelope. The differential

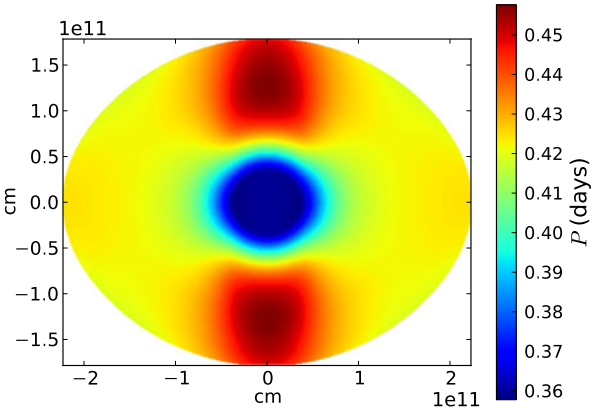

Fig. 3.2 Differential rotation in a $5M_\odot$ stellar model rotating at $\Omega = 0.7\Omega_K$

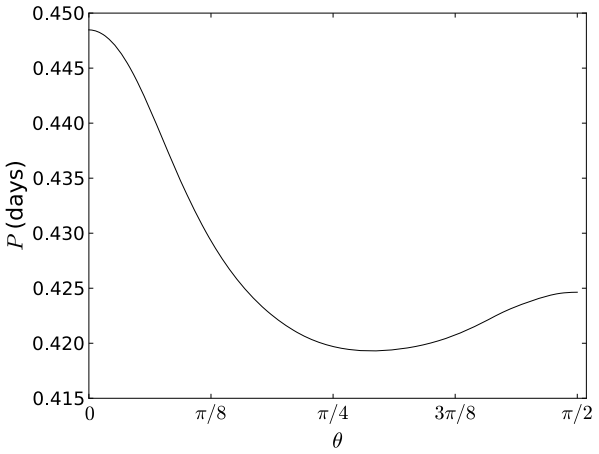

Fig. 3.3 The surface rotation as a function of colatitude. The stellar model is the same as that of Fig. 3.2

rotation is cylindrical in the isentropic core (as required by the Taylor–Proudman theorem) and almost shellular in the inner part of the radiative envelope.

The meridional circulation shown in Fig. 3.4 is dominated by the streamlines of the Stewartson layers lying along the tangent cylinder of the convective core. This flow pattern should not be taken at face value since the interior flows are computed without viscosity. The balance of forces in the Stewartson layer cannot be ensured, and therefore the flow pattern depends on the grid resolution.

In Fig. 3.5, we provide a view of the squared Brunt–Väisälä frequency. This shows the anisotropy of the buoyancy force, which, especially in the outer layers, influences the gravito-inertial modes that are part of the oscillation spectrum of such stars [9].

Besides the dynamics, we have also investigated the thermal structure of rotating stars and, more specifically, the distribution of the heat flux as a function of latitude. In [16], 2D models have been used to validate a very simple model of the latitudinal variations of the flux, which depends on a single parameter Ω/Ω_K. Such models

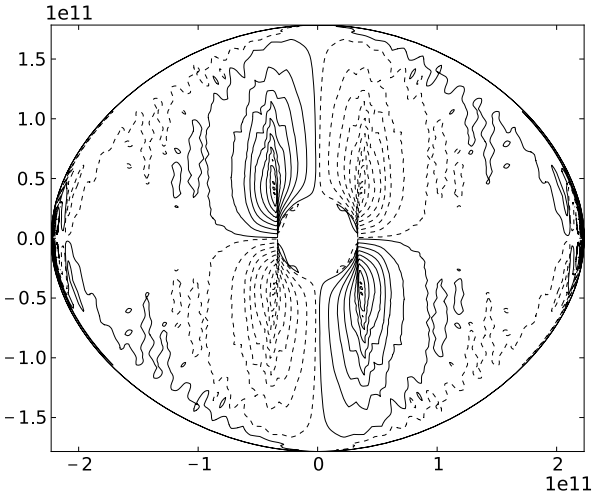

Fig. 3.4 Streamlines of the meridian circulation associated with the differential rotation shown in Fig. 3.2. *Solid lines* show counterclockwise circulation, and *dashed lines* clockwise one

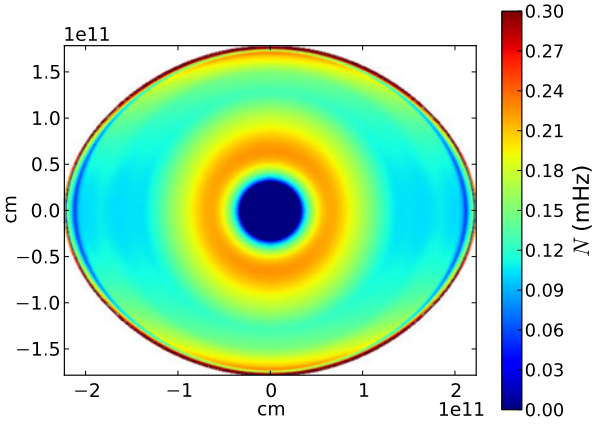

Fig. 3.5 The square of the Brunt–Väisälä frequency distribution in a meridian plane

are based on the idea that within an envelope the heat flux $\mathbf{F}$ satisfies $\mathrm{div}\,\mathbf{F} = 0$ and is almost anti-parallel to the local effective gravity $\mathbf{g}_e$. Since the mass distribution inside massive stars is concentrated, the Roche model can be used, leading to latitudinal flux variations that only depend on the rotation rate. This simple model has been successfully compared with the very few observations that are available and with complete two-dimensional models [16]. As shown in Fig. 3.6, the two models nicely match and notably differ from the model of von Zeipel, which predicts that $T_{\rm eff} \propto g_e^{1/4}$ as a consequence of neglecting of the baroclinicity of the configuration.

In Tables 3.1 and 3.2 we show the physical parameters obtained from the calculations of a series of stellar models with masses between 3 and $20 M_\odot$ and rotation rates up to 90 % of the breakup angular velocity. The models have been calculated

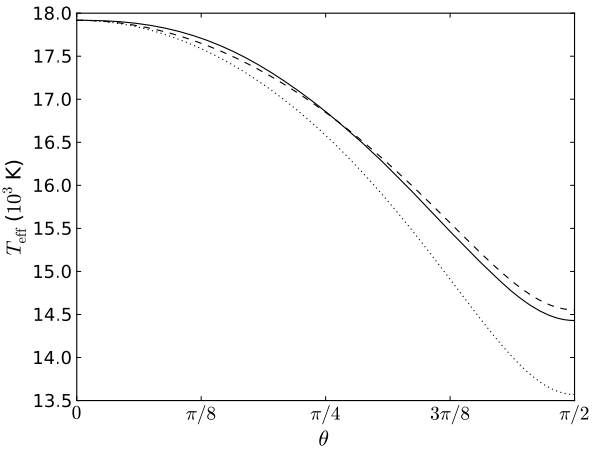

Fig. 3.6 Latitudinal flux variation (gravity darkening) at the surface of a rapidly rotating stellar model of $5M_\odot$. The *solid line* represents the full two-dimensional model, the *dashed line* the simplest model described in text and in [16], while the *dotted line* shows the prediction of von Zeipel hypothesis

Table 3.1 Fundamental parameters for a series of rotating stellar models[a]

M ($M_\odot$)	Ω/Ω_K[b]	R ($R_\odot$)	ε[c]	$P^{\rm s}_{\rm rot}$ (d)	$P^{\rm c}_{\rm rot}$ (d)	$v_{\rm eq}$ (km/s)	L ($L_\odot$)	$T_{\rm eff}$ (10^3 K)	$\log g_e$
3.0	0.0	1.97	0.00	–	–	0.0	81.2	12.36	4.33
3.0	0.3	1.96(p) 2.05(e)	0.04	0.70(p) 0.65(e)	0.54	158.6	80.0	12.50(p) 11.97(e)	4.33(p) 4.25(e)
3.0	0.5	1.95(p) 2.19(e)	0.11	0.46(p) 0.43(e)	0.36	255.5	78.4	12.69(p) 11.31(e)	4.34(p) 4.11(e)
3.0	0.7	1.94(p) 2.42(e)	0.20	0.38(p) 0.36(e)	0.30	340.4	77.0	12.84(p) 10.36(e)	4.34(p) 3.86(e)
3.0	0.9	1.93(p) 2.74(e)	0.29	0.35(p) 0.34(e)	0.28	411.5	76.4	12.92(p) 8.91(e)	4.34(p) 3.32(e)
5.0	0.0	2.62	0.00	–	–	0.0	542.8	17.23	4.30
5.0	0.3	2.60(p) 2.72(e)	0.04	0.83(p) 0.77(e)	0.66	177.7	533.2	17.44(p) 16.69(e)	4.31(p) 4.23(e)
5.0	0.5	2.58(p) 2.91(e)	0.11	0.55(p) 0.51(e)	0.44	286.5	520.9	17.70(p) 15.76(e)	4.31(p) 4.09(e)
5.0	0.7	2.57(p) 3.21(e)	0.20	0.45(p) 0.42(e)	0.36	381.9	510.4	17.92(p) 14.43(e)	4.32(p) 3.83(e)
5.0	0.9	2.56(p) 3.63(e)	0.30	0.42(p) 0.40(e)	0.33	461.6	505.3	18.02(p) 12.40(e)	4.32(p) 3.30(e)
10.0	0.0	3.87	0.00	–	–	0.0	5733.6	25.55	4.26
10.0	0.3	3.84(p) 4.02(e)	0.04	1.07(p) 0.98(e)	0.86	206.8	5619.0	25.85(p) 24.73(e)	4.27(p) 4.19(e)
10.0	0.5	3.81(p) 4.29(e)	0.11	0.70(p) 0.65(e)	0.57	333.6	5469.6	26.24(p) 23.35(e)	4.27(p) 4.05(e)

Table 3.1 (Continued)

M ($M_\odot$)	Ω/Ω_K[b]	R ($R_\odot$)	ε[c]	$P^{\rm s}_{\rm rot}$ (d)	$P^{\rm c}_{\rm rot}$ (d)	$v_{\rm eq}$ (km/s)	L ($L_\odot$)	$T_{\rm eff}$ (10^3 K)	$\log g_e$
10.0	0.7	3.78(p) 4.73(e)	0.20	0.57(p) 0.54(e)	0.46	444.8	5341.5	26.57(p) 21.35(e)	4.28(p) 3.80(e)
10.0	0.9	3.76(p) 5.37(e)	0.30	0.53(p) 0.51(e)	0.43	536.7	5279.3	26.73(p) 18.28(e)	4.28(p) 3.26(e)
20.0	0.0	5.70	0.00	–	–	0.0	43791.2	35.00	4.23
20.0	0.3	5.66(p) 5.91(e)	0.04	1.36(p) 1.24(e)	1.13	241.0	42921.1	35.41(p) 33.89(e)	4.23(p) 4.16(e)
20.0	0.5	5.61(p) 6.32(e)	0.11	0.89(p) 0.82(e)	0.74	388.5	41775.4	35.94(p) 31.97(e)	4.24(p) 4.01(e)
20.0	0.7	5.57(p) 7.00(e)	0.20	0.72(p) 0.68(e)	0.61	516.9	40790.9	36.39(p) 29.16(e)	4.24(p) 3.76(e)
20.0	0.9	5.54(p) 8.02(e)	0.31	0.67(p) 0.65(e)	0.56	621.0	40326.9	36.60(p) 24.82(e)	4.25(p) 3.22(e)

[a]From left to right: Mass, equatorial angular velocity, radius, flattening, central rotation period, surface rotation period, equatorial velocity, luminosity, effective temperature, logarithm of effective gravity (cgs). The values for the solar parameters used in the table are $M_\odot = 1.9891 \times 10^{33}$ g, $R_\odot = 6.95508 \times 10^{10}$ cm and $L_\odot = 3.8396 \times 10^{33}$ erg/s

[b]$\Omega_K = \sqrt{GM/R_e^3}$

[c]Flattening $\varepsilon = 1 - \frac{R_p}{R_e}$

using $L_{\max} = 64$ and 400 radial points distributed over eight domains. The virial and energy tests give an idea of the quality of the solutions. As we can see, the virial test values are very small, below a few 10^{-10}, as a result of the high precision of spectral methods. The energy test is also good enough (under around 10^{-5}), the larger values being a consequence of the use of tabulated opacities which have limited precision.

3.5 Conclusions

The computation of two-dimensional stellar models is a real numerical challenge that has been taken up by the ESTER project. The key difficulty is to derive simultaneously the bulk structure of the star and the mean velocity fields that pervade it. These large-scale flows come from either the baroclinicity of the radiative zones or from the anisotropic Reynolds stresses in the convective zones (although some Reynolds stresses might also be expected in the radiative zones if shear instabilities can generate some small-scale turbulence as suggested by [43]). At the moment, the ESTER code can produce dynamically self-consistent models, which include the background flows but no Reynolds stresses, for stars with masses larger than $1.5 M_\odot$ and rotation rates less than 90 % the break-up. The possibilities of the code have not yet been fully explored however.

Table 3.2 Fundamental parameters for a series of rotating stellar models (cont.)[a]

M ($M_\odot$)	Ω/Ω_K	p_c (dyn/cm^2)	ρ_c (g)	T_c (K)	p_s/p_c	ρ_s/ρ_c	Virial test[b]	Energy test[c]
3.0	0.0	1.34×10^{17}	40.8	2.43×10^{7}	9.61×10^{-15}	2.03×10^{-11}	5.08×10^{-11}	5.84×10^{-7}
3.0	0.3	1.34×10^{17}	41.0	2.43×10^{7}	9.92×10^{-15}	2.07×10^{-11}	8.01×10^{-11}	3.42×10^{-7}
3.0	0.5	1.35×10^{17}	41.3	2.42×10^{7}	1.03×10^{-14}	2.09×10^{-11}	2.03×10^{-10}	6.14×10^{-6}
3.0	0.7	1.35×10^{17}	41.5	2.42×10^{7}	1.07×10^{-14}	2.08×10^{-11}	2.67×10^{-10}	7.50×10^{-6}
3.0	0.9	1.36×10^{17}	41.6	2.42×10^{7}	1.09×10^{-14}	1.93×10^{-11}	2.31×10^{-10}	1.09×10^{-5}
5.0	0.0	8.00×10^{16}	21.3	2.76×10^{7}	3.86×10^{-14}	6.22×10^{-11}	1.20×10^{-10}	3.75×10^{-6}
5.0	0.3	8.04×10^{16}	21.4	2.75×10^{7}	3.97×10^{-14}	6.30×10^{-11}	8.41×10^{-11}	8.84×10^{-6}
5.0	0.5	8.09×10^{16}	21.6	2.75×10^{7}	4.11×10^{-14}	6.34×10^{-11}	7.51×10^{-11}	7.95×10^{-6}
5.0	0.7	8.13×10^{16}	21.7	2.75×10^{7}	4.23×10^{-14}	6.21×10^{-11}	8.01×10^{-11}	7.33×10^{-6}
5.0	0.9	8.16×10^{16}	21.8	2.74×10^{7}	4.29×10^{-14}	5.58×10^{-11}	1.06×10^{-10}	1.34×10^{-5}
10.0	0.0	4.31×10^{16}	9.44	3.20×10^{7}	1.53×10^{-13}	1.79×10^{-10}	8.96×10^{-12}	1.12×10^{-6}
10.0	0.3	4.33×10^{16}	9.50	3.20×10^{7}	1.56×10^{-13}	1.80×10^{-10}	4.91×10^{-11}	5.53×10^{-7}
10.0	0.5	4.35×10^{16}	9.58	3.19×10^{7}	1.60×10^{-13}	1.78×10^{-10}	5.18×10^{-11}	1.25×10^{-6}
10.0	0.7	4.38×10^{16}	9.65	3.19×10^{7}	1.64×10^{-13}	1.69×10^{-10}	2.59×10^{-11}	5.62×10^{-7}
10.0	0.9	4.39×10^{16}	9.69	3.18×10^{7}	1.66×10^{-13}	1.34×10^{-10}	4.54×10^{-11}	4.48×10^{-7}

Table 3.2 (Continued)

$M\ (M_\odot)$	Ω/Ω_K	p_c (dyn/cm^2)	ρ_c (g)	T_c (K)	p_s/p_c	ρ_s/ρ_c	Virial test[b]	Energy test[c]
20.0	0.0	2.79×10^{16}	4.88	3.62×10^{7}	3.26×10^{-13}	2.41×10^{-10}	1.54×10^{-11}	2.38×10^{-6}
20.0	0.3	2.80×10^{16}	4.91	3.61×10^{7}	3.31×10^{-13}	2.36×10^{-10}	7.25×10^{-11}	1.49×10^{-6}
20.0	0.5	2.81×10^{16}	4.94	3.61×10^{7}	3.39×10^{-13}	2.23×10^{-10}	1.79×10^{-11}	2.11×10^{-7}
20.0	0.7	2.82×10^{16}	4.98	3.60×10^{7}	3.46×10^{-13}	1.93×10^{-10}	7.16×10^{-11}	4.38×10^{-8}
20.0	0.9	2.83×10^{16}	5.00	3.60×10^{7}	3.49×10^{-13}	1.17×10^{-10}	4.09×10^{-11}	1.09×10^{-6}

[a]From left to right: Mass, equatorial angular velocity, central pressure, central density, central temperature, ratio between surface and central pressure, ratio between surface and central density, relative virial test and relative energy test. The values for the solar parameters used in the table are $M_\odot = 1.9891 \times 10^{33}$ g, $R_\odot = 6.95508 \times 10^{10}$ cm and $L_\odot = 3.8396 \times 10^{33}$ erg/s

[b]Virial test: $(2T_{\rm rel} + I\Omega_\star^2 + W + 3P + I_s + 2\Omega_\star L_z)/W$

[c]Energy test: $(\int_{(S)}(\xi\nabla T) \times d\mathbf{S} + \int_{(V)} \varepsilon\, dV)/\int_{(V)} \varepsilon\, dV$

As far as steady solutions are concerned, the main challenges are to enable the modelling of the lower-mass stars (solar type) with an outer convection zone and to take into account the effects of viscosity and Reynolds stresses in the bulk of the stars. These latter effects might indeed be crucial to the transport of elements.

The next important step will be to deal with time evolution. This should include:

- Dynamical evolution during PMS phase with a slow gravitational contraction inducing spin-up of the star;
- Dynamical evolution during main sequence with stellar wind, which forces a spin down and associated mixing;
- Nuclear evolution.

These steps need the right algorithm for temporal evolution, which is not known presently. Indeed, such an algorithm should be at the same time fast, stable and precise. We have managed to use spectral methods, which ensure rapidity and precision, but the stability remains a challenge. A better understanding of the properties of the discretized operators is certainly a key to improve the efficiency of the algorithms.

As shown by the foregoing examples, some realistic models can now be computed for intermediate mass and massive stars. These models are steady, and therefore the chemical composition must be given. To circumvent this constraint, one-dimensional models can be used to compute time evolution and the ensuing chemical composition. Then, the bulk relation between pressure and chemical composition shown by the 1D model can be inserted into the 2D model. In this way, steady models can include some stellar evolution.

The steady models described in this work are most relevant in the study of the oscillation properties of rotating stars. The interpretation of the frequency spectrum of such stars is indeed a challenging problem, and an intense use of 2D models will be necessary to find out how to invert data coming from, for instance, δ-Scuti stars.

Another use of these models is obviously the interpretation of interferometric data collected on some nearby fast rotating stars (α Aql, α Cep, α Leo, β Cas, etc.). Fast rotating stars have a surface brightness that strongly depends on latitude (gravity darkening). Accurate models are crucial to extract the physical parameters contained in the interferometric data from such stars.

Finally, steady two-dimensional models may also serve as proxies for the initial conditions of a collapsing massive star, although the final word will come from time-evolved models including mass-loss.

Acknowledgements The authors acknowledge the support of the French Agence Nationale de la Recherche (ANR) under grant ESTER (ANR-09-BLAN-0140). This work was also supported by the Centre National de la Recherche Scientifique (CNRS, UMR 5277), through the Programme National de Physique Stellaire (PNPS). The numerical calculations were carried out on the CalMip machine of the "Centre Interuniversitaire de Calcul de Toulouse" (CICT), which is gratefully acknowledged.

References

1. Bodenheimer, P.: Rapidly rotating stars. VII. Effects of angular momentum on upper-main models. Astrophys. J. **167**, 153 (1971)
2. Bodenheimer, P., Ostriker, J.P.: Rapidly rotating stars. VI. Pre-main—evolution of massive stars. Astrophys. J. **161**, 1101 (1970)
3. Bodenheimer, P., Ostriker, J.P.: Rapidly rotating stars. VIII. Zero-viscosity polytropic sequences. Astrophys. J. **180**, 159–170 (1973)
4. Bonazzola, S., Gourgoulhon, E., Marck, J.A.: Numerical approach for high precision 3D relativistic star models. Phys. Rev. D **58**, 104020 (1998)
5. Canuto, C., Hussaini, M.Y., Quarteroni, A., Zang, T.A.: Spectral Methods: Fundamentals in Single Domains. Springer, Berlin (2006)
6. Charbonnel, C., Talon, S.: The hot side of the lithium dip—LiBeB abundances beyond the main sequence. Astron. Astrophys. **351**, 635–643 (1999)
7. Clement, M.J.: On the solution of Poisson's equation for rapidly rotating stars. Astrophys. J. **194**, 709–714 (1974)
8. Deupree, R.G.: Structure of uniformly rotating stars. Astrophys. J. **735**, 69 (2011)
9. Dintrans, B., Rieutord, M.: Oscillations of a rotating star: a non-perturbative theory. Astron. Astrophys. **354**, 86–98 (2000)
10. Domiciano de Souza, A., Kervella, P., Jankov, S., Vakili, F., Ohishi, N., Nordgren, T.E., Abe, L.: Gravitational-darkening of Altair from interferometry. Astron. Astrophys. **442**, 567–578 (2005)
11. Eriguchi, Y.: Hydrostatic equilibria of rotating polytropes. Publ. Astron. Soc. Jpn. **30**, 507–518 (1978)
12. Eriguchi, Y., Müller, E.: A general computational method for obtaining equilibria of self-gravitating and rotating gases. Astron. Astrophys. **146**, 260–268 (1985)
13. Eriguchi, Y., Müller, E.: Structure of rapidly rotating axisymmetric stars. I—A numerical method for stellar structure and meridional circulation. Astron. Astrophys. **248**, 435–447 (1991)
14. Eriguchi, Y., Sugimoto, D.: Another equilibrium sequence of self-gravitating and rotating incompressible fluid. Prog. Theor. Phys. **65**, 1870–1875 (1981)
15. Espinosa Lara, F., Rieutord, M.: The dynamics of a fully radiative rapidly rotating star enclosed within a spherical box. Astron. Astrophys. **470**, 1013–1022 (2007)
16. Espinosa Lara, F., Rieutord, M.: Gravity darkening in rotating stars. Astron. Astrophys. **533**, A43 (2011)
17. Espinosa Lara, F., Rieutord, M.: Self-consistent 2D models of fast rotating stars with radiative envelopes. Astron. Astrophys. (2012, submitted)
18. Fornberg, B.: A Practical Guide to Pseudospectral Methods. Cambridge Univ. Press, Cambridge (1998)
19. Frischknecht, U., Hirschi, R., Thielemann, F.K.: Non-standard s-process in low metallicity massive rotating stars. Astron. Astrophys. **538**, L2 (2012)
20. Grandclément, P.: Introduction to spectral methods. In: Rieutord, M., Dubrulle, B. (eds.) Stellar Fluid Dynamics and Numerical Simulations: From the Sun to Neutron Stars, pp. 153–180. EDP Sciences (2006)
21. Grevesse, N., Noels, A.: The solar composition. In: Prantzos, N., Vangioni-Flam, E., Cassé, M. (eds.) Origin and Evolution of the Elements, pp. 15–25. Cambridge Univ. Press, Cambridge (1993)
22. Jackson, S.: Rapidly rotating stars. V. The coupling of the Henyey and the self-consistent methods. Astrophys. J. **161**, 579 (1970)
23. Jackson, S., MacGregor, K.B., Skumanich, A.: Models for the rapidly rotating Be star Achernar. Astrophys. J. **606**, 1196–1199 (2004)
24. Jackson, S., MacGregor, K.B., Skumanich, A.: On the use of the self-consistent-field method in the construction of models for rapidly rotating main-sequence stars. Astrophys. J. Suppl. Ser. **156**, 245–264 (2005)

25. James, R.A.: The structure and stability of rotating gas masses. Astrophys. J. **140**, 552 (1964)
26. Lovekin, C.C., Deupree, R.G., Short, C.I.: Surface temperature and synthetic spectral energy distributions for rotationally deformed stars. Astrophys. J. **643**, 460–470 (2006)
27. Maeder, A., Meynet, G.: Stellar evolution with rotation. VII. Low metallicity models and the blue to red supergiant ratio in the SMC. Astron. Astrophys. **373**, 555–571 (2001)
28. Mark, J.W.K.: Rapidly rotating stars. III. Massive main-sequence stars. Astrophys. J. **154**, 627 (1968)
29. Metzger, B.D., Giannios, D., Thompson, T.A., Bucciantini, N., Quataert, E.: The protomagnetar model for gamma-ray bursts. Mon. Not. R. Astron. Soc. **413**, 2031–2056 (2011)
30. Meynet, G., Maeder, A.: Stellar evolution with rotation. XI. Wolf–Rayet star populations at different metallicities. Astron. Astrophys. **429**, 581–598 (2005)
31. Ostriker, J.P., Bodenheimer, P.: Rapidly rotating stars. II. Massive white dwarfs. Astrophys. J. **151**, 1089 (1968)
32. Ostriker, J.P., Hartwick, F.D.A.: Rapidly rotating stars. IV. Magnetic white dwarfs. Astrophys. J. **153**, 797 (1968)
33. Ostriker, J.P., Mark, J.W.K.: Rapidly rotating stars. I. The self-consistent-field method. Astrophys. J. **151**, 1075–1088 (1968)
34. Reese, D.R., MacGregor, K.B., Jackson, S., Skumanich, A., Metcalfe, T.S.: Pulsation modes in rapidly rotating stellar models based on the self-consistent field method. Astron. Astrophys. **506**, 189–201 (2009)
35. Reese, D.R., Thompson, M.J., MacGregor, K.B., Jackson, S., Skumanich, A., Metcalfe, T.S.: Mode identification in rapidly rotating stars. Astron. Astrophys. **506**, 183–188 (2009)
36. Rieutord, M.: The dynamics of the radiative envelope of rapidly rotating stars. I. A spherical Boussinesq model. Astron. Astrophys. **451**, 1025–1036 (2006)
37. Rieutord, M.: Modeling rapidly rotating stars. In: Casoli, F., et al. (eds.) SF2A Proceedings 2006 (2006). arXiv:astro-ph/0702384
38. Rieutord, M., Espinosa Lara, F.: On the dynamics of a radiative rapidly rotating star. Commun. Asteroseismol. **158**, 99–103 (2009)
39. Roxburgh, I.W.: 2-dimensional models of rapidly rotating stars I. Uniformly rotating zero age main sequence stars. Astron. Astrophys. **428**, 171–179 (2004)
40. Shindo, M., Hashimoto, M., Eriguchi, Y., Mueller, E.: Rapidly rotating stars with either H burning or He burning core. Astron. Astrophys. **326**, 177–186 (1997)
41. Uryu, K., Eriguchi, Y.: Structures of rapidly rotating baroclinic stars—I. A numerical method for the angular velocity distribution. Mon. Not. R. Astron. Soc. **269**, 24 (1994)
42. Uryu, K., Eriguchi, Y.: Structures of rapidly rotating baroclinic stars—II. An extended numerical method for realistic stellar models. Mon. Not. R. Astron. Soc. **277**, 1411–1429 (1995)
43. Zahn, J.P.: Circulation and turbulence in rotating stars. Astron. Astrophys. **265**, 115 (1992)

Chapter 4
The Influence of Initial Conditions on Stellar Rotation History

J.P. Marques and M.J. Goupil

Abstract The question of whether the effects of different initial states persist during the main sequence is important, since it could shed light on the pre-main sequence phase.

In this work we discuss the effects of different initial states on the rotation profile during the main-sequence. We consider both solar-type stars and higher-mass stars. Solar-type stars are fully convective when they start their pre-main sequence evolution. They are braked by magnetic winds during the main sequence, and the effects of the initial conditions is soon forgotten. Lithium abundance, however, is a proxy for the rotation velocity at the ZAMS; it remains different for different initial conditions throughout the main sequence.

Higher-mass stars are not braked by winds, and they do not start their pre-main sequence evolution fully convective. Therefore, the question as to their initial rotation profiles may well be asked. We show that different initial rotation profiles lead to different profiles well into the main sequence. If we want to describe accurately stellar internal rotation, initial conditions need to be carefully considered.

4.1 Introduction

Internal transport of angular momentum remains an open problem in stellar physics. Several processes have been suggested: diffusion by turbulent viscosity, transport by meridional circulation [12, 35], torques due to magnetic fields [11, 14, 30] and transport by gravity waves [31]. An additional problem is magnetic braking by stellar winds [8], which is present in stars with significant convective envelopes. Addi-

J.P. Marques (✉)
Institut für Astrophysik, Georg-August-Universität Göttingen, Friedrich-Hund-Platz 1, 37077 Göttingen, Germany
e-mail: jmarques@astro.physik.uni-goettingen.de

J.P. Marques · M.J. Goupil
LESIA, Observatoire de Paris, CNRS UMR 8109, 92195 Meudon, France

M.J. Goupil
e-mail: mariejo.goupil@obspm.fr

M. Goupil et al. (eds.), *Studying Stellar Rotation and Convection*,
Lecture Notes in Physics 865, DOI 10.1007/978-3-642-33380-4_4,

tionally, the interaction between the star and the environment during the pre-main sequence (PMS) is essential in establishing initial conditions for the evolution of the internal rotation profile.

The effect of the initial conditions on the history of surface rotation velocities is well documented (see [3, 10] and references therein). Here we discuss the importance of the initial conditions on the internal rotation profile and surface chemical abundances. Our main goal is to see how far the imprint of the initial conditions persist and whether one should be more careful in considering them.

4.2 Transport of Angular Momentum

In convective zones, although there is differential rotation in latitude, the mean rotation rate at a given radius depends weakly on the radius. Therefore, it is often assumed in 1D stellar evolution codes that convective zones rotate as solid bodies [18, 20, 33].

In a radiative zone, we used the formalism of [35], refined in [12], to model the transport of angular momentum and chemical species by meridional circulation and shear-induced turbulence.

Turbulence is expected to be highly anisotropic due to the stable stratification in radiative zones; turbulence would then be much stronger in the horizontal than in the vertical direction. Thus, the hypothesis of "shellular rotation" can be used: as differential rotation is presumably weak along isobars, it is treated as a perturbation. All variables f can be split into a mean value over an isobar and a perturbation (as in [35]):

$$f(p,\vartheta) = \bar{f}(p) + \tilde{f}_2(p) P_2(\cos\vartheta), \tag{4.1}$$

where $P_2(\cos\vartheta)$ is the second-order Legendre polynomial, and p is the pressure.

The velocity of meridional circulation can be written in a spherical coordinate system as

$$\mathbf{U} = U_2(r) P_2(\cos\vartheta)\mathbf{e}_r + V_2(r)\frac{\mathrm{d}P_2(\cos\vartheta)}{\mathrm{d}\vartheta}\mathbf{e}_\vartheta, \tag{4.2}$$

where r is the mean radius of the isobar, and ϑ the colatitude. A positive U_2 corresponds to a circulation that rises at the poles and descends at the equator. The horizontal component V_2 can be obtained from U_2 using the equation of continuity in the anelastic approximation,

$$V_2 = \frac{1}{6\rho r}\frac{\mathrm{d}}{\mathrm{d}r}\left(\rho r^2 U_2\right), \tag{4.3}$$

where ρ is the density.

The transport of angular momentum obeys an advection–diffusion equation

$$\rho\frac{\mathrm{d}}{\mathrm{d}t}\left(r^2\Omega\right) = \frac{1}{5r^2}\frac{\partial}{\partial r}\left(\rho r^4 \Omega U_2\right) + \frac{1}{r^2}\frac{\partial}{\partial r}\left(r^4 \rho \nu_\mathrm{V}\frac{\partial \Omega}{\partial r}\right), \tag{4.4}$$

where ν_V is the vertical component of the turbulent viscosity, and $\mathrm{d}/\mathrm{d}t$ represents the Lagrangian time derivative. It is seen that a positive U_2 transports angular momentum inwards.

In a star in "shellular" rotation, isobaric and isopycnical (constant density) surfaces do not coincide (unless $\Omega(r)$ is constant, i.e., we have solid-body rotation). Thus, density varies along an isobar. The variation is given by the amount of differential rotation

$$\Theta = \frac{\tilde{\rho}}{\rho} = \frac{2r^2}{3g}\Omega\frac{\partial\Omega}{\partial r}. \tag{4.5}$$

In a region with a gradient of the mean molecular weight μ, meridional circulation will tend to create a variation of μ along an isobar. The strong horizontal turbulence tends to homogenize it in the horizontal direction, and thus the relative horizontal variation of the mean molecular weight, $\Lambda = \tilde{\mu}/\mu$, results from the competition between these two effects:

$$\frac{\mathrm{d}\Lambda}{\mathrm{d}t} = U_2\frac{\nabla_\mu}{H_P} - \frac{6D_\mathrm{h}}{r^2}\Lambda, \tag{4.6}$$

where D_h is the horizontal component of turbulent diffusion discussed below.

Finally, the vertical component of the meridional circulation is given by

$$U_2 = \frac{p}{c_p\rho T g[\nabla_\mathrm{ad} - \nabla + (\varphi/\delta)\nabla_\mu]}\left[\frac{L_r}{M^\star}(E_\Omega + E_\mu) + \frac{c_p T}{\delta}\frac{\mathrm{d}\Theta}{\mathrm{d}t}\right], \tag{4.7}$$

where c_p, T, g, ∇ and ∇_ad have their usual meaning (as defined in [9]). In Eq. (4.7) above, $M^\star$ is the reduced mass,

$$M^\star = m\left(1 - \frac{\Omega^2}{2\pi G\rho_m}\right), \tag{4.8}$$

where m and ρ_m are the mass and mean density inside an isobar, respectively. E_Ω and E_μ denote the so-called Ω- and μ-currents; explicit expressions are given in, e.g., [20]. The quantities φ and δ are obtained from the equation of state; they are defined as in [9]:

$$\delta = -\left(\frac{\partial\ln\rho}{\partial\ln T}\right)_{P,\mu}; \qquad \varphi = \left(\frac{\partial\ln\rho}{\partial\ln\mu}\right)_{P,T}. \tag{4.9}$$

The Ω-current contains $\Omega(r)$ and its derivatives. It is generally the driving term for the meridional circulation, whereas the μ-currents (containing μ and its derivatives) will generally oppose it.

Figure 4.1 shows an example of a U_2 profile (left panel) and corresponding 2D circulation (right panel). Since U_2 is negative everywhere in this example, the meridional circulation rises at the equator and sinks at the poles. There is one cell rotating counterclockwise in the quadrant shown. Figure 4.1 also shows, in the right panel, the temperature perturbation $\Delta T/T$. It is seen that, at a given radius, the pole is hotter than the equator.

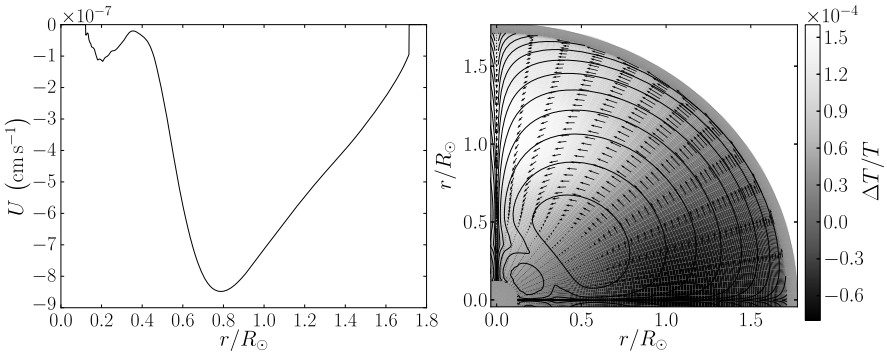

Fig. 4.1 *Left panel*: profile of the vertical component of the meridional circulation $U_2(r)$ as a function of normalized radius ($r/R_\odot$) for $1.5M_\odot$ stellar model at the middle of the main sequence. The rotation velocity at the equator is 70 km s^{-1} at the surface. *Right panel*: the corresponding 2D circulation pattern in a meridional plane and the temperature perturbation

4.2.1 Evolution of the Chemical Composition

The vertical advection of chemicals due to the large-scale meridional circulation coupled with a strong horizontal turbulent diffusion results in a vertical diffusion process (e.g., [4]). The equation of the chemical composition evolution can then be written as

$$\frac{\mathrm{d}X_i}{\mathrm{d}t} = \frac{\partial}{\partial m}\left[\left(4\pi r^2\rho\right)^2 (D_\mathrm{V} + D_\mathrm{eff})\frac{\partial X_i}{\partial m}\right] + \left.\frac{\mathrm{d}X_i}{\mathrm{d}t}\right|_\mathrm{nucl} + \left.\frac{\mathrm{d}X_i}{\mathrm{d}t}\right|_\mathrm{micro}, \tag{4.10}$$

where X_i is the abundance by mass of the ith nuclear species, and $D_\mathrm{V} = \nu_\mathrm{V}$ and D_eff are the vertical diffusivity and the diffusion coefficient associated with the meridional circulation.

A necessary condition for shear instability is the Richardson criterion as given by [32]. For the instability to grow, the turbulent viscosity ν_V must be greater than the molecular viscosity, ν, as expressed by the Reynolds criterion

$$\nu_\mathrm{V} > \nu\,\mathrm{Re}_\mathrm{c}, \tag{4.11}$$

where $\mathrm{Re}_\mathrm{c} \simeq 10$ is the critical Reynolds number [26]. When condition (4.11) is not satisfied, we use $D_\mathrm{V} = \nu_\mathrm{V} = \nu$.

4.2.2 Turbulent Coefficients of Diffusivity

The coefficient D_eff is given by [4]

$$D_\mathrm{eff} = \frac{(rU_2)^2}{30D_\mathrm{h}}. \tag{4.12}$$

We use the prescription of [15] for the horizontal component of turbulent diffusivity $D_{\rm h}$:

$$D_{\rm h}^2 = \frac{\beta}{10} r^3 \Omega |2V_2 - \alpha U_2|, \tag{4.13}$$

where

$$\alpha = \frac{1}{2} \frac{\partial \ln r^2 \Omega}{\partial \ln r}. \tag{4.14}$$

We take the coefficient $\beta = 1.5 \times 10^{-5}$ [23].

For the vertical component $D_{\rm V}$, we use the prescription of [32]:

$$D_{\rm V} = \frac{{\rm Ri_c}(K + D_{\rm h}) r^2}{N_T^2 + N_\mu^2 (1 + K/D_{\rm h})} \left(\frac{\partial \Omega}{\partial r} \right)^2, \tag{4.15}$$

where ${\rm Ri_c} = 1/6$ is the critical Richardson number, K the thermal diffusivity, N_T and N_μ the chemical and thermal parts of the Brunt–Väisälä frequency, $N^2 = N_T^2 + N_\mu^2$:

$$N_T^2 = \frac{g\delta}{H_P} (\nabla_{\rm ad} - \nabla); \qquad N_\mu^2 = \frac{g\varphi}{H_P} \nabla_\mu. \tag{4.16}$$

Other prescriptions have been used, and the problem of computing the diffusion coefficients is far from closed. A discussion is presented in Meynet et al., Chap. 1 of this volume.

4.3 Magnetic Braking

Stars less massive than 1.2 to $1.4 M_\odot$ have significant outer convective zones. A solar-type dynamo operates in this zone and generates a magnetic field. The coupling between the magnetic field and the plasma in the stellar wind strongly brakes the rotation of the star. The reason is that the wind is forced by the magnetic field to corotate with the surface of the star up to the Alfvén radius $r_{\rm A}$ (e.g., [17, 24]). Thus, the specific angular momentum carried by the wind is $\Omega_{\rm surface} r_{\rm A}^2$ and not $\Omega_{\rm surface} R_\star^2$, as it would be if there were no magnetic fields. For the Sun, $r_{\rm A} \simeq 10 R_\odot$, and the angular momentum lost by the Sun is 10^2 times larger with a magnetic field.

Following ([8], hereafter K88), the loss of angular momentum for a star of radius R and surface angular velocity Ω is

$$\dot{J} = \begin{cases} \frac{2}{3} \dot{M} R^2 \Omega (\frac{r_{\rm A}}{R})^2 & \text{for a radial field,} \\ \frac{2}{3} \dot{M} R^2 \Omega (\frac{r_{\rm A}}{R}) & \text{for a dipole,} \end{cases} \tag{4.17}$$

where $\dot{M}$ is the mass loss rate. The wind speed $v_{\rm wind}$ is proportional to the local escape velocity:

$$v_{\rm wind} = K_{\rm wind}\sqrt{\frac{2GM}{r}}, \tag{4.18}$$

where r is the distance to the center of the star. At $r = r_{\rm A}$, the Alfvén velocity $v_{\rm A}$ is equal to the wind velocity, and so,

$$v_{\rm A} = \frac{B_{\rm A}}{\sqrt{4\pi\rho}} = K_{\rm wind}\sqrt{\frac{2GM}{r_{\rm A}}}, \tag{4.19}$$

where $B_{\rm A}$ is the magnetic field at $r_{\rm A}$. From mass conservation,

$$\dot{M} = 4\pi\rho r_{\rm A}^2 v_{\rm wind}, \tag{4.20}$$

and the conservation of magnetic flux gives

$$\begin{aligned} B_0 R^2 &= B_{\rm A} r_{\rm A}^2 \quad \text{for a radial field,} \\ B_0 R^3 &= B_{\rm A} r_{\rm A}^3 \quad \text{for a dipole,} \end{aligned} \tag{4.21}$$

where B_0 is the magnetic field at the stellar surface. K88 assumed that the magnetic flux at the stellar surface scales with some power of the angular velocity,

$$B_0 = K_{\rm B}\frac{\Omega^a}{R^2}, \tag{4.22}$$

where a is expected, from theoretical considerations, to lie between 1 and 2. Thus, Eq. (4.17) becomes

$$\dot{J} = K_{\rm W}\Omega^{1+4an/3} R^{2-n} \dot{M}^{1-2n/3} M^{-n/3}, \tag{4.23}$$

where $K_{\rm W}$ contains the constants $K_{\rm wind}$ and K_B, M is the stellar mass, and $n = 2$ for a radial field, while $n = 3/7$ for a dipole. K88 chose $n = 1.5$, a value between both cases. With this choice, $\dot{J}$ is independent of the mass loss rate.

Measurements of magnetic fields in solar-type stars [25] seem to indicate a linear relation between B_0 and Ω up to values of around $10\Omega_\odot$, the value at which the magnetic field saturates. Thus, the exponent a in Eq. (4.22) is $a = 1$ for $\Omega < \Omega_{\rm sat}$ and $a = 0$ for $\Omega > \Omega_{\rm sat}$. Thus, Eq. (4.23) becomes

$$\dot{J} = \begin{cases} -K_{\rm W}\Omega^3 (\frac{R}{R_\odot})^{\frac{1}{2}} (\frac{M}{M_\odot})^{-\frac{1}{2}} & \text{for } \Omega < \Omega_{\rm sat}, \\ -K_{\rm W}\Omega\,\Omega_{\rm sat}^2 (\frac{R}{R_\odot})^{\frac{1}{2}} (\frac{M}{M_\odot})^{-\frac{1}{2}} & \text{for } \Omega \geq \Omega_{\rm sat}. \end{cases} \tag{4.24}$$

Hereafter, we will call Eq. (4.24) the K88 magnetic braking law.

The value of $\Omega_{\rm sat}$ is often set at 8–$14\Omega_\odot$ (as in [3]). There are indications that $\Omega_{\rm sat}$ varies with stellar mass (e.g., [1, 10]).

The parameter K_W in Eq. (4.24) is usually calibrated by requiring that solar models have $\Omega = \Omega_\odot = 2.86 \times 10^{-6}$ rad s^{-1}. The precise value of K_W needed to spin down the Sun to its current period depends on the prescription for the transport of angular momentum adopted (see below). The parameter K_W should depend on stellar mass (e.g., [10]).

Recently, [22] (hereafter RM12) have criticized the approach used in K88. Specifically, K88 assumed that the magnetic flux at the stellar surface scales with some power of the angular velocity, Eq. (4.22), whereas RM12 remarked instead that it is the magnetic field that should obey such a law, and thus, $B_0 \propto \Omega^a$. RM12 used $a = 1.5$ as a reasonable choice between the values expected from theory and consistent with [25]. RM12 used a radial field consideration to obtain

$$\dot{J} = \begin{cases} -K_{RM}\Omega^5 (\frac{R}{R_\odot})^{\frac{8}{3}} (\frac{M}{M_\odot})^{-\frac{2}{3}} & \text{for } \Omega < \Omega_{sat}, \\ -K_{RM}\Omega\Omega_{sat}^4 (\frac{R}{R_\odot})^{\frac{8}{3}} (\frac{M}{M_\odot})^{-\frac{2}{3}} & \text{for } \Omega \geq \Omega_{sat}. \end{cases} \tag{4.25}$$

We shall refer to Eq. (4.25) as the RM12 magnetic braking law. The value of K_{RM} does not depend on the stellar mass, and $\Omega_{sat} \simeq 3\Omega_\odot$ to reproduce rotation rates in young clusters.

4.4 Initial Conditions

Stars are fully convective as they start their pre-main sequence evolution on the Hayashi track. Assuming that convective zones rotate like solid bodies, the star should have a uniform angular velocity at the beginning of its evolution.

However, this is not a realistic assumption, since stars are not formed by the homologous contraction of the parental cloud. Instead, a hydrostatic core forms first, onto which matter accretes from the parental cloud during the *main accretion phase*. Once stellar winds dissipate the cloud, or the cloud is exhausted, the main accretion phase is over, and the star appears optically visible for the first time. Accretion may continue from a residual disk, but the mass of the star does not change significantly thereafter. The track of an accreting protostar in the HR diagram is called the *birthline* (after [29]). Initial conditions including the birthline are modeled in the following way: a protostar with a very small mass ($0.1 M_\odot$) starts accreting at a given rate, following the birthline in the HR diagram until it reaches its final mass. Then, accretion stops, and the usual pre-main sequence (PMS) evolution follows from that point. The main parameters of the birthline are the mass accretion rate $\dot{M}$ and initial deuterium abundance.

Figure 4.2 shows the evolution on the HR diagram of an accreting protostar, calculated with $\dot{M} = 10^{-5} M_\odot$ yr^{-1} and $\dot{M} = 2 \times 10^{-6} M_\odot$ yr^{-1}. For comparison, PMS tracks are also shown. It is clear, as shown for the first time by [21], that stars more massive than about $7 M_\odot$ (for $\dot{M} = 10^{-5} M_\odot$ yr^{-1}; $5 M_\odot$ for $\dot{M} = 2 \times 10^{-6} M_\odot$ yr^{-1}) do not have a PMS phase; they appear already at the ZAMS. Stars

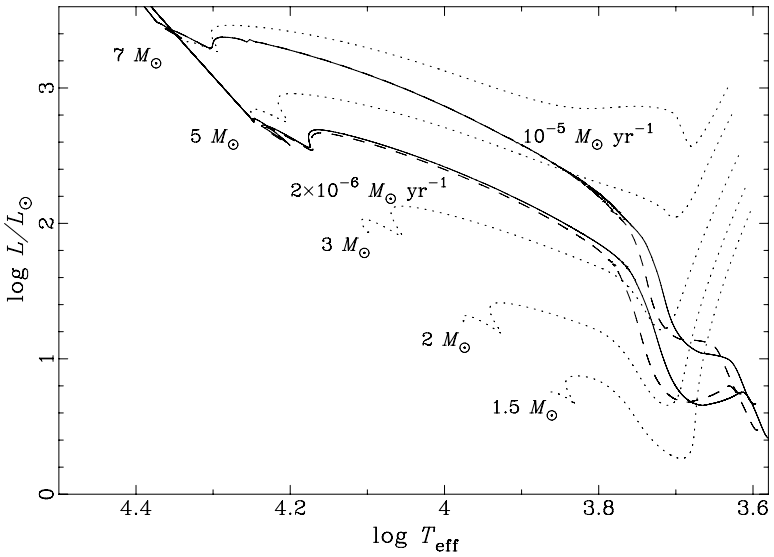

Fig. 4.2 Birthlines computed with two different accretion rates, $\dot{M} = 10^{-5} M_\odot$ yr^{-1} and $\dot{M} = 2 \times 10^{-6} M_\odot$ yr^{-1}. *Solid lines* indicate birthlines computed with a mixing-length parameter $\alpha = 1.6$, *dashed lines* indicate birthlines computed with a mixing-length parameter $\alpha = 1.3$. *Dotted lines* are classical PMS tracks, with masses labeled

more massive than $2M_\odot$ are no longer fully convective as they appear on the PMS. For these stars, a fully convective initial model is not a realistic assumption.

If, during the PMS, the only process slowing down stellar rotation were to be the magnetic braking by stellar winds mentioned above, stars would rotate much more rapidly than observed on the ZAMS. The PMS is too short for magnetic braking to slow down the star significantly. An additional process is needed during the PMS, most likely disk locking [3, 27].

Young stars are most often surrounded by a circumstellar disk left behind after the main accretion phase is over. The magnetic coupling between the star and the disk slows down the star (e.g., [27]); this effect is often modeled by assuming that the stellar surface co-rotates with the disk at a constant angular velocity [3] as long as the disk exists. Once the disk has disappeared, the star surface rotation evolves freely. The parameters of the model are the disk lifetime $\tau_{\rm disk}$ and rotation period $P_{\rm disk}$. The disk lifetime is expected to lie between 5 and 10 Myrs, while the rotation period is 1–10 days.

4.5 Solar-Type Stars

Solar-type stars appear fully convective on the PMS. Thus, an initial condition of uniform angular velocity is appropriate. As explained above, such stars are often surrounded by a circumstellar disk, and disk locking takes place. The parameters for

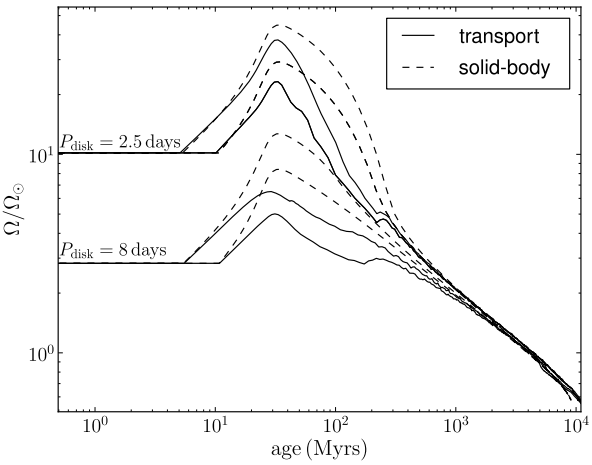

Fig. 4.3 Evolution of the surface angular velocity for $1M_\odot$ models with different initial conditions (see text). Loss of angular momentum was computed according to K88. *Solid lines* represent models including internal transport of angular momentum in radiative zones (solid-body rotation in convection zones), *dashed lines* represent models computed with solid-body rotation. The ZAMS is at an age of 50 Myrs

disk locking should not be the same for all stars. Indeed, the duration and Keplerian period for the disk depends on the environment in the star-forming region.

4.5.1 Evolution of the Rotation Rate

We have created a series of evolutionary models with $M = 1M_\odot$ using the code CESTAM [13]. Models were calculated using the framework for internal transport of angular momentum sketched above. We have also computed evolutionary models using solid-body rotation for comparison. Microscopic diffusion and settling were included according to the prescription of [19]; models calculated with transport of angular momentum also included rotation-induced mixing. The initial chemical composition and MLT parameter α were those of a solar model calibrated using the same physics and the solar mixture of [2]. The initial conditions for the evolution of the rotation profile were:

- $\tau_{\rm disk} = 5$ Myrs and $\tau_{\rm disk} = 10$ Myrs;
- $P_{\rm disk} = 2.5$ days (fast initial rotation) and $P_{\rm disk} = 8$ days (slow initial rotation).

Thus, we hoped to cover a reasonable range of conditions typical of observed disks around PMS stars.

Figure 4.3 shows the evolution of the surface rotation rate for models computed with the K88 magnetic braking law, computed with internal transport of angular momentum and using solid-body rotation. The constant $K_{\rm W}$ in Eq. (4.24) was calibrated to obtain the solar rotation rate at the solar age. For the models with internal transport of angular momentum, $K_{\rm W} = 6.5 \times 10^{47}$ g cm^2 s^2; for solid-body rotation, $K_{\rm W} = 4.9 \times 10^{47}$ g cm^2 s^2. The saturation rotation rate was set at $\Omega_{\rm sat} = 8\Omega_\odot$.

Disk locking is seen during the first 5 or 10 Myrs, depending on $\tau_{\rm disk}$. After an age $\tau_{\rm disk}$, the star is free to spin up as it contracts along the PMS. Magnetic braking by stellar winds is not efficient enough to slow down the star at this stage, but

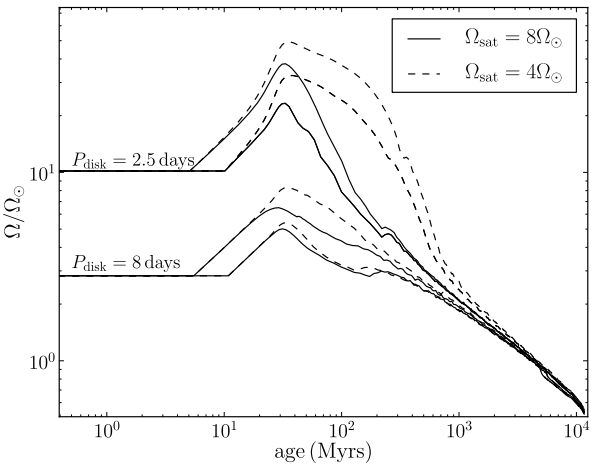

Fig. 4.4 Evolution of the surface angular velocity for $1M_\odot$ models with different initial conditions (see text). Loss of angular momentum was computed according to K88. *Solid lines* represent models calculated with $\Omega_{\rm sat} = 8\Omega_\odot$, *dashed lines* represent models computed $\Omega_{\rm sat} = 4\Omega_\odot$

it begins to slow down the star after the ZAMS. There are two regimes, depending on whether $\Omega > \Omega_{\rm sat}$ (saturated regime) or $\Omega < \Omega_{\rm sat}$ (unsaturated regime). For models computed with transport of angular momentum, we are always in the unsaturated regime for models with slow initial rotation. Models with fast initial rotation are in the saturated regime in the beginning, but as they slow down, they eventually enter the unsaturated regime. When Ω gets below $\Omega_{\rm sat}$, the rotation rate obeys the so-called Skumanich law [28], $\Omega \propto t^{-1/2}$. After about 1 Gyrs, all rotation histories converge to the same curve, a straight line in Fig. 4.3 corresponding to the Skumanich law (notice that Fig. 4.3 is a log–log plot). The internal Ω-profile does not depend on the initial conditions after the convergence of the rotation histories.

Models computed with solid-body rotation show faster rotation around the ZAMS. This is because magnetic winds must brake the whole star; in the case of transport of angular momentum, only the outer convection zone is initially braked, as it is weakly coupled to the radiative interior. Afterwards, angular momentum is transported from the faster rotating core, and the braking of the convection zone is slowed. Thus, the range of rotation periods in young clusters can constrain the efficiency of the transport of angular momentum (e.g., [6]).

Figure 4.4 shows the effect of changing the saturation angular velocity. All models shown were computed with transport of angular momentum. It is seen that a lower saturation threshold mimics a more efficient internal transport of angular momentum (compare with Fig. 4.3). This is because the braking is less efficient, therefore stars reach higher velocities at the ZAMS. Stars stay longer in the saturation regime, and thus the convergence of rotation histories occurs later, as seen in Fig. 4.4.

Finally, Fig. 4.5 shows a comparison between models computed with the braking laws of K88 and RM12. Models calculated with RM12 used $K_{\rm RM} = 4.25 \times 10^{38}$ g cm^2 s^4 in order to reproduce the solar rotation rate at the solar age. Two things are noticeable: first, because RM12 used $\Omega_{\rm sat} = 3\Omega_\odot$, stars stay in the saturated regime much longer; second, the unsaturated regime does not seem to follow the

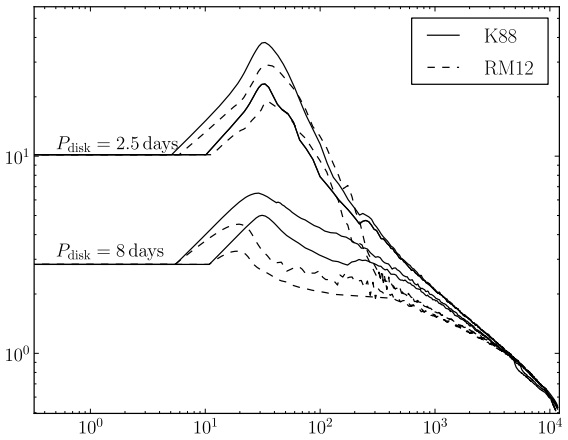

Fig. 4.5 Evolution of the surface angular velocity for $1M_\odot$ models with different initial conditions (see text). Loss of angular momentum was computed according to K88 (*solid lines*) and RM12 (*dashed lines*)

Skumanich law! Indeed, we expect $\Omega \propto t^{-1/4}$, since $\dot{J} \propto \Omega^5$ (compared to K88's $\dot{J} \propto \Omega^3$). RM12 have argued that their model reproduces *on average* the Skumanich law; first, models rotate faster than predicted by Skumanich law, then slower (see Fig. 4.5). However, RM12 have a strong dependence on radius; as a star evolves on the main sequence, its radius increases, and so, as seen in Fig. 4.5, the rotation rates of RM12 and K88 converge. In short, models computed with RM12 rotate more slowly than models computed with K88 before the middle of the MS. When they reach the solar age, however, their internal Ω-profiles are indistinguishable. Once again, the memory of the initial conditions is lost.

4.5.2 Evolution of the Surface Lithium Abundance

Lithium-7 is a fragile element, burned by proton capture at $T \simeq 2.5 \times 10^6$ K. This temperature corresponds to a region not too far below the convection zone in the Sun. This means that the ^{7}Li abundance in the outer convection zone is essentially equal to the initial abundance (a small fraction is burned during the PMS). The fact that $A(\mathrm{Li}) = 12 + \log N(\mathrm{Li})/N(\mathrm{H}) = 1.1$ in the solar convection zone, while the initial $A(\mathrm{Li}) = 3.26$, means that there is some process transporting lithium in the radiative zone. Microscopic diffusion and settling are not efficient enough to account for the deficit. Efficient convective overshoot below the convective zone could explain the discrepancy, but lithium depletion would, in this case, have happened in the PMS. Reference [16] show, however, that during the MS the lithium abundance decreases with age for solar twins. This is compatible with a diffusive process, such as rotation-induced mixing.

Figure 4.6 shows the evolution of the surface lithium abundances for the models shown in Fig. 4.3 (with transport of angular momentum). The evolution is of the kind shown in [16], but our models deplete lithium too much. This is compatible to what is known about the solar rotation profile in the radiative zone. Our models predict a

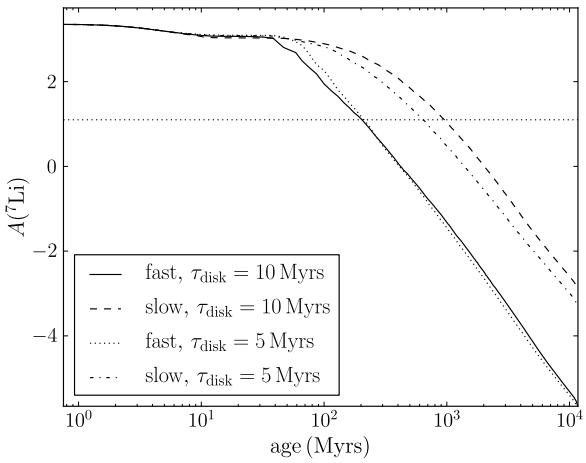

Fig. 4.6 Evolution of the surface lithium abundance for $1M_{\odot}$ models with different initial conditions (see text)

rotation profile that increases toward the center, while results from helioseismology show a flat rotation profile (e.g., [34] and references therein). Hence, there should be less shear, and so less efficient lithium depletion.

Figure 4.6 shows that the amount of lithium depletion depends strongly on the initial conditions. Before rotation histories converge, stars with higher initial rotation rates deplete lithium more efficiently. This can be clearly see in Fig. 4.6: the difference in lithium abundances is established before the convergence age. Thus, lithium abundance is a probe of the initial conditions, even if the rotation profile forgets them. Reference [5] have used internal gravity waves to obtain a flat solar rotation profile. Their models reproduce the observed lithium abundances, and they indicate a dependence of lithium abundance on the initial conditions. However, other solutions to the solar rotation problem have been proposed, such as magnetic fields [11, 14, 30].

4.6 Intermediate Mass Stars

Intermediate mass stars, in the context of PMS evolution, are stars that appear on the PMS with a radiative core. They have $1.8M_{\odot} < M < 8M_{\odot}$. The initial conditions for the evolution of the rotation profile are particularly difficult, since they do not experience magnetic braking (they have thin outer convection zones) and so the memory of the initial conditions is likely preserved. Different initial rotation velocities persist for the rest of the life of the star, since there is conservation of angular momentum. Another issue concerns the initial rotation profile. Since the initial PMS model is not fully convective, there is no reason to enforce solid-body rotation there. The question of the initial rotation profile could be important.

Models are often evolved from a state in solid-body rotation at the ZAMS (e.g., [7]). We know, however, that after evolving on the PMS and before, models should

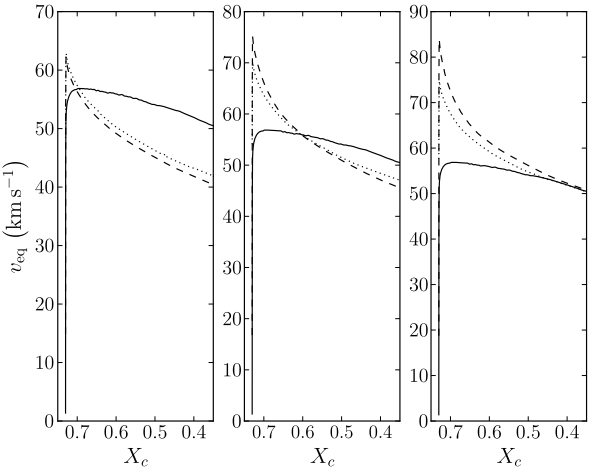

Fig. 4.7 Evolution of the rotation velocity for $5M_\odot$ models with different initial conditions (see text). *Solid lines* represent models PMS, *dashed lines* represent models BL, and *dotted lines* represent models ZAMS. The *left panel* shows models that have the same surface velocity at $X_c = 0.7$, the *middle panel* models that have the same surface velocity at $X_c = 0.6$, and the *right panel* models that have the same surface velocity at $X_c = 0.35$

not be in solid-body rotation at the ZAMS. To gauge the impact of introducing solid-body rotation at different stages, we computed $5M_\odot$ evolutions starting from models in solid-body rotation at the Hayashi track (model PMS), the birthline (model BL, see Fig. 4.2), and the ZAMS (model ZAMS). It is not realistic to enforce solid-body rotation at the birthline or ZAMS, of course.

Models have $X_i = 0.73$ and $Z_i = 0.01$, and no magnetic braking was included. Model PMS had an initial rotation velocity chosen in order to have $v_{eq} = 50\ \mathrm{km\,s^{-1}}$ at the ZAMS. The others had initial rotation velocities chosen in order to have the same velocity as model PMS at three different stages: when $X_c = 0.7$, $X_c = 0.6$, and $X_c = 0.35$. At these points, we compared the internal profiles.

Figure 4.7 shows the evolution of the rotation velocity for the models considered. It is clear that models PMS have a different evolution. The reason is that they arrive at the ZAMS with a relatively strong differential rotation, with the core rotating faster than the envelope. Thus, angular momentum is transported from the core to the envelope, where it compensates the slowing down caused by its slow expansion.

This can be seen in Fig. 4.8, showing the internal Ω-profiles corresponding to Fig. 4.7 when models have the same velocity. At $X_c = 0.7$, models BL have an envelope rotating faster than the core. This is because solid-body rotation was introduced at the birthline, before the convective core appears near the ZAMS. When a convective core appears due to the beginning of the nuclear reactions, it expands, leading to a decrease of the angular velocity in the core. Thus, BL models arrive at the ZAMS with an envelope rotating faster than the core. Models ZAMS, on the other hand, do not have time to change their structure significantly, thus rotating close to their initial condition: as solid bodies. Models PMS arrive at $X_c = 0.7$ with a relatively high differential rotation.

During the first half of the main sequence, models BL and ZAMS have accelerating cores, while models PMS have cores that slow down. The Ω-profile of the three cases converge after $X_c = 0.3$. Therefore, the imprint of the initial conditions is visible in the rotation profile for a large part of the main sequence.

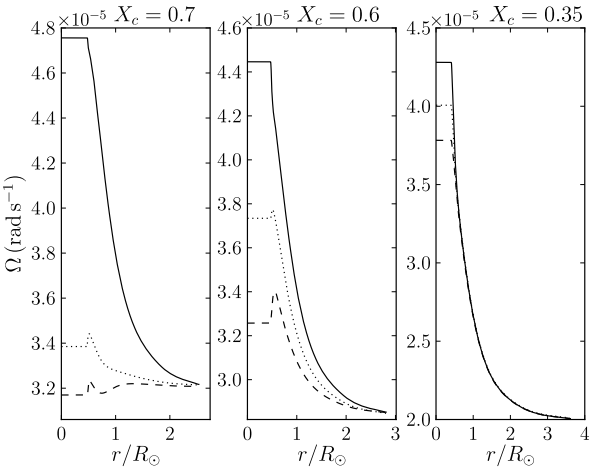

Fig. 4.8 Profile of Ω for $5M_\odot$ models with different initial conditions (see text). *Solid lines* represent models PMS, *dashed lines* represent models BL and *dotted lines* represent models ZAMS. The *left panel* shows models that have the same surface velocity at $X_c = 0.7$, the *middle panel* models that have the same surface velocity at $X_c = 0.6$, and the *right panel* models that have the same surface velocity at $X_c = 0.35$

4.7 Conclusions

We have presented a study of the impact of the initial conditions on the stellar rotation profile. We have considered stars which are braked by magnetic winds and those which are not. Stars that are braked lose the memory of the initial conditions relatively early on the MS. Both the surface rotation rates and the internal profile are the same afterwards, irrespective of the initial state.

On the other hand, stars that are not braked retain signatures of the initial conditions. Their rotation rate depends on their initial rotation velocity, since there is conservation of angular momentum. But their internal profiles also bear the mark of their history during the PMS and star formations.

It is known that meridional circulation and turbulent viscosity alone do not account for all the observed features of rotation in solar-type stars. Investigation of other mechanisms of transport of angular momentum in stars remains an important issue for future work.

References

1. Andronov, N., Pinsonneault, M., Sills, A.: Cataclysmic variables: An empirical angular momentum loss prescription from open cluster data. Astrophys. J. **582**, 358 (2003)
2. Asplund, M., Grevesse, N., Sauval, A.J.: The solar chemical composition. In: Barnes, T.G. III, Bash, F.N. (eds.) Cosmic Abundances as Records of Stellar Evolution and Nucleosynthesis. Astronomical Society of the Pacific Conference Series, vol. 336, p. 25 (2005)
3. Bouvier, J., Forestini, M., Allain, S.: The angular momentum evolution of low-mass stars. Astron. Astrophys. **326**, 1023 (1997)
4. Chaboyer, B., Zahn, J.P.: Effect of horizontal turbulent diffusion on transport by meridional circulation. Astron. Astrophys. **253**, 173 (1992)
5. Charbonnel, C., Talon, S.: Influence of gravity waves on the internal rotation and Li abundance of solar-type stars. Science **309**, 2189 (2005)

6. Denissenkov, P.A., Pinsonneault, M., Terndrup, D.M., Newsham, G.: Angular momentum transport in solar-type stars: testing the timescale for core-envelope coupling. Astrophys. J. **716**, 1269 (2010)
7. Eggenberger, P., Miglio, A., Montalban, J., Moreira, O., Noels, A., Meynet, G., Maeder, A.: Effects of rotation on the evolution and asteroseismic properties of red giants. Astron. Astrophys. **509**, A72 (2010)
8. Kawaler, S.D.: Angular momentum loss in low-mass stars. Astrophys. J. **333**, 236 (1988)
9. Kippenhahn, R., Weigert, A.: Stellar Structure and Evolution. Springer, Berlin (1991)
10. Krishnamurthi, A., Pinsonneault, M.H., Barnes, S., Sofia, S.: Theoretical models of the angular momentum evolution of solar-type stars. Astrophys. J. **480**, 303 (1997)
11. Maeder, A., Meynet, G.: Stellar evolution with rotation and magnetic fields. II. General equations for the transport by Tayler–Spruit dynamo. Astron. Astrophys. **422**, 225 (2004)
12. Maeder, A., Zahn, J.P.: Stellar evolution with rotation. III. Meridional circulation with MU-gradients and non-stationarity. Astron. Astrophys. **334**, 1000 (1998)
13. Marques, J.P., Goupil, M.J., Lebreton, Y., Talon, S., Palacios, A., Belkacem, K., Ouazzani, R.-M., Mosser, B., Moya, A., Morel, P., Pichon, B., Mathis, S., Zahn, J.-P., Turck-Chièze, S., Nghiem, P.P.: Seismic diagnostics for transport of angular momentum in stars 1. Rotational splittings from the PMS to the RGB. Astron. Astrophys. (2012, in press)
14. Mathis, S., Zahn, J.P.: Transport and mixing in the radiation zones of rotating stars. II. Axisymmetric magnetic field. Astron. Astrophys. **440**, 653 (2005)
15. Mathis, S., Palacios, A., Zahn, J.P.: On shear-induced turbulence in rotating stars. Astron. Astrophys. **425**, 243 (2004)
16. Meléndez, J., Ramírez, I., Casagrande, L., Asplund, M., Gustafsson, B., Yong, D., Do Nascimento, J.D., Castro, M., Bazot, M.: The solar, exoplanet and cosmological lithium problems. Astrophys. Space Sci. **328**, 193 (2010)
17. Mestel, L.: Magnetic braking by a stellar wind I. Mon. Not. R. Astron. Soc. **138**, 359 (1968)
18. Meynet, G., Maeder, A.: Stellar evolution with rotation. V. Changes in all the outputs of massive star models. Astron. Astrophys. **361**, 101 (2000)
19. Michaud, G., Proffitt, C.R.: Particle transport processes. In: Weiss, W.W., Baglin, A. (eds.) ASP Conf. Ser. 40: IAU Colloq. 137: Inside the Stars, p. 246 (1993)
20. Palacios, A., Talon, S., Charbonnel, C., Forestini, M.: Rotational mixing in low-mass stars. I Effect of the mu-gradients in main sequence and subgiant Pop I stars. Astron. Astrophys. **399**, 603–616 (2003)
21. Palla, F., Stahler, S.W.: The evolution of intermediate-mass protostars. I—Basic results. Astrophys. J. **375**, 288 (1991)
22. Reiners, A., Mohanty, S.: Radius-dependent angular momentum evolution in low-mass stars. I. Astrophys. J. **746**, 43 (2012)
23. Richard, D., Zahn, J.: Turbulence in differentially rotating flows. What can be learned from the Couette–Taylor experiment. Astron. Astrophys. **347**, 734–738 (1999)
24. Roxburgh, I.W.: Stellar winds and spindown in solar type stars. In: Stenflo, J.O. (ed.) Solar and Stellar Magnetic Fields: Origins and Coronal Effects. IAU Symposium, vol. 102, pp. 449–459 (1983)
25. Saar, S.H.: Recent magnetic fields measurements of stellar. Strassmeier, K.G., Linsky, J.L. (eds.) Stellar Surface Structure. IAU Symposium, vol. 176, p. 237 (1996)
26. Schatzman, E., Zahn, J.P., Morel, P.: Shear turbulence beneath the solar tachocline. Astron. Astrophys. **364**, 876 (2000)
27. Shu, F., Najita, J., Ostriker, E., Wilkin, F., Ruden, S., Lizano, S.: Magnetocentrifugally driven flows from young stars and disks. 1: A generalized model. Astrophys. J. **429**, 781 (1994)
28. Skumanich, A.: Time scales for CA II emission decay, rotational braking, and lithium depletion. Astrophys. J. **171**, 565 (1972)
29. Stahler, S.W.: The birthline for low-mass stars. Astrophys. J. **274**, 822 (1983)
30. Strugarek, A., Brun, A.S., Zahn, J.P.: Magnetic confinement of the solar tachocline: II. Coupling to a convection zone. Astron. Astrophys. **532**, A34 (2011)

31. Talon, S., Charbonnel, C.: Hydrodynamical stellar models including rotation, internal gravity waves, and atomic diffusion. I. Formalism and tests on Pop I dwarfs. Astron. Astrophys. **440**, 981 (2005)
32. Talon, S., Zahn, J.P.: Anisotropic diffusion and shear instabilities. Astron. Astrophys. **317**, 749 (1997)
33. Talon, S., Zahn, J.P., Maeder, A., Meynet, G.: Rotational mixing in early-type stars: the main-sequence evolution of a 9 $m_{\rm sun}$ star. Astron. Astrophys. **322**, 209 (1997)
34. Turck-Chièze, S., Palacios, A., Marques, J.P., Nghiem, P.A.P.: Seismic and dynamical solar models. I. The impact of the solar rotation history on neutrinos and seismic indicators. Astrophys. J. **715**, 1539 (2010)
35. Zahn, J.P.: Circulation and turbulence in rotating stars. Astron. Astrophys. **265**, 115 (1992)

Chapter 5
Numerical Exploration of Oscillation Modes in Rapidly Rotating Stars

Jérôme Ballot, François Lignières, and Daniel R. Reese

Abstract In this chapter, we show that two-dimensional oscillation codes help us to improve our knowledge of the effects of rapid rotation on acoustic (p) and gravity (g) modes. We first discuss how to solve the full problem of stellar oscillations in rapidly rotating stars by including the effects of the Coriolis force as well as those of the centrifugal distortion. We illustrate the development and the validation of a 2-D code using the Two-dimensional Oscillation Program (TOP) as an example. We then describe what strategies are being developed to explore the p- and g-mode spectra, how effective these methods are, and what intrinsic difficulties they face. In the last part of this chapter, we present results obtained with these techniques.

5.1 Introduction

Space-based missions CoRoT (Convection, Rotation, and planetary Transits) [2] and Kepler [40] opened a new area for asteroseismology by providing unprecedented long uninterrupted time series of high-precision photometric data over months or years. Nowadays, one of the limitations which hinders us from fully exploiting these data is the difficulty that we have in interpreting a number of the observed oscillation spectra. Whereas the structure of solar-like oscillation spectra is well understood, this is generally not the case for classical pulsators, which often exhibit more complex patterns. Stellar rotation is an identified source of complexity. Indeed, rapid rotation is very common for main-sequence intermediate- and high-mass stars

J. Ballot (✉) · F. Lignières
Institut de Recherche en Astrophysique et Planétologie, CNRS, UPS-OMP, Université de Toulouse, 14 avenue Edouard Belin, 31400 Toulouse, France
e-mail: jerome.ballot@irap.omp.eu

F. Lignières
e-mail: francois.lignieres@irap.omp.eu

D.R. Reese
Institut d'Astrophysique et Géophysique de l'Université de Liège, Allée du 6 Août 17, 4000 Liège, Belgium
e-mail: daniel.reese@ulg.ac.be

M. Goupil et al. (eds.), *Studying Stellar Rotation and Convection*, Lecture Notes in Physics 865, DOI 10.1007/978-3-642-33380-4_5,

[72] and may have a strong impact on the spectra of acoustic (p) modes—e.g., in δ Scuti and β Cephei stars—and gravity (g) modes—e.g., in γ Doradus and slowly pulsating B-type (SPB) stars.

Rotation has various effects on stellar oscillations, resulting from the appearance of the Coriolis and centrifugal forces. Whereas the former directly acts on the oscillatory motions, the latter distorts the star and modifies its structure. Thanks to the recent improvements of interferometric facilities, strong distortions have been measured in rapidly rotating stars. The Be star Achernar (α Eri) is probably the most famous and striking example [27]. Computing internal structures of distorted stars is the first challenge. In recent years, increasingly realistic models have been developed [21–23, 31, 37, 38, 53, 68, 70, 71], and a new generation of stellar models is now appearing (for a review, see Rieutord and Espinosa Lara, Chap. 3 of this volume). For a long time, the only way to obtain fully and consistently deformed stars was to consider polytropic models. If one was interested in realistic models, then one would have to consider a 1-D stellar model, obtained through classical evolution codes, which may include some effects of rotation on the structure (see the monograph [54] for more details) and deform it by considering the centrifugal distortion as a 2nd-order perturbation in Ω, as is done, for example, in [9, 43].

Rotation breaks the spherical symmetry of the oscillation problem by introducing a preferential axis. As a consequence, and in contrast to the nonrotating case, the oscillation problem is no longer separable with respect to the variables r (radius) and θ (colatitude). We then end up with a 2-D eigenvalue problem to solve. Several methods have been proposed to solve this problem. Approximate methods, such as the perturbative approach and the traditional approximation, have been devised, as well as solvers of the full problem (see, e.g., the review [61]).

A typical approach used in treating the effects of rotation on oscillation modes is to consider them as perturbation. One then transforms a 2-D problem into a sequence of 1-D problems, which is much simpler to solve. Methods which take into account the first-order effects of rotation were developed in [20, 41], second-order corrections were proposed by [12, 29, 35, 74, 79–81, 83], and even third-order terms were introduced by [39, 82]. Perturbative methods are valid as long as the rotation is slow enough. More precisely, the rotation rate, Ω, must satisfy the following conditions: $\Omega \ll \omega$ and $\Omega \ll \Omega_{\rm K}$, where ω is the pulsation frequency, while $\Omega_{\rm K} = \sqrt{GM/R^3}$ is the Keplerian break-up rotation rate, with G, M, R the gravitational constant, the mass and radius of the star, respectively. The first condition ensures that the effects of the Coriolis force are small, whereas the second ensures the centrifugal distortion is weak. Nevertheless, in practice we do not know a priori what constitutes a slow rotation. Only a comparison with complete 2-D computations allows us to quantify the condition on Ω (see Sect. 5.4.1).

For g modes, which have long periods, the assumption $\Omega \ll \omega$ is often not fulfilled. Another approach has been developed for this case. The traditional approximation, developed and commonly used in geophysics [30], consists in neglecting the tangential component of the rotation vector in the momentum equation, in assuming a spherical symmetry (i.e., neglecting the centrifugal distortion), and in neglecting

the perturbations of the gravitational potential (known as "the Cowling approximation" [19]). Within such approximations, the problem is again separable in r and θ. In contrast to the nonrotating case, the horizontal dependency of modes is not described with spherical harmonics but with Hough functions [91]. The traditional approximation has been applied to compute g modes in various stars, for example, in [5, 42, 44–46, 76, 87–89]. The validity of such an approximation can also be tested with full numerical computations (see Sect. 5.4.3).

To be able to treat arbitrarily high rotation rates, the full 2-D problem must be solved. Developing methods able to solve this problem with a reasonable accuracy is highly challenging. In this chapter, we present and discuss solvers for this difficult problem and their usage in asteroseismology. In Sect. 5.2, we present the relevant equations and methods to solve them. We emphasize the difficulties encountered in developing accurate numerical codes, before presenting the Two-dimensional Oscillation Program (TOP), developed by Reese et al. [63, 65]. We then describe in Sect. 5.3 how these codes can be used to compute and explore stellar oscillation spectra, and what strategies are introduced to find the modes of interest. In Sect. 5.4, we present some results obtained with these codes: how we test the limits of approximate methods, how the p- and g-mode spectra are modified by rapid rotation, what are the new families of modes that appear.

5.2 The Construction of an Oscillation Code for Rotating Stars

To our knowledge, three different methods have been implemented to compute stellar oscillation modes of rotating stars while fully taking into account the effects of rotation:

- The first method consists in finding the numerical solution of the boundary-value problem governing time-harmonic small amplitude perturbations.
- The second method considers the variational form of this boundary-value problem which expresses the eigenfrequencies as extrema of a functional of the flow. In [14], this equation is used to find the best solution assuming a truncated expansion on a suitable set of basis functions.
- A third method that has been mostly applied to compact stars [32] consists in solving the full time-dependent equations and to excite modes, for example, through initial perturbations. It is probably not efficient to determine the full eigenmode spectrum, but it is a natural way of investigate the nonlinear evolution of the perturbations.

With the exception of Clement's variational method [14], the direct resolution of the eigenvalue problem is the method that is most often used in stellar seismology [13, 25, 43, 50, 56, 63, 78]. In this section, we shall concentrate on it first by recalling the governing equations, then by discussing the possible numerical methods, and finally by illustrating, through the TOP code, the development and validation of a 2-D oscillation code.

5.2.1 The Governing Equations

The equations governing the oscillation modes in a rotating star can be written in different forms and with different levels of approximation [91]. For simplicity, we only present the equations governing small amplitude adiabatic perturbations of a uniformly rotating star:

$$\partial_t \rho + \boldsymbol{\nabla} \cdot (\rho_0 \mathbf{u}) = 0, \tag{5.1}$$

$$\rho_0 \partial_t \mathbf{u} + 2\rho_0 \boldsymbol{\Omega} \wedge \mathbf{u} = -\boldsymbol{\nabla} P + \rho \mathbf{g}_0 - \rho_0 \boldsymbol{\nabla} \psi, \tag{5.2}$$

$$\partial_t P + \mathbf{u} \cdot \boldsymbol{\nabla} P_0 = c_s^2 (\partial_t \rho + \mathbf{u} \cdot \boldsymbol{\nabla} \rho_0), \tag{5.3}$$

$$\Delta \psi = 4\pi G \rho, \tag{5.4}$$

where the equilibrium stellar model is described by its pressure, P_0, density, ρ_0, sound speed, c_s, and effective gravity, $\mathbf{g}_0 = -\boldsymbol{\nabla}(\psi_0 - \Omega^2 w^2/2)$, resulting from the gravitational potential, ψ_0, and the centrifugal potential that depends on the distance to the rotation axis, w. The perturbations are given by six dependent variables $\mathbf{u}$, ρ, P, ψ, corresponding to the perturbations of velocity, density, pressure, and gravitational potential, respectively.

We then look for normal mode solutions proportional to $\exp(-\mathrm{i}\omega t)$ and assume axial symmetry with respect to the rotation axis, which allows us to separate the dependence of the azimuthal coordinate, ϕ, with solutions proportional to $\exp(\mathrm{i}m\phi)$. As a result, the linear operators of the above equations only apply to the meridional plane. Solutions are then sought in the form $\rho = \Re\{\hat{\rho}(\mathbf{x}_M) \exp(\mathrm{i}m\phi - \mathrm{i}\omega t)\}$, where $\mathbf{x}_M$ is a point of the meridional plane. After including the boundary conditions at the star's surface, the system to be solved corresponds to a 2-D eigenvalue problem.

5.2.2 Discussion on the Mathematical and Numerical Options

When constructing a 2-D oscillation code, choices have to be made concerning the dependent variables, the coordinate system, the spatial discretization and the algebraic eigenvalue solver. The principal difficulty resides in the fact that we do not know in advance how the accuracy and efficiency of the code will depend on these choices. The series of papers by Clement [13–18], where he experimented with different methods, fully illustrates this difficulty. Typically, numerical problems manifest themselves by the presence of (many) spurious modes and/or by a failure of the solutions to converge as the numerical resolution grows. Below we briefly discuss the different mathematical and numerical options for the construction of a code, starting with the algebraic eigenvalue solver.

After discretization, the 2-D eigenvalue problem becomes an algebraic one and can be written in the form

$$\mathsf{A}\mathbf{F} = \lambda \mathsf{B}\mathbf{F}, \tag{5.5}$$

where A and B are $(N_V N_1 N_2) \times (N_V N_1 N_2)$ matrices that also include the boundary conditions, N_V is the number of dependent variables, and N_1 and N_2 denote the numbers of discretization points (or basis functions for spectral methods) for the two coordinates of the meridional plane. The efficiency and the accuracy of eigenvalue algorithms depend on the structure of these matrices. For our type of problem, A and B contain many zeros and thus belong to the class of sparse matrices. The way nonzero terms are distributed then depends on the specific problem considered and on the discretization method. In some cases, the nonzero terms can be confined around the main diagonal, thus forming a band matrix. There exist standard algorithms to find the eigenvalue of large matrices, the possibility of parallelizing them playing an important role in their final efficiency [73]. A difficulty that is not always acknowledged is that the determination of eigenvalues of a given matrix can be sensitive to the round-off errors on the matrix components. The amplitude of the resulting error depends on the structure of the matrix and more specifically on its conditioning. In some cases, it can be high enough to justify quadruple precision calculations [92].

The choice of the discretization method is crucial in many respects. Firstly, it is known to have a direct impact on the number of spurious modes (e.g., [93]). In a recent study dedicated to finite difference schemes, [62] proposes a method to minimize this number through a suitable choice of the numerical grid. Secondly, the discretization method affects the code's efficiency because it determines both the size and the structure of the matrices A and B. Indeed, if a method requires fewer discretization points N_1 and N_2 to represent a mode with a given accuracy, the product $N_1 N_2$ and thus the matrix size can be lowered. This argument favors high-order discretization schemes and spectral methods in particular. However, such schemes tend to lead to matrices with nonzero elements distributed throughout the entire matrix, whereas finite difference schemes produce band matrices, which reduce the storage requirements for the matrix. If the centrifugal deformation is neglected, a spherical harmonic expansion in latitude also leads to a banded structure because the Coriolis force only couples spherical harmonics of degree l and $l \pm 2$ [25]. The presence of near-discontinuities in evolved stellar interiors must also be taken into account when choosing a method. Typically, these can lead to applying a multidomain approach [56, 66].

Finally, the analytical form of the eigenvalue problem can also play an important role in the performance of the oscillation code. This includes the choice of dependent variables, coordinate system, and vector basis. Starting from the above linearized equations, one may try to lower the number of dependent variables N_V to diminish the matrix size. If, however, the order of the derivatives increases in the process, this is not necessarily a good idea because truncation errors generally increase with the derivative order. A suitable choice of the dependent variables can also be useful to ensure that the solution is smooth at the surface [63]. The question of the coordinate system arises because of the centrifugal deformation. Indeed, if one still uses spherical coordinates (r, θ, ϕ), the stellar surface no longer coincides with a constant-coordinate surface. To avoid the approximate treatment of the surface boundary conditions, one can use instead a surface-fitting coordinate system

(ζ, θ, ϕ) where ζ is specified by a relation $r = f(\zeta, \theta)$, $\zeta = 1$ corresponding to the star's surface [7]. The main disadvantage of these nonorthogonal coordinate systems is that writing differential operators can be quite cumbersome. For vectorial operators, this can be simplified by using the so-called natural basis associated with the coordinate system [36]. This holds in particular for the vector Laplacian.

5.2.3 Development and Validation of the TOP Code

In this subsection, the different steps in the construction of a 2-D oscillation code for rotating stars are described and illustrated in the case of the TOP code. While already suggested by the mathematical and numerical complexity of the problem, a step-by-step approach was actually imposed by the lack of accurate calculations to validate the code. Six low-order, low-degree modes computed by Clement [14] have been used for comparison, but the limited accuracy of these calculations did not allow more than a qualitative agreement [63].

The initial choices in building the TOP code were a surface-fitting coordinate system (ζ, θ, ϕ), a spectral method based on spherical harmonics in the angular coordinates (θ, ϕ) and a collocation spectral method based on Chebyshev polynomials in the pseudo-radial coordinate ζ. The possibility of using a polynomial spline-based method and finite difference schemes with or without the alternate grid approach [62] has been added since then. The algebraic eigenvalue solver returns a few eigenvalues near an initial guess. After a "shift and invert" transformation of the eigenvalue problem (Eq. (5.5)), the resulting system is solved with an iterative Arnoldi method including an accelerated convergence of the Chebyshev type [73]. The choice of spectral methods and the Arnoldi–Chebyshev solver has been made according to previous experience in the computation of gravito-inertial modes in spherical bodies [25, 69].

Various algebraic operations intervene when calculating the eigensolutions. These include calculating matrix–vector products, doing dot products, and solving linear systems for the shift and invert transformation. The first of these operations can be done efficiently using a sparse matrix multiplication, and the second is implemented using the BLAS[1] library [6]. The last operation is done through nonsparse LU factorization using the LAPACK[2] library. This requires explicitly creating the relevant matrix, a full matrix with typically 11 % nonzero elements in the fully spectral case, and a band matrix with typically 26 % nonzero elements (with respect to the relevant bands) in the finite difference case. Sparse solvers are not currently implemented in TOP—it is an open question whether or not such methods would lead to improved performances given the percentage of nonzero elements in both cases.

As a first step, a code taking into account the centrifugal deformation but neglecting the Coriolis force and the perturbation of the gravitational potential was

[1] Basic Linear Algebra Subprograms http://www.netlib.org/blas.

[2] Linear Algebra PACKage http://www.netlib.org/lapack.

developed [50]. After a validation at $\Omega = 0$, it was tested with the acoustic oscillations of a constant density ellipsoid. In this case, the eigenvalue problem is separable using ellipsoidal coordinates, thereby allowing alternate calculations with which to compare [49]. This code served as a reference for the development of a new code including the Coriolis force and the perturbation of the gravitational potential. The system of equations describing the oscillations in the two codes were completely different, thus providing an independent test for the treatment of the centrifugal deformation. This reference was indeed very useful for the purposes of debugging and validation. In the end, the agreement between the two codes reached a relative precision of $\Delta\omega/\omega \approx 10^{-7}$ for low-degree ($l \leq 3$), moderate-order ($n \leq 10$) p modes of rotating polytropic stellar models. To test the implementation of the Coriolis force and the perturbation of the gravitational potential in the new code, [63] used the variational principle as an independent and exact equation relating the frequencies and volume integrals involving the eigenmodes. Then the "variational frequency" obtained with a computed mode was compared with the original frequency, the difference being smaller than $\Delta\omega/\omega = 10^{-8}$.

The accuracy of the TOP code has been tested against the different numerical parameters. This not only includes the spatial resolution of the mode calculation ($L_{\max}$, the highest degree of the spherical harmonic expansion, N_r the number of Gauss–Lobatto collocation points for the Chebyshev spectral method or the number of grid points for the finite difference schemes) but also the numerical parameters of the stationary stellar model (its spatial resolution and the parameter that controls its convergence). As we have already mentioned, the round-off errors of the matrix components also affect the eigenvalue determination. In [92] it is shown that this effect can be measured by the dispersion of the frequency distribution obtained by changing the initial guess provided to the eigenvalue solver around the expected value of the eigenfrequency. Before giving some results on the TOP code, it must be recalled that the accuracy of any oscillation code strongly depends on the mode and on the stellar models considered. The TOP code's accuracy has been first determined for polytropic stellar models and a large set of pressure and gravito-inertial modes in [3, 50, 63]. For example, the relative frequency shift due to the numerical parameters can be as low as 10^{-9} for low-degree ($l \leq 3$), moderate-order ($n \leq 10$) p modes of polytropic stellar models with $\Omega/\Omega_{\rm K} \leq 0.6$. Such a high accuracy enables us to safely explore the p-mode asymptotic regime as in [48, 64]. For low-degree gravity modes followed up to $\Omega = 0.7\Omega_{\rm K}$, a relative accuracy of 5×10^{-8} has been achieved in [3]. If we now consider oscillations of the more realistic rotating stellar models of [53] computed with finite difference schemes, it has been shown in [65] that the accuracy is lowered between 10^{-3} and 10^{-2} for low-degree, high-order p modes, as based on the variational principle. Since then, a number of improvements and some corrections have been included in the code [67]: the use of a nonuniform radial grid suitable either for p modes or for g modes, an interpolation of the logarithm of the equilibrium density and pressure, which leads to better results in the near surface layers, a correct calculation of the ζ derivative of equilibrium quantities, which was mistakenly calculated with respect to r, a recalculation of the model's equipotential surfaces thereby removing some numerical inaccuracies, and the use of the alternate

grid approach in the finite differences thus removing spurious modes. As a result, the accuracy reached with the variational principle is now around 10^{-4} to 10^{-3}, depending on the rotation rate and the pulsation mode.

A by-product of the TOP code validation is that calculations of p modes and g modes in polytropic models of rotating stars can serve as a benchmark for existing and future 2-D oscillation codes. For instance, this has been the case with the recently developed ACOR code [56, 57].

5.3 Exploring Spectra

Before discussing exploration methods, it must be emphasized that any numerical exploration of the spectra faces two basic difficulties. First, spurious or badly resolved modes are generally computed together with well-resolved modes. As mentioned before, the number of spurious modes depends on the numerical method. But, the fact that some of the computed modes are not well resolved is hardly avoidable because the mode density is very high in most parts of the spectrum. This is particularly true among gravito-inertial modes. Second, the analysis of the numerical results is much more complicated than in the nonrotating case. When independent eigenvalue problems are solved for every degree l, each mode can generally be unambiguously labeled with its radial order n (see [85] for recent developments on this topic). In many cases, it boils down to node counting in 1-D functions. Here however, it is not necessarily easy, or even possible, to label the 2-D eigenfunctions with two quantum numbers by counting nodes.

To explore the oscillation spectra with a 2-D oscillation code, we may apply two complementary approaches: either following modes as functions of the rotation rate, or computing the full spectrum in a given frequency range at a chosen rotation rate. Past works proved that the first method is very useful and is absolutely needed for a first exploration. It is restricted to the necessarily limited number of followed modes and must be complemented with a detailed scanning of the spectrum at a fixed rotation rate.

5.3.1 Following Modes

The first method is a mode-by-mode approach. It consists in following the modes from zero rotation to a given rotation rate, Ω, and studying how the frequency varies and how the eigenfunctions are modified. It has been extensively and successfully used for example in [3, 15, 24, 50, 52, 63]. Such an exploration is a necessary phase in exploring the spectrum. It allows us to use the knowledge we have on the spectrum at zero rotation and focus at first on the modes that are a priori the most interesting for asteroseismology because they should have the widest horizontal scales.

The basis of the technique is as follows. Consider a p or g mode characterized by its degree l and radial order n in the nonrotating problem and denote its frequency

$\omega_{n,l}^{(0)}$. We have to follow the $2l+1$ components of this mode. Thus, we fix the azimuthal order m in the range $[-l, l]$ and follow the variations in frequency of the mode by increasing the rotation rate, step by step. A code such as TOP, based on the Arnoldi–Chebyshev method, requests an initial guess for the frequency and returns the closest solutions to this guess.

First, we have to choose a guess. It can be extrapolated from the solutions at lower rotation rates. A typical method is to compute a quadratic extrapolation from the three last points. For the first point at a nonzero rotation, the guess can be computed from the first-order perturbative term: $\omega_{n,l,m}^{(\text{guess})} = \omega_{n,l}^{(0)} + mC_{n,l}\Omega$, where $C_{n,l}$ is the Ledoux constant [41]. Generally, it is sufficient to consider the asymptotic values for $C_{n,l} \approx 0$ for p modes and $C_{n,l} \approx 1/[l(l+1)]$ for g modes.

To select the correct solutions among the ones found around the initial guess, the following strategy has been proposed in [3, 50, 63]:

1. For each calculated mode, we determine the two dominant degrees, l_1 and l_2, in the spherical harmonic expansion of the mode.
2. We compare l_1 and l_2 with the degree l of the mode we are following.
3. We select the solutions such that $l_1 = l$; if none of the solutions verifies this criterion, we select the solutions such that $l_2 = l$. For p modes, we can also allow the dominant degree to be shifted by $+2$, or even $+4$.
4. If more than one solution has been selected at this point, we choose the solution that gives the highest correlation with the mode at lower rotation.

It is easy to build an automatic procedure based on this strategy. Using such an approach, we easily follow low-degree modes. Moreover, we easily study how rotation progressively modifies the modes, thereby enabling us, for example, to determine the regime where approximate methods are valid.

Nevertheless, there are usually two practical problems we can encounter with the mode-following approach. A first issue comes from the so-called avoided crossings. Two modes with the same m and the same equatorial parity cannot have the same frequency. This implies that the two curves representing the evolution of frequency with Ω cannot cross each other: when the frequencies get closer and closer, the modes exchange their properties before moving away from each other. During an avoided crossing, the two modes have the mixed properties of the two initial modes. With a mode-following method, when the coupling is strong and the avoided crossing spans a large rotation range, the method can follow the wrong branch.

The second limitation originates in the density of modes. This remark is especially true for g modes, in particular in the sub-inertial domain ($\omega < 2\Omega$). We need the targeted mode to be close enough to the guess to be found in the returned solutions. When the modes are too dense, this can become really challenging. Indeed, according to the asymptotic relation for g modes from Tassoul [86], on a given period interval, the number of modes of degree l scales roughly as $\sqrt{l(l+1)}$. Moreover, in the sub-inertial domain, there are even more modes, since inertial modes appear. If the spatial resolutions were infinite, it would be impossible to find the desired solution, because there would always be an infinite number of other solutions closer to the initial guess than the targeted mode. In practice, the resolution is finite,

which naturally filters the solutions, but for high spatial resolutions this problem may persist. Another way of avoiding this difficulty is to add dissipation terms that spread the different frequencies into the complex plane.

There is another inconvenience of the mode-following technique: obviously, this only informs us on the modes we follow. We are then limited to information on modes that are present without rotation. Even if it is not a problem for p modes, it is a problem for low-frequency modes because inertial modes are not studied with such a technique.

5.3.2 Scanning the Spectrum

Another approach to spectrum exploration is to compute the spectrum at a fixed rotation rate over a given frequency interval. We can then scan the spectrum by progressively increasing the guess, step by step. If the incremental step is small enough, we can be sure that all the modes that can be accurately computed at the given resolution are indeed computed. To ensure the success of the scan, the following strategy can be used: at a given step, one uses as a guess the highest eigenfrequency found at the previous step. Such a strategy has limitations: firstly, if the mode density is very high, the step becomes very small; secondly, when the mode density decreases rapidly, the process can get stuck on the same set of solutions. A solution is to impose a minimal step size to ensure a strictly monotonic scan of the range.

Such a scan gives a complete picture of the spectrum—at a chosen spatial resolution—and can be useful for discovering new families of modes. However, the price paid is the computation of a lot of useless modes. Indeed, a major part of the time is spent on computing spurious modes or only marginally resolved modes which are unreliable.

It is nevertheless possible to accelerate the scan if we are interested in a certain class of modes that follow a known regularity (such as the large or small spacings). The exploration is significantly easier when the global structure of the spectrum is known. Thus, knowing asymptotic relations for classes of modes aids the rapid targeting of the correct frequency range in which to look for a given mode: when a mode of the family has been found, we can guess a small frequency interval where the next mode following this regularity should be found. Asymptotic relations for p and g modes are well known in the nonrotating case [86], and new relations have recently been derived analytically for a class of p modes (see Sect. 5.4.2) [58, 59].

5.3.3 Mode Labeling

A first way to label modes is based on following method: we label a mode with the numbers (n, l) that the mode has without rotation. It is a very convenient convention for a first exploration. It is one of the advantages of the mode-following technique.

Nevertheless, we have to keep in mind that the numbers l and n do not represent the node numbers in the horizontal and radial direction: l does not necessarily correspond to the dominant degree in the spherical harmonic expansion of the mode; the number of nodes along a radius generally varies with latitude.

A second, more physical, way to label modes is to be guided by ray-based asymptotic theories [47, 48, 65]. As detailed in Sect. 5.4.2.1, asymptotic theory for p modes in rotating stars allows us to classify computed modes into different families (island modes, chaotic modes, whispering gallery modes). It is then possible for whispering gallery modes and island modes to give labels $(\tilde{n}, \tilde{l})$ that really correspond to a number of nodes in the structure. For island modes, these new numbers are different from the numbers (n, l) given with the previous method—but $(\tilde{n}, \tilde{l})$ and (n, l) can be linked, as explained in Sect. 5.4.2.1.

5.4 Results

5.4.1 Testing Perturbative Methods

5.4.1.1 Deriving Perturbative Coefficients from 2-D Oscillation Codes

The mode-following technique has been applied to test approximate methods, especially perturbative approximations. In a kth-order perturbative approach, frequencies are developed as functions of Ω:

$$\omega_{n,l,m}^{(\mathrm{pert})} = \omega_{n,l}^{(0)} + \sum_{j=1}^{k} C_{n,l,m}^{j} \Omega^{j} + O\left(\Omega^{k+1}\right), \tag{5.6}$$

where $C_{n,l,m}^{j}$ are the perturbative coefficients.

The most natural method to compute these coefficients is to use the theories developed in the papers cited in Sect. 5.1. Nevertheless, using the mode-following technique, it is also possible to numerically compute the coefficients $C_{n,l,m}^{j}$ since they are directly related to the jth derivative of the function $\omega_{n,l,m}(\Omega)$ at $\Omega = 0$. To improve the accuracy, symmetry properties of the problem may be used as proposed in [3, 63]. By denoting $x = \Omega^2$,

$$y_{n,l,m}^{O} = \frac{\omega_{n,l,m} - \omega_{n,l,-m}}{2\Omega} \quad \text{and} \quad y_{n,l,m}^{E} = \frac{\omega_{n,l,m} - 2\omega_{n,l}^{(0)} + \omega_{n,l,-m}}{2\Omega^2} \tag{5.7}$$

for $m \geq 0$, we get

$$y_{n,l,m}^{O} = \sum_{j=0}^{k} C_{n,l,m}^{2j+1} x^{j} + O\left(x^{k+1}\right) \quad \text{and} \quad y_{n,l,m}^{E} = \sum_{j=0}^{k} C_{n,l,m}^{2j+2} x^{j} + O\left(x^{k+1}\right), \tag{5.8}$$

where we have used the symmetry $C^j_{n,l,-m} = (-1)^j C^j_{n,l,m}$. This symmetry is trivial: by changing Ω into $-\Omega$ and m into $-m$ in the equations, one recovers the same problem. We compute y^O and y^E on a fine grid of k points in Ω around zero to calculate the terms $C^j_{n,l,m}$ using $(k-1)$th-order interpolating polynomials. The determination of the coefficients $C^j_{n,l,m}$ is then accurate to the $(2k-1)$th-order in Ω. Coefficients can further be simplified by considering their dependence on m:

$$C^1_{n,l,m} = m\, C_{n,l}, \tag{5.9}$$

$$C^2_{n,l,m} = S^1_{n,l} + m^2 S^2_{n,l}, \tag{5.10}$$

$$C^3_{n,l,m} = m\, T^1_{n,l} + m^3 T^2_{n,l}. \tag{5.11}$$

The form of the 1st-, 2nd-, and 3rd-order coefficients comes from [41, 74, 82], respectively. Reference tables of coefficients computed in a polytropic model with a polytropic index $\mu = 3$ can be found in [3, 63] for p and g modes. Coefficients calculated from the complete 2-D problem can be used to test and validate the implementation of perturbative methods.

5.4.1.2 Limits of Perturbative Approach

To test the limits of perturbative methods, we can compare the frequencies predicted by a perturbative method with the frequencies computed with a 2-D oscillation code. Such limits have been derived for low-degree ($l \leq 3$) p and g modes. Several studies used perturbative coefficients derived from the fitting of polynomials, as described in the previous section [3, 50, 52, 63], whereas others used existing perturbative methods [9, 84].

In [3, 63] the domains of validity of perturbative approaches have been derived from computations in a fully distorted $\mu = 3$ polytropic model. To define the domains of validity of perturbative approaches, we fix the maximal departure $\delta\omega$ we allow between the perturbed frequencies $\omega^{(\mathrm{pert})}_{n,l,m}$ and the "exact" frequency $\omega_{n,l,m}$ computed from the complete 2-D problem. For each mode (n, l, m) and each approximation order, the domain of validity $[0, \Omega_V]$ is determined by Ω_V, defined to be the maximal value such that for all $\Omega \leq \Omega_V$, $|\omega^{(\mathrm{pert})}_{n,l,m}(\Omega) - \omega_{n,l,m}(\Omega)| \leq \delta\omega$. In Fig. 5.1 the polytropic model has been rescaled with the mass and radius of typical A-type stars ($M = 1.9 M_\odot$, $R = 2.3 R_\odot$), and the domains of validity are derived for a tolerated departure of 0.1 μHz, representative of errors in current seismic observations.

If we first focus on p modes, we notice that third-order terms do not significantly extend the validity domains. Second order is generally insufficient for rotation rates above $\Omega \approx 0.1\Omega_\mathrm{K}$ at low frequency and even less so at high frequency. Indeed, the extent of the validity domains clearly decreases for high-frequency p modes. More precisely, we notice that the validity range of first-order method is approximately limited by $\Omega_V = \Omega_\mathrm{K}\sqrt{2\delta\omega/\omega}$. We interpret this limit as due to an error of the size

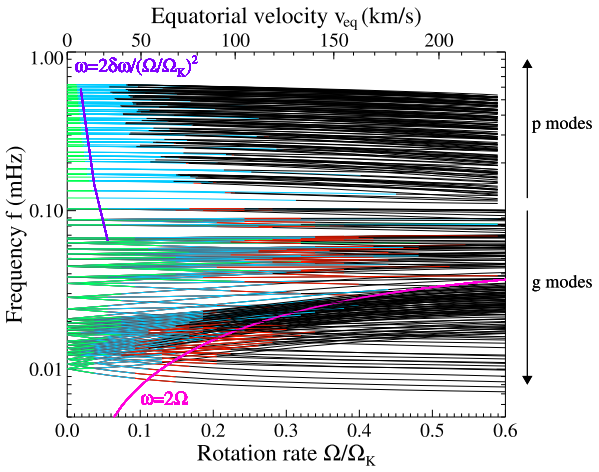

Fig. 5.1 Evolution of the frequencies of $l = 0, 1, 2, 3$ modes. Frequencies are computed in the co-rotating frame. Perturbative approximations have been tested for typical A-type stars (δ Scuti, γ Doradus). The *green/cyan/red parts* of the *curves* indicate that 1st/2nd/3rd order is sufficient to reproduce complete calculations within an error bar of $\delta\nu = 0.1$ μHz. The *magenta line* indicates $\omega = 2\Omega$, and the *purple curve* $\omega = 2\delta\omega\Omega_K^2/\Omega^2$

of the resonant cavity, that is, an error of the form $\delta\omega/\omega = \delta L/L$ (L is a length), and we identify $\delta L/L$ with the star's flatness $(R_e - R_p)/R_e$, which is know to be equal to $\frac{1}{2}(\Omega/\Omega_K)^2$ for small distortions. Comparisons done in [84] showed that validity domains of second-order methods can be extended by adding a correction accounting for avoided crossings. By including second-order near-degeneracy effects, high-frequency modes of solar-type stars has been reproduced up to $\Omega \approx 0.09\Omega_K$.

Concerning g modes, the most striking feature visible in Fig. 5.1 is the abrupt breakdown of the perturbative methods in the subinertial domain $\omega < 2\Omega$. We also attribute this limit to a change in the size of the resonant cavity that is not captured by perturbative methods. As described below (Sect. 5.4.3.1), this change is due to the appearance of a forbidden region where g modes cannot propagate.

5.4.2 Structure of p-Mode Spectra

5.4.2.1 Mode Classification

The numerical exploration of p-mode spectra has revealed that the spatial structures of the modes in rapidly rotating stars are quite different from those in the nonrotating case. When rotation increases, we notice that the kinetic energy of initially low-degree modes tends to concentrate in the equatorial region under the effect of the centrifugal force [13, 50]. Moreover, at a given rotation rate, modes present very different structures. It has only been possible to fully understand these differences and classify the modes thanks to the development of a ray theory of p modes in rotating stars [47, 48]. Details on this asymptotic theory can be found in the work of Pasek and Georgeot, Chap. 6 of this volume.

In the asymptotic regime, i.e., at high frequency, it is shown that the p-mode spectrum is the superimposition of different subspectra. Each subspectrum is associated

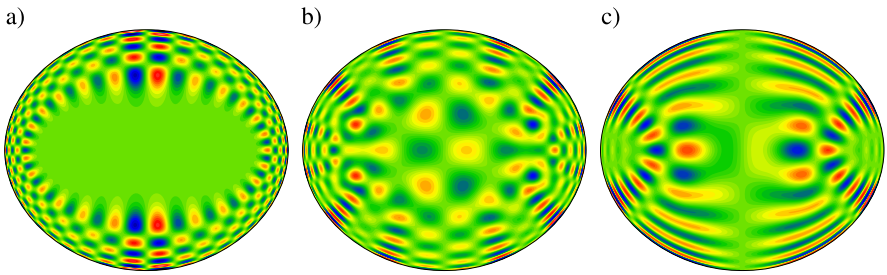

Fig. 5.2 Three examples of p modes in a $\mu = 3$ polytropic star rotating at $\Omega = 0.6\Omega_K$: (**a**) whispering gallery mode; (**b**) chaotic mode; (**c**) island mode. These plots show the variable $\hat{P}/\sqrt{\rho_0}$ in a meridional plane. Figure after [65]

with a specific family of acoustic rays. There are three families of rays, which lead to three families of modes: (a) the whispering gallery modes; (b) the chaotic modes; (c) the island modes. We exhibit a representative mode from each class in Fig. 5.2.

- The whispering gallery modes (Fig. 5.2(a)) are similar to the modes we find in nonrotating stars. At high rotation rates, they only exist if they have a large number of latitudinal nodes. For these modes, we are still able to recognize the original structure of the modes (i.e., at $\Omega = 0$).
- The chaotic modes (Fig. 5.2(b)) are associated with chaotic trajectories in the ray dynamics. It is essential to notice that, even if rays are chaotic, the modes that are built as constructive interferences of these rays do not have the properties of Hamiltonian chaos. Chaotic modes are characterized by more irregular nodal lines, and, in contrast to p modes of non-rotating stars, they propagate down to the star's center. For a given frequency range, they always correspond to modes with lower degrees than whispering gallery modes.
- The island modes (Fig. 5.2(c)) are associated with stable periodic trajectories in the ray dynamics. The energy of the mode is concentrated around this stable trajectory. It is possible to count the number of nodes along this trajectory (we denote this number $\tilde{n}$) and in the transversal direction (we denote it $\tilde{l}$). We find these modes by following low-degree modes. It is possible to link $\tilde{l}$ and $\tilde{n}$ to the degree l and order n of the corresponding mode at $\Omega = 0$ through the relations

$$\tilde{n} = 2n + \varepsilon \quad \text{and} \quad \tilde{l} = \frac{l - |m| - \varepsilon}{2}, \tag{5.12}$$

where $\varepsilon = (l + m) \bmod 2$ indicates the equatorial parity of the mode [60].

5.4.2.2 Regular Frequency Spacings

Regularities in frequency spectra are helpful in identifying modes in observations. In the absence of rotation, p-mode frequencies asymptotically follow Tassoul's relation [86], which to first order is $\omega_{n,l} = \Delta_0(n + l/2 + \alpha)$, where α is a slowly varying

function of frequency, and $\Delta_0 = \pi/\tau_c$ a constant directly related to the stellar structure (τ_c is the stellar acoustic radius). Such a relation is observationally verified in the Sun (e.g., [28]). The regularity in mode distribution is clearly found in other solar like stars (e.g., [8, 11, 55]). Finding this regular spacing is a first step toward identifying modes. Moreover, it is sometimes possible to measure Δ_0 and thus put constraints on the star, without necessarily identifying modes individually.

The evolution of these regularities as functions of the rotation rate has been explored numerically by [50, 64, 65]. When the rotation rate increases, the centrifugal force first induces a contraction of the p-mode spectrum toward low frequencies [50], as can be seen in Fig. 5.1. Moreover, Tassoul's relation is no longer followed. For instance, the so-called "small separation," $\omega_{n,l} - \omega_{n-1,l+2}$, which is small because it vanishes to first-order in Tassoul's development, is no longer small at high rotation rates. In rotating stars, a new organization of the spectrum appears. Empirically, low-degree modes have been shown to asymptotically follow

$$\omega_{n,l,m} = n\Delta_n + l\Delta_l + |m|\Delta_m + \alpha^{\pm}, \tag{5.13}$$

where Δ_n, Δ_l, Δ_m, and $\alpha^{\pm}$ are parameters that depend on the stellar structure [50, 64, 65]. The parameter α^+, respectively α^-, corresponds to symmetric modes ($\varepsilon = 0$), respectively antisymmetric modes ($\varepsilon = 1$). Equation (5.13) can also be expressed with the natural labeling of island modes defined in the previous section $(\tilde{n}, \tilde{l}, m)$. It reads

$$\omega_{\tilde{n},\tilde{l},m} = \tilde{n}\tilde{\Delta}_n + \tilde{l}\tilde{\Delta}_l + |m|\tilde{\Delta}_m + \tilde{\alpha}^{\pm} \tag{5.14}$$

with $\tilde{\Delta}_n = \Delta_n/2$, $\tilde{\Delta}_l = 2\Delta_l$, $\tilde{\Delta}_m = \Delta_l + \Delta_m$, $\tilde{\alpha}^+ = \alpha^+$, and $\tilde{\alpha}^- = \alpha^- + \Delta_l - \Delta_n/2$. It has been found numerically that $\tilde{\alpha}^+ \approx \tilde{\alpha}^- \approx \tilde{\alpha}$ [64]. The dependence on $|m|$ rather than m originates in the dominance of the effects of the centrifugal force over those of the Coriolis force which are negligible at high frequency—thus, in the asymptotic regime.

The parameter Δ_n plays a similar role to Δ_0 in nonrotating stars. Indeed, Δ_0 is known to scale as $\sqrt{M/V}$, where M/V is mean density of the star (e.g., [90]). For rotating stars, we also find a good correlation between Δ_n and $\sqrt{M/V}$ [64].

These empirical asymptotic relations have been explained thanks to the development of an asymptotic theory for island modes [58, 59]. Thus, it is possible to link the various parameters in Eq. (5.14) to internal properties of the star. The reader should refer to Chap. 6 of this volume for details.

5.4.3 Structure of g-Mode Spectra

Gravito-inertial modes are generally computed with some approximations on the effects of rotation: either using the traditional approximation, as mentioned in Sect. 5.1, or with 2-D oscillation codes fully taking into account the Coriolis force but ignoring [25, 77] or approximating [43] the centrifugal deformation. The focus of these 2-D calculations [10, 75] has been to determine the unstable modes

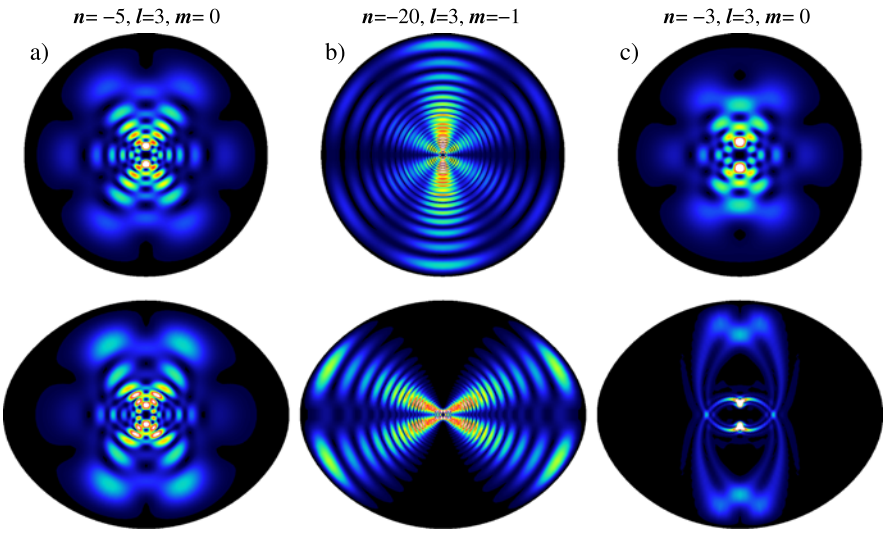

Fig. 5.3 Three examples of g modes in a $\mu = 3$ polytropic stellar model at zero rotation (*top*) and at $\Omega = 0.7\Omega_K$ (*bottom*). These plots show the kinetic energy of the modes in a meridional plane. (**a**) Mode that stays in the superinertial domain ($\omega > 2\Omega$) and is not too affected by rotation. (**b**) Mode that enters in the subinertial domain ($\omega < 2\Omega$), affected by the appearance of a forbidden region in the polar region. (**c**) Mode in the superinertial domain that becomes a rosette mode

of low-frequency pulsators like SPB stars and to compare the results with the observed frequency spectra. A systematic numerical exploration of the gravito-inertial spectrum performed with a complete 2-D oscillation code is still lacking. We started such an exploration with the TOP code by following low-degree gravity modes of $\mu = 3$ polytropic stellar models from $\Omega = 0$ to $\Omega = 0.7\Omega_K$. More precisely, we considered $l \leq 3$ modes in both low- and high-order ranges: $n \in [-14, -1]$ for $l = 1$, $n \in [-20, -16] \cup [-5, -1]$ for $l = 2$ and $l = 3$. The first results of this study have been published in [3, 4] and are summarized below.

5.4.3.1 Mode Classification

The computed modes can be classified in two distinct families according to their spatial distribution. The first family contains the vast majority of the followed modes and does not show striking differences with the modes reported in previous works. The spatial distribution of these modes is characterized by a smooth evolution with rotation, the horizontal and radial length scales remaining of the same order of magnitude as rotation grows. Figures 5.3(a) and 5.3(b) illustrate this evolution in two cases: when the mode remains superinertial ($\omega > 2\Omega$) and when the mode becomes subinertial ($\omega < 2\Omega$). The main change is the appearance of a polar, approximately conical, forbidden region for subinertial modes. The critical angle, which is also present in the traditional approximation, is close to $\arccos(\omega/2\Omega)$ when $N \gg \Omega$,

although a refined expression of the forbidden region can be determined with the method of characteristics [25].

In contrast with this first family, some of the followed modes undergo a drastic modification of their spatial distribution. As illustrated in Fig. 5.3(c), the length scales and the geometry of the initially $l = 3$ mode have been strongly modified. This change already appears at rather low rotation rates: near $\Omega \approx 0.1\Omega_{\rm K}$, this mode is already significantly affected. Several modes of this type are also found within a small frequency interval. To our knowledge, this type of mode has not been reported before. We called them "rosette" modes because of their spatial distribution. Along with this numerical exploration, we constructed a ray-based asymptotic theory for gravito-inertial modes. Just as for the island p modes, it turns out that it is possible to associate the rosette modes with island structure of phase space formed around periodic orbits [4].

5.4.3.2 Influence of the Centrifugal Distortion

Beyond mode classification, many other open issues on gravito-inertial modes can be addressed with this numerical exploration. The effects of the centrifugal force is one of them. Figure 5.4 displays the frequencies of the ($n = -13, \ldots, -10, l = 1,$ $m = -1, 0, 1$) modes as functions of the stellar rotation. The calculations performed with the centrifugally distorted stellar model are compared with computations made with a spherical model whose radius corresponds to the polar radius of the distorted model. This figure shows that the centrifugal distortion has a significant effect above $\Omega \approx 0.4\Omega_{\rm K}$ and that this effect is much stronger on the ($l = 1,\ m = -1$) modes than on the other $l = 1$ modes. This is not surprising as the outer turning point of lower-frequency gravity modes comes closer to the surface where the centrifugal distortion is stronger. Another interesting aspect of this comparison is to provide constraints on the validity of the traditional approximation. Indeed, this approximation ignores the centrifugal force and is thus expected to fail when centrifugal effects are important.

5.4.3.3 Period Spacings

Following low-degree gravity modes also enables us to investigate regular period spacings in rapidly rotating stars. At zero rotation, the uniform asymptotic period spacing of gravity modes of the same degree l and consecutive order n is a crucial tool for mode identification. At higher rotation rates, [4] finds that this period spacing is no longer uniform but is a function of the parameter $\eta = 2\Omega/\omega$ and of the azimuthal number m. These results are indeed well reproduced by the period spacing derived from the traditional approximation. Although some discrepancies arise when the centrifugal distortion becomes significant, these discrepancies remain small despite the fact that Fig. 5.4 suggests they are large for the period itself.

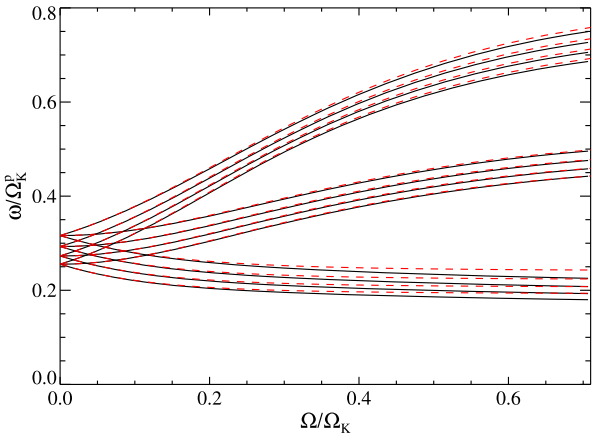

Fig. 5.4 Evolution of the frequencies of the ($n = -13, \ldots, -10,\ l = 1,\ m = -1, 0, 1$) modes. *Solid black lines* indicate the complete 2-D computations. *Dashed red lines* show the results obtained by ignoring the centrifugal distortion (the equilibrium model is kept spherical). To compare the two results, we assume that the polar radii of the distorted and spherical models are the same. On the y-axis, the frequencies are normalized by $\Omega_K^p = \sqrt{GM/R_p^3}$, where R_p is the common polar radius

5.4.3.4 Discussion and Further Works

These preliminary results from following low-degree modes suggest that the systematic numerical exploration using complete 2-D oscillations might be as fruitful for gravito-inertial modes as for p modes. A scanning exploration method will also be necessary, in particular to study purely inertial modes that cannot be followed from zero rotation. Again, the construction of an asymptotic theory is expected to complement the numerical approach by providing a global view of the mode properties. One of the issues that needs further attention is the validity of the traditional approximation (see [34] for a recent review on the subject). Here, we have seen contrasting indications because the traditional approximation cannot account for the centrifugal effects and most probably for the rosette modes but at the same time yields good predictions on the period spacings. Concerning mode stability, the strong discrepancies described in [1] are attributed to the importance of mode coupling which does not occur in the traditional approximation. It will also be important to test this approximation in the presence of convective layers (core or envelope). Indeed, the traditional approximation does not allow the propagation of gravito-inertial waves coming from the radiative layers into the convective zone, while this is possible in the general case for subinertial waves, as illustrated by the method of characteristics in [25]. Another issue concerns the existence of the so-called singular modes clearly observed for a Boussinesq fluid within a spherical container [26]. In this case, mode concentration onto a particular characteristic is caused by the wave focusing that occurs at the solid surface. Such modes have not been found in our compressible polytropic models, and this can be attributed to the fact that waves do

not experience focusing effect of solid-body boundary conditions at the star's surface. Instead, it is the near-surface abrupt density decrease that provokes the back refraction of outwards propagating wave, keeping them within the star without the focusing effect.

5.5 Conclusion

Exploring the oscillation spectra of stars with 2-D oscillation codes such as TOP is needed to fully understand the effects of rotation on stellar oscillations. As discussed in Sect. 5.2, developing such 2-D codes is highly challenging. The required numerical resources can become quite large: as soon as the star is not slowly rotating, it is not sufficient to consider only a few spherical harmonics to describe the modes. In the various works presented in this chapter, at least 20 and up to 80 spherical harmonics were requested—according to the rotation rate and the mode considered—to ensure the convergence of the solutions. This is necessary to reach a reasonable accuracy on the eigenfrequencies and the eigenmodes.

The mode-following technique, described in Sect. 5.3.1, is very useful in the exploration of the oscillation spectrum and in understanding how it is progressively modified by the inertial forces when the rotation rate grows. As we saw in Sect. 5.4.1, it also allows us to test approximate techniques, such as perturbative methods, and to see at which rotation rate these methods fail.

Nevertheless, to fully understand and interpret the change of the spectrum and mode properties with rotation, asymptotic ray theory has proven to be a powerful tool. For p modes (Sect. 5.4.2), it allows us to easily classify the modes, interpret the found regularities, and specify their links with the structure of the star. Following the path of this successful study, a similar exploration of g modes has been initiated (Sect. 5.4.3) opening the way for new explorations, especially for testing the traditional approximation or for exploring inertial modes.

Our improved understanding of frequency spacings gives us a new framework [51] to interpret the regularities observed in data (e.g., [33, 94]) and identify modes. Moreover, 2-D computations also help in interpreting spectroscopic and multicolor data of pulsating stars. Since these computations provide maps of the modes at the stellar surface—which are no longer spherical harmonics—it allows realistic predictions of temporal variations of the spectral line profiles and mode amplitude ratios between different photometric bands [67].

A future improvement will be to include nonadiabatic terms in the TOP code so as to be able to predict the stability or instability of modes. Such improvements will allow the construction of realistic spectra which can at last be confronted with observations, thereby allowing us to finally interpret pulsation spectra in rapidly rotating stars, currently a very difficult task. However, this will require new generations of 2-D models. We naturally imagine in the near future a symbiotic relationship between the ESTER code and the TOP code, the former providing models and the latter pulsation modes.

Acknowledgements The authors acknowledge financial support from the "Agence nationale de la recherche" for the SIROCO project. A part of this work was performed using high-performance computing resources from CALMIP ("CALcul en MIdi-Pyrénées"). D.R.R. gratefully acknowledges financial support through a postdoctoral fellowship from the "Subside fédéral pour la recherche 2011," University of Liège.

References

1. Aprilia, Lee, U., Saio, H.: Stability of g modes in rotating B-type stars. Mon. Not. R. Astron. Soc. **412**, 2265–2276 (2011)
2. Baglin, A., Auvergne, M., Barge, P., Deleuil, M., Catala, C., Michel, E., Weiss, W.: The COROT team: scientific objectives for a minisat: CoRoT. In: Fridlund, M., Baglin, A., Lochard, J., Conroy, L. (eds.) The CoRoT Mission: Pre-Launch Status. ESA Special Publication, vol. 1306, p. 33. ESA Publications Division, Noordwijk (2006)
3. Ballot, J., Lignières, F., Reese, D.R., Rieutord, M.: Gravity modes in rapidly rotating stars. Limits of perturbative methods. Astron. Astrophys. **518**, A30 (2010)
4. Ballot, J., Lignières, F., Prat, V., Reese, D.R., Rieutord, M.: 2D computations of g modes in fast rotating stars. In: Shibahashi, H., Takata, M., Lynas-Gray, A.E. (eds.) The 61st Fujihara Seminar: Progress in Solar/Stellar Physics with Helio- and Asteroseismology. ASP Conf. Proc., vol. 462, p. 389. Astronomical Society of the Pacific, San Francisco (2012)
5. Berthomieu, G., Gonczi, G., Graff, P., Provost, J., Rocca, A.: Low-frequency gravity modes of a rotating star. Astron. Astrophys. **70**, 597 (1978)
6. Blackford, L.S., Demmel, J., Dongarra, J., Duff, I., Hammarling, S., Henry, G., Heroux, M., Kaufman, L., Lumsdaine, A., Petitet, A., Pozo, R., Remington, K., Whaley, R.C.: An updated set of basic linear algebra subprograms (BLAS). ACM Trans. Math. Softw. **28**(2), 135–151 (2002)
7. Bonazzola, S., Gourgoulhon, E., Marck, J.: Numerical approach for high precision 3D relativistic star models. Phys. Rev. D **58**(10), 104020 (1998)
8. Bouchy, F., Carrier, F.: P-mode observations on α Cen A. Astron. Astrophys. **374**, L5–L8 (2001)
9. Burke, K.D., Reese, D.R., Thompson, M.J.: On the effects of rotation on acoustic stellar pulsations: validity domains of perturbative methods and close frequency pairs. Mon. Not. R. Astron. Soc. **414**, 1119–1126 (2011)
10. Cameron, C., Saio, H., Kuschnig, R., Walker, G.A.H., Matthews, J.M., Guenther, D.B., Moffat, A.F.J., Rucinski, S.M., Sasselov, D., Weiss, W.W.: MOST detects SPBe pulsations in HD 127756 and HD 217543: asteroseismic rotation rates independent of vsini. Astrophys. J. **685**, 489–507 (2008)
11. Chaplin, W.J., Appourchaux, T., Elsworth, Y., García, R.A., Houdek, G., Karoff, C., Metcalfe, T.S., Molenda-Żakowicz, J., Monteiro, M.J.P.F.G., Thompson, M.J., Brown, T.M., Christensen-Dalsgaard, J., Gilliland, R.L., Kjeldsen, H., Borucki, W.J., Koch, D., Jenkins, J.M., Ballot, J., Basu, S., Bazot, M., Bedding, T.R., Benomar, O., Bonanno, A., Brandão, I.M., Bruntt, H., Campante, T.L., Creevey, O.L., Di Mauro, M.P., Doğan, G., Dreizler, S., Eggenberger, P., Esch, L., Fletcher, S.T., Frandsen, S., Gai, N., Gaulme, P., Handberg, R., Hekker, S., Howe, R., Huber, D., Korzennik, S.G., Lebrun, J.C., Leccia, S., Martic, M., Mathur, S., Mosser, B., New, R., Quirion, P., Régulo, C., Roxburgh, I.W., Salabert, D., Schou, J., Sousa, S.G., Stello, D., Verner, G.A., Arentoft, T., Barban, C., Belkacem, K., Benatti, S., Biazzo, K., Boumier, P., Bradley, P.A., Broomhall, A., Buzasi, D.L., Claudi, R.U., Cunha, M.S., D'Antona, F., Deheuvels, S., Derekas, A., García Hernández, A., Giampapa, M.S., Goupil, M.J., Gruberbauer, M., Guzik, J.A., Hale, S.J., Ireland, M.J., Kiss, L.L., Kitiashvili, I.N., Kolenberg, K., Korhonen, H., Kosovichev, A.G., Kupka, F., Lebreton, Y., Leroy, B., Ludwig, H., Mathis, S., Michel, E., Miglio, A., Montalbán, J., Moya, A., Noels, A., Noyes, R.W., Pallé,

P.L., Piau, L., Preston, H.L., Roca Cortés, T., Roth, M., Sato, K.H., Schmitt, J., Serenelli, A.M., Silva Aguirre, V., Stevens, I.R., Suárez, J.C., Suran, M.D., Trampedach, R., Turck-Chièze, S., Uytterhoeven, K., Ventura, R., Wilson, P.A.: The asteroseismic potential of Kepler: first results for solar-type stars. Astrophys. J. Lett. **713**, L169–L175 (2010)
12. Chlebowski, T.: Nonradial oscillations of slowly rotating white dwarfs. Acta Astron. **28**, 441–463 (1978)
13. Clement, M.J.: Normal modes of oscillation for rotating stars. I—The effect of rigid rotation on four low-order pulsations. Astrophys. J. **249**, 746–760 (1981)
14. Clement, M.J.: Normal modes of oscillation for rotating stars. II Variational solutions. Astrophys. J. **276**, 724–736 (1984)
15. Clement, M.J.: Normal modes of oscillation for rotating stars. III—Variational calculations with an improved set of basis vectors. Astrophys. J. **301**, 185–203 (1986)
16. Clement, M.J.: Normal modes of oscillation for rotating stars. IV—Nonaxisymmetric variational solutions for 15 solar mass models. Astrophys. J. **339**, 1022–1037 (1989)
17. Clement, M.J.: Pulsation in rapidly rotating stars. In: Balona, L.A., Henrichs, H.F., Le Contel, J.M. (eds.) Pulsation; Rotation; and Mass Loss in Early-Type Stars. IAU Symposium, vol. 162, p. 117 (1994)
18. Clement, M.J.: Normal modes of oscillation for rotating stars. V. A new numerical method for computing nonradial eigenfunctions. Astrophys. J. Suppl. Ser. **116**, 57 (1998)
19. Cowling, T.G.: The non-radial oscillations of polytropic stars. Mon. Not. R. Astron. Soc. **101**, 367 (1941)
20. Cowling, T.G., Newing, R.A.: The oscillations of a rotating star. Astrophys. J. **109**, 149 (1949)
21. Deupree, R.G.: Stellar evolution with arbitrary rotation laws. I—Mathematical techniques and test cases. Astrophys. J. **357**, 175–187 (1990)
22. Deupree, R.G.: Stellar evolution with arbitrary rotation laws. 2: Massive star evolution to core hydrogen exhaustion. Astrophys. J. **439**, 357–364 (1995)
23. Deupree, R.G.: Structure of uniformly rotating stars. Astrophys. J. **735**, 69 (2011)
24. Deupree, R.G., Beslin, W.: Rotational splitting of pulsation modes. Astrophys. J. **721**, 1900–1907 (2010)
25. Dintrans, B., Rieutord, M.: Oscillations of a rotating star: a non-perturbative theory. Astron. Astrophys. **354**, 86–98 (2000)
26. Dintrans, B., Rieutord, M., Valdettaro, L.: Gravito-inertial waves in a rotating stratified sphere or spherical shell. J. Fluid Mech. **398**, 271–297 (1999)
27. Domiciano de Souza, A., Kervella, P., Jankov, S., Abe, L., Vakili, F., di Folco, E., Paresce, F.: The spinning-top Be star Achernar from VLTI-VINCI. Astron. Astrophys. **407**, L47–L50 (2003)
28. Duvall, T.L. Jr., Harvey, J.W.: Observations of solar oscillations of low and intermediate degree. Nature **302**, 24–27 (1983)
29. Dziembowski, W.A., Goode, P.R.: Effects of differential rotation on stellar oscillations—a second-order theory. Astrophys. J. **394**, 670–687 (1992)
30. Eckart, C.: Hydrodynamics of Oceans and Atmospheres. Pergamon, New York (1960)
31. Espinosa Lara, F., Rieutord, M.: The dynamics of a fully radiative rapidly rotating star enclosed within a spherical box. Astron. Astrophys. **470**, 1013–1022 (2007)
32. Font, J.A., Stergioulas, N., Kokkotas, K.D.: Non-linear hydrodynamical evolution of rotating relativistic stars: numerical methods and code tests. Mon. Not. R. Astron. Soc. **313**, 678–688 (2000)
33. García Hernández, A., Moya, A., Michel, E., Garrido, R., Suárez, J.C., Rodríguez, E., Amado, P.J., Martín-Ruiz, S., Rolland, A., Poretti, E., Samadi, R., Baglin, A., Auvergne, M., Catala, C., Lefevre, L., Baudin, F.: Asteroseismic analysis of the CoRoT δ Scuti star HD 174936. Astron. Astrophys. **506**, 79–83 (2009)
34. Gerkema, T., Zimmerman, J.T.F., Maas, L.R.M., van Haren, H.: Geophysical and astrophysical fluid dynamics beyond the traditional approximation. Rev. Geophys. **46**, RG2004 (2008)
35. Gough, D.O., Thompson, M.J.: The effect of rotation and a buried magnetic field on stellar oscillations. Mon. Not. R. Astron. Soc. **242**, 25–55 (1990)

36. Guarrigues, J.: Fondements de la mécanique des milieux continus. Hermes (2007)
37. Jackson, S., MacGregor, K.B., Skumanich, A.: Models for the rapidly rotating Be star Achernar. Astrophys. J. **606**, 1196–1199 (2004)
38. Jackson, S., MacGregor, K.B., Skumanich, A.: On the use of the self-consistent-field method in the construction of models for rapidly rotating main-sequence stars. Astrophys. J. Suppl. Ser. **156**, 245–264 (2005)
39. Karami, K.: Third order effect of rotation on stellar oscillations of a B star. Chin. J. Astron. Astrophys. **8**, 285–308 (2008)
40. Koch, D.G., Borucki, W.J., Basri, G., Batalha, N.M., Brown, T.M., Caldwell, D., Christensen-Dalsgaard, J., Cochran, W.D., DeVore, E., Dunham, E.W., Gautier, T.N., Geary, J.C., Gilliland, R.L., Gould, A., Jenkins, J., Kondo, Y., Latham, D.W., Lissauer, J.J., Marcy, G., Monet, D., Sasselov, D., Boss, A., Brownlee, D., Caldwell, J., Dupree, A.K., Howell, S.B., Kjeldsen, H., Meibom, S., Morrison, D., Owen, T., Reitsema, H., Tarter, J., Bryson, S.T., Dotson, J.L., Gazis, P., Haas, M.R., Kolodziejczak, J., Rowe, J.F., Van Cleve, J.E., Allen, C., Chandrasekaran, H., Clarke, B.D., Li, J., Quintana, E.V., Tenenbaum, P., Twicken, J.D., Wu, H.: Kepler mission design, realized photometric performance, and early science. Astrophys. J. Lett. **713**, L79–L86 (2010)
41. Ledoux, P.: The nonradial oscillations of gaseous stars and the problem of Beta Canis Majoris. Astrophys. J. **114**, 373 (1951)
42. Lee, U.: r modes of slowly pulsating B stars. Mon. Not. R. Astron. Soc. **365**, 677–687 (2006)
43. Lee, U., Baraffe, I.: Pulsational stability of rotating main sequence stars: the second order effects of rotation on the nonadiabatic oscillations. Astron. Astrophys. **301**, 419 (1995)
44. Lee, U., Saio, H.: Low-frequency oscillations of uniformly rotating stars. Mon. Not. R. Astron. Soc. **224**, 513–526 (1987)
45. Lee, U., Saio, H.: Low-frequency nonradial oscillations in rotating stars. I. Angular dependence. Astrophys. J. **491**, 839 (1997)
46. Lee, U., Jeffery, C.S., Saio, H.: Line profile variations caused by low-frequency non-radial pulsations of rapidly rotating stars. II. Mon. Not. R. Astron. Soc. **254**, 185–191 (1992)
47. Lignières, F., Georgeot, B.: Wave chaos in rapidly rotating stars. Phys. Rev. E **78**(1), 016215 (2008)
48. Lignières, F., Georgeot, B.: Asymptotic analysis of high-frequency acoustic modes in rapidly rotating stars. Astron. Astrophys. **500**, 1173–1192 (2009)
49. Lignières, F., Rieutord, M., Valdettaro, L.: Acoustic modes in spheroidal cavities. In: Combes, F., Barret, D., Thévenin, F. (eds.) SF2A-2001: Semaine de l'Astrophysique Francaise, p. 127 (2001)
50. Lignières, F., Rieutord, M., Reese, D.: Acoustic oscillations of rapidly rotating polytropic stars. I. Effects of the centrifugal distortion. Astron. Astrophys. **455**, 607–620 (2006)
51. Lignières, F., Georgeot, B., Ballot, J.: P-modes in rapidly rotating stars: looking for regular patterns in synthetic asymptotic spectra. Astron. Nachr. **331**, 1053 (2010)
52. Lovekin, C.C., Deupree, R.G.: Radial and nonradial oscillation modes in rapidly rotating stars. Astrophys. J. **679**, 1499–1508 (2008)
53. MacGregor, K.B., Jackson, S., Skumanich, A., Metcalfe, T.S.: On the structure and properties of differentially rotating, main-sequence stars in the 1–2 M_{solar} range. Astrophys. J. **663**, 560–572 (2007)
54. Maeder, A.: Physics, Formation and Evolution of Rotating Stars. Springer, Berlin (2009). Astron. Astrophys. Library
55. Michel, E., Baglin, A., Auvergne, M., Catala, C., Samadi, R., Baudin, F., Appourchaux, T., Barban, C., Weiss, W.W., Berthomieu, G., Boumier, P., Dupret, M., Garcia, R.A., Fridlund, M., Garrido, R., Goupil, M., Kjeldsen, H., Lebreton, Y., Mosser, B., Grotsch-Noels, A., Janot-Pacheco, E., Provost, J., Roxburgh, I.W., Thoul, A., Toutain, T., Tiphène, D., Turck-Chieze, S., Vauclair, S.D., Vauclair, G.P., Aerts, C., Alecian, G., Ballot, J., Charpinet, S., Hubert, A., Lignières, F., Mathias, P., Monteiro, M.J.P.F.G., Neiner, C., Poretti, E., de Renan Medeiros, J., Ribas, I., Rieutord, M.L., Cortés, T.R., Zwintz, K.: CoRoT measures solar-like oscillations and granulation in stars hotter than the sun. Science **322**, 558 (2008)

56. Ouazzani, R.: La rotation et son interaction avec les oscillations dans les étoiles. Ph.D. thesis, Université Pierre et Marie Curie (Paris 6), France (2011)
57. Ouazzani, R.M., Dupret, M.A., Reese, D.R.: Pulsations of rapidly rotating stars. I. The ACOR numerical code. Astron. Astrophys. (2012). doi:10.1051/0004-6361/201219548
58. Pasek, M., Georgeot, B., Lignières, F., Reese, D.R.: Regular modes in rotating stars. Phys. Rev. Lett. **107**(12), 121101 (2011)
59. Pasek, M., Lignières, F., Georgeot, B., Reese, D.R.: Regular oscillation sub-spectrum of rapidly rotating stars. Astron. Astrophys. (2012). doi:10.1051/0004-6361/201219716
60. Reese, D.: Modelling rapidly rotating stars. J. Phys. Conf. Ser. **118**(1), 012023 (2008)
61. Reese, D.R.: Oscillations in rapidly rotating stars. Astron. Nachr. **331**, 1038 (2010)
62. Reese, D.R.: Solving mesh-drift instability in first order finite-differences eigenvalue systems using alternate grids. J. Comput. Appl. Math. (submitted)
63. Reese, D., Lignières, F., Rieutord, M.: Acoustic oscillations of rapidly rotating polytropic stars. II. Effects of the Coriolis and centrifugal accelerations. Astron. Astrophys. **455**, 621–637 (2006)
64. Reese, D., Lignières, F., Rieutord, M.: Regular patterns in the acoustic spectrum of rapidly rotating stars. Astron. Astrophys. **481**, 449–452 (2008)
65. Reese, D.R., MacGregor, K.B., Jackson, S., Skumanich, A., Metcalfe, T.S.: Pulsation modes in rapidly rotating stellar models based on the self-consistent field method. Astron. Astrophys. **509**, 183–188 (2009)
66. Reese, D.R., Espinosa Lara, F., Rieutord, M.: The effects of μ gradients on pulsations of rapidly rotating stars. In: Neiner, C., Wade, G., Meynet, G., Peters, G. (eds.) IAU Symposium, vol. 272, pp. 535–536 (2011)
67. Reese, D.R., Prat, V., Barban, C., van't Veer-Menneret, C., MacGregor, K.B.: Mode visibilities in rapidly rotating stars. Astron. Astrophys. (accepted)
68. Rieutord, M., Espinosa Lara, F.: On the dynamics of a radiative rapidly rotating star. Commun. Asteroseismol. **158**, 99 (2009)
69. Rieutord, M., Valdettaro, L.: Inertial waves in a rotating spherical shell. J. Fluid Mech. **341**, 77–99 (1997)
70. Roxburgh, I.W.: 2-dimensional models of rapidly rotating stars I. Uniformly rotating zero age main sequence stars. Astron. Astrophys. **428**, 171–179 (2004)
71. Roxburgh, I.W.: 2-dimensional models of rapidly rotating stars. II. Hydrostatic and acoustic models with $\Omega = \Omega(r, \theta)$. Astron. Astrophys. **454**, 883–888 (2006)
72. Royer, F., Zorec, J., Gómez, A.E.: Rotational velocities of A-type stars. III. Velocity distributions. Astron. Astrophys. **463**, 671–682 (2007)
73. Saad, Y.: Numerical Methods for Large Eigenvalue Problems. Manchester University Press, Manchester (1992)
74. Saio, H.: Rotational and tidal perturbations of nonradial oscillations in a polytropic star. Astrophys. J. **244**, 299–315 (1981)
75. Saio, H., Cameron, C., Kuschnig, R., Walker, G.A.H., Matthews, J.M., Rowe, J.F., Lee, U., Huber, D., Weiss, W.W., Guenther, D.B., Moffat, A.F.J., Rucinski, S.M., Sasselov, D.: MOST detects g-modes in the late-type Be star β Canis Minoris (B8 Ve). Astrophys. J. **654**, 544–550 (2007)
76. Savonije, G.J.: Unstable quasi g-modes in rotating main-sequence stars. Astron. Astrophys. **443**, 557–570 (2005)
77. Savonije, G.J.: Non-radial oscillations of the rapidly rotating Be star HD 163868. Astron. Astrophys. **469**, 1057–1062 (2007)
78. Savonije, G.J., Papaloizou, J.C.B., Alberts, F.: Nonadiabatic tidal forcing of a massive uniformly rotating star. Mon. Not. R. Astron. Soc. **277**, 471 (1995)
79. Simon, R.: Rotational perturbation of a radial oscillation gaseous star. Astron. Astrophys. **2**, 390 (1969)
80. Smeyers, P., Denis, J.: Second order rotational perturbation of non-radial oscillations of a star. Astron. Astrophys. **14**, 311 (1971)
81. Sobouti, Y.: Normal modes of rotating fluids. Astron. Astrophys. **89**, 314–335 (1980)

82. Soufi, F., Goupil, M.J., Dziembowski, W.A.: Effects of moderate rotation on stellar pulsation. I. Third order perturbation formalism. Astron. Astrophys. **334**, 911–924 (1998)
83. Suárez, J.C., Goupil, M.J., Morel, P.: Effects of moderately fast shellular rotation on adiabatic oscillations. Astron. Astrophys. **449**, 673–685 (2006)
84. Suárez, J.C., Goupil, M.J., Reese, D.R., Samadi, R., Lignières, F., Rieutord, M., Lochard, J.: On the interpretation of echelle diagrams for solar-like oscillations effect of centrifugal distortion. Astrophys. J. **721**, 537–546 (2010)
85. Takata, M.: Mode classification of linear adiabatic oscillations of spherically symmetric stars. Publ. Astron. Soc. Jpn. **64**, 66 (2012)
86. Tassoul, M.: Asymptotic approximations for stellar nonradial pulsations. Astrophys. J. Suppl. Ser. **43**, 469–490 (1980)
87. Townsend, R.H.D.: Spectroscopic modelling of non-radial pulsation in rotating early-type stars. Mon. Not. R. Astron. Soc. **284**, 839–858 (1997)
88. Townsend, R.H.D.: Asymptotic expressions for the angular dependence of low-frequency pulsation modes in rotating stars. Mon. Not. R. Astron. Soc. **340**, 1020–1030 (2003)
89. Townsend, R.H.D.: Influence of the Coriolis force on the instability of slowly pulsating B stars. Mon. Not. R. Astron. Soc. **360**, 465–476 (2005)
90. Ulrich, R.K.: Determination of stellar ages from asteroseismology. Astrophys. J. Lett. **306**, L37–L40 (1986)
91. Unno, W., Osaki, Y., Ando, H., Saio, H., Shibahashi, H.: Nonradial Oscillations of Stars. University of Tokyo Press, Tokyo (1989)
92. Valdettaro, L., Rieutord, M., Braconnier, T., Fraysse, V.: Convergence and round-off errors in a two-dimensional eigenvalue problem using spectral methods and Arnoldi–Chebyshev algorithm. J. Comput. Appl. Math. **205**, 382–393 (2007)
93. Zhao, S.: On the spurious solutions in the high-order finite difference methods for eigenvalue problems. Comput. Methods Appl. Mech. Eng. **196**, 5031–5046 (2007)
94. Zwintz, K., Lenz, P., Breger, M., Pamyatnykh, A.A., Zdravkov, T., Kuschnig, R., Matthews, J.M., Guenther, D.B., Moffat, A.F.J., Rowe, J.F., Rucinski, S.M., Sasselov, D., Weiss, W.W.: Regular frequency patterns in the classical δ Scuti star HD 144277 observed by the MOST satellite. Astron. Astrophys. **533**, A133 (2011)

Chapter 6
Regular and Irregular Pressure Modes in Rapidly Rotating Stars

Michael Pasek and Bertrand Georgeot

Abstract In this lecture, we review the recent developments in the asymptotic characterization of the pressure-mode oscillation spectrum of rapidly rotating stars. We give an expository introduction to the asymptotic techniques based on ray dynamics that were used to obtain them, spanning results from Hamiltonian dynamical systems, chaos theory and complex quantum systems. Finally, such asymptotic techniques are applied to an important subset of the pressure mode spectrum to obtain a semi-analytical formula for regular frequency spacings.

6.1 Introduction

The asteroseismic data gathered by the space missions CoRoT [4] and Kepler [18] is giving us unprecedented information on oscillation modes of pulsating stars, for various parts of the HR diagram. Among them, non-evolved massive and intermediate mass stars are known to be mostly rapid rotators [32]. It is known from experience of solar-type pulsators that an asymptotic theory is important for mode identification and interpretation [12]. For slowly rotating stars (e.g. the Sun), the asymptotic theory of Tassoul [33, 36] has provided a successful bedrock for these studies. However, Tassoul's theory requires approximate spherical symmetry and thus cannot be used for rapidly rotating stars that can depart significantly from it [25]. The focus of this lecture is to explain the recent developments obtained in [20, 21, 27, 28] on

M. Pasek (✉)
IRAP, CNRS, 14, avenue Edouard Belin, 31400 Toulouse, France
e-mail: pasek@irsamc.ups-tlse.fr

M. Pasek
UPS-OMP, IRAP, Université de Toulouse, Toulouse, France

M. Pasek · B. Georgeot
LPT (IRSAMC), CNRS, 31062 Toulouse, France

M. Pasek · B. Georgeot
UPS, Laboratoire de Physique Théorique (IRSAMC), Université de Toulouse, 31062 Toulouse, France

M. Goupil et al. (eds.), *Studying Stellar Rotation and Convection*,
Lecture Notes in Physics 865, DOI 10.1007/978-3-642-33380-4_6,

building an asymptotic theory for pressure modes (p-modes) in rapidly rotating stars using acoustic ray dynamics. Results will be checked by comparisons with modes obtained by numerical computations of oscillations in a polytropic stellar model at different rotation rates. The lecture is organized as follows. In Sect. 6.2, we present the short-wavelength limit of acoustic waves and the evolution of its dynamics with rotation. The different classes of modes that can be constructed from the ray limit are then introduced in Sect. 6.3. In Sect. 6.4, we study in detail one important class of modes, namely the island modes, and give semi-analytical formulae for their amplitude distributions and frequencies. Finally, the chaotic modes are briefly introduced in Sect. 6.5. For a complementary introduction, one can see [19].

6.2 The Ray Limit of Acoustic Waves

6.2.1 Waves in Their Short-Wavelength Limit

Many wave equations are described by trajectories of a Hamiltonian system in the limit of short wavelength. Depending on the system considered, this limit takes different names. In the case of wave optics, this limit corresponds to geometrical optics. In the case of quantum mechanics, the short wavelength limit gives the classical limit where the quantum world recovers the classical mechanics of Newton. In the same way, the acoustic waves that cause pressure oscillations of stars have a similar limit in the form of *acoustic rays*.

Calculations that are detailed in [21] show that acoustic rays in stars are described by the eikonal equation

$$\omega^2 = \omega_c^2 + c_s^2 k^2, \tag{6.1}$$

where ω is the mode frequency, c_s the sound speed, and ω_c the cut-off frequency of the stellar model whose sharp increase in the outermost layers of the star provokes the back reflection of acoustic waves. An acoustic ray is a trajectory tangent to the wave vector $\mathbf{k}$ at the point $\mathbf{x}$; this naturally leads to Hamiltonian classical equations of motion [15].

6.2.2 Hamiltonian Systems

We have seen that the acoustic rays correspond to trajectories of a Hamiltonian system. Such systems are a subclass of dynamical systems, which are defined in a phase space with N spatial coordinates $q_1, q_2, \ldots, q_N$ and N associated momentum coordinates $p_1, p_2, \ldots, p_N$. Hamiltonian systems are characterized by the existence of a Hamiltonian function $H(q_1, q_2, \ldots, q_N, p_1, p_2, \ldots, p_N, t)$ that describes the evolution of the system through Hamilton's equations [2]

$$\frac{\partial H}{\partial p_i} = \dot{q}_i, \qquad \frac{\partial H}{\partial q_i} = -\dot{p}_i, \tag{6.2}$$

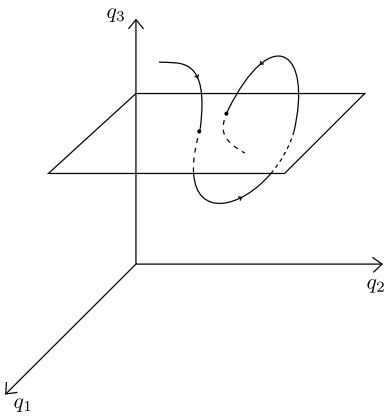

Fig. 6.1 Illustration of the construction of a Poincaré Surface of Section (PSS), where the fixed coordinate is q_3, and intersections are chosen for rays coming downwards

where dot denotes the time derivative. A simple example of such a system consists of a kinetic term plus a potential V with $H = \mathbf{p}^2/2 + V(\mathbf{q})$. The dynamics of the system takes place in phase space, and the volume of phase space is conserved through the evolution (no dissipation). Additionally, if H does not depend explicitly on time, there is a conserved quantity corresponding to the Hamilton function H itself, which is usually the energy of the system.

An important tool that will be used later is the Poincaré surface of section (PSS) [26]. Indeed, for systems with two degrees of freedom, the phase space is of dimension four and therefore hard to visualize. However, if there is a conserved quantity such as energy, the motion actually takes place on a manifold of dimension three. If additionally we choose a surface transverse to the flow of trajectories and plot crossings of these trajectories with this surface, the motion becomes discrete (sometimes called a "Poincaré map") and two-dimensional, thus easier to visualize (cf. Fig. 6.1). For many choices of the surface of section, the discrete dynamics of the Poincaré map is still Hamiltonian. In this new representation, the (discrete) time corresponds to the number of crossings of the PSS and does not necessarily reflect time in the continuous system: two trajectories of the continuous system may cross the surface of section at different times. The PSS enables us to view the different structures of phase space and in particular to easily distinguish between integrable and chaotic systems.

6.2.3 Integrable and Chaotic Hamiltonian Systems

Generic Hamiltonian systems fall between two extreme classes. The first corresponds to integrable systems. In this case, the system possess as many independent constants of motion as degrees of freedom. In Hamiltonian mechanics, two constants of motion f_1, f_2 are said to be independent, or in involution, if their Poisson

bracket vanishes, where the Poisson bracket is defined as [2]

$$\{f_1, f_2\} = \sum_{i=1}^{N} \left(\frac{\partial f_1}{\partial q_i} \frac{\partial f_2}{\partial p_i} - \frac{\partial f_1}{\partial p_i} \frac{\partial f_2}{\partial q_i} \right). \tag{6.3}$$

Thus, for an integrable system with a $2N$-dimensional phase space, N constants of motion $I_1, \ldots, I_n$ exist. For example, in systems with one degree of freedom, the conservation of energy is enough to ensure that the system is integrable. In the case of integrability, one can show that there exists a canonical change of variables (canonical means that this change of variables preserves the form of the equations of motion Eq. (6.2)) to a specific type of variables, called action-angle variables [2]. In this new set of coordinates, Hamilton's equations of motion become

$$\dot{I}_i = 0, \qquad \dot{\theta}_i = \omega_i, \tag{6.4}$$

where the ω_i are constant. It is easy to see that in this choice of variables, the motion takes place on N-dimensional tori in the $2N$-dimensional phase space. These surfaces are the so-called invariant tori, in the sense that they are invariant under the dynamics. It must be noted that these surfaces are tori in a topological sense, i.e. they may appear very distorted in a given choice of coordinates. For integrable systems with two degrees of freedom, trajectories follow two-dimensional tori and appear as lines on the PSS. Famous examples of classical integrable systems are the harmonic oscillator, the square and circular billiards, the two-body Kepler problem, etc. In a sense, integrable systems are exactly solvable models.

At the other extreme, there exist so-called chaotic systems. Their discovery was more recent. It is probably fair to say that up to the 20th century, there was a belief among scientists that most dynamical systems were integrable, the problem in understanding them being to find the right action-angle coordinates. Through the work of Poincaré and numerical simulations performed in the 20th century, it has been found that in general, many systems display various degrees of chaos. Chaotic systems have no constant of motion besides energy, and thus motion is not restricted to tori or other lower-dimensional surfaces in phase space. Rather, the motion is ergodic: most trajectories fill the energy shell densely. Hence, chaotic trajectories fill domains on the PSS. The most extreme degree of chaos corresponds to *hard chaos*, with an exponential separation of nearby trajectories, implying the famous exponential sensitivity to initial conditions (the "butterfly effect"). Famous examples of chaotic systems include the Sinai billiard, Bunimovich billiard (stadium), three-body Kepler problem, etc.

The generic transition to chaotic behaviour for a perturbed integrable system is described by the famous Kolmogorov–Arnold–Moser (KAM) theorem [2, 26]. Most Hamiltonian systems are between these two extremes, in the sense that their phase space displays integrable islands surrounded by chaotic seas; such systems are called mixed systems.

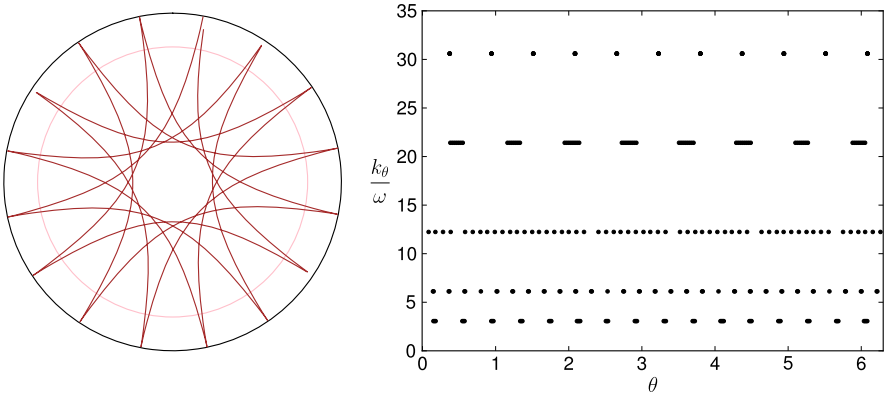

Fig. 6.2 Acoustic ray trajectories in a non-rotating star (*left*), and the associated Poincaré Surface of Section (*right*) taken at a fixed radial distance from the stellar surface corresponding to a radius $r = r_p$ (visible in *pink* on the *left figure*). The coordinates displayed on the surface of section are the scaled wavenumber latitudinal component k_θ/ω, where ω is the mode frequency, and the colatitude θ

6.2.4 Ray Dynamics in Rotating Stars

Equipped with the tools of Hamiltonian mechanics, one can study the dynamics of acoustic rays in rotating stars. This task was done in [20], with the Hamiltonian

$$H = \sqrt{c_s^2 \mathbf{k}^2 + \omega_c^2} \tag{6.5}$$

for a sequence of polytropic stellar models with different values of the rotation rate. It was found that for a non-rotating stellar model (i.e. $\Omega = 0$), the dynamical system is integrable, i.e. the ray trajectories are stable and localized on invariant tori in phase space. In Fig. 6.2 one can see that in a non-rotating polytropic stellar model, as expected, intersections of a ray with the PSS form lines (at a constant k_θ/ω).

When the rotation rate becomes significant, the ray trajectories are profoundly modified, and several types of rays emerge with different behaviours, following a KAM-type transition. In Fig. 6.3 one can see three types of rays computed for a polytropic stellar model of index $N = 3$ rotating at $\Omega/\Omega_K = 0.59$ (where $\Omega_K = \sqrt{GM/R_{\rm eq}^3}$ is the limiting rotation rate for which the centrifugal acceleration equals the gravity at the equator, M being the stellar mass and $R_{\rm eq}$ the equatorial radius). A first group corresponds to so-called whispering gallery rays, which follow the boundary (their name comes from the fact that the associated modes are responsible for the transmission of whispers from one part of a gallery to the other). A second group of rays forms *islands*, i.e. structures centred on a stable periodic ray. The main ones are 2-period and 6-period islands that are labelled according to the number of times their central periodic ray crosses the PSS. Both types of rays correspond to stable zones of phase space and accordingly, iterates of

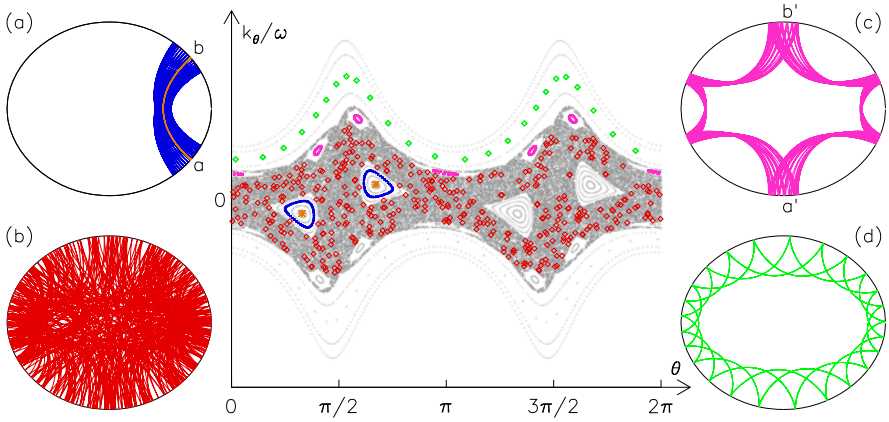

Fig. 6.3 Poincaré Surface of Section (*centre panel*) for a star rotating at $\Omega/\Omega_k = 0.59$, with the corresponding rays in position space (*panels* (**a**), (**b**), (**c**) and (**d**)). (**a**) 2-period island ray (*blue*) with the central periodic ray shown as the *orange line* between points *a* and *b*, (**b**) a chaotic ray (*red*), (**c**) a 6-period island ray (*magenta*), (**d**) a whispering gallery ray (*green*). These rays are highlighted by their respective colours on the PSS. The coordinates displayed on the PSS are the scaled wavenumber latitudinal component k_θ/ω, where ω is the mode frequency, and the colatitude θ (from [21])

the Poincaré map corresponding to the same trajectory form lines on the PSS. In contrast, there exists a third type of rays, called chaotic rays, which are unstable trajectories of the Hamiltonian system. Iterates from one such trajectory fill up a whole two-dimensional area in the Poincaré Surface of Section, corresponding to the property of ergodicity. Acoustic rays in rotating stars have therefore a rich dynamic, and we see in the sequel how this can be used to infer asymptotic properties of p-modes.

6.3 Construction of Modes from the Ray Limit

6.3.1 Modes Associated to the Different Types of Rays

Knowing the ray limit of the wave equation, it is possible to infer properties of the modes using tools which have been developed in the quantum chaos domain [17, 26]. An important result is that, asymptotically, one can associate different types of modes to the different phase space zones [7, 29]. But phase space is not well defined in quantum mechanics. Position and momentum represent independent bases with respect to which the wavefunction can be written, whereas classical phase space distributions are functions of both. This is due to the fact that the momentum and position operators do not commute in a wave context. Nevertheless, it is possible to define phase space distributions for wave functions [11, 37], e.g. Husimi

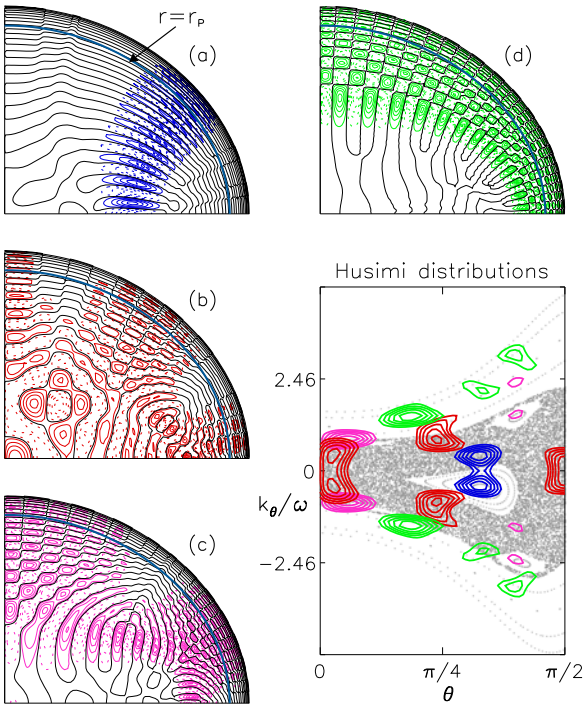

Fig. 6.4 Four typical modes with $m = 0$ of a stellar model rotating at $\Omega/\Omega_K = 0.59$ and their corresponding Husimi distributions on the PSS. (**a**) A 2-period island mode (*blue*), (**b**) a chaotic mode (*red*), (**c**) a 6-period island mode (*magenta*) and (**d**) a whispering gallery mode (*green*). The coordinates displayed on the surface of section are the scaled wavenumber latitudinal component k_θ/ω, where ω is the mode frequency, and the colatitude θ (from [21])

distributions that project wavefunctions onto Gaussian wavepackets of width Δ_x such that

$$\mathscr{H}(\mathbf{x}, \tilde{\mathbf{k}}) = \left| \int \Psi(\mathbf{x}') \exp\left(\frac{-\|\mathbf{x}' - \mathbf{x}\|^2}{2\Delta_x^2} \right) \exp\left(i\omega \tilde{\mathbf{k}} \cdot \mathbf{x}'\right) d\mathbf{x}' \right|^2, \tag{6.6}$$

where $\Psi(\mathbf{x}')$ is the mode amplitude distribution in position space,

$$\exp\left(-\|\mathbf{x}' - \mathbf{x}\|^2/\left(2\Delta_x^2\right)\right) \exp(i\omega\tilde{\mathbf{k}})$$

the Gaussian wavepacket, and $\tilde{\mathbf{k}} = \mathbf{k}/\omega$ the scaled-wavevector. This procedure implies that one cannot obtain details smaller than a certain scale set by the frequency (or $\hbar$ in quantum mechanics), according to the uncertainty principle $\Delta_x \Delta_{\tilde{k}} \approx 1/\omega$, where $\Delta_{\tilde{k}}$ is the width of the wavepackets in the scaled-wavevector representation. Figure 6.4 shows the phase space distributions on the Poincaré section of several p-modes in a rapidly rotating stellar model together with their amplitude distributions. This allows one to check that, indeed, to each of the four classes of trajectories shown in Fig. 6.3 one can associate specific modes which are localized in the corresponding phase space regions in the high-frequency limit.

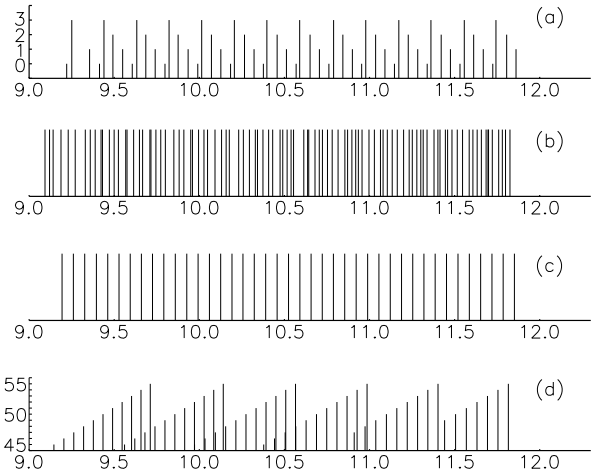

Fig. 6.5 Frequency sub-spectra of four classes of modes for $\Omega/\Omega_K = 0.59$ and $m = 0$. Frequencies are given in units of ω_1, which is the lowest acoustic mode frequency of the stellar model. (**a**) 2-period island modes, (**b**) chaotic modes, (**c**) 6-period island modes, (**d**) some whispering gallery modes; For sub-spectra (**a**) and (**d**), the height of the vertical bar specifies one of the two quantum numbers (from [21])

6.3.2 The Different Subspectra

The different types of modes mentioned at the end of the previous section correspond to independent subspectra. Near-integrable regions (stable islands and whispering galleries) produce regular sub-spectra, in the sense that we can write their mode frequencies as $\omega_i = f_i(n_i, \ell_i, m)$, where n_i, ℓ_i, m run through the integers. On the other hand, the chaotic region produces an irregular sub-spectrum with specific statistical properties. This can be seen in Fig. 6.5, where the numerical spectra of the four classes of modes are represented. Spectra (a), (c) and (d) correspond to near-integrable zones in phase space and can be described by a function of integers (quantum numbers). This is similar to what happens in a spherical star, although the spectra are described by a different function of the quantum numbers. Subspectrum (b) corresponds to the chaotic phase space region and is not expected to show such a regularity. It should be noted that in observational data, these four different spectra will be present in the same frequency range, and thus some care is needed in separating them. However, this task can be made easier by exploiting the difference in visibility of the modes.

6.3.3 Visibility of the Modes

The presence of different sets of modes in numerical computations does not imply that they are all equally present in observational data. Indeed, several factors can influence the visibility of the modes. One of the most important effects is the cancellation of mode amplitudes in the disk-integrated light. In the data displayed in Fig. 6.6, we estimate this effect by integrating the surface Lagrangian temperature perturbation of axisymmetric modes computed for the $\Omega = 0.59\Omega_K$ rotating

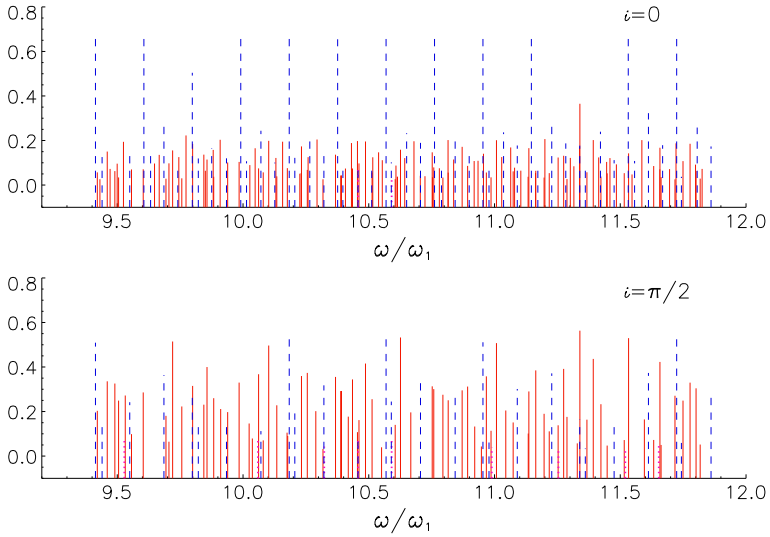

Fig. 6.6 Frequency spectra for $m = 0$ modes and $\Omega/\Omega_K = 0.59$, where the amplitudes are given by the visibility (disk-averaging factor) for a star seen pole-on $i = 0$ (*upper panel*) and equator-on $i = \pi/2$ (*lower panel*). Frequencies are given in units of ω_1, which is the lowest acoustic mode frequency of the stellar model. 2-period island modes (*blue*), chaotic modes (*red*), 6-period island modes (*magenta*) (from [21])

polytropic star. The normalization is such that the disk-averaging factor of a hypothetical mode uniformly distributed on the surface and seen pole-on is unity. Figure 6.6 shows the spectrum of modes whose disk-averaging factor exceeds 2.5 percent. The results show that many more modes are visible for rapidly rotating stars than for spherical stars (three times more for the rotation considered). Among the four classes of modes, the 2-period island modes and the chaotic modes have similar visibilities and are significantly more visible than the 6-period island modes and the whispering-gallery modes. At high rotation rates, we thus expect the oscillation spectrum of p-modes to be dominated by the 2-period island modes and chaotic modes.

6.4 Asymptotic Theory of Island Modes

6.4.1 Regularities in Numerical Computations of Oscillation Spectra

The numerical exploration of p-modes in rapidly rotating stellar models has hinted at the existence of a subset of modes that have regular frequency spacings in the high-frequency regime [22, 30] (see also the contribution of J. Ballot and F. Lignières in this volume). Two examples of such modes are shown in Fig. 6.7.

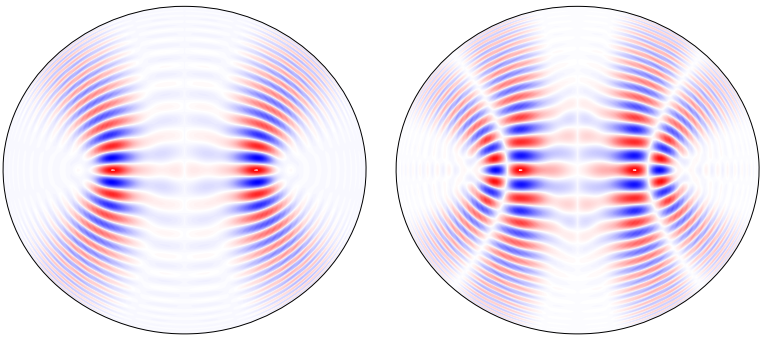

Fig. 6.7 Pressure amplitude $P\sqrt{d/\rho_0}$ on a meridional plane for a polytropic stellar model, with d the distance to the rotation axis and ρ_0 the equilibrium density of the model. The modes shown correspond to $n = 50$, $m = 0$ and $\ell = 0$ (*left*), $\ell = 1$ (*right*) at a rotation rate of $\Omega/\Omega_K \simeq 0.460$, where $\Omega_K = (GM/R_{\rm eq}^3)^{1/2}$ is the limiting rotation rate for which the centrifugal acceleration equals the gravity at the equator, M being the stellar mass and $R_{\rm eq}$ the equatorial radius. Colours denote pressure amplitude, from *red* (maximum positive value) to *blue* (minimum negative value) through *white* (null value)

For slowly rotating pulsating stars, asymptotic frequency regularities were, and still are, successfully used for mode identification and frequency inversion. The theoretical basis for such studies is Tassoul's formula [33], whose first order may be written as follows:

$$\omega_{n,\ell} \simeq \Delta\left(n_s + \frac{\ell_s}{2} + \frac{1}{4} + \alpha_s\right), \tag{6.7}$$

where n_s, ℓ_s are quantum numbers, α_s is a constant that depends on surface properties, and Δ is the large frequency separation such that

$$\Delta = 2\pi\left(2\int_0^R \frac{dr}{c(r)}\right)^{-1}. \tag{6.8}$$

Tassoul's formula for frequency regularities can only be derived for a (nearly) spherical star. Nevertheless, as we have seen, similar regularities are also found in the oscillation spectrum of rapidly rotating stellar models. It would thus be desirable to derive an asymptotic formula akin to Tassoul's to describe these spacings. We explain here how it is indeed feasible, at least for some specific regular subsets of the p-mode spectrum. Among these regular subsets, we will focus on the subset of 2-period island modes that is the largest group of near-integrable modes. They should be also the most visible regular modes in observations, from the results of disk-averaging computations [21] (see Sect. 6.3.3).

As we have seen, when the spatial distributions of island modes are projected onto phase space with Husimi distributions, the island modes fall on the 2-period stable island structures of phase space. So, island modes are localized on stable islands in the high-frequency regime. Therefore, solutions to an approximate wave equation in the vicinity of the stable island's central ray should turn out to be close

in frequencies and in amplitude distributions to the full island modes. The manner in which this approximate wave equation can be obtained and solved is described in [3] and sketched in the following. For previous applications of the method, one can consult e.g. [34, 35, 38].

6.4.2 Asymptotic Formula for the Island Mode Spectrum

For high-frequency p-modes, it is reasonable to neglect the perturbations of the gravitational potential (Cowling approximation) [1], as well as the Coriolis force, whose effect on pulsation frequencies is known to be weak in this regime [22, 30]. We thus obtain the following equation on pressure perturbations Φ_m in the meridional plane of the star as [21]:

$$\Delta\Phi_m + \frac{\omega^2}{\tilde{c}_s^2}\Phi_m = 0, \tag{6.9}$$

where ω is the frequency of the harmonic perturbation, d is the distance to the rotation axis, $\tilde{c}_s$ is such that

$$\tilde{c}_s = \frac{c_s}{\sqrt{1 - \frac{1}{\omega^2}(\omega_c^2 + \frac{c_s^2(m^2-1/4)}{d^2})}}, \tag{6.10}$$

and the quantum number m is the azimuthal node number of the mode. As explained previously, this equation gives the propagation of rays in the $\omega \to \infty$ limit. Now, we assume that the ray limit has been derived and that the stable periodic ray in the centre of the main stable island is known. We will call this ray γ. The mode amplitude is now expressed as $\Phi_m(s,\xi) = \exp(i\omega \int^s \frac{ds'}{\tilde{c}_s}) U_m(s,\xi,\omega)$, using the local coordinates (s,ξ) where s is the arc length along the ray, and ξ the transverse coordinate. For high frequencies ω, the transverse envelope of the mode is assumed to decay on a scale proportional to $1/\sqrt{\omega}$ away from the ray γ. Thus, the distance to the ray ξ can be assumed to be $O(1/\sqrt{\omega})$, and one can approximate Eq. (6.9) by a parabolic equation of the form:

$$\frac{\partial^2 V_m}{\partial \nu^2} - K(s)\nu^2 V_m + \frac{2i}{\tilde{c}_s(s)}\frac{\partial V_m}{\partial s} = 0, \tag{6.11}$$

where $\nu = \sqrt{\omega}\xi$, $V_m = U_m/\sqrt{\tilde{c}_s}$, and the function $K(s)$ is such that

$$K(s) = \frac{1}{\tilde{c}_s(s)^3}\frac{\partial^2 \tilde{c}_s}{\partial \xi^2}\bigg|_{\xi=0}. \tag{6.12}$$

In the first two terms of the previous expression, one can recognize the equation for a quantum harmonic oscillator [13]. The appearance of such a form can be understood as follows. The small deviations around the equilibrium position of a classical

mechanical system can be approximated by an equation for a harmonic oscillator [2]. Similarly, when one studies a wave equation on small distances, the bottom of the potential well can often be approximated by a quadratic function, and the wave equation takes the form of a quantum harmonic oscillator.

The lowest frequency solution to a quantum harmonic oscillator equation is a Gaussian wavepacket such that

$$V_m^0 = A(s)\exp\left(i\frac{\Gamma(s)}{2}\nu^2\right), \tag{6.13}$$

where $\Gamma(s)$ is an unknown complex-valued function, and $A(s)$ the amplitude of the wavepacket. This corresponds to a solution of Eq. (6.11) at a fixed s, i.e. at a fixed position on the ray. It is possible then to view the transverse variation of the mode along the ray as resulting from the propagation of the Gaussian wavepacket along the ray. Its width will thus be related to the properties of the rays near to the stable periodic ray γ. The evolution of the width of this wavepacket can be written in the form of a Hamiltonian system by a simple change of variable $\Gamma(s) = p(s)/z(s)$ with $p(s) = \tilde{c}_s^{-1}\, dz(s)/ds$. This Hamiltonian system is thus

$$\frac{dz}{d\tau} = \tilde{c}_s^2 p, \tag{6.14}$$

$$\frac{dp}{d\tau} = -\tilde{c}_s^2 K z, \tag{6.15}$$

where the (time-dependent) Hamiltonian function is

$$H_0(p, z, \tau) = \tilde{c}_s^2\frac{p^2}{2} + \tilde{c}_s^2 K\frac{z^2}{2}, \tag{6.16}$$

τ being the time coordinate. Since these equations are periodic in time, it is possible to transform this evolution into a map defined by a so-called monodromy matrix M:

$$\begin{bmatrix} z(\tau + T_\gamma) \\ p(\tau + T_\gamma) \end{bmatrix} = M \begin{bmatrix} z(\tau) \\ p(\tau) \end{bmatrix}. \tag{6.17}$$

The eigenvalues $\exp(\pm i\alpha)$ and eigenvectors $\mathbf{v}^\pm$ of M will hence fully describe the evolution of the wavepacket along the ray. Other solutions of Eq. (6.11) will be proportional to Hermite polynomials as

$$V_m^\ell(s, \nu) = \left(\frac{i}{\sqrt{2}}\right)^\ell \left(\frac{\bar{z}}{z}\right)^{\ell/2} H_\ell\left(\sqrt{\mathrm{Im}(\Gamma)}\nu\right)\frac{\exp(i\frac{\Gamma}{2}\nu^2)}{\sqrt{z}}, \tag{6.18}$$

with H_ℓ the Hermite polynomials of order ℓ. Finally, we can write the island mode solutions of Eq. (6.9) as

$$\Phi_m^\ell(s, \nu) = \sqrt{\tilde{c}_s} V_m^\ell(s, \nu)\exp\left(i\omega\int^s \frac{ds'}{\tilde{c}_s}\right). \tag{6.19}$$

Propagation of the wavepacket along the stable ray corresponds to the accumulation of a dynamical phase. For the mode to be univalued, this phase must be a multiple of 2π after a period of propagation, and hence it can be written that

$$\omega_{n,\ell,m} \oint_\gamma \frac{ds}{\tilde{c}_s} - \frac{\alpha + 2\pi N_r}{2} - (\alpha + 2\pi N_r)\ell = 2\pi n + \pi, \tag{6.20}$$

where the so-called stability angle α is obtained from the eigenvalues of the monodromy matrix M, N_r is the winding number of the eigenvector $\mathbf{v}$, and the last term on the right-hand side is the phase acquired from the reflection of the acoustic waves on the boundary. By re-ordering the terms of the last formula, one obtains an expression for mode frequencies in the asymptotic regime:

$$\omega_{n,\ell,m} = \frac{1}{\oint_\gamma \frac{ds}{\tilde{c}_s}} \left[2\pi \left(n + \frac{1}{2} \right) + \left(\ell + \frac{1}{2} \right) (2\pi N_r + \alpha) \right]. \tag{6.21}$$

This equation is valid asymptotically for n large and $\ell \ll n$. The quantum numbers n and ℓ correspond to the number of nodes in the directions parallel and transverse to the stable periodic ray γ. The island mode frequencies $\omega_{n,\ell,m}$ are thus essentially described by two quantities,

$$\delta_n(m) = \frac{2\pi}{\oint_\gamma \frac{ds}{\tilde{c}_s}} \quad \text{and} \quad \delta_\ell(m) = \frac{2\pi N_r + \alpha}{\oint_\gamma \frac{ds}{\tilde{c}_s}}. \tag{6.22}$$

The quantities δ_n and δ_ℓ probe the sound velocity and its transverse derivatives along the path of the periodic ray γ. It is also possible to derive an expression for the frequency difference $\delta_m = \omega_{n,\ell,m} - \omega_{n,\ell,0}$ that is equivalent to a rotational splitting in the co-rotating frame. Under the assumptions that the location of the stable ray does not change with m/ω and that n is large, we obtain

$$\delta_m(\ell = 0) \simeq \left[\frac{m^2}{\omega^2} \pi \frac{\oint_\gamma \frac{c_s}{d^2} ds}{(\oint_\gamma \frac{ds}{c_s})^2} \right] n. \tag{6.23}$$

This m^2 dependence of the splitting is to be contrasted with the usual first-order perturbation theory proportional to m, which comes from the effect of the Coriolis force [16]. The m^2 dependence is expected to be dominant in the high-frequency regime, where the Coriolis force is negligible. Indeed, the numerical computations that take into account the Coriolis force show the same dependence at high frequencies [28, 31].

6.4.3 Comparison with Numerical Modes

The result of comparison between the asymptotic formula (6.21) and the numerically computed modes of polytropic stellar models is shown in Fig. 6.8. These numerical computations take into account the Coriolis force and perturbations of the

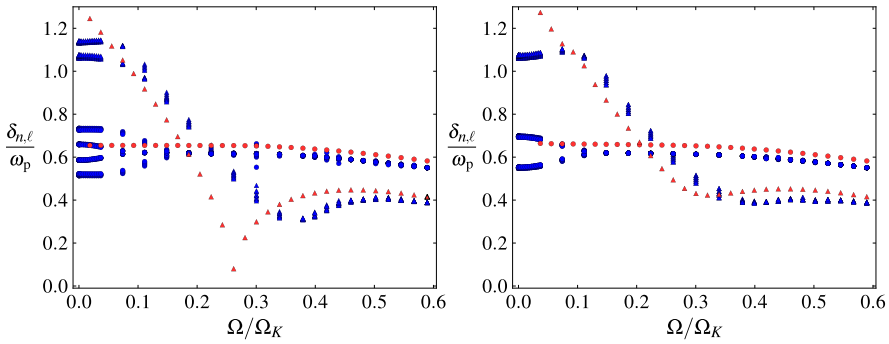

Fig. 6.8 Comparison of frequency spacings δ_n and δ_ℓ, computed from numerical simulations and semi-analytical formulae for different values of the rotation rate Ω/Ω_K, where $\Omega_K = (GM/R_{\rm eq}^3)^{1/2}$. The frequency spacings are normalized by $\omega_p = (GM/R_p^3)^{1/2}$ with R_p the polar radius. *Circles*: δ_n; *triangles*: δ_ℓ; *red*: semi-analytical results of Eq. (6.22); *blue*: numerical results. Numerical results correspond to different sets of regularities between modes of consecutive quantum numbers n or ℓ in the set $n \in [42, 51]$, $\ell \in \{0, 1\}$ for $m = 0$; and $n \in [42, 51]$, $\ell = 0$; $n \in \{42, 44, 46, 48, 50\}$, $\ell = 1$ for $m \in \{-1, 1\}$. *Left panel*: regularities for $m = 0$; *right panel*: for $|m| = 1$ (from [28])

gravitational potential. The agreement is good at high rotation rates and degrades at low rotation rates, where the theory is not supposed to apply. Additionally, for $m = 0$, the agreement degrades around $\Omega/\Omega_K \approx 0.26$. Indeed, at this rotation rate there is a bifurcation of the central periodic ray of the stable island, which splits into two separate rays. It is known that in this case, one should refine the theory in order to properly take into account this phenomenon [28]. By comparison with numerical results, we also see that the behaviour of δ_m expressed in Eq. (6.23) is indeed valid for rotation rates higher than $\Omega/\Omega_K \simeq 0.4$.

The theory developed in Sect. 6.4.2 also enables us to construct the amplitude distribution of the modes in terms of transverse Hermite polynomials modulated with the longitudinal coordinate. The result of comparison of the asymptotic amplitude distribution with the numerically computed modes is shown in Fig. 6.9. Again, the agreement is good, showing that the method used gives access not only to the mode frequencies, but also to the amplitude distribution with good accuracy.

6.5 Chaotic Spectrum

In the preceding section, we presented asymptotic formulae enabling us to predict the frequencies and amplitudes of the 2-period island modes, which should be among the most visible ones. However, we noticed in Sect. 6.3.3 that modes associated with chaotic phase space zone also presented high disk-averaging factors (see Fig. 6.6) and thus should be present in observed spectra. It is known from results in quantum chaos that no simple asymptotic formula can be constructed for chaotic modes. However, one can expect several specific properties. As concerns

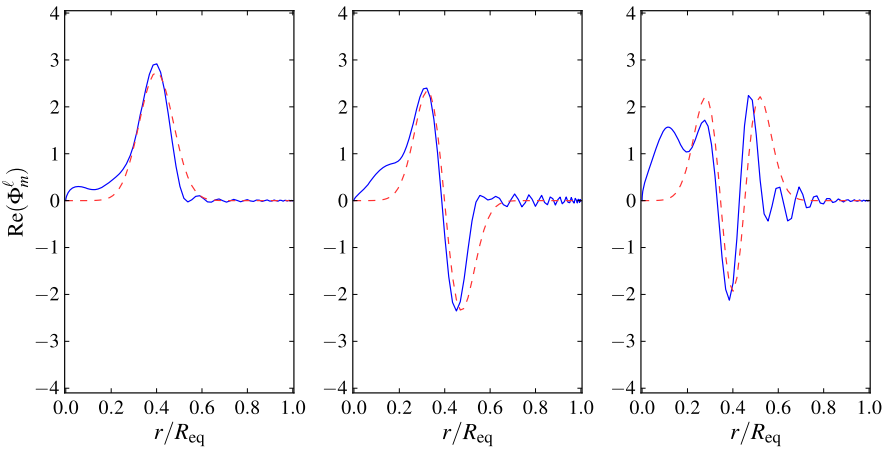

Fig. 6.9 Normalized amplitude distributions (real part of Φ_m^ℓ) on the equator as functions of position $r/R_{\rm eq}$ (where $R_{\rm eq}$ is the equatorial radius of the stellar model) for semi-analytical (*red dashed line*) and numerical (*blue continuous line*) modes. Modes are for $\Omega/\Omega_K \simeq 0.460$. The modes shown correspond to $n = 50$, $m = 0$ and $\ell = 0$ (*left*), $\ell = 1$ (*middle*), $\ell = 2$ (*right*). The first two modes are the same as in Fig. 6.7

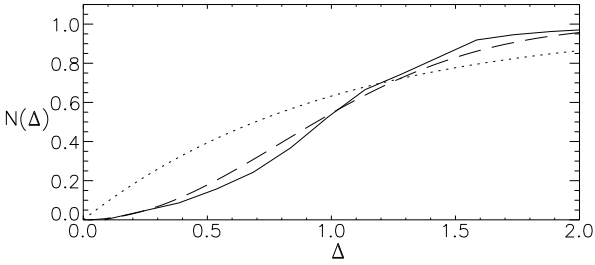

Fig. 6.10 Integrated spacing distribution $N(\Delta)$ of chaotic modes for $m = 0$ and $\Omega/\Omega_K = 0.59$ (*full line*); *dashed line*: Random Matrix Theory results; *dotted line*: Poisson distribution from uncorrelated spectra (from [20])

the spectrum, there is a conjecture [10] which has been verified on many examples. It states that statistical properties of spectra corresponding to chaotic modes should be the same as the ones predicted by Random Matrix Theory. The latter is a theory without adjustable parameter [9] which approximates Hamiltonian matrices by large random matrices with Gaussian-distributed entries. In Fig. 6.10 we show one statistical quantity that can be extracted from spectra, the integrated nearest-neighbour spacing distribution. The numerical data from the chaotic subspectrum of a rapidly rotating star is close to the Random Matrix result and far from the result for uncorrelated spectra. The conjecture is thus verified by the chaotic subset of the numerical acoustic stellar modes. As concerns the amplitude distribution, one expects these modes to be ergodic asymptotically on the chaotic phase space zone. More precisely, they are conjectured [6] as behaving as superposition of plane waves with wave vectors in random directions. Since the centre of the star is located in the chaotic phase space zone for high rotation rates, chaotic modes should be the modes which give information about the stellar core.

6.6 Conclusion

In this lecture we have reviewed the recent theoretical results on the p-mode oscillation spectrum of rapidly rotating stars. We think that there are strong arguments supporting the view that the tools of dynamical systems and quantum chaos are adequate to obtain insights on this problem. Indeed, the asymptotic structure of the p-mode spectrum for high rotation rates is fundamentally different from the non-rotating case, and this can be understood from acoustic ray theory. The dynamics of acoustic rays shows a transition from an integrable to a mixed system when the rotation rate increases. Thus, for a sufficiently large rotation rate, the spectrum should be divided into well-defined regular and irregular parts. Since these modes have striking differences in their amplitude distributions, it is expected from disk-averaging that only a fraction of them should be visible in observations. The most visible regular modes are the so-called island modes. Their asymptotic frequencies and amplitude distributions are obtained from ray theory in the form of semi-analytical formulae. In particular, the formula for frequency spacings relates regularities in the spectrum to internal properties of the star. On the other hand, for the irregular subset, only the statistical properties of chaotic modes can be predicted. These results were all validated by comparison with numerical modes of polytropic stellar models at different rotation rates.

From the first results of CoRoT, some regularity seems to be detected in rapidly rotating δ Scuti stars [14, 24]. Identification of the regular spectra should lead to better understanding of the stellar interior. This calls for more work to connect the present theory with observations [23]. In particular, observations of chaotic modes hold great promise since they would allow us to probe the stellar core.

The present theory could be extended in different ways. Indeed, though the results for polytropic stellar models are expected to be generic, applications of our methods to more refined or "realistic" stellar models is desirable. Some efforts have already been taken in this direction, see [31]. Also, the present ray formalism cannot treat discontinuities in a proper manner, but this could be incorporated in the formalism following the method of [8]. An important extension would concern other types of modes. Indeed, gravity modes were recently shown to be related to a ray theory [5], but the fundamental differences between the dynamics of acoustic and gravity rays require further study before applying the ideas reviewed here.

Acknowledgements We thank F. Lignières and D.R. Reese with whom part of this work has been done. We also thank J. Ballot for fruitful discussions, the ANR project SIROCO for funding and CALMIP ("CALcul en MIdi-Pyrénées") for the use of their supercomputer.

References

1. Aerts, C., Christensen-Dalsgaard, J., Kurtz, D.W.: Asteroseismology. Springer, Berlin (2010)
2. Arnold, V.I.: Mathematical Methods of Classical Mechanics. Springer, Berlin (1978)
3. Babich, V., Buldyrev, V.S.: Short-Wavelength Diffraction Theory: Asymptotic Methods. Springer Series on Wave Phenomena, vol. 4. Springer, Berlin (1991)

4. Baglin, A., Auvergne, M., Barge, P., Deleuil, M., Catala, C., Michel, E., Weiss, W., COROT Team: Scientific objectives for a minisat: CoRoT. In: Fridlund, M., Baglin, A., Lochard, J., Conroy, L. (eds.) The CoRoT Mission Pre-Launch Status—Stellar Seismology and Planet Finding. ESA Special Publication, vol. 1306, p. 33 (2006)
5. Ballot, J., Lignières, F., Prat, V., Reese, D.R., Rieutord, M.: 2D computations of g modes. arXiv:1109.6856 [astro-ph]
6. Berry, M.V.: Regular and irregular semiclassical wavefunctions. J. Phys. A, Math. Gen. **10**, 2083–2091 (1977)
7. Berry, M.V., Robnik, M.: Semiclassical level spacings when regular and chaotic orbits coexist. J. Phys. A, Math. Gen. **17**, 2413–2421 (1984)
8. Blümel, R., Antonsen, T.M. Jr., Georgeot, B., Ott, E., Prange, R.E.: Ray splitting and quantum chaos. Phys. Rev. Lett. **76**, 2476–2479 (1996)
9. Bohigas, O.: Random matrix theories and chaotic dynamics. In: Giannoni, M.J., Voros, A., Zinn-Justin, J. (eds.) Chaos and Quantum Physics, Les Houches Lectures Session LII, pp. 87–199. Elsevier, Amsterdam (1991)
10. Bohigas, O., Giannoni, M.J., Schmit, C.: Characterization of chaotic quantum spectra and universality of level fluctuation laws. Phys. Rev. Lett. **52**, 1–4 (1984)
11. Chang, S.J., Shi, K.J.: Evolution and exact eigenstates of a resonant quantum system. Phys. Rev. A **34**, 7–22 (1986)
12. Christensen-Dalsgaard, J.: Helioseismology. Rev. Mod. Phys. **74**, 1073–1129 (2002)
13. Cohen-Tannoudji, C., Diu, B., Laloe, F.: Quantum Mechanics, vol. 1. Wiley/VCH, New York/Weinheim (1986)
14. García Hernández, A., Moya, A., Michel, E., Garrido, R., Suárez, J.C., Rodríguez, E., Amado, P.J., Martín-Ruiz, S., Rolland, A., Poretti, E., Samadi, R., Baglin, A., Auvergne, M., Catala, C., Lefevre, L., Baudin, F.: Asteroseismic analysis of the CoRoT δ Scuti star HD 174936. Astron. Astrophys. **506**, 79–83 (2009)
15. Gough, D.O.: Linear adiabatic stellar pulsation. In: Zahn, J.P., Zinn-Justin, J. (eds.) Astrophysical Fluid Dynamics, Les Houches, 1987, pp. 399–560 (1993)
16. Goupil, M.J.: Effects of rotation on stellar p-mode frequencies. In: The Rotation of Sun and Stars. Lecture Notes in Physics, vol. 765, pp. 45–99. Springer, Berlin (2009)
17. Gutzwiller, M.C.: Chaos in Classical and Quantum Mechanics. Springer, Berlin (1990)
18. Koch, D.G., Borucki, W.J., Basri, G., Batalha, N.M., Brown, T.M., Caldwell, D., Christensen-Dalsgaard, J., Cochran, W.D., DeVore, E., Dunham, E.W., Gautier, T.N. III, Geary, J.C., Gilliland, R.L., Gould, A., Jenkins, J., Kondo, Y., Latham, D.W., Lissauer, J.J., Marcy, G., Monet, D., Sasselov, D., Boss, A., Brownlee, D., Caldwell, J., Dupree, A.K., Howell, S.B., Kjeldsen, H., Meibom, S., Morrison, D., Owen, T., Reitsema, H., Tarter, J., Bryson, S.T., Dotson, J.L., Gazis, P., Haas, M.R., Kolodziejczak, J., Rowe, J.F., Van Cleve, J.E., Allen, C., Chandrasekaran, H., Clarke, B.D., Li, J., Quintana, E.V., Tenenbaum, P., Twicken, J.D., Wu, H.: Kepler mission design, realized photometric performance, and early science. Astrophys. J. Lett. **713**, L79 (2010)
19. Lignières, F.: Asymptotic theory of stellar oscillations based on ray dynamics. In: Rozelot, J.P., Neiner, C. (eds.) The Pulsations of the Sun and the Stars. Lecture Notes in Physics, vol. 832, p. 259. Springer, Berlin (2011)
20. Lignières, F., Georgeot, B.: Wave chaos in rapidly rotating stars. Phys. Rev. E **78**(1), 016215 (2008)
21. Lignières, F., Georgeot, B.: Asymptotic analysis of high-frequency acoustic modes in rapidly rotating stars. Astron. Astrophys. **500**, 1173–1192 (2009)
22. Lignières, F., Rieutord, M., Reese, D.: Acoustic oscillations of rapidly rotating polytropic stars. I. Effects of the centrifugal distortion. Astron. Astrophys. **455**, 607–620 (2006)
23. Lignières, F., Georgeot, B., Ballot, J.: P-modes in rapidly rotating stars: looking for regular patterns in synthetic asymptotic spectra. Astron. Nachr. **331**, 1053 (2010)
24. Mantegazza, L., Poretti, E., Michel, E., Rainer, M., Baudin, F., García Hernández, A., Semaan, T., Alvarez, M., Amado, P.J., Garrido, R., Mathias, P., Moya, A., Suárez, J.C., Auvergne, M.,

Baglin, A., Catala, C., Samadi, R.: Pulsation spectrum of δ Scuti stars: the binary HD 50870 as seen with CoRoT and HARPS. Astron. Astrophys. **542**, A24 (2012)
25. Monnier, J.D., Zhao, M., Pedretti, E., Thureau, N., Ireland, M., Berger, P.M.J.P., Millan-Gabet, R., Van Belle, G., ten Brummelaar, T., McAlister, H., Ridgway, S., Turner, N., Sturmann, L., Sturmann, J., Berger, D.: Imaging the surface of Altair. Science **317**(5836), 342–345 (2007)
26. Ott, E.: Chaos in Dynamical Systems, 2nd edn. Cambridge University Press, Cambridge (2002)
27. Pasek, M., Georgeot, B., Lignières, F., Reese, D.R.: Regular modes in rotating stars. Phys. Rev. Lett. **107**(12), 121101 (2011)
28. Pasek, M., Lignières, F., Georgeot, B., Reese, D.R.: Regular oscillation sub-spectrum of rapidly rotating stars. Astron. Astrophys. **546**, A11 (2012)
29. Percival, I.C.: Regular and irregular spectra. J. Phys. B, At. Mol. Phys. **6**, L229–L232 (1973)
30. Reese, D., Lignières, F., Rieutord, M.: Regular patterns in the acoustic spectrum of rapidly rotating stars. Astron. Astrophys. **481**, 449–452 (2008)
31. Reese, D.R., MacGregor, K.B., Jackson, S., Skumanich, A., Metcalfe, T.S.: Pulsation modes in rapidly rotating stellar models based on the self-consistent field method. Astron. Astrophys. **506**, 189–201 (2009)
32. Royer, F.: On the rotation of A-type stars. In: The Rotation of Sun and Stars. Lecture Notes in Physics, vol. 765, pp. 207–230. Springer, Berlin (2009)
33. Tassoul, M.: Asymptotic approximations for stellar nonradial pulsations. Astrophys. J. Suppl. Ser. **43**, 469–490 (1980)
34. Tureci, H.E., Schwefel, H.G.L., Stone, A.D., Narimanov, E.E.: Gaussian-optical approach to stable periodic orbit resonances of partially chaotic dielectric micro-cavities. Opt. Express **10**, 752 (2002)
35. Vagov, A., Schomerus, H., Zalipaev, V.V.: Asymptotic-boundary-layer method for unstable trajectories: semiclassical expansions for individual scar wave functions. Phys. Rev. E **80**(5), 056202 (2009)
36. Vandakurov, Y.V.: The frequency distribution of stellar oscillations. Astron. Zh. **44**, 786 (1967)
37. Wigner, E.: On the quantum correction for thermodynamic equilibrium. Phys. Rev., Ser. II **40**, 749–759 (1932)
38. Zalipaev, V.V., Kusmartsev, F.V., Popov, M.M.: High-energy localized eigenstates of an electronic resonator in a magnetic field. J. Phys. A, Math. Gen. **41**(6), 065101 (2008)

Chapter 7
Low-Frequency Oscillations in Rotating Stars

Umin Lee

Abstract We review the properties of low-frequency oscillations in uniformly rotating stars. Rotation not only yields a new class of modes, like inertial modes and r-modes, but also significantly modifies the properties of low-frequency g-modes. For slow rotation rates where $|\Omega/\omega| \ll 1$, we can treat the rotation frequency Ω as a small parameter for perturbation analysis, but for $|\Omega/\omega| \not\ll 1$, we have to properly solve the oscillation equation given as a set of partial differential equations, taking account of the effects of the Coriolis force and the centrifugal force, where ω stands for the oscillation frequency observed in the corotating frame of the star. The Coriolis force couples modes having different spherical harmonic degrees l, and the centrifugal force deforms the equilibrium structure. Rapid rotation affects the stability and the frequency of low-frequency modes. We discuss perturbation theory, the traditional approximation, linear mode coupling, series expansion methods, and weakly nonlinear calculations, which are applied to low-frequency modes in rotating stars.

7.1 Introduction

There are classes of stars in which rotation has significant effects on the oscillations. In Jupiter, for example, low-frequency periodic phenomena, which are susceptible to rapid rotation, were reported by [14, 41]. Besides low-frequency phenomena, high-frequency oscillations in Jupiter were once claimed to have been detected (see [42]). Jovian p-modes were calculated, taking account of the effects of the rapid rotation on the modes and the equations of state appropriate for the planet (see, e.g., [27, 55]). For rapidly rotating neutron stars, it was suggested that r-modes could be excited by the instability associated with gravitational wave radiation [1, 20], which prompted numerous theoretical studies concerning the instability and frequency spectrum of the r-modes (e.g., [7, 38, 40, 60]). For slowly pulsating B (SPB) stars, many low-frequency nonradial modes have been detected (e.g., [56–58]), which are believed to

U. Lee (✉)
Astronomical Institute, Tohoku University, Sendai, Miyagi 980-8578, Japan
e-mail: lee@astr.tohoku.ac.jp

M. Goupil et al. (eds.), *Studying Stellar Rotation and Convection*,
Lecture Notes in Physics 865, DOI 10.1007/978-3-642-33380-4_7,

be excited by the opacity bump mechanism associated with iron metal lines [18, 19, 21]. Low-frequency g-modes are likely influenced by rotation since the frequency of the modes of interest can be comparable to or smaller than the rotation frequency. The effects of rotation on such low-frequency modes have to be properly accounted for to reliably determine the frequency spectrum and stability.

Oscillations of stars are governed by a set of linear partial differential equations (LPDEs), which is derived by linearizing the basic equations for the fluid dynamics. For normal mode analysis, we assume that the time dependence of the perturbations is given by the factor $e^{i\omega t}$, where ω denotes the oscillation frequency in the corotating frame and is treated as the eigenvalue of the differential equations with appropriate boundary conditions imposed at the center and the surface of the stars. For nonrotating stars, the angular dependence of the perturbations can be represented by using a single spherical harmonic function $Y_l^m(\theta, \phi)$, and this separation of variables makes it possible to reduce the set of LPDEs to a set of linear ordinary differential equations (LODEs), which is rather easy to handle analytically and numerically.

For rotating stars, however, the separation of variables between the radial coordinate r and the angular coordinates (θ, ϕ) is not possible in general because of the Coriolis term and of the rotational deformation of the equilibrium structure, and we have either to directly solve the set of LPDEs or to employ series expansion for the perturbations using spherical harmonic functions to reduce the set of LPDEs to a set of LODEs. To obtain reliable eigenvalues and eigenfunctions, we have to prepare a good number of mesh points in the angular direction for the LPDEs or to use a long series expansion, which inevitably demands a significant amount of numerical resources for calculation.

Besides the difficulty associated with the separation of variables for the oscillations, the equilibrium structure of a rotating star is deformed by centrifugal force, and it is not an easy task to construct rotationally deformed models for evolving stars. We note that it is rather easy to calculate rotationally deformed polytropes, for which modal analyses could be carried out by solving the oscillation equations given as a set of LPDEs. For slow rotation, the effects of centrifugal force appear as a second-order term of the rotation rate Ω, but, as Ω increases, we need higher-order terms to correctly represent both the deformed equilibrium structure and the oscillations, which makes the analysis more difficult.

7.2 Perturbation Analysis

For slow rotation, we can apply a perturbation method to oscillations in rotating stars regarding the rotation frequency Ω as a small parameter. The effects of the Coriolis force and the centrifugal force on the oscillation may be parameterized effectively by the quantities $m\Omega/\omega$ and $\bar{\Omega}^2 = \Omega^2/\sigma_0^2$, where $\sigma_0^2 = GM/R^3$, M and R are the mass and radius of the star, and G is the gravitational constant. The oscillation frequency σ in an inertial frame is related to ω by

$$\sigma = \omega - m\Omega, \tag{7.1}$$

where m is the azimuthal order (wavenumber) of the mode, and we have assumed that the time and azimuthal dependence of the oscillations is given by the factor $e^{\mathrm{i}(m\phi+\omega t)}$. For slow rotation, we may expand the eigenfrequency (and the eigenfunction) of a mode in terms of $\bar{\Omega}$:

$$\begin{aligned}\bar{\omega} &= \bar{\omega}_0 + D_1(m\bar{\Omega}/\bar{\omega}_0) + D_2(m\bar{\Omega}/\bar{\omega}_0)^2 + E_2\bar{\Omega}^2 + \cdots \\ &= \bar{\omega}_0 + mC_1\bar{\Omega} + C_2\bar{\Omega}^2 + \cdots,\end{aligned} \tag{7.2}$$

where $\bar{\omega} = \omega/\sigma_0$, $C_1 = D_1/\bar{\omega}_0$, and $C_2 = D_2(m/\bar{\omega}_0)^2 + E_2$, and the coefficients C_1 and C_2 are tabulated, for example, in [45] for low l and low radial order adiabatic p-, f-, and g-modes of a polytropic model for uniform rotation. The first-order term comes from the Coriolis force, the effects of which differ between the prograde and retrograde modes as indicated by the factor m, where in our convention the modes with $m\omega < 0$ ($m\omega > 0$) are prograde (retrograde) modes. The second-order terms include both the Coriolis force and the centrifugal force, and the effects on the frequency are the same for both the prograde and retrograde modes. Note that the expansion to third order in $\bar{\Omega}$ was discussed by [49]. Note also that the coefficient C_1 for an adiabatic mode is given by (e.g., [54])

$$C_1 = \frac{\int_0^R [2\xi^r/\xi^h + 1](\xi^h)^2\rho r^2\,dr}{\int_0^R [(\xi^r/\xi^h)^2 + l(l+1)](\xi^h)^2\rho r^2\,dr}, \tag{7.3}$$

where ξ^r and ξ^h denote the radial and horizontal components of the displacement vector $\boldsymbol{\xi}$ of the mode in the nonrotating star, and for low-frequency modes, we have $C_1 \sim [l(l+1)]^{-1}$ since $|\xi^r/\xi^h| \ll 1$.

Equation (7.2) may suggest that the centrifugal force is essential for high-frequency p-modes of $(\bar{\Omega}/\bar{\omega})^2 \ll \bar{\Omega}^2$ and that the Coriolis force is essential for low-frequency g-modes of $(\bar{\Omega}/\bar{\omega})^2 \gg \bar{\Omega}^2$. For $\bar{\Omega} \sim 1$ or $|\bar{\Omega}/\bar{\omega}| \gtrsim 1$, we cannot regard $\bar{\Omega}$ as a small parameter anymore.

Inertial modes are rotationally induced modes, and the Coriolis force is the restoring force for them. For inertial modes in isentropic stars for which the Brunt–Väisälä frequency N vanishes throughout the interior, we can expand the oscillation frequency $\bar{\omega}$ as

$$\bar{\omega} = \kappa_0\bar{\Omega}\left(1 + \kappa_2\bar{\Omega}^2 + \cdots\right), \tag{7.4}$$

where the coefficient κ_2 contains the contributions from both the Coriolis and centrifugal forces. The coefficients κ_0 and κ_2 were calculated, e.g., by [40, 60] for polytropes. For r-modes of order m and l', which are generated by the conservation of the radial component of the total vorticity measured in an inertial frame (e.g., [54]) and form a subclass of inertial modes, we have the analytical expression for κ_0:

$$\kappa_0 = 2m/\left[l'\left(l'+1\right)\right], \tag{7.5}$$

where $l' = |m| + 2j - 1$ for even modes and $l' = |m| + 2(j-1)$ for odd modes with j being a positive integer. For r-modes in isentropic stars, only the nodeless

odd r-mode of $l' = |m|$ exists (e.g., [60]). For stars with a radiative region, however, there exist both even and odd r-modes, and we have the nodeless fundamental r-mode and its overtones for a given $l' \geq |m|$ (e.g., [61]). It is interesting to note that although expansion (7.4) is still applicable to the r-modes in radiative stars, it is not to inertial modes, for which expansion (7.2) should be used. Inertial modes in radiative stars recover their mode character only when the rotation frequency dominates the Brunt–Väisälä frequency N.

For low-frequency modes of $|\bar{\Omega}/\bar{\omega}| \gtrsim 1$, we cannot treat the rotation frequency Ω as a small parameter, a situation which is likely to happen for g-modes in rapidly rotating stars. Low-frequency g-modes excited in SPB stars are such an example, and the properties of the modes are significantly modified by the effects of rotation.

7.3 Low-Frequency Oscillations

For low-frequency oscillations of $|\Omega/\omega| \gtrsim 1$, we need to solve the problem using nonperturbative methods. In this section, we ignore the effects of the centrifugal force on the oscillations and neglect the rotational deformation of the stars, that is, we assume that the star is spherically symmetric and the physical quantities in the equilibrium depend only on r. The linearized basic equations for adiabatic oscillations in uniformly rotating stars may be given, in the Cowling approximation, by

$$-\rho\omega^2\xi^r - 2\mathrm{i}\rho\omega\Omega\sin\theta\xi^\phi = -\frac{\partial p'}{\partial r} - \rho'\frac{\partial \Phi}{\partial r}, \tag{7.6}$$

$$-\rho\omega^2\xi^\theta - 2\mathrm{i}\rho\omega\Omega\cos\theta\xi^\phi = -\frac{1}{r}\frac{\partial p'}{\partial \theta}, \tag{7.7}$$

$$-\rho\omega^2\xi^\phi + 2\mathrm{i}\rho\omega\Omega\cos\theta\xi^\theta + 2\mathrm{i}\rho\omega\Omega\sin\theta\xi^r = -\frac{1}{r\sin\theta}\frac{\partial p'}{\partial \phi}, \tag{7.8}$$

$$\rho' + \frac{1}{r^2}\frac{\partial}{\partial r}\left(r^2\rho\xi^r\right) + \frac{1}{r\sin\theta}\frac{\partial}{\partial\theta}\left(\sin\theta\rho\xi^\theta\right) + \frac{1}{r\sin\theta}\frac{\partial}{\partial\phi}\left(\rho\xi^\phi\right) = 0, \tag{7.9}$$

and

$$\frac{p'}{p} = \Gamma_1\left(\frac{\rho'}{\rho} + A\xi^r\right), \tag{7.10}$$

where $\boldsymbol{\xi} = (\xi^r, \xi^\theta, \xi^\phi)$ is the displacement vector, and p' and ρ' are the Eulerian perturbations of the pressure and density, respectively, and

$$\Gamma_1 = \left(\frac{\partial \ln p}{\partial \ln \rho}\right)_{\mathrm{ad}}, \qquad A = \frac{d\ln\rho}{dr} - \frac{1}{\Gamma_1}\frac{d\ln p}{dr}. \tag{7.11}$$

Using the horizontal components (7.7) and (7.8), we obtain

$$\xi^\theta = \frac{1}{r\omega^2}\frac{1}{1-\nu^2\mu^2}\left(\frac{\partial}{\partial\theta} - \frac{\mathrm{i}\nu\mu}{\sin\theta}\frac{\partial}{\partial\phi}\right)\frac{p'}{\rho} + \frac{\nu^2\mu\sin\theta}{1-\nu^2\mu^2}\xi^r, \tag{7.12}$$

$$\xi^{\phi} = \frac{1}{r\omega^2}\frac{1}{1-\nu^2\mu^2}\left(\mathrm{i}\nu\mu\frac{\partial}{\partial\theta} + \frac{1}{\sin\theta}\frac{\partial}{\partial\phi}\right)\frac{p'}{\rho} + \frac{\mathrm{i}\nu\sin\theta}{1-\nu^2\mu^2}\xi^r, \tag{7.13}$$

where $\mu = \cos\theta$, $\nu = 2\Omega/\omega$, and we have assumed that $\nu^2\mu^2 \neq 1$. Substituting ξ^{θ} and ξ^{ϕ} into Eqs. (7.6) and (7.9), we obtain after some manipulation

$$\begin{aligned} &r\frac{\partial}{\partial r}\frac{\xi^r}{r} + \left(3 - \frac{V}{\Gamma_1}\right)\frac{\xi^r}{r} + \frac{V}{\Gamma_1}\frac{p'}{\rho g r} + \frac{1}{c_1\bar{\omega}^2}\mathscr{L}_{\nu}\left(\frac{p'}{\rho g r}\right) \\ &\quad = \frac{\partial}{\partial\mu}\left[\frac{\nu^2\mu(1-\mu^2)}{1-\nu^2\mu^2}\frac{\xi^r}{r}\right] + \frac{m\nu}{1-\nu^2\mu^2}\frac{\xi^r}{r}, \end{aligned} \tag{7.14}$$

$$\begin{aligned} &r\frac{\partial}{\partial r}\frac{p'}{\rho g r} - \left(c_1\bar{\omega}^2 + rA\right)\frac{\xi^r}{r} + (rA + U - 1)\frac{p'}{\rho g r} \\ &\quad = -c_1\bar{\omega}^2\nu^2\frac{1-\mu^2}{1-\nu^2\mu^2}\frac{\xi^r}{r} + \frac{\nu}{1-\nu^2\mu^2}\left[\nu\mu\left(1-\mu^2\right)\frac{\partial}{\partial\mu} - m\right]\frac{p'}{\rho g r}, \end{aligned} \tag{7.15}$$

where $\mathscr{L}_{\nu}$ is the differential operator defined by

$$\mathscr{L}_{\nu} \equiv \frac{\partial}{\partial\mu}\left(\frac{1-\mu^2}{1-\nu^2\mu^2}\frac{\partial}{\partial\mu}\right) - \frac{1}{1-\nu^2\mu^2}\left(\frac{m^2}{1-\mu^2} + m\nu\frac{1+\nu^2\mu^2}{1-\nu^2\mu^2}\right), \tag{7.16}$$

and

$$V = -\frac{d\ln p}{d\ln r}, \qquad U = \frac{d\ln M_r}{d\ln r}, \qquad M_r = \int_0^r 4\pi r^2\rho\, dr, \qquad c_1 = \frac{(r/R)^3}{M_r/M}, \tag{7.17}$$

and $g = GM_r/r^2$. Here, we have assumed that the ϕ dependence of the perturbations is given by the factor $e^{\mathrm{i}m\phi}$. For given ν and m, the Hough function $\Theta_{km}(\mu;\nu)$ is defined as the eigenfunction of the second-order linear differential equation called Laplace tidal equation (e.g., [39]):

$$\mathscr{L}_{\nu}\left[\Theta_{km}(\mu;\nu)\right] = -\lambda_{km}(\nu)\Theta_{km}(\mu;\nu), \tag{7.18}$$

where $\lambda_{km}(\nu)$ is the eigenvalue, and k is an integer used as a modal index (e.g., [36]). We may normalize the function Θ_{km} such that

$$\int_{-1}^{1} d\mu\, \Theta^*_{k'm}\Theta_{km} = \delta_{kk'}, \tag{7.19}$$

where the asterisk indicates complex conjugation, and $\delta_{kk'}$ is the Kronecker delta. It is convenient to define the function $\tilde{\Theta}_{km}(\theta,\phi)$,

$$\tilde{\Theta}_{km}(\theta,\phi) \equiv \Theta_{km}(\mu;\nu)e^{\mathrm{i}m\phi}/\sqrt{2\pi}, \tag{7.20}$$

which, as $\nu \to 0$, tends to the spherical harmonic function $Y^m_{l_k}(\theta,\phi)$ with $\lambda_{km} \to l_k(l_k+1)$, where $l_k = |m| + k$, and k is a nonnegative integer. When $\nu = 0$, since

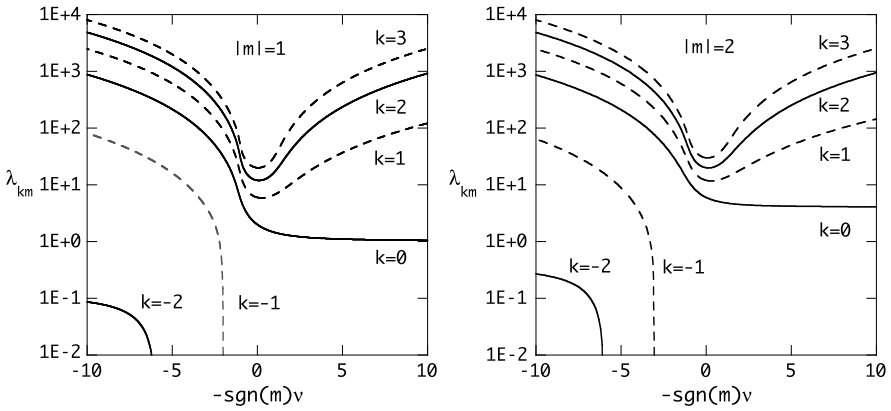

Fig. 7.1 Eigenvalue of Laplace's tidal equation λ_{km} versus $-\mathrm{sgn}(m)\nu$ for $|m| = 1$ and 2, where $\mathrm{sgn}(m) \equiv m/|m|$ and $\nu \equiv 2\Omega/\omega$. *Solid* and *dashed lines* are for even and odd modes, respectively

$\mathscr{L}_{\nu=0}(Y_l^m) = -l(l+1)Y_l^m$ and the terms on the right-hand side of Eqs. (7.14) and (7.15) vanish, the separation of variables using a single spherical harmonic function $Y_l^m(\theta, \phi)$ becomes possible so that $\xi^r \propto Y_l^m$ and $p' \propto Y_l^m$.

Figure 7.1 depicts the eigenvalue λ_{km} as a function of ν for $|m| = 1$ and 2. For a given azimuthal wavenumber m, λ_{km} depends on the parameter ν and tends to $l_k(l_k+1)$ with $l_k = |m| + k$ as $\nu \to 0$ for $k \geq 0$, which corresponds to $\tilde{\Theta}_{km} \to Y_{l_k}^m$ as $\nu \to 0$. The quantity $\sqrt{\lambda_{km}}$ represents a kind of surface wavenumber. Except for the prograde sectoral modes ($k = 0$), we have $\lambda_{km} \propto \nu^2$ as $|\nu| \to \infty$. The prograde sectoral modes (associated with λ_{0m} for modes with $m\omega < 0$) in rapidly rotating stars are special modes whose surface wavenumber is lower than the value at $\nu = 0$ and hardly changes with ν, tending to m^2 as $|\nu| \to \infty$ (e.g., [8, 51]). Note that g-modes belong to λ_{km} with $k \geq 0$. On the other hand, r-modes, which are retrograde modes, belong to λ_{km} with negative k [36]. In the limit as $\Omega \to 0$, we have $\omega \to 2m\Omega/l'_k(l'_k+1)$, where $l'_k = |m| + |k+1|$ for negative integer k. Note that $\lambda_{km} \to 0$ as $\omega \to 2m\Omega/l'_k(l'_k+1)$. A few examples of the functions Θ_{km}, Θ^{θ}_{km}, and Θ^{ϕ}_{km} for g- and r-modes are given in [36].

7.4 Traditional Approximation

A local analysis of waves in the short-wavelength and low-frequency limits gives a dispersion relation (e.g., [54])

$$\omega^2 \approx \frac{N^2 k_H^2 + (2\boldsymbol{\Omega} \cdot \mathbf{k})^2}{k^2}, \tag{7.21}$$

where N denotes the Brunt–Väisälä frequency, $\mathbf{k} = k_r \mathbf{e}_r + k_\theta \mathbf{e}_\theta + k_\phi \mathbf{e}_\phi \equiv k_r \mathbf{e}_r + \mathbf{k}_H$ is the wavenumber vector, $k = |\mathbf{k}|$, and $k_H = |\mathbf{k}_H|$. Because the waves are nearly incompressible so that $\mathbf{k} \cdot \boldsymbol{\xi} = k_r \xi^r + \mathbf{k}_H \cdot \boldsymbol{\xi}_H \approx 0$ in this limit, we obtain $|\xi^r/\xi_H| \approx$

$|k_H/k_r|$, where $\boldsymbol{\xi} = \xi^r \mathbf{e}_r + \xi^\theta \mathbf{e}_\theta + \xi^\phi \mathbf{e}_\phi \equiv \xi^r \mathbf{e}_r + \boldsymbol{\xi}_H$. If $|N^2|$ is much larger than both ω^2 and $(2\Omega)^2$, the dispersion relation leads to $k_H^2/k^2 \ll 1$ and hence to $|k_H/k_r| \ll 1$. This also means that $|\xi^r/\xi_H| \ll 1$ for the incompressible waves. Since $\mathbf{k}$ is almost radial, we may approximate $(2\boldsymbol{\Omega}\cdot\mathbf{k})^2 \approx (2\Omega_r k_r)^2$ in the dispersion relation, suggesting that only the radial component of $\boldsymbol{\Omega}$ is important and that the horizontal component of $\boldsymbol{\Omega}$ can be ignored in determining the frequency ω of the waves. This approximation is called the traditional approximation.

Many properties of low-frequency oscillations of uniformly rotating stars are well explained by using the traditional approximation (e.g., [32, 36]; see also [6]), in which the tangential component $-\Omega\sin\theta\mathbf{e}_\theta$ in $\boldsymbol{\Omega} = \Omega\cos\theta\mathbf{e}_r - \Omega\sin\theta\mathbf{e}_\theta$ is neglected, corresponding to the neglect of the terms on the right-hand side of Eqs. (7.14) and (7.15). Under the traditional approximation (and the Cowling approximation), the separation of variables becomes possible, which is the most favorable property of the approximation, and the angular dependence of the oscillations is given by the Hough function $\Theta_{km}(\mu;\nu)$ (e.g., [39]). The components of the displacement vector $\boldsymbol{\xi}(\mathbf{x},t)$ are then given by

$$\xi^r = \xi^r(r)\tilde{\Theta}_{km}(\theta,\phi)e^{\mathrm{i}\omega t}, \tag{7.22}$$

$$\xi^\theta = \frac{1}{r\omega^2}\frac{p'(r)}{\rho(r)}\tilde{\Theta}^\theta_{km}(\theta,\phi)e^{\mathrm{i}\omega t}, \tag{7.23}$$

$$\xi^\phi = \frac{1}{r\omega^2}\frac{p'(r)}{\rho(r)}\mathrm{i}\tilde{\Theta}^\phi_{km}(\theta,\phi)e^{\mathrm{i}\omega t}, \tag{7.24}$$

and p' and ρ' are given by

$$p' = p'(r)\tilde{\Theta}_{km}(\theta,\phi)e^{\mathrm{i}\omega t}, \tag{7.25}$$

$$\rho' = \rho'(r)\tilde{\Theta}_{km}(\theta,\phi)e^{\mathrm{i}\omega t}, \tag{7.26}$$

where

$$\tilde{\Theta}^\theta_{km}(\theta,\phi) = \frac{1}{(1-\nu^2\mu^2)\sqrt{1-\mu^2}}\left[-\left(1-\mu^2\right)\frac{d}{d\mu} + m\nu\mu\right]\tilde{\Theta}_{km}(\theta,\phi), \tag{7.27}$$

$$\tilde{\Theta}^\phi_{km}(\theta,\phi) = \frac{1}{(1-\nu^2\mu^2)\sqrt{1-\mu^2}}\left[-\nu\mu\left(1-\mu^2\right)\frac{d}{d\mu} + m\right]\tilde{\Theta}_{km}(\theta,\phi). \tag{7.28}$$

The radial functions $\xi^r(r)$ and $p'(r)$ associated with λ_{km} are obtained by solving the following LODEs with appropriate boundary conditions at the center and surface of the star:

$$r\frac{dz_1}{dr} = \left(\frac{V}{\Gamma_1} - 3\right)z_1 + \left(\frac{\lambda_{km}}{c_1\bar{\omega}^2} - \frac{V}{\Gamma_1}\right)z_2, \tag{7.29}$$

$$r\frac{dz_2}{dr} = \left(c_1\bar{\omega}^2 + rA\right)z_1 + (1 - U - rA)z_2, \tag{7.30}$$

where $z_1 = \xi^r(r)/r$ and $z_2 = p'(r)/\rho g r$. Note that replacing λ_{km} with $l(l+1)$, we regain the differential equation for adiabatic oscillations of nonrotating stars in the Cowling approximation.

The inner boundary condition imposed at the stellar center may be obtained by substituting $z_j \propto r^\beta$, $V = rA = 0$, and $U = 3$ into Eqs. (7.29) and (7.30). Then, the regularity condition for the displacement vector at the center given by $\beta \geq -1$ leads to $\lambda_{km} \geq 2$, a condition which is not satisfied by prograde sectoral g-modes of λ_{0m} with $l = -m = 1$ and is not always satisfied by r-modes (see Fig. 7.1). Note that if we calculate oscillation modes using series expansion method discussed below (without the traditional approximation), we can always find prograde sectoral g-modes of $l = -m = 1$ and retrograde r-modes that satisfy the regularity condition at the stellar center.

The kinetic energy $\langle E_K \rangle$, averaged over the period, of a mode associated with λ_{km} may be given by

$$\begin{aligned}\langle E_K \rangle &= \frac{\omega^2}{4} \int \rho \boldsymbol{\xi}^* \cdot \boldsymbol{\xi} \, dV \\ &= \int \frac{\rho g r^3}{4} \left[c_1 \bar{\omega}^2 |z_1|^2 + \left(\lambda_{km} + \nu \frac{\partial \lambda_{km}}{\partial \nu} \right) \frac{|z_2|^2}{c_1 \bar{\omega}^2} \right] dr, \end{aligned} \tag{7.31}$$

where we have used the normalization given by (7.19), and

$$\begin{aligned}\int_{-1}^{1} d\mu \left(|\Theta_{km}^{\theta}|^2 + |\Theta_{km}^{\phi}|^2 \right) &= \left(\lambda_{km} + \nu \frac{\partial \lambda_{km}}{\partial \nu} \right) \int_{-1}^{1} d\mu \, |\Theta_{km}|^2 \\ &= \lambda_{km} + \nu \frac{\partial \lambda_{km}}{\partial \nu} \end{aligned} \tag{7.32}$$

for positive λ_{km}. The expression of the kinetic energy $\langle E_K \rangle$ is the same as that given by [35].

7.5 Linear Mode Coupling

The terms on the right-hand sides of Eqs. (7.14) and (7.15), which are neglected under the traditional approximation, bring about mode coupling between low-frequency modes associated with different λ_{km}s. Here, we again ignore the effects of the centrifugal force. Since the functions $\Theta_{km}(\mu; \nu)$ form a complete set for given m and ν, we may expand the functions ξ^r and p' in terms of $\tilde{\Theta}_{km}$ as

$$\xi^r(r, \theta, \phi, t) = e^{\mathrm{i}\omega t} \sum_{k'} \xi^r_{k'}(r) \tilde{\Theta}_{k'm}(\theta, \phi), \tag{7.33}$$

$$p'(r, \theta, \phi, t) = e^{\mathrm{i}\omega t} \sum_{k'} p'_{k'}(r) \tilde{\Theta}_{k'm}(\theta, \phi), \tag{7.34}$$

and substituting these expansions into Eqs. (7.14) and (7.15), multiplying by $\tilde{\Theta}^*_{km}$, and integrating over $\sin\theta\, d\theta\, d\phi$, we obtain

$$r\frac{dz_1^k}{dr}+\left(3-\frac{V}{\Gamma_1}\right)z_1^k+\left(\frac{V}{\Gamma_1}-\frac{\lambda_{km}}{c_1\bar{\omega}^2}\right)z_2^k=\sum_{k'}\left(\int_{-1}^{1}d\mu\,\tilde{\Theta}^*_{km}\mathscr{C}^{(1)}\tilde{\Theta}_{k'm}\right)z_1^{k'}, \tag{7.35}$$

$$\begin{aligned}r\frac{dz_2^k}{dr}&-\left(c_1\bar{\omega}^2+rA\right)z_1^k+(rA+U-1)z_2^k\\&=-c_1\bar{\omega}^2\sum_{k'}\left(\int_{-1}^{1}d\mu\,\tilde{\Theta}^*_{km}\mathscr{C}^{(3)}\tilde{\Theta}_{k'm}\right)z_1^{k'}+\sum_{k'}\left(\int_{-1}^{1}d\mu\,\tilde{\Theta}^*_{km}\mathscr{C}^{(2)}\tilde{\Theta}_{k'm}\right)z_2^{k'},\end{aligned} \tag{7.36}$$

where

$$z_1^k=\frac{\xi_k^r(r)}{r},\qquad z_2^k=\frac{p_k'(r)}{\rho g r}, \tag{7.37}$$

the operators $\mathscr{C}^{(j)}$ are defined as

$$\mathscr{C}^{(1)}=\frac{m\nu}{1-\nu^2\mu^2}+\frac{\partial}{\partial\mu}\frac{\nu^2\mu(1-\mu^2)}{1-\nu^2\mu^2}, \tag{7.38}$$

$$\mathscr{C}^{(2)}=\frac{\nu^2\mu(1-\mu^2)}{1-\nu^2\mu^2}\frac{\partial}{\partial\mu}-\frac{m\nu}{1-\nu^2\mu^2}, \tag{7.39}$$

$$\mathscr{C}^{(3)}=\nu^2\frac{1-\mu^2}{1-\nu^2\mu^2}, \tag{7.40}$$

and the summation in Eqs. (7.35) and (7.36) should be over $k'\geq 0$ for $|\nu|<1$ and $-\infty<k'<+\infty$ for $|\nu|\geq 1$. Note that since $\mathscr{C}^{(j)}(-\mu)=\mathscr{C}^{(j)}(\mu)$ for $j=1,2,3$, the integral $\int_{-1}^{1}d\mu\,\Theta_{km}\mathscr{C}^{(j)}\Theta_{k'm}$ vanishes if the parities of the functions Θ_{km} and $\Theta_{k'm}$ are different. The terms on the right-hand side of Eqs. (7.35) and (7.36) lead to the mode coupling between modes associated with different λ_{km}s. It may be convenient to formally write the set of Eqs. (7.35) and (7.36) as

$$r\frac{d\mathbf{Z}}{dr}=\mathsf{A}\mathbf{Z},\qquad \mathbf{Z}=\begin{pmatrix}\mathbf{z}_1\\ \mathbf{z}_2\end{pmatrix}, \tag{7.41}$$

where $(\mathbf{z}_1)_k=z_1^k$ and $(\mathbf{z}_2)_k=z_2^k$, and A is the coefficient matrix.

If we consider the coupling between two modes associated with λ_{im} and λ_{jm}, we can approximate Eqs. (7.35) and (7.36) as

$$r\frac{d\mathbf{z}_1}{dr}=\left[\left(\frac{V}{\Gamma_1}-3\right)\mathsf{I}+\mathsf{C}^{(1)}\right]\mathbf{z}_1+\left(\frac{\Lambda}{c_1\bar{\omega}^2}-\frac{V}{\Gamma_1}\mathsf{I}\right)\mathbf{z}_2, \tag{7.42}$$

$$r\frac{d\mathbf{z}_2}{dr}=\left[\left(c_1\bar{\omega}^2+rA\right)\mathsf{I}-c_1\bar{\omega}^2\mathsf{C}^{(3)}\right]\mathbf{z}_1+\left[(1-rA-U)\mathsf{I}+\mathsf{C}^{(2)}\right]\mathbf{z}_2, \tag{7.43}$$

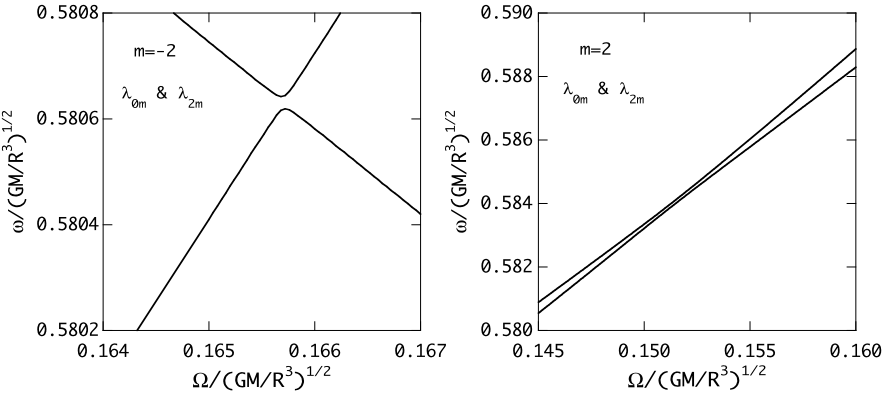

Fig. 7.2 Avoided crossing between two g-modes associated with λ_{0m} and λ_{2m} for $|m| = 2$, where the *left* ($m = -2$) and *right* ($m = 2$) *panels* are for prograde and retrograde modes, respectively. The eigenfrequency $\bar{\omega}$ is obtained by solving Eqs. (7.42) and (7.43) for the polytropic model of the index $n = 3$ and $\Gamma_1 = 5/3$

where I is the unit matrix,

$$\mathbf{z}_1 = \begin{pmatrix} z_1^i \\ z_1^j \end{pmatrix}, \qquad \mathbf{z}_2 = \begin{pmatrix} z_2^i \\ z_2^j \end{pmatrix}, \qquad \Lambda = \begin{pmatrix} \lambda_{im} & 0 \\ 0 & \lambda_{jm} \end{pmatrix}, \tag{7.44}$$

and

$$\mathsf{C}^{(p)} = \left(\int_{-1}^{1} d\mu \, \Theta_{km}^{*} \mathscr{C}^{(p)} \Theta_{k'm} \right) \tag{7.45}$$

for $p = 1, 2, 3$ and $k, k' = i$ and j.

As an example of mode coupling, we calculate avoided crossings between two g-modes associated with different λ_{km}s. Figure 7.2 plots the eigenfrequency $\bar{\omega}$ of $|m| = 2$ g-modes of λ_{0m} and λ_{2m} as a function of $\bar{\Omega}$ computed for the polytropic model of $n = 3$ and $\Gamma_1 = 5/3$, where we have solved Eqs. (7.42) and (7.43) as an eigenvalue problem for $\bar{\omega}$.

For mode coupling between adiabatic g-modes associated with λ_{im} and λ_{jm}, for example, [34] have derived a dispersion relation given by

$$\mathscr{D}_i(\omega)\mathscr{D}_j(\omega) = \varepsilon_{ij}, \tag{7.46}$$

where $\mathscr{D}_i(\omega) = \tan\Psi_i$, $\Psi_i = -\int_0^1 k_i \, dx + \chi_0$, $x \equiv r/R$, χ_0 is the phase constant depending on the structure of the star, $k_i = x^{-1}\sqrt{\lambda_{im}} N/\omega$ is the wavenumber in the radial direction for low-frequency g-modes associated with λ_{im}, and ε_{ij} is the coupling coefficient between the g-modes given by

$$\varepsilon_{ij} = \left(\int_0^1 \frac{dx}{x} \frac{|\lambda_{im}|^{1/2} G_{ij} \cos\chi_i \sin\chi_j + |\lambda_{jm}|^{1/2} G_{ji} \cos\chi_j \sin\chi_i}{|\lambda_{im}|^{1/4} |\lambda_{jm}|^{1/4}} \right)^2, \tag{7.47}$$

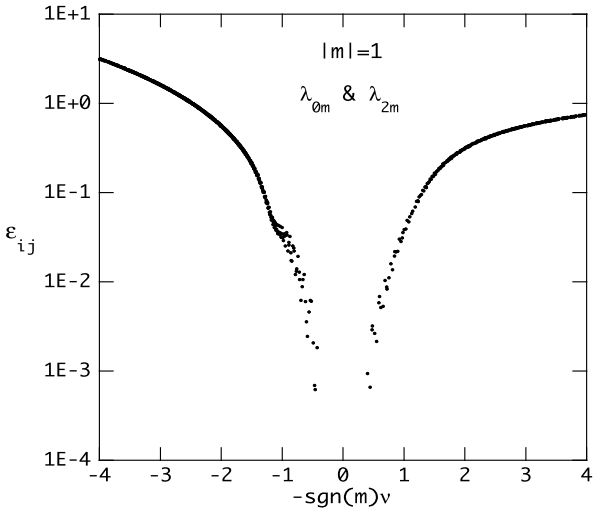

Fig. 7.3 Coupling coefficient ε_{ij} between g-modes of λ_{0m} and λ_{2m} for $|m| = 1$, where we have used the polytropic model of $n = 3$ and $\Gamma_1 = 5/3$

where $\chi_i = -\int_0^x k_i\, dx + \chi_0$, and G_{ij} is the matrix element that brings about coupling between the modes [34]. Note that since the matrix element G_{ij} is proportional to the ratio $\nu = 2\Omega/\omega$, the coupling coefficient ε_{ij} is proportional to ν^2, and $\varepsilon_{ij} \to 0$ as $\nu \to 0$. For given i and j, we may solve Eq. (7.46) for the frequency ω as a function of Ω. As an example, the coupling coefficient ε_{ij} between g-modes of λ_{0m} and λ_{2m} for $|m| = 1$ is plotted versus $-\mathrm{sgn}(m)\nu$ in Fig. 7.3, where $\chi_0 = 0$, and the polytropic model of the index $n = 3$ and $\Gamma_1 = 5/3$ is used. The coupling coefficient ε_{ij} is smaller for prograde modes than for retrograde modes, indicating that retrograde modes are more strongly influenced by mode coupling than prograde modes.

For frequency resonance at $\omega \simeq \omega_i \simeq \omega_j$ between two modes associated with λ_{im} and λ_{jm}, defining $\delta = \omega - \omega_i$ and $\Delta = \omega_i - \omega_j = \omega - \delta - \omega_j$, we may rewrite Eq. (7.46) as

$$\mathscr{D}_i(\omega_i + \delta)\mathscr{D}_j(\omega_j + \delta + \Delta) = \varepsilon_{ij}, \tag{7.48}$$

which leads to

$$\delta = -\frac{\Delta}{2} \pm \sqrt{\frac{\Delta^2}{4} + \frac{\varepsilon_{ij}}{(\partial\mathscr{D}_i/\partial\omega)(\partial\mathscr{D}_j/\partial\omega)}}, \tag{7.49}$$

where we have assumed $\mathscr{D}_i(\omega_i) = 0$, $\mathscr{D}_j(\omega_j) = 0$, $|\delta| \ll |\omega|$, and $|\Delta| \ll |\omega|$. Since $\varepsilon_{ij} > 0$, if $(\partial\mathscr{D}_i/\partial\omega)(\partial\mathscr{D}_j/\partial\omega) > 0$, we have avoided crossing at the resonance, while if $(\partial\mathscr{D}_i/\partial\omega)(\partial\mathscr{D}_j/\partial\omega) < 0$, we have instability as $|\Delta| \to 0$. If we regard $\omega(\partial\mathscr{D}/\partial\omega)$ as the mode energy, we have instability when the energies of the two modes have different signs at the resonance (e.g., [35]; see also [13]).

7.6 Series Expansion Method

We now discuss the series expansion method employed to calculate nonradial oscillations of uniformly rotating stars. To calculate low-frequency modes in rotating stars, we sometimes take account of only the Coriolis force, ignoring the effects of rotational deformation due to the centrifugal force [31, 33]. In this section, however, we describe the series expansion method that takes into consideration the rotational deformation of the models. To include the effects of rotational deformation in the series expansion method, we apply the Chandrasekhar–Milne expansion ([11, 12]; see also [50]) to nonrotating models, which could be a polytrope or a stellar model computed with a stellar evolution code. The detail of the formulation used to calculate nonadiabatic low-frequency modes in uniformly rotating stars is given in [30].

We employ a coordinate system (a, θ, ϕ) for a rotationally deformed star, where the coordinate a is regarded as the mean distance of an equipotential surface measured from the star center, and it is related to spherical polar coordinates (r, θ, ϕ) by

$$r = a\big[1 + \varepsilon(a, \theta)\big], \tag{7.50}$$

where

$$\varepsilon = \alpha(a) + \beta(a) P_2(\cos\theta) \tag{7.51}$$

with $P_2(\cos\theta) = (3\cos^2\theta - 1)/2$ being a Legendre polynomial. Assuming ε to be proportional to Ω^2, we calculate the functions $\alpha(a)$ and $\beta(a)$ by applying the Chandrasekhar–Milne expansion to the hydrostatic and Poisson equations for the star [11, 12]. The term α represents the spherical expansion, and β the deformation of the star due to rotation.

Note that we determine the function $\varepsilon(a, \theta)$ so that the physical quantity $f(r, \theta)$ in the equilibrium state of a uniformly rotating star depends only on the *mean* radial distance a, that is, $f(r, \theta) = \bar{f}(a)$. Assuming that $\bar{f}(a) = f_0(a)$ with f_0 being the equilibrium quantity of the nonrotating star, we define a mapping between the structures of the rotating and nonrotating stars in terms of the mean radius a. Applying the assumption to the gravitational potential and making use of the Chandrasekhar–Milne expansion, we can determine the function $\varepsilon(a, \theta)$.

In the coordinate system $(x^j) = (x^a, x^\theta, x^\phi) = (a, \theta, \phi)$, the metric tensor g_{ij} is written as

$$\begin{aligned} ds^2 &= g_{ij}\, dx^i\, dx^j \\ &= (1 + 2\varepsilon)\big(da^2 + a^2\, d\theta^2 + a^2 \sin^2\theta\, d\phi^2\big) \\ &\quad + 2a\frac{\partial \varepsilon}{\partial a}\, da^2 + 2a\frac{\partial \varepsilon}{\partial \theta}\, da\, d\theta + O\big(\bar{\Omega}^4\big), \end{aligned} \tag{7.52}$$

with which the linearized Euler's equation, for example, may be given by (e.g., [60])

$$-\omega^2 \delta x_i + \nabla_i\left(\frac{p'}{\rho} + \Phi'\right) + A_i \frac{p'}{\rho} + \delta x^j A_j \frac{1}{\rho}\nabla_i p + 2i\omega\Omega \delta x^j \nabla_j \phi_i = 0, \tag{7.53}$$

where the repeated indices imply summation over the indices from 1 to 3, $A_i = \nabla_i \ln \rho - \Gamma_1^{-1} \nabla_i \ln p$, $(\phi^i) = (0, 0, 1)$ is the rotational Killing vector, ∇_j is the covariant derivative with respect to the coordinate x^j, $\nabla_j p = \partial p / \partial x^j$, $\nabla_j \phi_k = \partial \phi_k / \partial x^j - \Gamma^l_{jk} \phi_l$ with Γ^l_{jk} being the Christoffel symbol, $(\delta x^j) = (\delta x^a, \delta x^\theta, \delta x^\phi) = (\delta a, \delta\theta, \delta\phi)$ is the Lagrangian variation of the coordinates, and $\delta x_i = g_{ij} \delta x^j$. Here, the last term on the left-hand side of Eq. (7.53) represents the Coriolis term:

$$\delta x^j \nabla_j \phi_a = -\left(1 + 2\varepsilon + a \frac{\partial \varepsilon}{\partial a}\right) a \sin^2\theta \delta x^\phi + O\left(\bar{\Omega}^4\right), \tag{7.54}$$

$$\delta x^j \nabla_j \phi_\theta = -\left[(1 + 2\varepsilon)\cos\theta + \frac{\partial \varepsilon}{\partial \theta} \sin\theta\right] a^2 \sin\theta \delta x^\phi + O\left(\bar{\Omega}^4\right), \tag{7.55}$$

$$\begin{aligned} \delta x^j \nabla_j \phi_\phi = &-\left(1 + 2\varepsilon + a \frac{\partial \varepsilon}{\partial a}\right) a \sin^2\theta \delta x^a \\ &- \left[(1 + 2\varepsilon)\cos\theta + \frac{\partial \varepsilon}{\partial \theta} \sin\theta\right] a^2 \sin\theta \delta x^\theta + O\left(\bar{\Omega}^4\right). \end{aligned} \tag{7.56}$$

Note that the displacement vector $\boldsymbol{\xi}$, in the noncoordinate basis, is given by $(\xi^a, \xi^\theta, \xi^\phi) = (\delta a, a\delta\theta, a \sin\theta \delta\phi)$. Because of the Coriolis term $2i\omega\Omega \delta x^j \nabla_j \phi_i$ that includes the deformation effects, the oscillation frequency $\bar{\omega}$ will be consistent up to the third order in $\bar{\Omega}$, which makes it possible to calculate the oscillation frequency of r-modes correct to the order of $\bar{\Omega}^3$.

Assuming that the equilibrium state of a uniformly rotating star is axisymmetric, we approximate small amplitude oscillations of the star using a finite series expansion in terms of spherical harmonic functions $Y^m_l(\theta, \phi)$ with different ls for a given m. For a given azimuthal wavenumber m, the displacement vector $\boldsymbol{\xi}(a, \theta, \phi, t)$ is given by

$$\frac{\xi^a}{a} = e^{i\omega t} \sum_{j=1}^{j_{\max}} S_{l_j}(a) Y^m_{l_j}(\theta, \phi), \tag{7.57}$$

$$\frac{\xi^\theta}{a} = e^{i\omega t} \sum_{j=1}^{j_{\max}} \left[H_{l_j}(a) \frac{\partial}{\partial \theta} Y^m_{l_j}(\theta, \phi) + T_{l'_j}(a) \frac{1}{\sin\theta} \frac{\partial}{\partial \phi} Y_{l'_j}(\theta, \phi)\right], \tag{7.58}$$

$$\frac{\xi^\phi}{a} = e^{i\omega t} \sum_{j=1}^{j_{\max}} \left[H_{l_j}(a) \frac{1}{\sin\theta} \frac{\partial}{\partial \phi} Y^m_{l_j}(\theta, \phi) - T_{l'_j}(a) \frac{\partial}{\partial \theta} Y_{l'_j}(\theta, \phi)\right], \tag{7.59}$$

and p' is given by

$$p'(a, \theta, \phi, t) = e^{i\omega t} \sum_{j=1}^{j_{\max}} p'_{l_j}(a) Y^m_{l_j}(\theta, \phi), \tag{7.60}$$

where $l_j = |m| + 2(j-1)$ and $l'_j = l_j + 1$ for even modes, and $l_j = |m| + 2j - 1$ and $l'_j = l_j - 1$ for odd modes, where $j = 1, 2, \ldots, j_{\max}$, and $j_{\max}$ is the length of the expansions. Note that the surface angular pattern of p' is symmetric (antisymmetric) with respect to the equator for even (odd) modes.

Substituting these expansions into the linearized basic equations, we obtain a finite set of coupled first-order LODEs for the expansion coefficients $S_{l_j}(a)$ and $p'_{l_j}(a)$, which may be formally given, for example, for adiabatic oscillations in the Cowling approximation, as

$$a\frac{d\mathbf{Y}}{da} = \mathsf{C}\mathbf{Y}, \quad \mathbf{Y} = \begin{pmatrix} \mathbf{y}_1 \\ \mathbf{y}_2 \end{pmatrix}, \tag{7.61}$$

where

$$\mathbf{y}_1 = \begin{pmatrix} S_{l_1}/a \\ S_{l_2}/a \\ \vdots \\ S_{l_{j_{\max}}}/a \end{pmatrix}, \qquad \mathbf{y}_2 = \begin{pmatrix} p'_{l_1}/\rho g a \\ p'_{l_2}/\rho g a \\ \vdots \\ p'_{l_{j_{\max}}}/\rho g a \end{pmatrix}, \tag{7.62}$$

and C is the coefficient matrix. For given m and Ω, we solve the differential equation (7.61) as an eigenvalue problem of ω by imposing appropriate boundary conditions at the center and surface of the star. The linear differential equations for nonadiabatic oscillations as well as the boundary conditions are given in [30]. Since we assume that the perturbed quantities are proportional to $e^{\mathrm{i}(m\phi+\omega t)}$, we regard modes having negative ω_{I} as being pulsationally unstable, where $\omega_{\mathrm{I}} \equiv \mathrm{Im}(\omega)$ is the imaginary part of ω. Note that when $\omega_{\mathrm{R}} \equiv \mathrm{Re}(\omega) > 0$, modes associated with negative (positive) m are prograde (retrograde) modes seen in the co-rotating frame of the star.

If we neglect the rotational deformation and assume that $j_{\max} \to \infty$, the differential equation (7.61) should be equivalent to the differential equation (7.41), and there should exist a one-to-one correspondence between the vectors $\mathbf{Y}$ and $\mathbf{Z}$ such that $\mathbf{Z} = \mathsf{B}\mathbf{Y}$ with B being a transformation matrix.

7.7 Stability of g-Modes and r-Modes in Rotating SPB Stars

It is well known that low-frequency g- and r-modes in SPB stars are excited by the opacity κ mechanism associated with the metal opacity bump located in the temperature region of $T \sim 2 \times 10^5$ K (e.g., [18, 19, 21]; see, e.g., [28, 53] for r-modes). As an optimal condition for the opacity mechanism of excitation, we may say that the κ-mechanism is most effective when the thermal-timescale at the Fe opacity bump is comparable to pulsation periods in the corotating frame (see, e.g., [21]), and for the instability, this excitation must exceed the total amount of damping occurring in the interior. In this section we present some results of the stability analysis of SPB stars obtained by applying the series expansion method to nonadiabatic oscillations of the

stars. For the stability analysis discussed in this section, we employ the Cowling approximation, neglecting the Eulerian perturbation of the gravitational potential, and we ignore the effect of rotational spherical expansion on the oscillation, that is, we set $\alpha = 0$ in Eq. (7.51). For the length of the series expansions, we use $j_{\max} = 10$. Stellar models used for modal analysis are calculated with a standard stellar evolution code using the OPAL opacity [23, 24]. No effects of rotation are included in the stellar evolution calculation (but see, e.g., [58]).

For slow rotation, we can treat $\bar{\Omega}$ as a small parameter to expand the oscillation frequency ω of a nonadiabatic mode as $\bar{\omega}(\bar{\Omega}) = \bar{\omega}_0 + mC_1\bar{\Omega} + C_2\bar{\Omega}^2 + \cdots$, where ω_0 is the oscillation frequency of the mode for the nonrotating star. Here, the coefficients C_1 and C_2 as well as ω_0 are complex for the nonadiabatic mode, C_1 stands for the Coriolis effects, and C_2 for the effects of both the centrifugal and the Coriolis forces. The real part $C_{1\mathrm{R}}$ of C_1 for a nonadiabatic mode is approximately equal to the coefficient C_1 given by (7.3) for the corresponding adiabatic mode. We note that negative (positive) $C_{1\mathrm{I}} = \mathrm{Im}(C_1)$ means that the Coriolis force due to slow rotation has a destabilizing (stabilizing) effect on retrograde modes with $m > 0$ and a stabilizing (destabilizing) effect on prograde modes with $m < 0$, and that a negative (positive) $C_{2\mathrm{I}}$ means a destabilizing (stabilizing) effect on both prograde and retrograde modes. For a given m, we obtain the complex coefficients C_1 and C_2 numerically by computing the eigenfrequency ω of a mode for three different rotation frequencies, e.g., $\bar{\Omega} = 0$, 10^{-3}, and -10^{-3}. We have confirmed that the complex coefficient C_1 thus computed is in good agreement with that obtained using the method by [10]. Examples of the complex coefficients C_1 and C_2 are given, e.g., in [2] for $4M_\odot$ main sequence stars.

We now examine the stability of g- and r-modes in B stars rotating at finite $\bar{\Omega}$. Figure 7.4 plots the growth rate $\eta \equiv -\omega_{\mathrm{I}}/\omega_{\mathrm{R}}$ of unstable g- and r-modes of the $4M_\odot$ ZAMS model versus $-\mathrm{sgn}(m)\bar{\omega}_{\mathrm{R}}$ for $\bar{\Omega} = 0.01$ and 0.4, where $\mathrm{sgn}(m) = m/|m|$, and the modes of $l = |m|$ ($l = |m| + 1$) stand for even (odd) g-modes and those of $l' = m$ stand for odd r-modes. For $\bar{\Omega} = 0.01$, many low l and high radial order g-modes are found unstable, and the growth rate η as a function of $\bar{\omega}_{\mathrm{R}}$ is almost symmetric about the axis of $\bar{\omega}_{\mathrm{R}} = 0$. Note also that the unstable g-modes with $(|m|, l) = (1, 2)$ and $(2, 2)$ have almost the same complex frequencies. For $\bar{\Omega} = 0.4$, however, the symmetry of the frequency spectra about the axis $\bar{\omega}_{\mathrm{R}} = 0$ is lost, and a number of low-frequency retrograde g-modes with $\bar{\omega}_{\mathrm{R}} \lesssim 0.5$ are found stable, although most of the prograde g-modes remain unstable. Instead of the stabilized retrograde g-modes, there appear many unstable odd r-modes of $l' = m = 1$ and 2 in the frequency region of $\bar{\omega}_{\mathrm{R}} \lesssim 0.5$. Note that the upper limit of the r-mode frequency is given by $\bar{\omega} = 2m\bar{\Omega}/[l'(l'+1)]$, which is 0.4 and 4/15 for odd r-modes of $l' = m = 1$ and 2 for $\bar{\Omega} = 0.4$.

Figure 7.5 plots the growth rate η versus $-\mathrm{sgn}(m)\bar{\omega}_{\mathrm{R}}$ for low l unstable g and r-modes of a slightly evolved $4M_\odot$ main sequence model, whose effective temperature T_{eff} is lower than that of the ZAMS model. For $\bar{\Omega} = 0.01$, the frequency spectra of low l g-modes, the distribution of which is again almost symmetric about the axis of $\bar{\omega}_{\mathrm{R}} = 0$, become dense because of the enhanced Brunt–Väisälä frequency N in the interior and the number of unstable g-modes has increased markedly compared to that for the ZAMS model. Rapid rotation tends to stabilize the retrograde

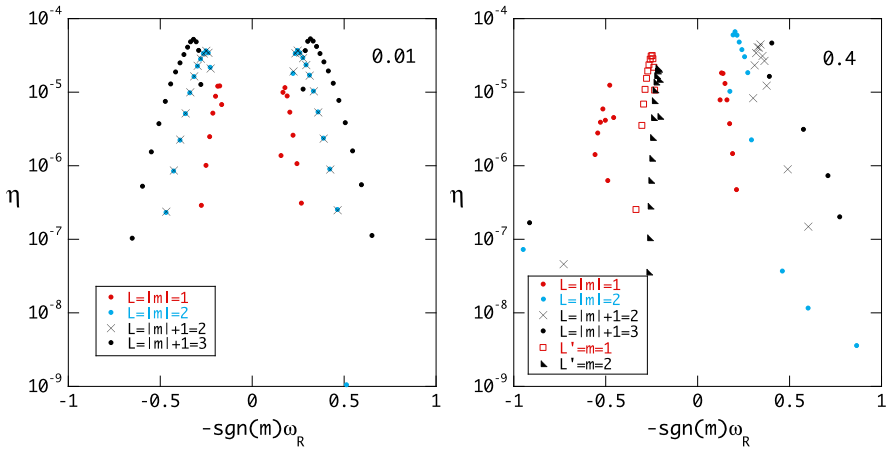

Fig. 7.4 Growth rate $\eta \equiv -\omega_{\rm I}/\omega_{\rm R}$ versus $-{\rm sgn}(m)\bar{\omega}_{\rm R}$ for unstable g- and r-modes of the $4M_\odot$ ZAMS model of $X = 0.7$ and $Z = 0.02$, where the modes of $l = |m|$ ($l = |m| + 1$) stand for even (odd) g-modes and those of $l' = m$ stand for r-modes. The model parameters are $\log(L/L_\odot) = 2.371$ and $\log(T_{\rm eff}) = 4.1654$. The *left* and *right panels* are for the cases of $\bar{\Omega} = 0.01$ and 0.4, respectively. Modes with $m < 0$ ($m > 0$) are prograde (retrograde) modes

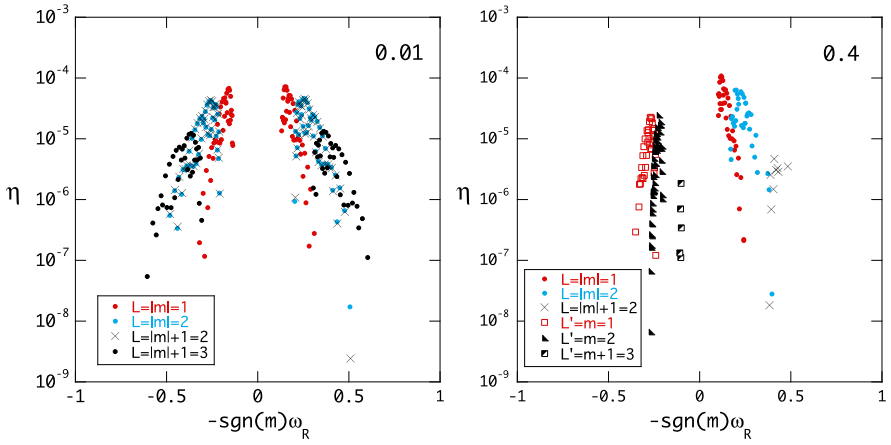

Fig. 7.5 Same as Fig. 7.4 but for a slightly evolved $4M_\odot$ main sequence model, where the model parameters are $\log(L/L_\odot) = 2.564$, $\log(T_{\rm eff}) = 4.0836$, and $X_c = 0.1076$. Note that the modes of $l' = m$ ($l' = m + 1$) are odd (even) r-modes

g-modes, and, in fact, almost all of the retrograde g modes that are unstable at $\bar{\Omega} = 0.01$ are stabilized at $\bar{\Omega} = 0.4$ for the evolved main sequence model. This stabilization effect on retrograde g-modes is stronger for main sequence models with lower effective temperatures. The stabilization of retrograde low l g-modes at $\bar{\Omega} = 0.4$ is not complete for the $4M_\odot$ ZAMS model compared to the stabilization obtained for the evolved model having lower effective temperature.

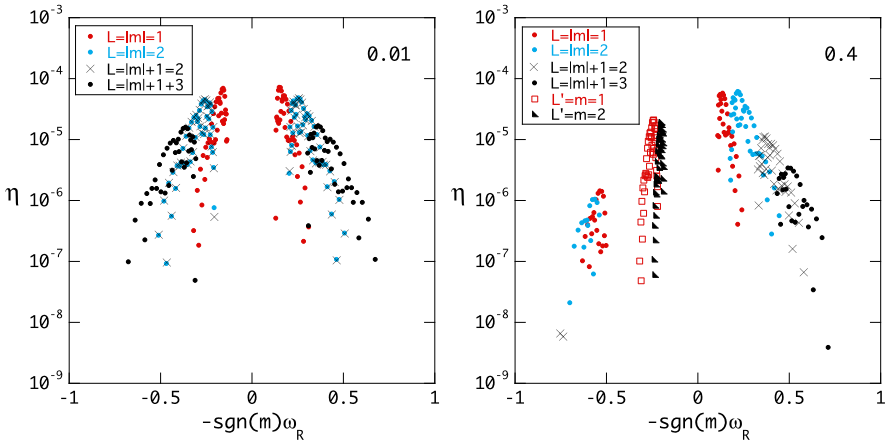

Fig. 7.6 Same as Fig. 7.5 but for the growth rates calculated by using the traditional approximation applied to nonadiabatic oscillations, where no effects of rotational deformation are included

Applying the traditional approximation to nonadiabatic oscillations (see [52]), we have carried out a similar stability analysis for the evolved $4M_\odot$ main sequence model. The result of the analysis is given by Fig. 7.6, in which the growth rate η is plotted versus $-\mathrm{sgn}(m)\bar{\omega}_\mathrm{R}$ for low l g- and r-modes for the cases of $\bar{\Omega} = 0.01$ and 0.4. Note that no effects of rotational deformation are included under the traditional approximation. It is interesting to note that for $\bar{\Omega} = 0.01$, the two methods of calculation yield quite similar results for the pulsational stability of low l g-modes. For the case of rapid rotation such as $\bar{\Omega} = 0.4$, however, there arise appreciable differences between the stability results obtained by the two methods of calculation. Although the series expansion method indicates that almost all retrograde low l g-modes are stable at $\bar{\Omega} = 0.4$, the traditional approximation suggests that some of the retrograde g-modes remain unstable. This tendency is also found for the prograde g-modes, that is, although almost all odd prograde g-modes of $l = 2$ and 3 are found stable in the series expansion method, many odd prograde g-modes remain unstable in the traditional approximation. Note that the stability results for the r-modes are almost the same between the two methods of calculation, except that no even r-modes of $l' = m + 1 = 3$ are found unstable under the traditional approximation.

The difference in the stability results between the two methods of calculation is attributable to whether or not the effects of linear mode coupling are accounted for in the mode calculation. In the nonadiabatic analysis under the traditional approximation, no effects of mode coupling between low-frequency g-modes associated with different λ_{km}s are taken into account. The series expansion method, however, inevitably includes the coupling effects (e.g., [2]). This mode coupling effect can be important in determining the stability of modes in rapidly rotating stars. In Fig. 7.7, $\tau \equiv w(R)/\int_0^R |dw/dr|\,dr$ (with $w(r)$ being the work integral) is plotted versus $\bar{\omega}_\mathrm{R}$ of low-frequency g-modes associated with different λ_{km}s computed under the

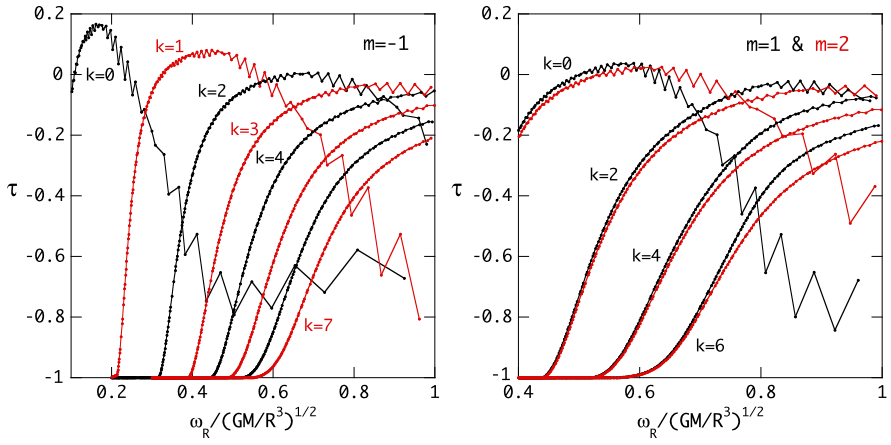

Fig. 7.7 $\tau \equiv w(R)/\int_0^R |dw/dr|\,dr$ with $w(r)$ being the work integral plotted as a function of $\bar{\omega}_{\rm R}$ for low-frequency g-modes associated with different λ_{km}s for the evolved $4M_\odot$ main sequence model, where the *left* and *right panels* are for prograde and retrograde modes, respectively. Nonadiabatic g-modes are calculated under the traditional approximation

traditional approximation. Here, unstable (stable) modes have positive (negative) τ, and $\tau = -1$ implies no excitation regions in the interior for the mode. As indicated by the figure, unstable retrograde g-modes of λ_{0m} are in a sea of stable g-modes with dense frequency spectra associated with $\lambda_{2m}, \lambda_{4m}, \ldots$, and it is likely that the unstable g-modes are stabilized if they are strongly coupled with the stable g-modes. Almost the same coupling effects occur to unstable odd prograde g-modes of λ_{1m}, which are stabilized as a result of mode coupling with stable odd g-modes, as suggested by comparing Figs. 7.5 and 7.6. Although unstable sectoral prograde g-modes of λ_{0m} are also in a sea of stable g-modes of λ_{km} with $k \geq 2$, the stability of the sectoral modes is less affected by the coupling since the coupling is not strong enough, where the strength of the coupling may be estimated by the coupling coefficient ε_{ij} defined by Eq. (7.47). As shown by Fig. 7.3 for the polytropic model and by [2] for stars with a convective core, ε_{ij} for sectoral prograde modes of λ_{0m} is smaller than that for retrograde modes and that for nonsectoral prograde modes.

For low-frequency modes observed in rapidly rotating B type stars like SPBe stars, retrograde g-modes are found to be almost completely stabilized by the rapid rotation, and prograde g-modes, which remain unstable, show, in an inertial frame, frequency grouping according to the azimuthal wavenumber m, since $\sigma = \omega - m\Omega \approx -m\Omega$ for the rapid rotation [9, 46, 58]. Fitting theoretical model calculations to observed frequencies, it is possible to obtain the information about the rotation speed of the oscillating stars (e.g., [9]). Since the stability of r-modes, which are retrograde modes, is hardly affected by rapid rotation, the r-modes could be responsible for some of very-long-period pulsations observed in some SPBe stars.

7.8 Parametric Instability: Weakly Nonlinear Oscillation

To estimate the amplitudes of low-frequency modes excited in SPB stars, weakly nonlinear theory of oscillation can be useful. Here, we assume the parametric instability by nonlinear coupling between three oscillation modes, that is, one unstable mode (parent mode) and two stable modes (daughter modes), as the mechanism of the amplitude saturation of the modes. Nonlinear evolution of small-amplitude oscillation modes in a uniformly rotating star may be modeled by the oscillation equation with nonlinear terms:

$$\ddot{\boldsymbol{\zeta}} + \mathsf{B}(\dot{\boldsymbol{\zeta}}) + \mathsf{C}(\boldsymbol{\zeta}) = \mathbf{a}^{(2)}(\boldsymbol{\zeta}, \boldsymbol{\zeta}), \tag{7.63}$$

where $\dot{\boldsymbol{\zeta}} = d\boldsymbol{\zeta}/dt$, $\ddot{\boldsymbol{\zeta}} = d^2\boldsymbol{\zeta}/dt^2$, $\mathsf{B}(\boldsymbol{\zeta}) = 2\boldsymbol{\Omega} \times \boldsymbol{\zeta}$, and C is the differential operator. Here, $\mathbf{a}^{(2)}(\boldsymbol{\zeta}, \boldsymbol{\zeta})$ represents a collection of nonlinear terms of second order in $\boldsymbol{\zeta}$, and the ith component of $\mathbf{a}^{(2)}$ is given by (see, e.g., [48])

$$a_i^{(2)}(\boldsymbol{\zeta}, \boldsymbol{\zeta}) = -\frac{1}{\rho}\nabla_j\left\{p\left[(\Gamma_1 - 1)\Pi_i^j + \Xi_i^j + \Psi\delta_i^j\right]\right\} - \frac{1}{2}\zeta^k\zeta^l\nabla_k\nabla_l\nabla_i\Phi, \tag{7.64}$$

where ∇_j denotes the covariant derivative, $\Pi_i^j = (\nabla_i\zeta^j)\nabla\cdot\boldsymbol{\zeta}$, $\Xi_i^j = (\nabla_i\zeta^k)(\nabla_k\zeta^j)$, $\Psi = (1/2)\Pi[(\Gamma_1 - 1)^2 + \partial\Gamma_1/\partial\ln\rho] + (1/2)(\Gamma_1 - 1)\Xi$, $\Pi = \delta_j^i\Pi_i^j = (\nabla\cdot\boldsymbol{\zeta})^2$, $\Xi = \delta_j^i\Xi_i^j = (\nabla_j\zeta^k)(\nabla_k\zeta^j)$, δ_j^i is the Kronecker delta, and Φ is the gravitational potential. Note that we have applied the Cowling approximation, neglecting the Eulerian perturbation of the gravitational potential.

Following [48], we use the eigenvalues ω and eigenfunctions $\boldsymbol{\xi}$ satisfying the linear oscillation equation given by $-\omega^2\boldsymbol{\xi} + \mathrm{i}\omega\mathsf{B}(\boldsymbol{\xi}) + \mathsf{C}(\boldsymbol{\xi}) = 0$ to expand the displacement vector $\boldsymbol{\zeta}(\mathbf{x}, t)$ and its time derivative $\dot{\boldsymbol{\zeta}}(\mathbf{x}, t)$ in the nonlinear equation:

$$\begin{bmatrix}\boldsymbol{\zeta}(\mathbf{x}, t)\\ \dot{\boldsymbol{\zeta}}(\mathbf{x}, t)\end{bmatrix} = \sum_A c_A(t)\begin{bmatrix}\boldsymbol{\xi}_A(\mathbf{x})\\ \mathrm{i}\omega_A\boldsymbol{\xi}_A(\mathbf{x})\end{bmatrix}, \tag{7.65}$$

for which $\sum_A(\dot{c}_A - \mathrm{i}\omega_A c_A)\boldsymbol{\xi}_A(\mathbf{x}) = 0$, where the subscript A stands for a collection of numbers such as harmonic degree l, azimuthal order m, and the radial order n used to identify a linear mode. Substituting expansion (7.65) into the left-hand side of Eq. (7.63), substituting the expansion $\boldsymbol{\zeta}(\mathbf{x}, t) = \sum_B c_B^*(t)\boldsymbol{\xi}_B^*(\mathbf{x})$ into $\mathbf{a}^{(2)}(\boldsymbol{\zeta}, \boldsymbol{\zeta})$, making a scaler product between $\boldsymbol{\xi}_A^*$ and Eq. (7.63), and integrating over the volume of the star, we obtain after some manipulation

$$\dot{\hat{c}}_A = -\mathrm{i}\omega_A\sum_{B,C}\left(\frac{\kappa_{ABC}^*}{\varepsilon_A}\right)\hat{c}_B^*(t)\hat{c}_C^*(t)e^{-\mathrm{i}\Delta\omega t}, \tag{7.66}$$

where $\hat{c}_A(t) = c_A(t)\exp(-\mathrm{i}\omega_A t)$, $c_A(t) = \langle\boldsymbol{\xi}_A, \omega_A\boldsymbol{\zeta}(t) - \mathrm{i}\dot{\boldsymbol{\zeta}}(t) - \mathrm{i}\mathsf{B}(\boldsymbol{\zeta}(t))\rangle/b_A$ with $b_A = 2\omega_A\langle\boldsymbol{\xi}_A, \boldsymbol{\xi}_A\rangle - \langle\boldsymbol{\xi}_A, \mathrm{i}\mathsf{B}(\boldsymbol{\xi}_A)\rangle$, $\kappa_{ABC} = \langle\boldsymbol{\xi}_A^*, \mathbf{a}^{(2)}(\boldsymbol{\xi}_B, \boldsymbol{\xi}_C)\rangle$, $\varepsilon_A = \omega_A b_A$, and $\Delta\omega = \omega_A + \omega_B + \omega_C$, where $\langle\boldsymbol{\xi}_A, \boldsymbol{\xi}_B\rangle = \int d^3\mathbf{x}\,\rho(\mathbf{x})\boldsymbol{\xi}_A^*(\boldsymbol{x})\cdot\boldsymbol{\xi}_B(\mathbf{x})$, and we have

used a modified orthogonal relation given by $\langle \boldsymbol{\xi}_A, \mathrm{i}\mathsf{B}(\boldsymbol{\xi}_B)\rangle - (\omega_A + \omega_B)\langle \boldsymbol{\xi}_A \boldsymbol{\xi}_B\rangle = 0$ for $A \neq B$.

For nonlinear mode coupling between three modes A, B, and C, we obtain

$$\dot{\hat{c}}_A = -\gamma_A \hat{c}_A - \mathrm{i}\omega_A \eta^*_{ABC} \hat{c}^*_B(t)\hat{c}^*_C(t)e^{-\mathrm{i}\Delta\omega t}, \tag{7.67}$$

and two similar equations for $\dot{\hat{c}}_B$ and $\dot{\hat{c}}_C$, where we have included the effects of linear destabilization ($\gamma < 0$) and stabilization ($\gamma > 0$) of the modes, and we have normalized the eigenfunctions $\boldsymbol{\xi}_A$, $\boldsymbol{\xi}_B$, and $\boldsymbol{\xi}_C$ such that $\varepsilon_A = \varepsilon_B = \varepsilon_C = GM^2/R$, which leads to $\kappa_{ABC}/\varepsilon_A = \kappa_{BCA}/\varepsilon_B = \kappa_{CAB}/\varepsilon_C \equiv \eta_{ABC}/2$. In the following, we regard mode A as the parent mode and modes B and C as the daughter modes.

Parametric instability between three modes occurs when the amplitude of the parent mode, $|c_A|$, exceeds the critical amplitude given by (e.g., [3, 17])

$$|c_{A:c}|^2 = \frac{1}{|\eta_{ABC}|^2 Q_B Q_C}\left[1 + \left(\frac{\Delta\omega}{\gamma_B + \gamma_C}\right)^2\right], \tag{7.68}$$

where $Q_j = -\omega_j/\gamma_j$. The equilibrium amplitude of the parent mode is then given by

$$|c_{A:e}|^2 = \frac{1}{|\eta_{ABC}|^2 Q_B Q_C}\left[1 + \left(\frac{\Delta\omega}{\Delta\gamma}\right)^2\right], \tag{7.69}$$

and those of the daughter modes by $|c_{B:e}|^2 = |c_{A:e}|^2 Q_B/Q_A$, $|c_{C:e}|^2 = |c_{A:e}|^2 Q_C/Q_A$, where $\Delta\gamma = \gamma_A + \gamma_B + \gamma_C$. Here, we have assumed that $Q_B Q_C > 0$, $Q_C Q_A > 0$, and $Q_A Q_B > 0$, that is, the signs of ω_B and ω_C are the same but are different from that of ω_A, because the parent mode A is assumed unstable ($\gamma_A < 0$) and the daughter modes B and C stable ($\gamma_B > 0$ and $\gamma_C > 0$). Since ω_B and ω_C have the same sign, in order to obtain a resonant coupling satisfying $\Delta\omega \sim 0$, we need $|\omega_B| \lesssim |\omega_A|$ and $|\omega_C| \lesssim |\omega_A|$. We use the condition $\Delta\gamma > 0$ as the criteria for an effectively stable equilibrium state of three-mode coupling (e.g., [3, 59]).

One of the selection rules giving nonzero coupling coefficient $\eta_{ABC} \neq 0$ is

$$m_A + m_B + m_C = 0, \tag{7.70}$$

and another selection rule may be simply stated that the coupling coefficient η_{ABC} is nonzero only when the mode triad is composed of three even modes or of one even mode and two odd modes (e.g., [48]). For $m_A < 0$, for example, we have two cases because of the selection rule (7.70), that is, both m_B and m_C are positive or one of m_B and m_C is negative so that $m_B m_C < 0$. In the former case, if the parent mode is a prograde (retrograde) mode, the two daughter modes are prograde (retrograde) modes. In the latter case, however, if the parent mode is a prograde mode having $\omega_A > 0$, the daughter mode with $m < 0$ is a retrograde mode since $\omega_B < 0$ and $\omega_C < 0$. On the other hand, if the parent mode is a retrograde mode having $\omega_A < 0$, the daughter mode with $m < 0$ is a prograde mode since $\omega_B > 0$ and $\omega_C > 0$.

To evaluate the coupling coefficient η_{ABC}, we use the eigenfunctions ξ_A and the eigenfrequencies ω_A computed under the traditional approximation and the Cowling

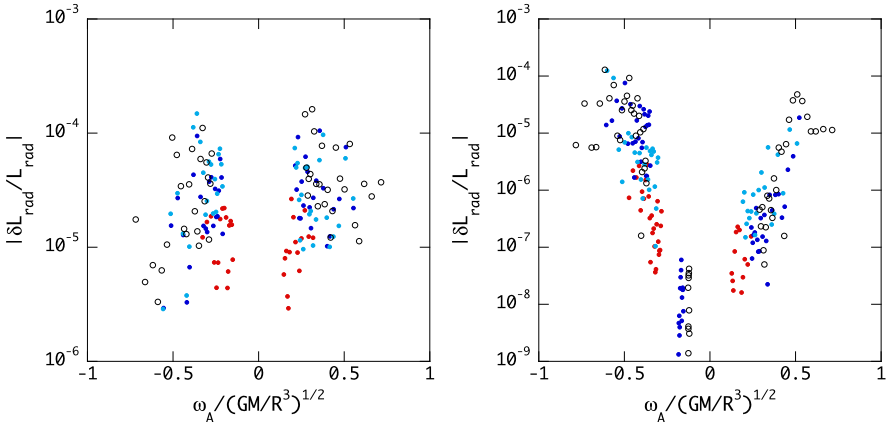

Fig. 7.8 Amplitudes $|\delta L_{\rm rad}/L_{\rm rad}|$ of unstable parent modes of a $4M_\odot$ main sequence model as a function of $\bar{\omega}_A$ for $\bar{\Omega} = 0.01$ (*left panel*) and $\bar{\Omega} = 0.2$ (*right panel*), where the *red*, *blue*, *cyan dots* and *black open circle* stand for the parent modes of $(l_A, m_A) = (1, -1), (2, -1), (2, -2)$, and $(3, -2)$, respectively. For $m_A < 0$, prograde (retrograde) modes have positive (negative) $\bar{\omega}_A$

approximation for adiabatic modes, and the linear damping and growth rates γ are obtained by nonadiabatic mode calculation, where we have employed the method of calculation given by [52] for both adiabatic and nonadiabatic modes. The displacement vector $\boldsymbol{\xi}$ in the traditional approximation is given by Eqs. (7.22) to (7.24) for adiabatic modes. The angular dependence $\Theta_{km}(\mu; \nu)$ is given by the solution to the Laplace tidal equation (7.18), and we have carried out numerical evaluation of integrals like $\int \Theta_{k_A m_A} \Theta_{k_B m_B} \Theta_{k_C m_C} \, d\mu$ for the coupling coefficient η_{ABC}. The details of the method of calculation for the coupling coefficient under the traditional approximation are given in [29].

For a given unstable parent mode A, there are numerous possible combinations of a pair of stable daughter modes B and C. Among the combinations, we choose the one that gives the smallest critical amplitude $|c_{A:c}|$ for the parent mode A. Since we can only prepare a limited set of daughter modes to calculate $|c_{A:c}|$, the critical amplitude thus determined should be regarded as an upper limit for the parent mode.

An example of amplitude calculations carried out for low-frequency unstable modes of a $4M_\odot$ main sequence model with $\log(T_{\rm eff}) = 4.142$ and $\log(L/L_\odot) = 2.470$ and with the initial abundance $(X, Z) = (0.7, 0.02)$ is given in Fig. 7.8, where the amplitude $|\delta L_{\rm rad}/L_{\rm rad}|$ of the parent (unstable) g- and r-modes is plotted versus $\bar{\omega}_{\rm R}$ for the cases of $\bar{\Omega} = 0.01$ and 0.2. Here, we use a set of daughter (stable) modes having $|m| = 0$ to $|m| = 5$, and $l = |m|$ (even modes) and $l = |m| + 1$ (odd modes) in the frequency interval $0.05 \le \bar{\omega} \le 2$, where we have also included stable r-modes in the set for the case of $\bar{\Omega} = 0.2$. As shown by the figure, the distribution of the amplitudes as a function of $\bar{\omega}_A$ for $\bar{\Omega} = 0.01$ is almost symmetric about the axis of $\bar{\omega}_A = 0$, although the deviation from symmetry is already appreciable. Rapid rotation significantly modifies the amplitude distribution of the parent modes. For $\bar{\Omega} = 0.2$, the symmetry of the distribution about $\bar{\omega}_A = 0$ is lost, and there appear,

on the retrograde side, almost vertical sequences of points for the parent r-modes, which have very small amplitudes. For both of the cases, the maximum amplitude is of the order of 10^{-4}, which may be consistent with observed low-amplitude modes raging from $\sim$0.1 mmag to $\sim$1 mmag (e.g., [5, 15, 22, 43]). Although the amplitudes determined by the parametric instability may depend on the evolutionary stages of the stars, considering that the amplitude we obtain should be regarded as an upper limit for the parent mode, the maximum amplitudes we obtain may be too small to explain observed high-amplitude modes. For observed amplitudes exceeding $\sim$1 mmag, we have to look for possibilities other than the parametric instability to provide amplitude saturation mechanisms which would allow the larger saturation amplitudes. For example, nonlinear couplings between a parent mode and many pairs of daughter modes, and between a daughter mode, which may be parametrically excited, and granddaughter modes (e.g., [26]) could be among such possibilities. It is also necessary to lift the traditional approximation in order to correctly evaluate the growth and damping rates γ of low-frequency modes and the coupling coefficient η_{ABC} between the modes.

7.9 Conclusion

We have reviewed the properties of low-frequency oscillations in uniformly rotating stars. The methods of analysis for the low-frequency modes discussed include the perturbation analysis for slow rotation, traditional approximation, and series expansion method. We also discussed linear mode coupling between low-frequency modes under the traditional approximation and suggested that the mode coupling can be important in determining the pulsational stability of the modes. We presented some results of the stability analysis of low-frequency g- and r-modes in rotating SPB stars obtained by the series expansion method. We also suggested that the weak nonlinear theory of oscillation applied to low-frequency modes in SPB stars can be useful in determining their amplitudes, e.g., by the parametric instability between three small amplitude modes.

Because of the Coriolis force and the centrifugal force in rotating stars, we can expect neither the separation of variables for the oscillations nor spherical symmetry for the equilibrium structure, which makes it difficult to solve oscillation problems. We have shown that one can use the series expansion method to investigate the frequency spectrum and stability of low-frequency modes as in [30], who employed the Chandrasekhar–Milne expansion to calculate the rotational deformation making use of the equilibrium structure of the nonrotating star. Many attempts have also been made to carry out two-dimensional calculation for the oscillations of rotating stars (e.g., [4, 16, 25, 37, 44]; see also [47]), where the differential equations for the oscillations and equilibrium models are solved as sets of partial differential equations. The series expansion method is flexible enough to be applied to nonadiabatic oscillations of stars and can be less demanding numerically than the two-dimensional calculations mentioned above. But, when the advance of astero-seismological observations requires a good precision in theoretical oscillation calculations, we think

that two-dimensional calculation will be found to have advantages in the studies of oscillations in rotating stars.

References

1. Andersson, N.: A new class of unstable modes of rotating relativistic stars. Astrophys. J. **502**, 708 (1998)
2. Aprilia, Lee, U., Saio, H.: Stability of g modes in rotating B-type stars. Mon. Not. R. Astron. Soc. **412**, 2265–2276 (2011)
3. Arras, P., Flanagan, E.E., Morsink, S.M., Schenk, A.K., Teukolsky, S.A., Wasserman, I.: Saturation of the r-mode instability. Astrophys. J. **591**, 1129–1151 (2003)
4. Ballot, J., Lignières, F., Reese, D.R., Rieutord, M.: Gravity modes in rapidly rotating stars. Limits of perturbative methods. Astron. Astrophys. **518**, A30 (2010)
5. Balona, L.A., Pigulski, A., Cat, P.D., Handler, G., Gutiérrez-Soto, J., Engelbrecht, C.A., Frescura, F., Briquet, M., Cuypers, J., Daszyńska-Daszkiewicz, J., Degroote, P., Dukes, R.J., Garcia, R.A., Green, E.M., Heber, U., Kawaler, S.D., Lehmann, H., Leroy, B., Molenda-Żaaowicz, J., Neiner, C., Noels, A., Nuspl, J., Østensen, R., Pricopi, D., Roxburgh, I., Salmon, S., Smith, M.A., Suárez, J.C., Suran, M., Szabó, R., Uytterhoeven, K., Christensen-Dalsgaard, J., Kjeldsen, H., Caldwell, D.A., Girouard, F.R., Sanderfer, D.T.: Kepler observations of the variability in B-type stars. Mon. Not. R. Astron. Soc. **413**, 2403–2420 (2011)
6. Berthomieu, G., Gonczi, G., Graff, P., Provost, J., Rocca, A.: Low-frequency gravity modes of a rotating star. Astron. Astrophys. **70**, 597 (1978)
7. Beyer, H.R., Kokkotas, K.D.: On the r-mode spectrum of relativistic stars. Mon. Not. R. Astron. Soc. **308**, 745–750 (1999)
8. Bildsten, L., Ushomirsky, G., Cutler, C.: Ocean g-modes on rotating neutron stars. Astrophys. J. **460**, 827 (1996)
9. Cameron, C., Saio, H., Kuschnig, R., Walker, G.A.H., Matthews, J.M., Guenther, D.B., Moffat, A.F.J., Rucinski, S.M., Sasselov, D., Weiss, W.W.: MOST detects SPBe pulsations in HD 127756 and HD 217543: Asteroseismic rotation rates independent of vsini. Astrophys. J. **685**, 489–507 (2008)
10. Carroll, B.W., Hansen, C.J.: The nonadiabatic analysis of nonradial modes of stellar oscillation in the presence of slow rotation. Astrophys. J. **263**, 352–365 (1982)
11. Chandrasekhar, S.: The equilibrium of distorted polytropes. I. The rotational problem. Mon. Not. R. Astron. Soc. **93**, 390–406 (1933)
12. Chandrasekhar, S.: The equilibrium of distorted polytropes. III. The double star problem. Mon. Not. R. Astron. Soc. **93**, 462 (1933)
13. Craik, A.D.D.: Wave Interactions and Fluid Flows. Cambridge University Press, Cambridge (1988)
14. Deming, D., Mumma, M.J., Espenak, F., Jennings, D.E., Kostiuk, T., Wiedemann, G., Loewenstein, R., Piscitelli, J.: A search for p-mode oscillations of Jupiter—serendipitous observations of nonacoustic thermal wave structure. Astrophys. J. **343**, 456–467 (1989)
15. Diago, P.D., Gutiérrez-Soto, J., Auvergne, M., Fabregat, J., Hubert, A.M., Floquet, M., Frémat, Y., Garrido, R., Andrade, L., de Batz, B., Emilio, M., Espinosa Lara, F., Huat, A.L., Janot-Pacheco, E., Leroy, B., Martayan, C., Neiner, C., Semaan, T., Suso, J., Catala, C., Poretti, E., Rainer, M., Uytterhoeven, K., Michel, E., Samadi, R.: Pulsations in the late-type Be star HD 50 209 detected by CoRoT. Astron. Astrophys. **506**, 125–131 (2009)
16. Dintrans, B., Rieutord, M.: Oscillations of a rotating star: a non-perturbative theory. Astron. Astrophys. **354**, 86–98 (2000)
17. Dziembowski, W.: Nonlinear mode coupling in oscillating stars. I—Second order theory of the coherent mode coupling. Acta Astron. **32**, 147–171 (1982)
18. Dziembowski, W.A., Pamiatnykh, A.A.: The opacity mechanism in B-type stars—I. Unstable modes in Beta Cephei star models. Mon. Not. R. Astron. Soc. **262**, 204–212 (1993)

19. Dziembowski, W.A., Moskalik, P., Pamyatnykh, A.A.: The opacity mechanism in B-type stars—II. Excitation of high-order g-modes in main sequence stars. Mon. Not. R. Astron. Soc. **265**, 588 (1993)
20. Friedman, J.L., Morsink, S.M.: Axial instability of rotating relativistic stars. Astrophys. J. **502**, 714 (1998)
21. Gautschy, A., Saio, H.: On non-radial oscillations of B-type stars. Mon. Not. R. Astron. Soc. **262**, 213–219 (1993)
22. Huat, A.L., Hubert, A.M., Baudin, F., Floquet, M., Neiner, C., Frémat, Y., Gutiérrez-Soto, J., Andrade, L., de Batz, B., Diago, P.D., Emilio, M., Espinosa Lara, F., Fabregat, J., Janot-Pacheco, E., Leroy, B., Martayan, C., Semaan, T., Suso, J., Auvergne, M., Catala, C., Michel, E., Samadi, R.: The B0.5IVe CoRoT target HD 49330. I. Photometric analysis from CoRoT data. Astron. Astrophys. **506**, 95–101 (2009)
23. Iglesias, C.A., Rogers, F.J.: Updated OPAL opacities. Astrophys. J. **464**, 943 (1996)
24. Iglesias, C.A., Rogers, F.J., Wilson, B.G.: Spin-orbit interaction effects on the Rosseland mean opacity. Astrophys. J. **397**, 717–728 (1992)
25. Ipser, J.R., Lindblom, L.: The oscillations of rapidly rotating Newtonian stellar models. Astrophys. J. **355**, 226–240 (1990)
26. Kumar, P., Goodman, J.: Nonlinear damping of oscillations in tidal-capture binaries. Astrophys. J. **466**, 946 (1996)
27. Lee, U.: Acoustic oscillations of Jupiter. Astrophys. J. **405**, 359–374 (1993)
28. Lee, U.: r modes of slowly pulsating B stars. Mon. Not. R. Astron. Soc. **365**, 677–687 (2006)
29. Lee, U.: Amplitudes of low-frequency modes in rotating B-type stars. Mon. Not. R. Astron. Soc. **420**, 2387–2398 (2012)
30. Lee, U., Baraffe, I.: Pulsational stability of rotating main sequence stars: the second order effects of rotation on the nonadiabatic oscillations. Astron. Astrophys. **301**, 419 (1995)
31. Lee, U., Saio, H.: Overstable convective modes in uniformly rotating massive main-sequence stars. Mon. Not. R. Astron. Soc. **221**, 365–376 (1986)
32. Lee, U., Saio, H.: Low-frequency oscillations of uniformly rotating stars. Mon. Not. R. Astron. Soc. **224**, 513–526 (1987)
33. Lee, U., Saio, H.: Non-adiabatic analysis of low-frequency oscillations of uniformly rotating stars. Mon. Not. R. Astron. Soc. **225**, 643–651 (1987)
34. Lee, U., Saio, H.: Asymptotic analysis of low-frequency non-radial oscillations of uniformly rotating stars. Mon. Not. R. Astron. Soc. **237**, 875–901 (1989)
35. Lee, U., Saio, H.: Energy of oscillation—the role of the negative energy mode in overstable nonradial oscillations of rotating stars. Astrophys. J. **360**, 590–603 (1990)
36. Lee, U., Saio, H.: Low-frequency nonradial oscillations in rotating stars. I. Angular dependence. Astrophys. J. **491**, 839 (1997)
37. Lignières, F., Rieutord, M., Reese, D.: Acoustic oscillations of rapidly rotating polytropic stars. I. Effects of the centrifugal distortion. Astron. Astrophys. **455**, 607–620 (2006)
38. Lindblom, L., Owen, B.J., Morsink, S.M.: Gravitational radiation instability in hot young neutron stars. Phys. Rev. Lett. **80**, 4843–4846 (1998)
39. Lindzen, R.S., Holton, J.R.: A theory of the quasi-biennial oscillation. J. Atmos. Sci. **25**, 1095–1107 (1968)
40. Lockitch, K.H., Friedman, J.L.: Where are the r-modes of isentropic stars? Astrophys. J. **521**, 764–788 (1999)
41. Magalhaes, J.A., Weir, A.L., Conrath, B.J., Gierasch, P.J., Leroy, S.S.: Slowly moving thermal features on Jupiter. Nature **337**, 444–447 (1989)
42. Mosser, B., Gautier, D., Schmider, F.X., Delache, P.: A tentative identification of Jovian global oscillations. Astron. Astrophys. **251**, 356–364 (1991)
43. Neiner, C., Gutiérrez-Soto, J., Baudin, F., de Batz, B., Frémat, Y., Huat, A.L., Floquet, M., Hubert, A.M., Leroy, B., Diago, P.D., Poretti, E., Carrier, F., Rainer, M., Catala, C., Thizy, O., Buil, C., Ribeiro, J., Andrade, L., Emilio, M., Espinosa Lara, F., Fabregat, J., Janot-Pacheco, E., Martayan, C., Semaan, T., Suso, J., Baglin, A., Michel, E., Samadi, R.: The pulsations

of the B5IVe star HD 181231 observed with CoRoT and ground-based spectroscopy. Astron. Astrophys. **506**, 143–151 (2009)
44. Reese, D., Lignières, F., Rieutord, M.: Acoustic oscillations of rapidly rotating polytropic stars. II. Effects of the Coriolis and centrifugal accelerations. Astron. Astrophys. **455**, 621–637 (2006)
45. Saio, H.: Rotational and tidal perturbations of nonradial oscillations in a polytropic star. Astrophys. J. **244**, 299–315 (1981)
46. Saio, H., Cameron, C., Kuschnig, R., Walker, G.A.H., Matthews, J.M., Rowe, J.F., Lee, U., Huber, D., Weiss, W.W., Guenther, D.B., Moffat, A.F.J., Rucinski, S.M., Sasselov, D.: MOST detects g-modes in the late-type Be star β Canis Minoris (B8 Ve). Astrophys. J. **654**, 544–550 (2007)
47. Savonije, G.J.: Unstable quasi g-modes in rotating main-sequence stars. Astron. Astrophys. **443**, 557–570 (2005)
48. Schenk, A.K., Arras, P., Flanagan, É.É., Teukolsky, S.A., Wasserman, I.: Nonlinear mode coupling in rotating stars and the r-mode instability in neutron stars. Phys. Rev. D **65**(2), 024001 (2002)
49. Soufi, F., Goupil, M.J., Dziembowski, W.A.: Effects of moderate rotation on stellar pulsation. I. Third order perturbation formalism. Astron. Astrophys. **334**, 911–924 (1998)
50. Tassoul, J.L.: Theory of Rotating Stars. Princeton University Press, Princeton (1978)
51. Townsend, R.H.D.: Asymptotic expressions for the angular dependence of low-frequency pulsation modes in rotating stars. Mon. Not. R. Astron. Soc. **340**, 1020–1030 (2003)
52. Townsend, R.H.D.: Influence of the Coriolis force on the instability of slowly pulsating B stars. Mon. Not. R. Astron. Soc. **360**, 465–476 (2005)
53. Townsend, R.H.D.: Kappa-mechanism excitation of retrograde mixed modes in rotating B-type stars. Mon. Not. R. Astron. Soc. **364**, 573–582 (2005)
54. Unno, W., Osaki, Y., Ando, H., Saio, H., Shibahashi, H.: Nonradial Oscillations of Stars. University of Tokyo Press, Tokyo (1989)
55. Vorontsov, S.V.: The inverse problem of helioseismology—the speed of sound in the solar interior. Sov. Astron. Lett. **15**, 21 (1989)
56. Waelkens, C.: Slowly pulsating B stars. Astron. Astrophys. **246**, 453–468 (1991)
57. Waelkens, C., Aerts, C., Kestens, E., Grenon, M., Eyer, L.: Study of an unbiased sample of B stars observed with Hipparcos: the discovery of a large amount of new slowly pulsating B stars. Astron. Astrophys. **330**, 215–221 (1998)
58. Walker, G.A.H., Kuschnig, R., Matthews, J.M., Cameron, C., Saio, H., Lee, U., Kambe, E., Masuda, S., Guenther, D.B., Moffat, A.F.J., Rucinski, S.M., Sasselov, D., Weiss, W.W.: MOST detects g-modes in the Be star HD 163868. Astrophys. J. Lett. **635**, L77–L80 (2005)
59. Wu, Y., Goldreich, P.: Gravity modes in ZZ Ceti stars. IV. Amplitude saturation by parametric instability. Astrophys. J. **546**, 469–483 (2001)
60. Yoshida, S., Lee, U.: Inertial modes of slowly rotating isentropic stars. Astrophys. J. **529**, 997–1010 (2000)
61. Yoshida, S., Lee, U.: Rotational modes of nonisentropic stars and the gravitational radiation-driven instability. Astrophys. J. Suppl. Ser. **129**, 353–366 (2000)

Chapter 8
Prospects for Asteroseismology of Rapidly Rotating B-Type Stars

Hideyuki Saio

Abstract In rapidly rotating stars, Coriolis forces and centrifugal deformations modify the properties of oscillations; the Coriolis force is important for low-frequency modes, while the centrifugal deformation affects mainly p-modes. Here, we discuss properties of g- and r-mode oscillations in rotating stars. Predicted frequency spectra of high-order g-modes (and r-modes) excited in rapidly rotating stars show frequency groupings associated with azimuthal order m. We compare such properties with observations in rapidly rotating Be stars and discuss what is learnt from such comparisons.

8.1 Oscillations in Main-Sequence B-Stars

Thanks to OPAL and OP opacity tables [5, 27], we now understand that radial and nonradial oscillations found in main-sequence B-stars; i.e., β Cephei and SPB (Slowly pulsating B) stars, are excited by the kappa-mechanism associated with the Fe opacity bump at $T \sim 2 \times 10^5$ K [21, 23, 28, 36]. Low-order p- and g-modes are excited in β Cephei stars, while high-order g-modes are excited in SPB stars. Figure 8.1 shows their positions in the HR diagram and predicted instability regions; solid and dotted lines are for models without and with core overshooting, respectively. The instability regions bounded by solid lines are roughly consistent with β Cephei (inverted triangles) and SPB (triangles) stars, which are mostly slow rotators.

Stellar oscillations give us useful information on the stellar interior that is hard to obtain by other means. For β Cephei stars having low-order p- and g-modes, mode identifications are less ambiguous, so that detailed asteroseismic studies are possible. Comparing observed frequencies with theoretical ones yields best estimates of physical parameters as well as the extent of core-overshooting for each star. In addition, rotational m-splittings of p- and g-modes, which have different depth sensitivity, can be used to measure the strength of differential rotation in the stellar interior. Such asteroseismic analyses have been done for some β Cephei stars, e.g.,

H. Saio (✉)
Astronomical Institute, Graduate School of Science, Tohoku University, Sendai, Japan
e-mail: saio@astr.tohoku.ac.jp

M. Goupil et al. (eds.), *Studying Stellar Rotation and Convection*,
Lecture Notes in Physics 865, DOI 10.1007/978-3-642-33380-4_8,

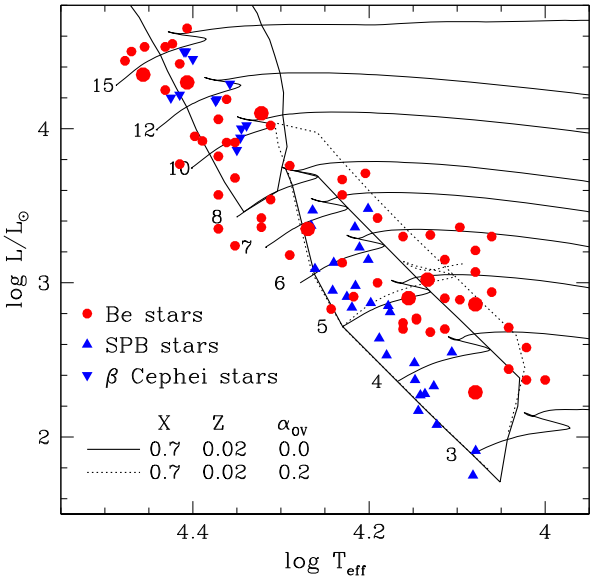

Fig. 8.1 Positions of rapidly rotating Be stars (*filled circles*) in the HR diagram are shown along with the well-known B-type main-sequence variables SPB (*triangles*) and β Cep stars (*inverted triangles*). *Big filled circles* indicate the Be stars with nonradial pulsations detected by space photometry from the MOST and CoRoT satellites. Parameters of Be stars are taken mainly from [22, 53] and those of SPB stars from [15, 39]. Also shown are theoretical instability boundaries for p- and g-modes. *Solid lines* for evolutionary tracks and instability boundaries are from models without core overshooting, while *dotted lines* come from models with a core overshooting of $0.2H_p$ (H_p = pressure scale height). Theoretical models were obtained using a standard chemical composition of $(X, Z) = (0.70, 0.02)$ with OPAL opacity tables [27]

ν Eri [4, 13, 20, 47], θ Oph [9, 34], HD 129929 [18], β CMa [35], 12 Lac [16], and δ Cet [1]. Although results are still somewhat controversial, they seem to indicate that the extent of core overshooting in β Cephei stars ranges around 0.1–0.3H_p, and the core-to-envelope ratios of rotation rates are approximately 3–5.

In contrast to the cases of β Cephei stars, detailed seismic analysis for SPB stars is difficult, because g-mode frequencies are densely distributed, affected strongly by stellar evolution, and modified significantly even by moderate stellar rotation; these properties make mode identifications difficult (see De Cat [14] for a review on SPB stars).

Although a detailed frequency fitting between theory and observation for each SPB star might be difficult, a collective property as simple as the distribution of SPB stars in the HR diagram gives us useful information on the extent of convective-core overshooting. The "red" (or cooler) boundary of the SPB (g-mode) instability region corresponds to the disappearance of convective cores. The Brunt–Väisälä frequency in a radiative dense core is very high, and hence the wavelengths of a g-mode become very short there, which, in turn, cause strong radiative damping [19, 21, 23]. This is the reason why the cool boundary from models with a core overshooting

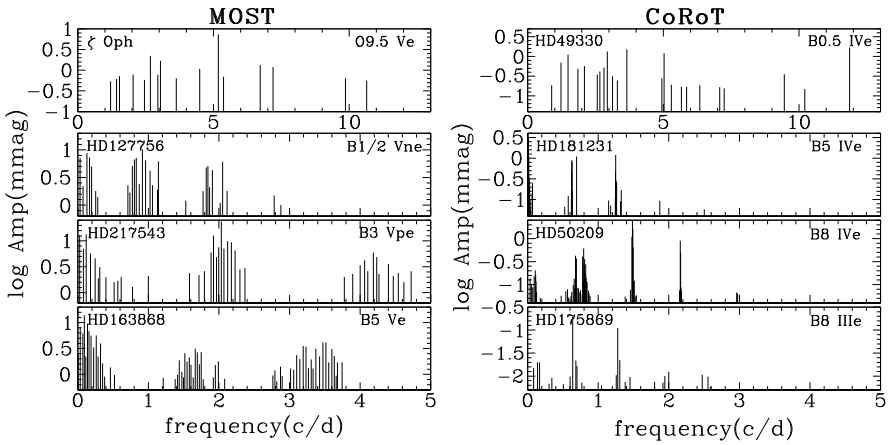

Fig. 8.2 Frequency-amplitude diagrams for light variations detected in Be stars by the MOST (*left panel*) and the CoRoT (*right panel*) satellites. In addition to these stars, MOST detected in the late-type Be star β CMi small amplitude oscillations with frequencies of 3.26 and 3.28 c/d [45]. Frequencies and amplitudes adopted from [52]—ζ Oph, [10]—HD 127756 & HD 217543, [51]—HD 163868, [26]—HD49330, [37]—HD 181231, [17]—HD 50209, and [25]—HD 175869. Note that the stars observed by CoRoT tend to be more evolved (with the spectral luminosity class IV) than the stars observed by MOST

of $0.2H_p$ (dotted lines in Fig. 8.1) is redder than that from models without core overshooting (solid lines). Figure 8.1 shows that the observed SPB stars lay within the instability boundary obtained from models without core overshooting. This indicates that, in contrast to the cases of β Cephei stars, mixing by core overshooting should be weak in SPB stars, i.e., in the slowly rotating main-sequence stars of 3–8$M_\odot$. We need further accumulation of fundamental parameter data of SPB stars to confirm the property.

Also plotted in Fig. 8.1 are the positions of rapidly rotating Be stars (filled circles). Be stars are B-type stars which have (or had sometime before) Balmer lines in emission. The emission lines arise from a circumstellar disk ejected from the star due to rapid rotation. Many Be stars are known to show spectroscopic and photometric variations on various time-scales; in particular, short-term (order of a day) photometric (e.g., Balona [7]) and line-profile (e.g., Rivinius and Baade [43]) variations are thought to be caused by radial and nonradial pulsations of Be stars, although rotational modulations were also suggested for the photometric variations. The Be stars with short-term photometric variations are sometimes called λ Eri variables [7]. Interestingly, Be stars tend to be located in the β Cephei (p-mode) and SPB (g-mode) instability regions, supporting pulsation (oscillation) origin of the short-term variations. Recently, the MOST and CoRoT satellites have found multiperiodic light variations in several Be stars, of which amplitude diagrams are shown in Fig. 8.2. The multiperiodicity strongly supports the explanation that the short-term variations of Be stars are caused by pulsations rather than rotational modulations.

The frequency spectra in the top panels of Fig. 8.2 for the hot Be stars, ζ Oph and HD 49330, show wide ranges of periodicities ranging from about a day to a few hours, while the lower panels show relatively long and grouped periods. The difference can be understood by the fact that the hottest two stars lay in the β Cephei instability range (Fig. 8.1) and p-modes and low-order g-modes are excited, while the other relatively cooler Be stars lay in the SPB instability range where long-period g-modes are excited. Figure 8.1 shows that some cool Be stars, including some whose variability are detected by CoRoT (large filled circles), lay outside of the SPB instability range obtained from models without convective core overshooting. This indicates that an extensive mixing around the convective core should be occurring if nonradial g-modes are excited in those Be stars. The analyses for HD 181231 and HD 175869 by Neiner et al. [38] do indicate the presence of such mixing. Future observation of other cool Be stars should tell whether such extensive mixing is ubiquitous in rapidly rotating Be stars.

In contrast to the broad frequency spectra of the hottest Be stars (top panels of Fig. 8.2) without other remarkable features, the spectra of the relatively cooler Be stars show conspicuous frequency groups which are regularly separated. This property comes from strong rotation effects on high-order g-modes whose intrinsic frequencies are comparable with or less than the rotation frequencies.

8.2 Oscillations in Rotating Stars

Stellar rotation affects the oscillations in two ways: through the centrifugal force, which deforms the equilibrium structure from spherical symmetry, and the Coriolis force, which represents the angular momentum conservation when matter moves. In this section we discuss rotation effects mainly on low-frequency modes (for p-modes, see, e.g., Goupil [24]).

8.2.1 Coriolis and Centrifugal Force Effects

The effects of Coriolis and centrifugal forces can be seen from the equation of motion, which may be written in the inertial frame as

$$\frac{\partial \mathbf{v}}{\partial t} + \mathbf{v} \cdot \nabla \mathbf{v} = -\frac{1}{\rho} \nabla p - \nabla \psi, \tag{8.1}$$

where $\mathbf{v}$ is the fluid velocity, ρ the matter density, p the pressure, and ψ the gravitational potential. The velocity consists of the oscillation velocity $\mathbf{v}'$ and the rotation velocity $r \sin\theta \Omega \mathbf{e}_\phi$, where $\mathbf{e}_\phi$ is the unit vector of ϕ direction. In equilibrium state without oscillations, Eq. (8.1) is reduced to

$$-r \sin\theta \Omega^2 \mathbf{e}_\varpi = -\frac{1}{\rho_0} \nabla p_0 - \nabla \psi_0, \tag{8.2}$$

where

$$\mathbf{e}_\varpi \equiv \sin\theta \mathbf{e}_r + \cos\theta \mathbf{e}_\theta = \mathbf{e}_\phi \times \mathbf{e}_z \tag{8.3}$$

is the outwardly pointing unit vector perpendicular to the rotation axis.

Writing the variables in Eq. (8.1) as the sum of the equilibrium value and (Eulerian) perturbation due to oscillations, e.g., $p = p_0 + p'$, subtracting Eq. (8.2), and disregarding nonlinear terms with respect to the perturbed quantities, we obtain

$$\frac{\partial \mathbf{v}'}{\partial t} + \Omega \frac{\partial}{\partial \phi}\mathbf{v}' + \mathbf{v}' \cdot \nabla(r\sin\theta\Omega\mathbf{e}_\phi) = -\frac{1}{\rho}\nabla p' + \frac{\rho'}{\rho^2}\nabla p - \nabla\psi', \tag{8.4}$$

where the subscript $_0$ for equilibrium quantities is dropped for ease of notation.

The relation between oscillation velocity and the Lagrangian displacement $\boldsymbol{\xi}$ is somewhat different in a rotating star. Since $\mathrm{d}\boldsymbol{\xi}/\mathrm{d}t$ corresponds to the Lagrangian velocity of oscillation, the Eulerian oscillation velocity $\mathbf{v}'$ is written as

$$\mathbf{v}' = \frac{\mathrm{d}\boldsymbol{\xi}}{\mathrm{d}t} - \boldsymbol{\xi} \cdot \nabla(r\sin\theta\Omega\mathbf{e}_\phi) = \frac{\partial \boldsymbol{\xi}}{\partial t} + \Omega\frac{\partial \boldsymbol{\xi}}{\partial \phi} - \boldsymbol{\xi} \cdot \nabla(r\sin\theta\Omega\mathbf{e}_\phi). \tag{8.5}$$

We express the temporal and azimuthal dependence of an oscillation mode as

$$\mathrm{e}^{\mathrm{i}(\sigma t + m\phi)}, \tag{8.6}$$

where σ is the oscillation frequency observed in the inertial frame, and m is the azimuthal order of the oscillation. Equation (8.6) means that we adopt the convention that prograde modes correspond to $m < 0$, i.e., an oscillation propagates in the positive direction of ϕ (or in the direction of rotation velocity) if $m < 0$. Then, Eq. (8.5) becomes

$$\mathbf{v}' = \mathrm{i}\omega\boldsymbol{\xi} - \mathrm{i}\sigma r\sin\theta\mathbf{e}_\phi\boldsymbol{\xi} \cdot \nabla\Omega, \tag{8.7}$$

where

$$\omega \equiv \sigma + m\Omega \tag{8.8}$$

is the frequency in the frame rotating with an angular frequency of Ω. Note that in the case of uniform rotation, ω is constant in the stellar interior and can be adopted as eigenfrequency.

Substituting this expression of $\mathbf{v}'$ into Eq. (8.1), we obtain

$$-\omega^2\boldsymbol{\xi} + 2\mathrm{i}\omega\Omega(\mathbf{e}_z \times \boldsymbol{\xi}) + r\sin\theta\left(\boldsymbol{\xi} \cdot \nabla\Omega^2\right)\mathbf{e}_\varpi = -\frac{1}{\rho}\nabla p' + \frac{\rho'}{\rho^2}\nabla p - \nabla\psi', \tag{8.9}$$

where $\mathbf{e}_z$ is the unit vector parallel to the rotation axis. The second term in the left-hand side, $2\mathrm{i}\omega\Omega(\mathbf{e}_z \times \boldsymbol{\xi})$, corresponds to the Coriolis force. The centrifugal-force effect is hidden in ∇p, which is, in the nonrotating case, equal to $-\mathbf{e}_r GM_r\rho/r^2$. In the presence of rotation the centrifugal force modifies $\rho^{-1}\nabla p$ by the order of $r\sin\theta\Omega^2\mathbf{e}_\varpi$ and hence breaks spherical symmetry. Thus, the importance of the centrifugal force is measured as $f_{\mathrm{cen}} \equiv r^3\sin\theta\Omega^2/GM_r$, which indicates that the effect of centrifugal forces is largest at the equator on the stellar surface, where $f_{\mathrm{cen}} = R_{\mathrm{eq}}^3\Omega^2/GM < 1$ with R_{eq} being the equatorial radius, and minimum near the center, where $f_{\mathrm{cen}} \to \frac{4\pi}{3}\sin\theta\Omega^2/G\rho_{\mathrm{c}} \ll 1$ with ρ_{c} being the central density.

On the other hand, the importance of the Coriolis force can be measured by

$$f_{\rm cor} \equiv \frac{2\Omega}{\omega}, \tag{8.10}$$

which determines the relative importance between the first two terms on the left-hand side of Eq. (8.9); when $f_{\rm cor} > 1$, the Coriolis term is larger than the acceleration term (first term) and vice versa. Obviously, for a given rotation frequency, g-modes are affected more strongly by Coriolis force than p-modes because the frequencies of p-modes in the corotating frame are larger than those of g-modes.

The p-mode frequencies are bounded as $\omega^2 \gtrsim 10GM/R^3$ (see, e.g., Cox [11]), while the rotation frequency is limited by $\Omega^2 < GM/R^3$. Therefore, for p-modes, $f_{\rm cor} < 1$, i.e., the effects of Coriolis forces are always small for p-modes, while the effect of centrifugal force (deformation) can be significant for p-modes because the amplitudes of p-modes are confined to outer layers. Actually, Reese et al. [42] have shown that p-mode properties are significantly modified in rapidly rotating deformed stars.

For g-modes, on the other hand, the opposite is true: $f_{\rm cor}$ can be larger than unity even in a slowly rotating star for high-order g-modes, while the effect of centrifugal force is small even in rapidly rotating stars because the amplitude of g-modes is confined to inner layers where the centrifugal deformation is small. The insensitivity of g-mode frequencies to the centrifugal deformation has been shown numerically by Ballot et al. [6].

As seen in Eq. (8.9), in the *absence* of rotation, the horizontal displacement $\boldsymbol{\xi}_{\rm h}$ is proportional to $\nabla_{\rm h}(p'/\rho + \psi')$ with

$$\nabla_{\rm h} \equiv \mathbf{e}_\theta \frac{\partial}{\partial\theta} + \mathbf{e}_\phi \frac{1}{\sin\theta}\frac{\partial}{\partial\phi}, \tag{8.11}$$

which makes the angular dependence of an oscillation mode representable by a single spherical harmonic $Y_\ell^m(\theta,\phi)$ (see Cox [11], Unno et al. [50], or Aerts et al. [2] for details). This simple property is lost in the presence of rotation even if the centrifugal deformations are neglected, because of the presence of the Coriolis force. Then, we express the angular dependence of oscillation by using a sum of terms associated with spherical harmonics as

$$\boldsymbol{\xi} = \sum_{j=1}^{J}\left[S^j Y_{l_j}^m \mathbf{e}_r + H^j \nabla_{\rm h} Y_{l_j}^m + T^j\left(\nabla_{\rm h} Y_{l'_j}^m\right)\times \mathbf{e}_r\right] \quad \text{and} \quad p' = \sum_{j=1}^{J} p'^j Y_{l_j}^m, \tag{8.12}$$

where $l_j = |m| + 2(j-1) + I$ and $l'_j = l_j + 1 - 2I$ with $I = 0$ for even modes and $I = 1$ for odd modes, and J means the truncation length. Other scalar variables are expressed in a way similar to p'. The eigenfunction for a scalar variable of an even (odd) mode which consists of terms proportional to $Y_{l_j}^m$ with even (odd) values of $(l_j - |m|)$ is symmetric (antisymmetric) about the equatorial plane.

As seen in the above equations, we can still assign azimuthal degree m and the (even or odd) parity of a mode, but no longer a latitudinal degree. To identify the latitudinal behavior of a g-mode, we sometimes use in this paper the notation ℓ_0

for the latitudinal degree the mode would have as $\Omega \to 0$. When we discuss the observational properties, we use the effective degree ℓ which represents the value of l_j for the component with the maximum amplitude on the stellar surface among the other components in Eq. (8.12), and we use ℓ' for the corresponding toroidal component.

Note that toroidal components are needed in representing the displacement vectors, because the toroidal velocity fields couple, through the Coriolis force, with spheroidal velocity fields which generate variations in density, pressure, temperature, etc.

8.2.2 r-Modes

Purely toroidal motions in a nonrotating spherical star do not disturb stellar structure, so that no restoring force nor oscillations arise. In the presence of rotation, however, the latitudinal gradient of the vertical component of the angular frequency of rotation $\Omega \cos\theta$ causes a restoring force for toroidal motions so that toroidal oscillations occur; we call these oscillations r-modes (or global Rossby modes). All the r-modes are retrograde in the corotating frame (see, e.g., Pedlosky [40] and Saio [44]). If we assume that the displacement is purely toroidal and neglect the centrifugal deformation, the toroidal oscillation would have the limiting frequency, $\omega_{\rm rlim}$, given as

$$\omega_{\rm rlim} \equiv \frac{2m\Omega}{\ell'(\ell'+1)} \tag{8.13}$$

in the corotating frame. Actual frequencies of r-modes in the corotating frame deviate from $\omega_{\rm rlim}$; the deviation is larger for higher radial order modes (Provost et al. [41], Saio [44]). The deviation arises because the Coriolis forces associated with toroidal motion generate spheroidal motions, i.e., vertical motion and density perturbations are generated, and hence buoyancy plays a role in the restoring forces for r-modes. Because of these effects, r-modes are sometimes called "mixed modes" (Townsend [48]) or "q-modes" (quasi g-modes; Savonije [46]). The coupling with spheroidal motions makes it possible for r-modes (mainly toroidal oscillations) to be excited thermally by the kappa-mechanism in the same way as g-modes are excited. Stability analyses by Townsend [48], Savonije [46], and Lee [30] indicate that some r-modes are actually excited by the kappa-mechanism in intermediate mass (around 3–8$M_\odot$) main sequence stars, in which g-modes are also excited (SPB stars).

8.2.3 Latitudinal Amplitude Distributions

Latitudinal distributions of oscillation amplitudes are expressed as shown in Eq. (8.12), which indicates a dependency on the ratio $f_{\rm cor}$. The distributions are important in understanding the visibilities of excited modes.

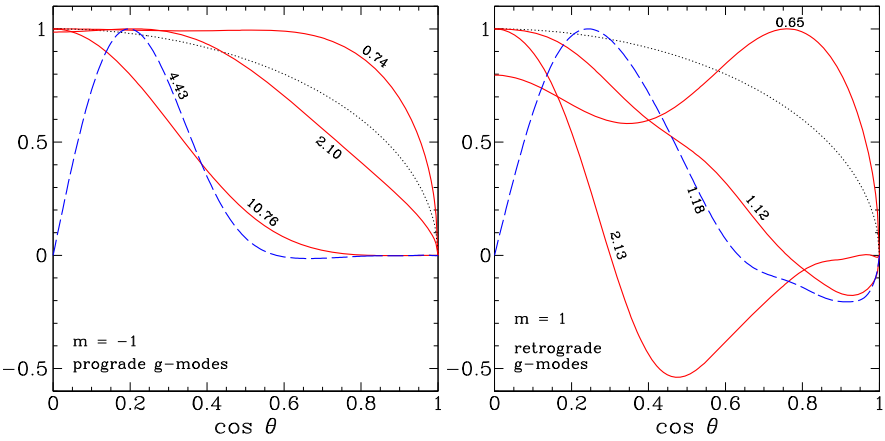

Fig. 8.3 Amplitude distributions for scalar variables of g-modes with $m = \pm 1$ and $\ell_0 = 1$ and 2 as functions of $\cos\theta$, where θ is colatitude. *Left* and *right panels* are for prograde ($m = -1$) and retrograde ($m = 1$) g-modes, respectively. *Solid* and *dashed lines* are for even ($\ell_0 = 1$) and odd ($\ell_0 = 2$) modes, respectively. A number along each line indicates the value of $f_{\rm cor} = 2\Omega/\omega$ for the mode. Note that an additional nodal line appears for retrograde modes when $f_{\rm cor} > 1$, which would reduce the visibility. *Dotted line* shows the associated Legendre function $P_1^1(\cos\theta)$

Figure 8.3 shows latitudinal distributions of the amplitude of p' as functions of $\cos\theta$ for selected g-modes of $m = \pm 1$ and $\ell_0 = 1, 2$, in a $4.5 M_\odot$ ZAMS model of rigid rotation at an angular frequency of $0.220\sqrt{GM/R^3}$ (or with a period of 0.96 days, $V_{\rm eq} = 130$ km/s). Although the adopted rotation rate is moderate, the Coriolis force significantly affects the amplitude distribution of g-modes, because frequencies are so low that the parameter $f_{\rm cor} = 2\Omega/\omega$ is larger than around 1. These eigenfunctions have been obtained by the method of Lee and Baraffe [32] without using the "traditional" approximation in which the horizontal component of rotational angular velocity, $-\Omega \sin\theta \mathbf{e}_\theta$, is neglected. The results are very similar to those obtained by using the traditional approximation (see, e.g., Lee and Saio [33]), indicating that the approximation is well suited for low-frequency oscillations in which the horizontal velocity is much larger than the radial one.

Generally, amplitudes of oscillation modes with large $f_{\rm cor}$ tend to be confined to equatorial regions. This property is consistent with the behavior of the eigenvalue λ of the Laplace tidal equation (e.g., Lee and Saio [33] and Aerts et al. [2]), which governs angular dependence of oscillation in the traditional approximation. As $f_{\rm cor}$ increases, λ increases rapidly except for sectoral prograde modes ($\ell_0 = -m$); a large λ corresponds to a large effective degree ℓ, i.e., $\lambda \to \ell_0(\ell_0 + 1)$ as $\Omega \to 0$.

Solid lines in Fig. 8.3 are for $\ell_0 = |m| = 1$, i.e., sectoral modes that have no latitudinal nodal lines when $\Omega = 0$. The prograde modes ($m = -1$) keep this property even for a large $f_{\rm cor}$, while for retrograde modes ($m = 1$), a latitudinal nodal line appears for the cases with $f_{\rm cor} > 1$, which reduces visibility of the mode due to cancellation on the surface.

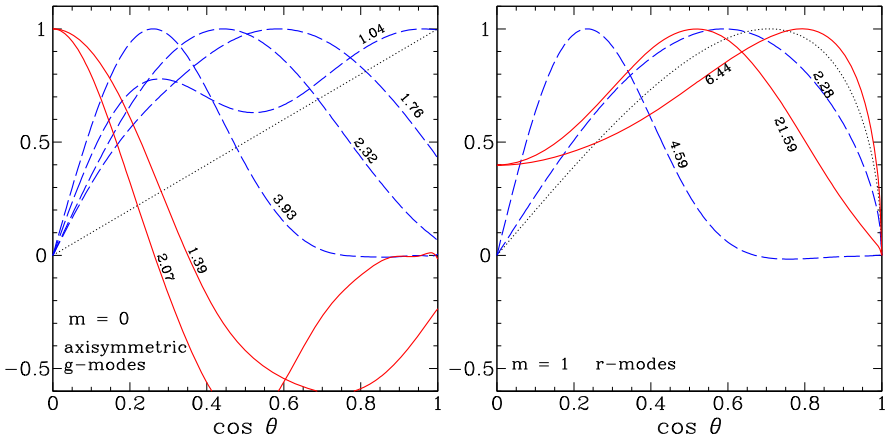

Fig. 8.4 The same as Fig. 8.3 but for g-modes of $m = 0$ (*left panel*) and r-modes of $m = 1$ (*right panel*). In the *left panel*, *solid* and *dashed lines* are $\ell_0 = 2$ (even) and $\ell_0 = 1$ (odd) modes, respectively. In the *right panel*, *solid lines* are for even modes with $\ell = \ell' - 1 = 1$, and *dashed lines* are for odd modes with $\ell = \ell' + 1 = 2$. *Dotted lines* shows the Legendre function of $P_1(\cos\theta)$ (*left panel*) and $P_2^1(\cos\theta)$ (*right panel*)

The left panel of Fig. 8.4 shows latitudinal amplitude distributions of axisymmetric ($m = 0$) g-modes (dashed lines for $\ell_0 = 1$ modes, and solid lines for $\ell_0 = 2$ modes). Similarly to nonaxisymmetric modes, amplitudes of axisymmetric modes tend to be confined in equatorial zones as $f_{\rm cor}$ increases; in particular, for $\ell_0 = 1$ modes, the amplitude weight shifts from the pole to low latitudes.

The right panel of Fig. 8.4 shows amplitude (p') distributions of selected r-modes of $m = 1$ in the same model as in Fig. 8.3. Red solid lines are for even r-modes with $\ell' = \ell + 1 = 2$, and blue dashed lines are for odd r-modes with $\ell' = \ell - 1 = 1$, where ℓ' and ℓ are the latitudinal degrees for the dominant toroidal component and for the corresponding spheroidal component, respectively. (The parity refers to the property of scalar variables.)

For r-modes of $m = 1$ (right panel of Fig. 8.4), a low-order mode close to the limiting frequency $\omega_{\rm rlim}$ (Eq. (8.13)) and a relatively high-order mode are shown for each parity. (For low-order r-modes of $m = 1$, $f_{\rm cor} \sim \ell'(\ell' + 1)$.) The amplitude distribution of a higher-order r-mode tends to be more confined to the equatorial region, which is similar to high-order g-modes having large $f_{\rm cor}$. An important difference from retrograde g-modes is that no additional latitudinal nodal-line appears for r-modes. The stability analyses for r-modes by Townsend [48] and Lee [30] indicate that odd r-modes are more easily excited in B-type main-sequence stars, while Savonije [46] found even (symmetric with respect to the equator) r-modes to be excited in some models. We expect odd r-modes to be detected unless the inclination angle between rotation axis and the line-of-sight is close to 90°.

8.2.4 Expected Frequency Ranges of g- and r-Modes

High-order g-modes (Gautschy and Saio [23], Dziembowski et al. [21]) and r-modes (Townsend [48], Savonije [46], Lee [30]) are excited by the kappa-mechanism at the Fe-opacity bump in intermediate mass (around 3–8$M_\odot$) main-sequence stars. Some g-modes are, however, damped in rapidly rotating stars ($f_{\rm cor} > 1$) due to mode couplings. The mode coupling occurs when two normal modes with the same m and parity but with different ℓ_0 have similar oscillation frequencies, as these two modes are no longer independent in the presence of the Coriolis force. Lee [29] has found that the mode couplings tend to damp retrograde g-modes. The effects of the mode couplings are discussed in detail by Aprilia et al. [3] and by Lee in [31] and in Chap. 7 of this volume. The damping effects can also be significant on prograde g-modes except for sectoral modes ($\ell_0 = -m$). Although some prograde tesseral ($\ell_0 > -m$) g-modes might still remain excited in rapidly rotating stars, the effective degrees (ℓ) of these modes might be too high to be detectable. Therefore, most visible modes should be low-degree prograde sectoral ($\ell_0 = -m$) g-modes and (retrograde) r-modes in rapidly rotating intermediate mass stars.

For high-order g-modes in rapidly oscillating stars, $\omega \ll |m|\Omega$ with ω being frequencies in the corotating frame, so that we expect to observe these modes at $\sigma = |\omega - m\Omega| \sim |m|\Omega$.

Since sectoral prograde g-modes are expected most visible as discussed above, we expect groups of frequencies slightly above Ω and 2Ω for $m = -1$ and -2 modes, respectively. (Modes with higher $|m|$ are expected to be less visible due to cancellation.)

For r-modes with $m = 1$, only odd modes ($\ell' = 1$) seem to be excited in B-type stars, which have $\omega \sim \Omega$ and whose observational frequencies are very small, $\sigma \ll \Omega$. Symmetric (even) r-modes of $m = 2$ ($\ell = 2$) are also excited in some cases for which $\ell' = 3$ and hence $\omega_{\rm rlim} = \frac{1}{3}\Omega$. Therefore, frequencies in the observer's frame are slightly larger than $\frac{5}{3}\Omega$.

In summary, we expect to observe groups of frequencies at approximately

$$\text{g-modes:} \quad \Omega, \quad 2\Omega, \quad \text{and} \quad \text{r-modes:} \quad 0, \quad \frac{5}{3}\Omega, \tag{8.14}$$

where we have assumed arbitrarily that modes with effective degrees $\ell \le 2$ are visible.

Figure 8.5 shows growth rates and azimuthal order m of the low-degree ($\ell \le 2$) modes excited in a 4.5$M_\odot$ main-sequence model of rigid rotation at various speeds. The abscissa indicates the frequencies in the observer's frame. Red (solid) and blue (dotted) lines are for even and odd modes, respectively. In the model of the lowest rotation frequency ($\overline{\Omega} = 0.073$, bottom panel), no r-modes are excited, and we see no appreciable effects of rotation on the stability of g-modes; rotation only disperses frequencies by the effect of transformation from corotating to inertial frames, $\sigma = \omega - m\Omega$.

In the second lowest rotation case with a normalized angular frequency of rotation $\overline{\Omega} = 0.15$, $m = 1$ odd r-modes with $\ell' = \ell - 1 = 1$ are excited; they have very small frequencies in the observer's frame, because $\omega_{\rm rlim} = \Omega$ (Eq. (8.13)).

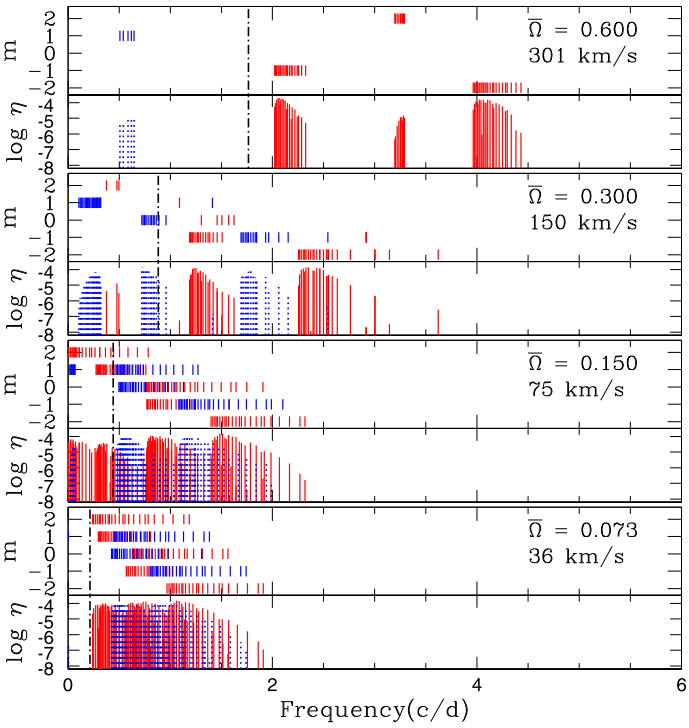

Fig. 8.5 Growth rates and azimuthal order m of low-degree ($\ell \leq 2$) modes excited in $4.5M_{\odot}$ main-sequence models with various rotation frequencies, where the results were obtained by the method of Lee and Baraffe [32]. The cyclic rotation frequency is indicated by a vertical *dash-dotted line* at each panel, and $\overline{\Omega}$ is the corresponding angular frequency of rotation normalized by $\sqrt{GM/R^3}$ with R being the mean stellar radius; equatorial rotation velocity is also shown. Horizontal axis indicates the frequency in the observer's frame

As the rotation frequency increases ($\overline{\Omega} > 0.2$), retrograde ($m > 0$) g-modes tend to be damped, while prograde g-modes remain excited. Due to the damping of retrograde g-modes and the increasing effect of $-m\Omega$, frequency groupings become conspicuous as the rotation frequency increases. In a sufficiently rapidly rotating case (as in the top panel), well-populated frequency groups of prograde sectoral ($\ell = -m$) g-modes are formed around 1.2Ω and 2.3Ω corresponding to $m = -1$ and -2, respectively.

The r-modes also form groups, because the frequency deviation $|\omega_{\rm rlim} - \omega|$ of an r-mode is usually much smaller than $m\Omega$. The group at smallest frequencies corresponds to $m = 1$ anti-symmetric r-modes $\ell' = \ell - 1 = 1$. In the fastest rotation case (top panel) all the excited retrograde ($m > 0$) modes are r-modes. Note that in this model, $m = 2$ r-modes with $\ell = \ell' - 1 = 2$ symmetric with respect to the equator are excited; their observational frequencies are slightly larger than $|\omega_{\rm rlim} - m\Omega| = \frac{5}{3}\Omega$. The excitation of symmetric $m = 2$ r-modes in a sufficiently rapid rotator agree with the results of Savonije [46].

Figure 8.5 shows that frequency groupings appear even in stars whose rotation rates are considerably less than the critical rate. This is consistent with the finding of Balona et al. [8] from Kepler data that several B stars with relatively large $V \sin i$ show frequency groupings.

8.3 Comparisons with Frequency Groups of Be Stars

The characteristic frequency groupings obtained for several Be stars (Fig. 8.2) were fitted with models (e.g., Cameron et al. [10], Neiner et al. [38]). Such fittings give estimates for rotation frequencies and in some cases, the constraint to the internal mixing in rapidly rotating stars. In this section, we discuss what we learn from model fittings to low-frequency oscillations of Be stars.

8.3.1 HD 50209

We will discuss, as an example, a model fitting to low-frequency oscillations of the late-type (B8IVe) Be star HD 50209 detected by CoRoT ([17]); the amplitude spectrum consists of five frequency groups around 0.1 c/d, 0.6–0.8 c/d, 1.5 c/d, 2.2 c/d, and 3 c/d (or six groups if the 0.6–0.8 c/d group is separated into two groups) as shown in Fig. 8.2 and in the left-bottom panel of Fig. 8.6.

The fundamental parameters of HD 50209 have been derived by Diago et al. [17] as $\log T_{\rm eff} = 4.134 \pm 0.051$, $\log L = 3.02 \pm 0.39$, and $\log g = 3.56 \pm 0.11$ (with $\Omega/\Omega_{\rm crit} = 0.90$). The estimated position of HD 50209 in the HRD is shown in the right panel of Fig. 8.6 by a filled square with error bars. At the center of the parameter ranges the critical rotation rate is around 0.7 c/d. Since prograde g-modes of $m = -1$ form a group around frequencies slightly larger than the rotation frequency, the 0.6–0.8 c/d group should be fitted by assuming a rotation frequency of approximately 0.6 c/d. The rotation frequency should not be far from the critical rate; i.e., the radius should be sufficiently large, otherwise no clear frequency groupings would be expected (see Fig. 8.5). Two models of $5.0 M_\odot$ and $5.5 M_\odot$ stars rotating at a rate of 0.6 c/d (0.007 mHz) were examined; their positions on the HRD are shown by filled circles in Fig. 8.6. In both cases, a substantial core overshooting (more than $0.3 H_p$) must be included to meet the above requirements for $T_{\rm eff}$ and luminosity within the spectroscopic estimates. The requirement of substantial core overshooting for the model of HD 50209 is common to the models for other CoRoT Be stars, HD 175869, and HD 181231 as discussed in Neiner et al. [38].

Both models produce similarly good fits to observed frequency groups of HD 50209. A comparison with the $5.5 M_\odot$ model is shown in the left panel of Fig. 8.6, where the method of Lee and Baraffe [32] was used for the stability analysis. To fit the three (0.6–0.8, around 1.5, and 2.2 c/d) groups with g-modes, we have

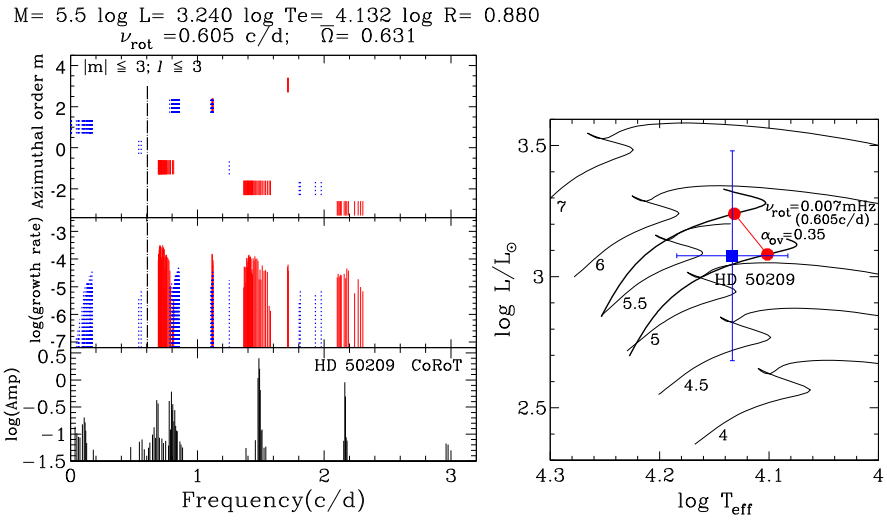

Fig. 8.6 *Left panel*: Frequencies of excited modes in a model of a $5.5M_{\odot}$ star rotating at a rate of 0.605 c/d are compared with observed frequencies of HD 50209 (*bottom panel*) adopted from Diago et al. [17]; the rotation frequency of the model is indicated by the *dash-dotted vertical line*. The *top panel* shows azimuthal order m (prograde modes correspond to $m < 0$), and the *middle panel* shows growth rates of excited modes. *Solid* (*red*) and *dashed* (*blue*) *lines* are even and odd modes, respectively. *Right panel*: The positions of HD 50209 (*filled square* with error bars) on the HRD and two models (*filled circles*) that are reasonably consistent with the observed frequency groups; a fit by one of the models is shown in the *left panel*. Evolutionary tracks are calculated with a standard composition of $(X, Z) = (0.70, 0.02)$. The thick two tracks for $5.0M_{\odot}$ and $5.5M_{\odot}$ are from evolution including overshooting of $0.35H_p$ around the convective core; the other tracks are without overshooting

to consider azimuthal orders up to 3 ($|m| \leq 3$). (The frequencies at around 3 c/d are probably harmonics of large-amplitude frequencies at approximately 1.5 c/d as indicated by Diago et al. [17].)

One can interpret the smallest frequency group at around 0.1 c/d as due to $m = 1$ anti-symmetric r-modes. Diago et al. [17] estimate an inclination angle of $i \sim 60°$ for HD 50209 for a rotation frequency of 90–95 % of the critical rate. With this inclination angle, r-modes would suffer from no serious surface cancellation (see right panel of Fig. 8.4) and would be detectable if the r-modes produce enough temperature variations. It is interesting to note that a very low-frequency group is common in SPBe stars that show g-mode pulsations, but it does not appear in hot Be stars (ζ Oph and HD 49330) with p-mode pulsations (Fig. 8.2). This agrees with the theoretical prediction for the excitation range of r-modes on the HRD as obtained by Townsend [48] and supports the identification of the very low frequency groups in SPBe stars as r-modes. In this model, symmetric r-modes of $m = 2$ and 3 are excited, but they have no observational correspondence.

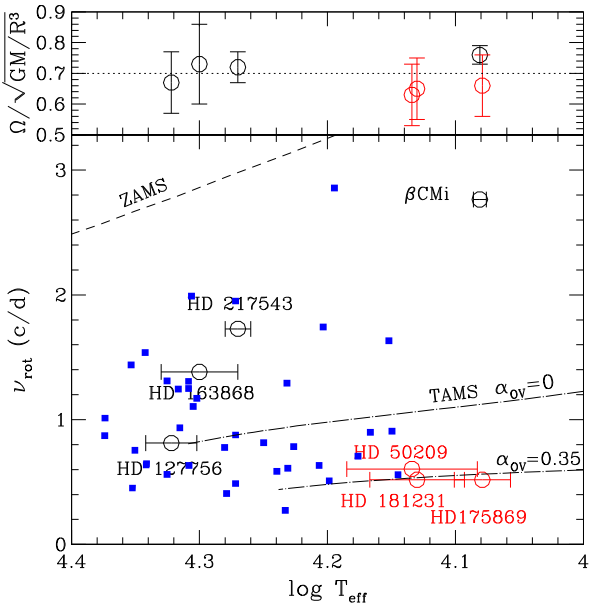

Fig. 8.7 Effective temperature versus rotation frequencies estimated by model fittings for Be stars observed by MOST and CoRoT (*large circles* with error bars). The *top panel* shows rotation frequency normalized by $\sqrt{GM/R^3}$, where R is the mean radius. With this normalization, the critical rotation frequency corresponds to approximately 0.7. *Filled squares* are λ Eri variables whose rotation frequencies are assumed to be 80 % of the observed frequencies listed in Balona [7]. The *dashed line* indicates the critical rotation for zero-age main-sequence models as a function of $\log T_{\rm eff}$. *Dotted–dashed lines* show critical rotation of TAMS (terminal-age main sequence) models without and with substantial convective core overshooting

8.3.2 Rotation Rates of Be Stars

Figure 8.7 plots rotation frequencies obtained by fitting theoretical predictions for frequency groups against those observed for several Be stars observed by MOST and CoRoT (a similar diagram is shown in [10]). The lower panel shows the rotation frequency of the Be stars (with error bars) as a function of the effective temperature. The Be stars observed by CoRoT tend to have low rotation frequencies compared to those observed by MOST. This is due to the fact that CoRoT-observed Be stars tend to be more evolved, having spectral luminosity class IV. This apparent difference disappears if the rotation frequency is normalized by $\sqrt{GM/R^3}$ as plotted in the top panel of Fig. 8.7, where R is mean radius. With this normalization critical rotation corresponds to $\Omega/\sqrt{GM/R^3} \sim 0.7$. This indicates that all Be stars shown can be considered rotating nearly critically, which agrees with recent spectroscopic estimates by Townsend et al. [49] and Cranmer [12].

Dashed and dot-dashed lines in the bottom panel of Fig. 8.7 show critical rotation frequency as a function $\log T_{\rm eff}$ for ZAMS and TAMS (terminal age main-sequence) models, respectively. For TAMS models, critical rotations with and without substan-

tial core overshooting cases are shown. Obviously, substantial overshooting would need to be assumed for models to be consistent with the CoRoT observations of Be stars.

Also plotted in this figure are rotation frequencies of λ Eri variables (filled squares); a group of Be stars which show short-term (order of a day) periodic light variations known from ground-based observations (e.g., Balona [7]). Folded light curves of λ Eri variables, some of which show double-wave character, are consistent with the grouped frequency distributions obtained for relatively late-type Be stars monitored by MOST and CoRoT satellites. In fact, the folded light curve of HD 181231 from CoRoT observations (Neiner et al. [37]), for example, is similar to typical light curves of λ Eri variables. Since a model with a rotation frequency about 20 % smaller than the frequency at the group of $m = -1$ modes fits well to such a characteristic frequency distribution, rotation frequencies of λ Eri variables are assumed as 80 % of the observed frequencies, and those values are plotted in Fig. 8.7. This figure shows that the distribution of λ Eri rotation rates are consistent with Be star models rotating nearly critically if a substantial core-overshooting of around $0.35 H_p$ is assumed to occur in these stars. Since models without core overshooting are consistent with the slowly rotating SPB stars, rapid rotation seems the cause of the substantial mixing needed around the convective core (Neiner et al. [38]).

8.4 Conclusion

Rapid stellar rotation modifies properties of oscillations in complex ways and makes comparisons between observational and theoretical results difficult. In particular, low-order p- and g-modes excited in early type Be stars in the β Cephei instability region show complex frequency spectra affected considerably both by deformation of the equilibrium structure and by the Coriolis force. The frequency distributions of these stars are such that it would seem impossible to identify modes and so compare with theoretical results.

In contrast to the p-modes, rapid rotation helps us to identify the azimuthal degree m of low-frequency modes, because observational frequencies of these modes form groups, i.e., g-modes with the same m have similar frequencies. This property can be used to identify m and to estimate the rotation frequency of each star. The rotation rates thus obtained for several Be stars indicate that Be stars rotate nearly critically, which confirms conclusions drawn from spectroscopic analyses. In addition, in order to fit observations of some Be stars, models with substantial core-overshooting are needed. This indicates that extensive internal mixing exterior to the convective core occurs in rapidly rotating stars as discussed in Neiner et al. [38]. Furthermore, it might be possible in the near future to compare each g-mode (and r-mode) frequency (or period spacings) with theory in order to obtain detailed information on the stellar interior. Rapid rotations are advantageous in this case because we can identify the azimuthal order m, while effects of centrifugal deformation remain small, as shown by Ballot et al. [6].

Acknowledgement I am grateful to Alfred Gautschy and Umin Lee for helpful comments.

References

1. Aerts, C., Marchenko, S.V., Matthews, J.M., Kuschnig, R., Guenther, D.B., Moffat, A.F.J., Rucinski, S.M., Sasselov, D., Walker, G.A.H., Weiss, W.W.: δ Ceti is not monoperiodic: seismic modeling of a β Cephei star from MOST space-based photometry. Astrophys. J. **642**, 470–477 (2006)
2. Aerts, C., Christensen-Dalsgaard, J., Kurtz, D.W.: Asteroseismology. Springer, Berlin (2010)
3. Aprilia, Lee, U., Saio, H.: Stability of g modes in rotating B-type stars. Mon. Not. R. Astron. Soc. **412**, 2265–2276 (2011)
4. Ausseloos, M., Scuflaire, R., Thoul, A., Aerts, C.: Asteroseismology of the β Cephei star ν Eridani: massive exploration of standard and non-standard stellar models to fit the oscillation data. Mon. Not. R. Astron. Soc. **355**, 352–358 (2004)
5. Badnell, N.R., Bautista, M.A., Butler, K., Delahaye, F., Mendoza, C., Palmeri, P., Zeippen, C.J., Seaton, M.J.: Updated opacities from the opacity project. Mon. Not. R. Astron. Soc. **360**, 458–464 (2005)
6. Ballot, J., Lignières, F., Prat, V., Reese, D.R., Rieutord, M.: 2D computations of g modes. arXiv:1109.6856 [astro-ph]
7. Balona, L.A.: Tests of the pulsation and starspot models for the periodic Be-stars. Mon. Not. R. Astron. Soc. **277**, 1547 (1995)
8. Balona, L.A., Pigulski, A., Cat, P.D., Handler, G., Gutiérrez-Soto, J., Engelbrecht, C.A., Frescura, F., Briquet, M., Cuypers, J., Daszyńska-Daszkiewicz, J., Degroote, P., Dukes, R.J., Garcia, R.A., Green, E.M., Heber, U., Kawaler, S.D., Lehmann, H., Leroy, B., Molenda-Żaaowicz, J., Neiner, C., Noels, A., Nuspl, J., Østensen, R., Pricopi, D., Roxburgh, I., Salmon, S., Smith, M.A., Suárez, J.C., Suran, M., Szabó, R., Uytterhoeven, K., Christensen-Dalsgaard, J., Kjeldsen, H., Caldwell, D.A., Girouard, F.R., Sanderfer, D.T.: Kepler observations of the variability in B-type stars. Mon. Not. R. Astron. Soc. **413**, 2403–2420 (2011)
9. Briquet, M., Morel, T., Thoul, A., Scuflaire, R., Miglio, A., Montalbán, J., Dupret, M.A., Aerts, C.: An asteroseismic study of the β Cephei star θ Ophiuchi: constraints on global stellar parameters and core overshooting. Mon. Not. R. Astron. Soc. **381**, 1482–1488 (2007)
10. Cameron, C., Saio, H., Kuschnig, R., Walker, G.A.H., Matthews, J.M., Guenther, D.B., Moffat, A.F.J., Rucinski, S.M., Sasselov, D., Weiss, W.W.: MOST detects SPBe pulsations in HD 127756 and HD 217543: asteroseismic rotation rates independent of vsini. Astrophys. J. **685**, 489–507 (2008)
11. Cox, J.P.: Theory of Stellar Pulsation. Princeton University Press, Princeton (1980)
12. Cranmer, S.R.: A statistical study of threshold rotation rates for the formation of disks around Be stars. Astrophys. J. **634**, 585–601 (2005)
13. Daszyńska-Daszkiewicz, J., Walczak, P.: Complex asteroseismology of the B-type main sequence pulsators. Highlights Astron. **15**, 364–365 (2010)
14. De Cat, P.: Observational asteroseismology of slowly pulsating B stars. Commun. Asteroseismol. **150**, 167 (2007)
15. De Cat, P., Aerts, C.: A study of bright southern slowly pulsating B stars. II. The intrinsic frequencies. Astron. Astrophys. **393**, 965–981 (2002)
16. Desmet, M., Briquet, M., Thoul, A., Zima, W., De Cat, P., Handler, G., Ilyin, I., Kambe, E., Krzesinski, J., Lehmann, H., Masuda, S., Mathias, P., Mkrtichian, D.E., Telting, J., Uytterhoeven, K., Yang, S.L.S., Aerts, C.: An asteroseismic study of the β Cephei star 12 Lacertae: multisite spectroscopic observations, mode identification and seismic modelling. Mon. Not. R. Astron. Soc. **396**, 1460–1472 (2009)
17. Diago, P.D., Gutiérrez-Soto, J., Auvergne, M., Fabregat, J., Hubert, A.M., Floquet, M., Frémat, Y., Garrido, R., Andrade, L., de Batz, B., Emilio, M., Espinosa Lara, F., Huat, A.L., Janot-Pacheco, E., Leroy, B., Martayan, C., Neiner, C., Semaan, T., Suso, J., Catala, C., Poretti, E.,

Rainer, M., Uytterhoeven, K., Michel, E., Samadi, R.: Pulsations in the late-type Be star HD 50 209 detected by CoRoT. Astron. Astrophys. **506**, 125–131 (2009)
18. Dupret, M.A., Thoul, A., Scuflaire, R., Daszyńska-Daszkiewicz, J., Aerts, C., Bourge, P.O., Waelkens, C., Noels, A.: Asteroseismology of the β Cep star HD 129929. II. Seismic constraints on core overshooting, internal rotation and stellar parameters. Astron. Astrophys. **415**, 251–257 (2004)
19. Dziembowski, W.A.: Nonradial oscillations of evolved stars. I. Quasiadiabatic approximation. Acta Astron. **21**, 289–306 (1971)
20. Dziembowski, W.A., Pamyatnykh, A.A.: The two hybrid B-type pulsators: ν Eridani and 12 Lacertae. Mon. Not. R. Astron. Soc. **385**, 2061–2068 (2008)
21. Dziembowski, W.A., Moskalik, P., Pamyatnykh, A.A.: The opacity mechanism in B-type stars—II. Excitation of high-order G-modes in main sequence stars. Mon. Not. R. Astron. Soc. **265**, 588 (1993)
22. Frémat, Y., Neiner, C., Hubert, A.M., Floquet, M., Zorec, J., Janot-Pacheco, E., Renan de Medeiros, J.: Fundamental parameters of Be stars located in the seismology fields of COROT. Astron. Astrophys. **451**, 1053–1063 (2006)
23. Gautschy, A., Saio, H.: On non-radial oscillations of B-type stars. Mon. Not. R. Astron. Soc. **262**, 213–219 (1993)
24. Goupil, M.J.: Effects of rotation on stellar p-mode frequencies. In: The Rotation of Sun and Stars. Lecture Notes in Physics, vol. 765, pp. 45–99. Springer, Berlin (2009)
25. Gutiérrez-Soto, J., Floquet, M., Samadi, R., Neiner, C., Garrido, R., Fabregat, J., Frémat, Y., Diago, P.D., Huat, A.L., Leroy, B., Emilio, M., Hubert, A.M., Andrade, O.T.L., de Batz, B., Janot-Pacheco, E., Espinosa Lara, F., Martayan, C., Semaan, T., Suso, J., Auvergne, M., Chaintreuil, S., Michel, E., Catala, C.: Low-amplitude variations detected by CoRoT in the B8IIIe star HD 175869. Astron. Astrophys. **506**, 133–141 (2009)
26. Huat, A.L., Hubert, A.M., Baudin, F., Floquet, M., Neiner, C., Frémat, Y., Gutiérrez-Soto, J., Andrade, L., de Batz, B., Diago, P.D., Emilio, M., Espinosa Lara, F., Fabregat, J., Janot-Pacheco, E., Leroy, B., Martayan, C., Semaan, T., Suso, J., Auvergne, M., Catala, C., Michel, E., Samadi, R.: The B0.5IVe CoRoT target HD 49330. I. Photometric analysis from CoRoT data. Astron. Astrophys. **506**, 95–101 (2009)
27. Iglesias, C.A., Rogers, F.J.: Updated OPAL opacities. Astrophys. J. **464**, 943 (1996)
28. Kiriakidis, M., El Eid, M.F., Glatzel, W.: Heavy element opacities and the pulsations of Beta Cepheid stars. Mon. Not. R. Astron. Soc. **255**, 1P–5P (1992)
29. Lee, U.: Pulsational stability of g-modes in slowly pulsating B stars. Astrophys. J. **557**, 311–319 (2001)
30. Lee, U.: r modes of slowly pulsating B stars. Mon. Not. R. Astron. Soc. **365**, 677–687 (2006)
31. Lee, U.: Pulsation in rapidly rotating stars. Commun. Asteroseismol. **157**, 203–208 (2008)
32. Lee, U., Baraffe, I.: Pulsational stability of rotating main sequence stars: the second order effects of rotation on the nonadiabatic oscillations. Astron. Astrophys. **301**, 419 (1995)
33. Lee, U., Saio, H.: Low-frequency nonradial oscillations in rotating stars. I. Angular dependence. Astrophys. J. **491**, 839 (1997)
34. Lovekin, C.C., Goupil, M.J.: Rotation and convective core overshoot in θ Ophiuchi. Astron. Astrophys. **515**, A58 (2010)
35. Mazumdar, A., Briquet, M., Desmet, M., Aerts, C.: An asteroseismic study of the β Cephei star β Canis Majoris. Astron. Astrophys. **459**, 589–596 (2006)
36. Moskalik, P., Dziembowski, W.A.: New opacities and the origin of the Beta Cephei pulsation. Astron. Astrophys. **256**, L5–L8 (1992)
37. Neiner, C., Gutiérrez-Soto, J., Baudin, F., de Batz, B., Frémat, Y., Huat, A.L., Floquet, M., Hubert, A.M., Leroy, B., Diago, P.D., Poretti, E., Carrier, F., Rainer, M., Catala, C., Thizy, O., Buil, C., Ribeiro, J., Andrade, L., Emilio, M., Espinosa Lara, F., Fabregat, J., Janot-Pacheco, E., Martayan, C., Semaan, T., Suso, J., Baglin, A., Michel, E., Samadi, R.: The pulsations of the B5IVe star HD 181231 observed with CoRoT and ground-based spectroscopy. Astron. Astrophys. **506**, 143–151 (2009)

38. Neiner, C., Mathis, S., Saio, H., Lovekin, C., Eggenberger, P., Lee, U.: Seismic modelling of the late Be stars HD 181231 and HD 175869 observed with CoRoT: a laboratory for mixing processes. Astron. Astrophys. **539**, A90 (2012)
39. Niemczura, E.: The main parameters of SPB stars on the basis of IUE spectra. In: Aerts, C., Bedding, T.R., Christensen-Dalsgaard, J. (eds.) IAU Colloq. 185: Radial and Nonradial Pulsations as Probes of Stellar Physics. Astronomical Society of the Pacific Conference Series, vol. 259, p. 230 (2002)
40. Pedlosky, J.: Geophysical Fluid Dynamics. Springer, Berlin (1982)
41. Provost, J., Berthomieu, G., Rocca, A.: Low frequency oscillations of a slowly rotating star—quasi toroidal modes. Astron. Astrophys. **94**, 126 (1981)
42. Reese, D.R., MacGregor, K.B., Jackson, S., Skumanich, A., Metcalfe, T.S.: Pulsation modes in rapidly rotating stellar models based on the self-consistent field method. Astron. Astrophys. **506**, 189–201 (2009)
43. Rivinius, T., Baade, D., Štefl, S.: Non-radially pulsating Be stars. Astron. Astrophys. **411**, 229–247 (2003)
44. Saio, H.: R-mode oscillations in uniformly rotating stars. Astrophys. J. **256**, 717–735 (1982)
45. Saio, H., Cameron, C., Kuschnig, R., Walker, G.A.H., Matthews, J.M., Rowe, J.F., Lee, U., Huber, D., Weiss, W.W., Guenther, D.B., Moffat, A.F.J., Rucinski, S.M., Sasselov, D.: MOST detects g-modes in the late-type Be star β Canis Minoris (B8 Ve). Astrophys. J. **654**, 544–550 (2007)
46. Savonije, G.J.: Unstable quasi g-modes in rotating main-sequence stars. Astron. Astrophys. **443**, 557–570 (2005)
47. Suárez, J.C., Moya, A., Amado, P.J., Martín-Ruiz, S., Rodríguez-López, C., Garrido, R.: Seismology of β Cephei stars: Differentially rotating models for interpreting the oscillation spectrum of ν Eridani. Astrophys. J. **690**, 1401–1411 (2009)
48. Townsend, R.H.D.: Kappa-mechanism excitation of retrograde mixed modes in rotating B-type stars. Mon. Not. R. Astron. Soc. **364**, 573–582 (2005)
49. Townsend, R.H.D., Owocki, S.P., Howarth, I.D.: Be-star rotation: how close to critical? Mon. Not. R. Astron. Soc. **350**, 189–195 (2004)
50. Unno, W., Osaki, Y., Ando, H., Saio, H., Shibahashi, H.: Nonradial Oscillations of Stars. University of Tokyo Press, Tokyo (1989)
51. Walker, G.A.H., Kuschnig, R., Matthews, J.M., Cameron, C., Saio, H., Lee, U., Kambe, E., Masuda, S., Guenther, D.B., Moffat, A.F.J., Rucinski, S.M., Sasselov, D., Weiss, W.W.: MOST detects g-modes in the Be star HD 163868. Astrophys. J. Lett. **635**, L77–L80 (2005)
52. Walker, G.A.H., Kuschnig, R., Matthews, J.M., Reegen, P., Kallinger, T., Kambe, E., Saio, H., Harmanec, P., Guenther, D.B., Moffat, A.F.J., Rucinski, S.M., Sasselov, D., Weiss, W.W., Bohlender, D.A., Božić, H., Hashimoto, O., Koubský, P., Mann, R., Ruždjak, D., Škoda, P., Šlechta, M., Sudar, D., Wolf, M., Yang, S.: Pulsations of the Oe star ζ Ophiuchi from MOST satellite photometry and ground-based spectroscopy. Astrophys. J. Lett. **623**, L145–L148 (2005)
53. Zorec, J., Frémat, Y., Cidale, L.: On the evolutionary status of Be stars. I. Field Be stars near the Sun. Astron. Astrophys. **441**, 235–248 (2005)

Part II
Convection and Associated Seismology

Chapter 9
Connections Between Stellar Oscillations and Turbulent Convection

K. Belkacem and R. Samadi

Abstract Since the advent of space asteroseismology, enabled by the CoRoT and Kepler space-craft, solar-like oscillations have appeared to be a common feature of low-mass stars from the main-sequence to the red-giant phases. In this context, scaling relations that relate asteroseismological quantities and stellar parameters are an essential tool in the study a large class of stars. Most of these relations concern the connection between pulsations and turbulent convection. Therefore, a deep investigation of this connection is necessary to obtain insight into the processes underlying mode driving and damping and consequently to improve our knowledge of the scaling relations. This is a key step that will permit us to perform a leap forward in our understanding of stellar interiors.

9.1 Introduction

The relation between pulsations and convection is a longstanding problem in stellar physics (see the review by [35, 36]). For solar-like pulsators, and more precisely for the Sun, most of the first efforts had focused on the precise determination of mode frequencies; the issue of their driving and damping was subsidiary and mainly intended to settle the question of their physical nature (e.g., [37, 38]). Recently, the modelling of mode coupling with turbulent convection has become of primary interest since it appears that mode amplitudes are, potentially, a powerful seismic diagnostic for the solar-like stars as observed by CoRoT and Kepler. In this article, we aim to provide a comprehensive overview of mode driving and damping processes for solar-like oscillations with particular emphasis on the scaling relations that, for the majority of them, results from the connection between oscillatory and convective phenomena.

K. Belkacem (✉) · R. Samadi
LESIA, UMR8109, Observatoire de Paris, Université Pierre et Marie Curie, Université Denis Diderot, 92195 Meudon Cedex, France
e-mail: kevin.belkacem@obspm.fr

R. Samadi
e-mail: reza.samadi@obspm.fr

M. Goupil et al. (eds.), *Studying Stellar Rotation and Convection*,
Lecture Notes in Physics 865, DOI 10.1007/978-3-642-33380-4_9,

9.1.1 A Brief History on the Energetical Aspects of Solar-Like Oscillations

The mechanism of acoustic noise generation by turbulence is a longstanding problem in fluid mechanics [51], and its manifestation in stellar physics is what we name *solar-like oscillations*. The discovery of solar five-minute oscillations by [32] and [48], reinforced by their interpretation in terms of normal modes by [72] and [47], has made the issue of their excitation and damping of primary interest.

The problem of the stability of these modes was the first question to be addressed. Whether or not solar p-modes were overstable was investigated to determine whether mode driving is related to some κ-mechanisms, as in classical pulsators [35, 36]. Such a stability analysis was performed by [1, 2, 37], who concluded that most of the solar p-modes are unstable, but later studies [6, 37], by including the effect of turbulent pressure and turbulent viscosity, found them to be stable. The subsequent observational evidence, which revealed normal modes with Lorentzian profiles[1] (e.g., [34]), has supported the latter view, and it is now clear that solar five-minute oscillations are stable (i.e., their amplitudes result from a balance between driving and damping).

On mode driving, a first attempt to explain the observed solar five minute oscillations was carried out by [73] and was followed by [70]. The latter generalised the approach of [50] to a stratified atmosphere and concluded that the Reynolds stresses should be the major source of acoustic wave generation. Except for a transient debate on the relative contributions of the Reynolds stresses and the non-adiabatic part of gas pressure, this conclusion is still favoured today. A noticeable leap forward has been made by [38]. Despite an under-estimation of the observed amplitudes [56], the work of [38] still constitutes the foundation of the current formalisms for modelling mode driving. Since these pioneering works, different improved models have been developed [5, 15, 16, 18, 25, 29, 40, 61, 62]. These approaches differ from each other either in the way the turbulent convection or the excitation processes are described.

For mode damping, the situation is more confusing in the sense that there is no clear consensus on the dominant physical mechanisms at work. Such disagreements are mainly related to the strong coupling between convection and oscillation, which makes the problem difficult when the characteristic times associated with the convective motions are of the same order as the oscillation periods. While it was indisputable that solar p-modes are stable, non-adiabatic calculations (e.g., [1]) were unable to reach this conclusion, thus emphasising the need of an extra physical ingredient. [39] proposed that the shear due to Reynolds stresses, modelled by eddy-viscosity, is of the same order of magnitude as the non-adiabatic component of the perturbation of gas pressure. [41] and [6] found that the damping is dominated by

[1] A Lorentzian profile in the Fourier time domain corresponds to an exponentially damped oscillation in the time domain.

the modulation of turbulent pressure, while [30, 42], and [21] also include the perturbation of the dissipation rate of kinetic energy into heat that acts to compensate the perturbation of turbulent pressure.

It seems that the main shortcut available in modelling mode-damping rates is the way in which turbulent convection is described. One major deficiency of those formalisms is that they use of the mixing-length theory, thus reducing the whole of the turbulent cascade to a single length scale. While this can be an acceptable assumption for modelling the convective background, the perturbation of the mixing-length cannot account for the relation between oscillations and the turbulent cascade. [75] proposed an alternative approach using a Reynolds stress formalism (e.g., [24]) to model convection and, using a perturbation method, computed mode damping rates. However, in their analysis some modes are found unstable, contrary to the observational evidence. Here, then, is the current the state of art for the Sun.

2006 saw the start of the era of space asteroseismology with the space-borne mission CoRoT [52], allowing us for the first time to observe stars on long time scales and with almost no interruptions. This led to the first detection of solar-like oscillations in stars with sufficient accuracy to measure individual mode parameters (including mode amplitudes and linewidths). HD 49933 is, historically, the first representative of a long series that were to follow [3]. This is particularly the case with the discovery of thousands of red giants exhibiting solar-like oscillations. The launch of the Kepler spacecraft in 2009 now provides observations of hundreds of main-sequence solar-like stars.

In this lecture, we will discuss the great potential of those space observations which should enable us, using the relations bounding mode-parameters and stellar-parameters, to improve our understanding of mode damping and driving and their connection with convective properties across the HR diagram.

9.1.2 Mode Damping and Driving in Solar-Like Pulsators: A Difficult Problem

Before discussing the current modelling of mode damping and driving, it is worthwhile that we make some quantitative remarks.

Modes in solar-like pulsators are mainly driven and damped in the uppermost part of the convective region, i.e., in the superadiabatic region near the photosphere and at the transition between the convective and radiative atmosphere. In these layers, convection becomes inefficient, and convective velocities increase rapidly over a relatively small radial scale to sustain the convective flux. As a result, in this region the convective time scale reaches a minimum (which is of the order of 5 min), while the kinetic flux is maximal. Given the fact that the efficiency of the driving crucially depends on the magnitude of the kinetic flux and the convective time scale (see Sect. 9.2.1), acoustic modes with periods of the order of few minutes can be efficiently excited in the uppermost part of the convective region. Concerning the thermal structure of the uppermost layers, the thermal time scale (also called the

thermal relaxation time scale) is also of the order of 5 min. This is of the utmost importance since it defines how the star's structure reacts to any thermal perturbation and will, as we will see later, defines the strength of thermal normal-mode leakages (see Sect. 9.2.2). In the Sun, several millions of modes (stochastically excited by turbulent convection as well as damped) have been detected. The maximum amplitude of the excitations is found at a frequency of about 3 mHz with typical values of amplitudes of 2.5 part per million (ppm) (see [53] for details). In terms of mode surface oscillation velocities, the observed maximum amplitude is about 20 $\mathrm{cm\,s^{-1}}$, which immediately allows us to deduce that solar (and solar-like) oscillations are small perturbations of turbulent convection, thus justifying the widely used and commonly accepted linear approximation to model them. More interestingly, the frequency of the peak amplitude (around 3 mHz) corresponds to a time scale of about 5 min. For mode damping the frequencies are found to be of the order of several μHz, corresponding to life-times of several days.

These numbers enable us to make some comments. It turns out that the linear approximation for modelling normal modes in solar-like stars is reasonable, given the ratio between mode amplitudes and turbulent convection velocities. However, while the structure of modes can be described using a perturbative approach, it is impossible to use such an assumption for modelling mode driving. Indeed, we are in the opposite situation where one has to describe the influence of an overwhelming dominant process, turbulent convection, on a very small one, pulsations. In this sense, mode driving is a nonlinear problem. The situation is seen to be even more complex when we note that the characteristic convective time scale and length scale are almost equal to the respective characteristic modal scales. For mode damping, the interaction between convection and pulsation is still subject to the same difficulties as when considering mode driving, except that one can linearise the equation by neglecting the driving terms in the wave equations. The result is that one resolves mode damping and driving as two well-separated sets of equations. While this certainly constitutes a real simplification, other problems arise from the need to consider the thermal coupling between the background and the pulsations. The thermal relaxation time scale, as previously introduced, is also of the same order of magnitude as both the convective time-scale and the modal period, so what may be called a *triple resonance* occurs in the superadiabatic layers.

Our quantitative picture referred to the Sun, but the situation is similar in almost all solar-like pulsators.

9.2 Mode Driving and Damping by Turbulent Convection

For acoustic modes (p-modes), the total mode energy (potential and kinetic) is

$$E_{\mathrm{osc}}(t) = \int_{\mathscr{V}} \rho |\mathbf{V}_{\mathrm{osc}}|^2 \, \mathrm{d}^3 r, \tag{9.1}$$

where $\mathscr{V}$ is the star volume, $\mathbf{V}_{\mathrm{osc}}$ the mode velocity at the position $\mathbf{r}$, and ρ the mean density.

Let η a linear damping rate, and $\mathscr{P}$ be the amount of energy injected per unit time into a mode by an arbitrary driving source (which acts over a time scale much shorter than $1/\eta$). The variation of $E_{\rm osc}$ with time is then given by

$$\frac{\mathrm{d}E_{\rm osc}}{\mathrm{d}t} = \mathscr{P} - 2\eta E_{\rm osc}. \tag{9.2}$$

Solar-like oscillations are known to be stable modes, so there is a stationary state that is obtained by averaging Eq. (9.2) over a long time scale

$$\overline{\frac{\mathrm{d}E_{\rm osc}}{\mathrm{d}t}} = 0 \quad \Longleftrightarrow \quad \overline{E}_{\rm osc} = \frac{\overline{\mathscr{P}}}{2\eta}, \tag{9.3}$$

where $\overline{(\,)}$ refers to a time average.

Equation (9.3) shows that mode energy is controlled by the balance between mode driving ($\mathscr{P}$) and damping (η). For ease of notation, we will henceforth drop the $\overline{(\,)}$ from $\mathscr{P}$. The next step consists in modelling separately mode driving and damping, which are discussed in detail in Sects. 9.2.1 and 9.2.2, respectively.

9.2.1 Modelling Mode Driving ($\mathscr{P}$)

Turbulent motions and associated entropy fluctuations taking place at the uppermost part of the convective envelope are believed to excite solar-like oscillations through a mechanism that we will briefly highlight below.[2] We start from the perturbed momentum and continuity equations

$$\frac{\partial \rho \mathbf{V}}{\partial t} + \boldsymbol{\nabla} : (\rho \mathbf{V}\mathbf{V}) + \boldsymbol{\nabla} P_1 - \rho_1 \mathbf{g}_0 = 0, \tag{9.4}$$

$$\frac{\partial \rho_1}{\partial t} + \boldsymbol{\nabla}.(\rho \mathbf{V}) = 0, \tag{9.5}$$

where P, ρ, $\mathbf{V}$, and $\mathbf{g}$ denote, respectively, the gas pressure, density, velocity, and gravity. In Eqs. (9.4) and (9.5), the subscript 0 denotes Eulerian fluctuations, and the subscript 1 denotes equilibrium quantities. These equations must be supplemented by an Eulerian description of the perturbed equation of state

$$P_1 = c_s^2 \rho_1 + \alpha_s s_1 + \mathscr{R}(\rho_1, s_1), \tag{9.6}$$

where s is the entropy, $\alpha_s = (\partial P_0/\partial s_0)_\rho$, $c_s = \Gamma_1\, P_0/\rho_0$ is the average sound speed, and $\Gamma_1 = (\partial \ln P_0/\partial \ln \rho_0)_s$ the adiabatic exponent. The term $\mathscr{R}(\rho_1, s_1)$ in the RHS of Eq. (9.6) represents higher-order terms. The later are shown to have a negligible

[2] A detailed derivation can be found in [61].

contribution to mode driving (see [38], GK hereafter). The velocity field is decomposed into a component due to the oscillations ($\mathbf{V}_{\rm osc}$) and a component due to the turbulent motions ($\mathbf{u}$), that is, $\mathbf{V} = \mathbf{V}_{\rm osc} + \mathbf{u}$.

By combining Eqs. (9.4), (9.5), and (9.6) we obtain the inhomogeneous wave equation

$$\rho_0 \left(\frac{\partial^2}{\partial t^2} - \mathbf{L} \right) [\mathbf{V}_{\rm osc}] + \mathbf{D}[\mathbf{V}_{\rm osc}] = \frac{\partial}{\partial t} \mathbf{S} - \mathbf{C} \tag{9.7}$$

with

$$\mathbf{S} \equiv \Big[\underbrace{\boldsymbol{\nabla} : (\rho_0 \mathbf{u}\mathbf{u}) - \boldsymbol{\nabla} : \langle \rho_0 \mathbf{u}\mathbf{u} \rangle}_{\text{Reynolds stress contribution}} - \underbrace{\boldsymbol{\nabla} (\bar{\alpha}_s s_t)}_{\text{Entropy contribution}} \Big], \tag{9.8}$$

where s_t is the *Eulerian* turbulent entropy fluctuations. The terms in Eq. (9.8) are the driving sources, namely the Reynolds stress tensor and a source term due to entropy fluctuations, respectively. The last term $\mathbf{C}$ in the RHS of Eq. (9.5) involves higher-order driving terms that are found to be negligible (see SG and GK). Finally, the term $\mathbf{D}$ in the LHS of Eq. (9.7) gathers terms that couple linearly the oscillation- and turbulence-induced fluctuations.

To solve the inhomogeneous wave equation (Eq. (9.7)), we first solve the homogeneous equation (i.e., Eq. (9.7) without the forcing terms on the RHS), supplemented by appropriate boundary conditions. The solutions are the adiabatic eigendisplacement ($\boldsymbol{\xi}$) and associated eigenfrequency ($\omega_{\rm osc}$). Then, we assume that the solution of Eq. (9.7) takes the form

$$\delta \mathbf{r}_{\rm osc} \equiv \frac{1}{2} \big(A(t) \boldsymbol{\xi}(\mathbf{r}) e^{-i \omega_{\rm osc} t} + cc \big), \tag{9.9}$$

where cc indicates complex conjugate, $\omega_{\rm osc}$ is the mode eigenfrequency, and $A(t)$ is the instantaneous amplitude resulting from both driving and damping. Substituting Eq. (9.9) into Eq. (9.7), multiplying by $\boldsymbol{\xi}^*(\mathbf{r}, t)$, and integrating over the stellar volume gives, finally,

$$\frac{\mathrm{d}A}{\mathrm{d}t} + \Delta\sigma A = \frac{1}{2\omega_{\rm osc}^2 I} \int \boldsymbol{\xi}^* \cdot \frac{\partial \mathbf{S}}{\partial t} \, \mathrm{d}^3 x \quad \text{with } I \equiv \int_0^M \boldsymbol{\xi}^* . \boldsymbol{\xi} \, \mathrm{d}m, \tag{9.10}$$

where the term $\Delta\sigma$ comes from the contribution of $\mathbf{D}$. The latter is replaced by the damping rate η in order to take (a posteriori) all sources of damping into account. Indeed, the real part of $\mathbf{D}$ results in a (negligible) frequency shift, while the imaginary part contributes to the damping.

Equation (9.10) is straightforwardly solved, and one obtains the solution for A

$$A(t) = \frac{i e^{-\eta t}}{2\omega_{\rm osc} I} \int_{-\infty}^{t} \mathrm{d}t' \int_{\mathscr{V}} \mathrm{d}^3 x \, e^{(\eta + i\omega_{\rm osc})t'} \boldsymbol{\xi}^*(\mathbf{x}) \, . \, \mathbf{S}\big(\mathbf{x}, t'\big), \tag{9.11}$$

where the spatial integration is performed over the stellar volume ($\mathscr{V}$).

In order to simplify subsequent theoretical derivations, we will consider the Reynolds source term only. In addition, since the excitation arises from a turbulent medium, the sources are random and such that $A(t)$ cannot been determined in a deterministic way. We thus derive an expression for the average squared $\langle |A|^2 \rangle$, where the average is performed over a larger set of independent realisations. Furthermore, it can been shown with the help of Eq. (9.2) that $\langle |A|^2 \rangle$ is related to $\mathscr{P}$ and η according to $\mathscr{P} = \eta I \omega_{\rm osc}^2 \langle |A|^2 \rangle$. Finally, by using Eq. (9.11) we establish the following expression for $\mathscr{P}$ (see SG for a detailed derivation)

$$\mathscr{P} = \frac{1}{8I} \int_{\mathscr{V}} \mathrm{d}^3 x_0 \, \rho_0^2 \int_{-\infty}^{+\infty} \mathrm{d}^3 r \, \mathrm{d}\tau \, e^{-i\omega_{\rm osc}\tau} \left(\nabla_i \xi_j^*\right)_1 \left\langle (u_i u_j)_1 (u_k u_m)_2 \right\rangle (\nabla_k \xi_m)_2, \tag{9.12}$$

where x_0 is the position in the star, $\mathbf{r}$ and τ are the spatial and temporal correlation lengths associated with turbulence, and the subscripts 1 and 2 refer to the quantities evaluated at the spatial and temporal positions $[\mathbf{x}_0 - \frac{\mathbf{r}}{2}, -\frac{\tau}{2}]$ and $[\mathbf{x}_0 + \frac{\mathbf{r}}{2}, \frac{\tau}{2}]$.

We further assume that the eigendisplacement is spatially decoupled from the source terms. In other words, $\boldsymbol{\xi}$ varies on a scale larger than the characteristic scale of turbulence. This permits us to reduce Eq. (9.12) to

$$\mathscr{P} = \frac{1}{8I} \int_{\mathscr{V}} \mathrm{d}^3 x_0 \, \rho_0^2 \nabla_i \xi_j^* \nabla_k \xi_m \int_{-\infty}^{+\infty} \mathrm{d}^3 r \, \mathrm{d}\tau \, e^{-i\omega_{\rm osc}\tau} \left\langle (u_i \, u_j)_1 (u_k u_m)_2 \right\rangle. \tag{9.13}$$

The second integral of Eq. (9.13) involves the term $\langle (u_i u_j)_1 (u_k u_m)_2 \rangle$, which is a two-point spatial *and* temporal correlation product between $u_i u_j$ and $u_k u_m$. If one adopts the quasi-normal approximation (hereafter QNA), it is possible to decompose the fourth-order correlation product as follows

$$\begin{aligned} \left\langle (u_i u_j)_1 (u_k u_m)_2 \right\rangle = & \left\langle (u_i u_j)_1 \right\rangle \left\langle (u_k u_m)_2 \right\rangle + \left\langle (u_i)_1 (u_m)_2 \right\rangle \left\langle (u_j)_1 (u_k)_2 \right\rangle \\ & + \left\langle (u_i)_1 (u_k)_2 \right\rangle \left\langle (u_j)_1 (u_m)_2 \right\rangle. \end{aligned} \tag{9.14}$$

Note that, strictly, the decomposition of Eq. (9.14) is only valid when the velocity is normally distributed (see [14] for an extensive discussion).

We now define $\phi_{i,j}$ to be the spatio-temporal Fourier transform of $\langle (u_i)_1 (u_j)_2 \rangle$. For an inhomogeneous, incompressible, isotropic, and stationary turbulence, there is a relation between $\phi_{i,j}$ and the kinetic energy spectrum E, which is [8]

$$\phi_{ij}(\mathbf{k}, \omega) = \frac{E(k, \omega)}{4\pi k^2} \left(\delta_{ij} - \frac{k_i k_j}{k^2} \right), \tag{9.15}$$

where k and ω are the wavenumber and frequency associated with the turbulent elements, and $\delta_{i,j}$ is the Kronecker symbol. Following [70], for each layer, we decompose $E(k, \omega)$ as

$$E(k, \omega) = E(k) \chi_k(\omega), \tag{9.16}$$

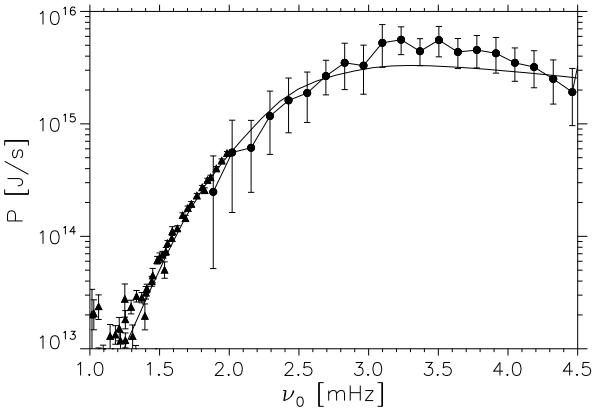

Fig. 9.1 Solar p-mode excitation rates $\mathscr{P}$ as functions of the frequency $\nu_{\rm osc} = \omega_{\rm osc}/(2\pi)$. The *dots* correspond to the observational data obtained by the GONG network, as derived by [9], and the *triangles* correspond to observational data obtained by the GONG network as derived by [59] for $\ell = 0$ to $\ell = 35$. The *solid line* corresponds to theoretical $\mathscr{P}$ computed as detailed in [18]

where $E(k)$ is the time-averaged kinetic energy spectrum, and $\chi_k(\omega)$ is the frequency component of $E(k,\omega)$. Note that $\chi_k(\omega)$ and $E(k)$ satisfy the normalisation conditions

$$\int_{-\infty}^{+\infty} d\omega\, \chi_k(\omega) = 1 \quad \text{and} \quad \int_0^{\infty} \mathrm{d}k\, E(k) = \frac{1}{2}\langle \mathbf{u}^2 \rangle = \frac{3}{2} u_0^2, \tag{9.17}$$

where we have defined the characteristic velocity $u_0^2 \equiv \langle u_z^2 \rangle$ with u_z the vertical component of the velocity field.

Now, using Eqs. (9.14) to (9.16), Eq. (9.13) can be written for *radial* modes as

$$\mathscr{P} = \frac{\pi^3}{2I}\left(\frac{16}{15}\right) \int_0^M \mathrm{d}m\, \frac{\rho_0 u_0^3}{k_0^4} \left|\frac{\mathrm{d}\xi_{\rm r}}{\mathrm{d}r}\right|^2 \tilde{S}_R(r, \omega_{\rm osc}), \tag{9.18}$$

where we have defined the dimensionless source function

$$\tilde{S}_R = \left(k_0^4/u_0^3\right) \int_0^{\infty} \mathrm{d}k\, \frac{E^2(k,r)}{k^2} \int_{-\infty}^{+\infty} \mathrm{d}\omega\, \chi_k(\omega_{\rm osc} + \omega, r)\chi_k(\omega, r), \tag{9.19}$$

and where we have introduced the characteristic wavenumber $k_0 \equiv 2\pi/\Lambda$, where Λ is a characteristic size of the most-energetic eddies.[3] A similar dimensionless source function can be derived for the source term associated with the entropy fluctuations. We also point out that the present formalism has been generalised for non-radial acoustic modes [16] as well as gravity modes [17].

For solar modes, the most recent and realistic calculation of $\mathscr{P}$ has been undertaken by [18]. This calculation is compared in Fig. 9.1 with helio-seismic data. The theoretical calculation results in an overall agreement with the seismic data. We stress that this result had been obtained *without* adjustments of free parameters.

[3] This characteristic size can be determined from the kinetic $E(k)$ or by default using some prescriptions (for more details, see Sect. 11.5.1 in [60]).

To explain qualitatively the variation of $\mathscr{P}$ with mode frequency, we rewrite Eq. (9.18) in a more convenient form by introducing the flux of kinetic energy ($F_{\rm kin}$). For isotropic turbulence,

$$F_{\rm kin} = \langle u_z \, E_{\rm kin} \rangle \approx \frac{3}{2} \rho_0 u_0^3, \tag{9.20}$$

where $E_{\rm kin} \equiv (1/2)\rho_0 \mathbf{u}^2$ is the specific kinetic energy. Substituting Eq. (9.20) into Eq. (9.18) yields the relation

$$\mathscr{P} \propto \frac{1}{I} \int_0^M \Lambda^4 F_{\rm kin} \left| \frac{{\rm d}\xi_{\rm r}}{{\rm d}r} \right|^2 \tilde{S}_R(r, \omega_{\rm osc}) \, {\rm d}m, \tag{9.21}$$

where we have introduced the characteristic life-time $\tau_0 \equiv \Lambda / u_0$.

Equation (9.21) permits us to highlight the key mode-driving quantities (for more details, we refer the reader to [60]).

- *The mode inertia* (I): The lower the mode frequency, the larger the eigendisplacement in the interior. Hence, Eq. (9.10) implies an increase of I with decreasing frequency. As a consequence, for the same amount of energy, it is more difficult to drive low-frequency modes than high-frequency ones. This is the main cause of the rapid decreases of $\mathscr{P}$ with decreasing frequency as seen in Fig. 9.1.
- *The eddy characteristic size* (Λ): As seen in Eq. (9.21), mode-driving scales locally as Λ^4. There is, however, no simple physical principle from which this characteristic size can be derived. Nevertheless, this size can be obtained thanks to 3D hydrodynamical simulations; according to [63], it varies rather slowly in the upper part of the convective zone where the driving is the most efficient. The simulations also show that, from one stellar model to another, this size scales as the pressure scale-height (H_p) at the photosphere [33, 65] and scales rather well as the ratio $T_{\rm eff}/g$, where g is the surface gravity.
- *The flux of kinetic energy* ($F_{\rm kin}$): In the framework of the mixing-length approach, it can be shown that $F_{\rm kin}$ is roughly proportional to the convective flux F_c (see the lecture notes by [22]). The latter increasing as we go up into the convective region. In the upper part of the convective envelope (where mode-driving is most efficient), F_c is almost constant and scales as $T_{\rm eff}^4$, where $T_{\rm eff}$ is the effective temperature. Next, in the transition region between the convective zone and the atmosphere, F_c (and hence $F_{\rm kin}$) decreases rapidly.
- *The mode compressibility* (${\rm d}\xi_{\rm r}/{\rm d}r$): This quantity reaches its maximum in the transition region between the convective and radiative regions, where the temperature decreases rapidly. The maximum of the mode compressibility is also shown to increase with increasing frequency. Therefore, the mode compressibility, together with the mode inertia, favours high-frequency modes.
- *The (dimensionless) source function at the mode frequency* ($\tilde{S}_R$): As described by Eq. (9.19), this term depends on the shape of the kinetic energy spectrum $E(k)$ or, more precisely on χ_k, the Fourier transform of the time-correlation function of the velocity field at a given wavenumber k (e.g., [49], Chap. V-10). $\chi_k(\omega)$ is a

Lorentzian function $(1/(1+(\tilde{\tau}_k\omega_{\rm osc})^2))$ [18, 20, 62], where the characteristic time $\tilde{\tau}_k$ scales as τ_0 [62]. The quantity $\chi_k(\omega)$ decreases rapidly with increasing $\omega_{\rm osc}$. The characteristic time τ_0 reaches a minimal value $\tau_0^{\rm min}$ in the super-adiabatic layers and is of the order of 5 minutes. Therefore, for modes with a frequency larger than $\nu_{\rm osc} \gtrsim 3$ mHz, the source function $\tilde{S}_R$ decreases rapidly with frequency. This latter term balances the effect of the mode compressibility, and the net result is, as seen in Fig. 9.1, a slow decrease with $\nu_{\rm osc}$ for $\nu_{\rm osc} \gtrsim 3$ mHz.

9.2.2 Mode Damping (η)

The calculation of mode-damping rates is a difficult problem for solar-like stars, as explained in Sect. 9.1.2. The assumption of adiabatic pulsation must be abandoned, resulting in a higher-order problem to be solved. The full computation of the non-adiabatic equations is therefore required, and currently only a few codes are able to do this (by including the perturbation of turbulent convection, see the review by [43]).

Our objective is not to provide here an exhaustive view of the non-adiabatic problem but rather to discuss the different physical processes at work. Consequently, it is worthwhile to explicitly derive those contributions.

Let us start with the equations governing stellar fluids. To this end, several preliminary assumptions are useful. We first neglect viscous effects, as is usually accepted in the stellar context, and we also neglect the effects of rotation and of the magnetic field on the structure of the star and so on the oscillations. Hence, the equations read

$$\frac{\partial \rho}{\partial t} + \boldsymbol{\nabla} \cdot (\rho \mathbf{V}) = 0, \tag{9.22}$$

$$\frac{\partial V}{\partial t} + \mathbf{V} \cdot \boldsymbol{\nabla}\mathbf{V} + \nabla\psi + \frac{1}{\rho}\boldsymbol{\nabla} P = 0, \tag{9.23}$$

$$\Delta\psi - 4\pi G\rho = 0, \tag{9.24}$$

$$T\frac{\mathrm{d}S}{\mathrm{d}t} - \epsilon - \frac{1}{\rho}\boldsymbol{\nabla}\cdot\mathbf{F} = 0, \tag{9.25}$$

where ρ is the density, $\mathbf{V}$ the fluid velocity, ψ the gravitational potential, G the gravitational constant, T the temperature, S the specific entropy, P the total pressure (i.e., the gas, turbulent, and radiative pressure), ϵ the rate of energy generation, and $\mathbf{F}$ the energy flux. Note that one must also include equations to describe the radiative and the convective fluxes, as well as the equation of state.

The logical continuation is to perturb the set of Eqs. (9.22)–(9.25). To this end, several additional assumptions are required. First, that the background is at rest, i.e., any dynamical processes such as convection are ignored except through the inclusion of the convective flux in the energy equation or turbulent pressure in the

momentum conservation equation. This is indeed an inconsistent procedure since a perturbation from the mean structure can be related to the oscillatory or convective motion. However, it makes the problem tractable since retaining it prevents us from solving the problems of convection and oscillation simultaneously. Moreover, such a simplification permits us to separate the issues of mode damping and driving (as already mentioned in Sect. 9.1.2).

To perform the perturbation procedure, it is useful to use a Lagrangian variation projected onto spherical harmonics, such that any quantity $y(\mathbf{r}, t)$ reads

$$\delta y(\mathbf{r}, t) = \delta y(\mathbf{r}) Y_\ell^m(\theta, \phi) e^{i\sigma t}, \tag{9.26}$$

where Y_ℓ^m is the spherical harmonic with degree ℓ and azimuthal number m. Note that the frequency $\sigma = \omega_{\rm osc} + i\eta$ is a complex quantity, where $\omega_{\rm osc}$ is the modal frequency, and η the damping rate. To avoid superfluous complexity, we will restrict our discussion to radial modes, and radiative pressure will be neglected. Finally, the perturbed equations governing the problem are found to be (see [42] for a detailed derivation)

$$\frac{\delta\rho}{\rho} + \frac{1}{r^2}\frac{\partial}{\partial r}\left(r^2\xi_r\right) = 0, \tag{9.27}$$

$$\sigma^2\xi_r - \frac{\mathrm{d}\delta\psi}{\mathrm{d}r} - \frac{1}{\rho}\frac{\mathrm{d}\delta P}{\mathrm{d}r} - g\frac{\delta\rho}{\rho} = 0, \tag{9.28}$$

$$\sigma^2 r\xi_h - \delta\psi - \frac{\delta P}{\rho} = 0, \tag{9.29}$$

$$i\sigma T\delta S + \frac{\mathrm{d}\delta L}{\mathrm{d}m} + \delta[\beta_{\rm g} \otimes \boldsymbol{\nabla}\mathbf{V}_{\rm conv} + \mathbf{V}_{\rm conv} \cdot \boldsymbol{\nabla} P_g] = 0, \tag{9.30}$$

where $\otimes$ stands for the tensorial product, $\delta\rho$ is the perturbation of density, P_g the gas pressure, ξ_r, ξ_h the radial and horizontal eigenfunctions, $\delta\psi$ is the perturbation of the gravitational potential, δP the perturbation of total pressure, δS the perturbation of specific entropy, δL the perturbation of luminosity (including both radiative and convective luminosity), $\mathbf{V}_{\rm conv}$ the convective velocity, and $\beta_{\rm g}$ the non-diagonal part of the gas pressure tensor. To derive Eqs. (9.27)–(9.30), it was assumed that turbulence is isotropic and ϵ is null. We recall that one also has to add an expression for the perturbation of the radiative and convective fluxes as well as the perturbed equation of state [42].

Hence, it is possible to write down the integral expression of mode-damping rates by combining Eq. (9.28) (multiplied by $\xi_r^\star$) with Eq. (9.29), then integrating over the star's mass. This gives, finally,

$$\eta = \frac{1}{2\omega_{\rm osc} I}\int_0^M \mathscr{I}\left[\frac{\delta\rho}{\rho}^* \frac{\delta P}{\rho}\right]\mathrm{d}m, \tag{9.31}$$

where the star denotes the complex conjugate, $\mathscr{I}$ the imaginary part, and I the mode inertia.

Equation (9.31) is the integral expression of the damping rates. To get more insight into the physical mechanisms at work, it is useful to recast Eq. (9.31) by first noting that the perturbation of total pressure is the sum of gas and turbulent pressure ($\delta P = \delta P_{\rm turb} + \delta P_g$). In addition, if we use the thermodynamic relation

$$\frac{\delta P_g}{P_g} = P_T \frac{\delta S}{c_v} + \Gamma_1 \frac{\delta \rho}{\rho}, \tag{9.32}$$

where

$$P_T = (\Gamma_3 - 1)\frac{c_v \rho T}{P} \quad \text{and} \quad (\Gamma_3 - 1) = \left(\frac{\partial \ln T}{\partial \ln \rho}\right)_s, \tag{9.33}$$

then Eq. (9.31), together with Eq. (9.32), permits us to express the damping rate in a more explicit form

$$\eta = \frac{1}{2\omega_{\rm osc} I} \int_0^M \mathscr{I}\left[\left(\frac{\delta\rho}{\rho}^* T \delta S\right)(\Gamma_3 - 1) + \left(\frac{\delta\rho}{\rho}^* \frac{\delta P_{\rm turb}}{\rho}\right)\right] {\rm d}m. \tag{9.34}$$

One can then go a step further by inserting Eq. (9.30) (where the last term of this equation is named $\delta\epsilon_2$ for short) into Eq. (9.34), to obtain

$$\begin{aligned}
\eta = & \underbrace{\frac{1}{2\omega_{\rm osc} I} \int_0^M \mathscr{I}\left(\frac{\delta\rho}{\rho}^* \frac{\delta P_{\rm turb}}{\rho}\right) {\rm d}m}_{\text{turbulent pressure contribution}} + \underbrace{\frac{1}{2\omega_{\rm osc}^2 I} \int_0^M \mathscr{R}e\left[(\Gamma_3 - 1)\frac{\delta\rho}{\rho}^* \frac{{\rm d}\delta L_c}{{\rm d}m}\right] {\rm d}m}_{\text{convective flux contribution}} \\
& + \underbrace{\frac{1}{2\omega_{\rm osc}^2 I} \int_0^M \mathscr{R}e\left[(\Gamma_3 - 1)\frac{\delta\rho}{\rho}^* \frac{{\rm d}\delta L_r}{{\rm d}m}\right] {\rm d}m}_{\text{radiative flux contribution}} \\
& - \underbrace{\frac{1}{2\omega_{\rm osc}^2 I} \int_0^M \mathscr{R}e\left[(\Gamma_3 - 1)\frac{\delta\rho}{\rho}^* \delta\epsilon_2\right] {\rm d}m}_{\text{dissipation of kinetic energy contribution}},
\end{aligned} \tag{9.35}$$

where $\mathscr{R}e$ denotes the real part.

The first term of Eq. (9.35) is the contribution of turbulent pressure, which originates on the perturbation of the mean part of the Reynolds stress tensor. The oscillation loses part of its energy by performing a work $\delta P_{\rm turb}\, {\rm d}V$, where the variation of volume ${\rm d}V$ induced by the oscillation is related to the mode compressibility $\nabla \cdot \boldsymbol{\xi} = -\delta\rho/\rho$. These losses of energy are mainly controlled by the phase differences between $\delta\rho$ and $\delta P_{\rm turb}$. The second term of Eq. (9.35) is the damping associated with the perturbation of the convective heat flux. This contribution is certainly the more complex to evaluate, since it depends strongly on how the convection and oscillations are coupled, and consequently it depends on the dynamic modelling of convection. The third contribution to the damping rates is related to the perturbation of the radiative flux. It contains two dominant terms: the opacity effect that is

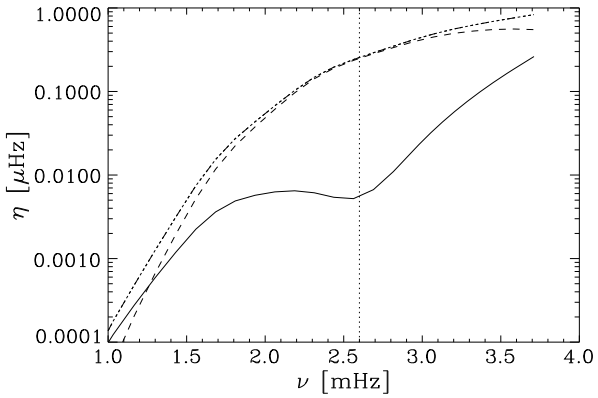

Fig. 9.2 Damping rates versus mode frequency, computed for a model of a star with a mass of $M = 1.1 M_\odot$ and an effective temperature of $T_{\rm eff} = 6026$ K on the main sequence. The *solid line* corresponds to the total damping rate, the *dash-dotted line* to the contribution of the perturbation of turbulent pressure (the second term of the integrand of Eq. (9.34)), and the *dashed line* to the absolute value of the contribution of the entropy perturbations (the first term of the integrand of (Eq. 9.34)). The latter being negative, it partially compensates for the former leading to an effective damping shown by the *solid line*. The *vertical dotted line* corresponds to $\nu_{\rm max}$

responsible for the instability of modes in classical pulsators but negligible in solar-type stars (see [57] for a discussion on opacity-driven modes) and a contribution related to temperature fluctuations δT. Finally, the last contribution of Eq. (9.35) is the contribution to the damping associated with the perturbation of the dissipation rate of turbulent kinetic energy into heat. This contribution was introduced by [46] and more recently by [42]; it partly compensates the effect of turbulent pressure ($\eta_{\rm turb}$), and, in the limit of a fully ionised gas in which radiative pressure can be ignored, the sum vanishes. Note that Eq. (9.35) contains what is nowadays considered as the dominant contributions, but additional possible sources of damping have been investigated and discussed by [44] and [13].

Figure 9.2 displays the mode damping versus the mode frequency as well as the two contributions expressed in Eq. (9.34). The calculation is performed with the MAD code [42]. It turns out that the contribution of turbulent pressure dominates the damping and is partly compensated by the contribution of entropy. Both contributions have roughly the same order of magnitude, and hence the total mode damping is small compared to the absolute values of both the entropy and turbulent pressure. In addition, we note that the depression (or plateau) of the damping rates is the result of the maximum compensation between the two contributions. This turns out to be the case for all the models, from the main-sequence to the red-giant phases.

9.3 Scaling Relations as the Result of the Connections Between Pulsations and Convection

Scaling relations between asteroseismic quantities and stellar parameters such as stellar mass, radius, effective temperature, and luminosity have been derived from

ground-based observational data by several authors (e.g., [45, 55]). More recently, the space-missions CoRoT and Kepler have confirmed those results by providing accurate and homogeneous observations of solar-like oscillations of hundreds of main-sequence stars and thousands of red-giant stars.

Scaling relations are essential to study a large set of stars for which, in general, little is known: to provide a first-order estimate for mass and radius (e.g., [7, 55]), or to probe the populations of red giants [54]. Scaling laws can also lead to a better understanding of the underlying physical mechanisms governing the energetical behaviour of modes [19, 21]. In the following sections, we will describe this connection between convection and pulsations and demonstrate that it is a promising approach to the problem of inference of properties of turbulent convection in stars.

9.3.1 Relation Between Mode Line-Width with Effective Temperature

For mode linewidths (or equivalently mode damping rates), scaling relations have been investigated only very recently. This is the result of the need for long-time and almost-uninterrupted monitoring to resolve individual modes and to enable their precise measurements.

Reference [44], and later [27], have investigated the dependence of mode-damping rates on global stellar parameters. From ground-based measurement, [27] found that mode linewidths follow a power-law of the form $\eta \propto T_{\rm eff}^4$ (where $T_{\rm eff}$ the effective temperature) and no clear tendency emerged when η is scaled with the ratio L/M. Nevertheless, these measurements are based on short-term observations and derived from an inhomogeneous set of analysis and instruments, resulting in a large dispersion. This was settled by [10, 11] (Fig. 9.3, top panel) using a homogeneous sample of CoRoT data. They found that a unique power-law hardly describes the entire range of effective temperature covered by main-sequence and red-giant stars and proposed that mode linewidths of main-sequence stars follow a power-law of $T_{\rm eff}^{16\pm2}$, while red-giant stars only slightly depend on effective temperature ($T_{\rm eff}^{-0.3\pm0.9}$). The latter result was later confirmed and extended by Kepler observations (Fig. 9.3, bottom panel) to main-sequence and sub-giant stars [4].

The theoretical work of [27], based on the formalism developed by [6, 44] and [25], predicted a power-law of $\eta \propto T_{\rm eff}^4$, which disagrees with CoRoT and Kepler observations. In contrast, [21], based on the formalism of [42], were able to reproduce both CoRoT and Kepler observations. Therefore, in the following we will mainly discuss the results of [21].

9.3.1.1 The Scaling Relation as a Probe for Damping Mechanisms

The relation between mode linewidths and effective temperatures is an important constraint for the modelling of damping rates. While it is difficult to settle the issue

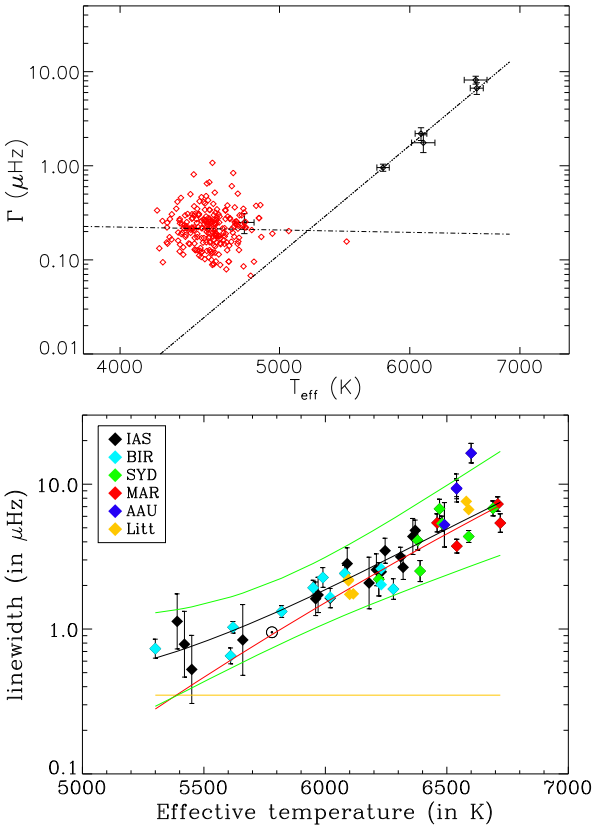

Fig. 9.3 *Top*: Measured mode linewidths versus $T_{\rm eff}$ for the red giants ($T_{\rm eff} < 5000$ K) and for the main-sequence stars ($T_{\rm eff} > 5000$ K) observed by CoRoT [10]. From [10]. *Bottom*: Average mode linewidth at maximum mode height (and their 3-σ error bars) as a function of effective temperature, for sub-giant and main-sequence stars observed by Kepler [4]. From [4]

of the dominant contribution for the Sun, this relation permits us a significant insight elsewhere. A striking example concerns the contribution of turbulent viscosity to mode damping rates that had long been thought to be a dominant contribution [37, 39]. To investigate it, let us start with its integral expression, given by [37, 46],

$$\eta \propto \frac{1}{3I} \int \mathrm{d}m\, \nu_t \left| r \frac{\mathrm{d}}{\mathrm{d}r} \left(\frac{\xi_{\rm r}}{r} \right) \right|^2, \tag{9.36}$$

where ν_t is the turbulent viscosity. The simplest description of ν_t is based on the concept of eddy viscosity. This involves assuming that $\nu_t \propto u_0 \Lambda$, where u_0 is the largest eddy velocity, and Λ the largest eddy size. It can be shown that Eq. (9.36) can be simplified [60] to

$$\eta \propto \left(\frac{\omega_{\rm osc}}{c_s} \right)^2 \Lambda u_0. \tag{9.37}$$

To go further, one must express the velocity u_0 as a function of stellar parameters. To this end, we note that the kinetic energy flux $F_{\rm kin}$ is roughly proportional to

the convective flux $F_{\rm conv}$, which can further be approximated to be the total flux ($F_{\rm conv} \approx F_{\rm tot} \propto T_{\rm eff}^4$). Therefore,

$$u_0 \propto T^{4/3} \rho_s^{-1/3}, \tag{9.38}$$

where ρ_s is the surface density.

The last step is to describe the surface density, which does not scale with the mean density. To this end, we note that the optical depth can be approximated by $\tau \approx \rho \kappa H_p$, where κ is the mean opacity. For low-mass stars, κ is dominated by H^- opacity such that $\kappa \propto \rho^{1/2} T^9$. Then considering that in the photosphere $\tau = 2/3$, this latter scaling, together with Eqs. (9.38) and (9.49), permits us to express Eq. (9.37) as

$$\eta \propto T^{2.5} g^{3/2}. \tag{9.39}$$

From Eq. (9.39) it turns out that the damping rates related to turbulent viscosity exhibit a dependence with effective temperature that is very different from those derived from the observations (Fig. 9.3). Therefore, this result supports that the damping from turbulent viscosity is not the dominant contribution. This result further illustrates that scaling relations of mode damping rates are a powerful tool in obtaining important constraints on the underlying physical mechanisms governing mode linewidths. Moreover, as we will show below, this provides a way to validate their modelling.

A full computation of damping rates and a subsequent comparison with observations has been recently performed by [21]. Among several formalisms, we uses the description proposed by [42], which includes the time-dependent convection (TDC) treatment [21]. The results of this computation are summarised in Fig. 9.4. It can be seen that there is an overall agreement between the theoretical computations and the CoRoT and Kepler observations to an accuracy of observational error. This overall agreement with both CoRoT and Kepler observations demonstrates that the main physical picture is well reproduced by modelling.

9.3.1.2 Towards an Improved Scaling Relation

While a full computation of mode damping rates reproduces the observations, the dependence of η on the effective temperature with such a large exponent is far to be obvious. Hence, to get more insight into this relation, let us distinguish between the effect of the inertia and the work integral (see Eq. (9.35)). For the latter, it is useful to consider Eq. (9.31) which exhibits two terms related to the non-adiabatic part of the total pressure and the turbulent pressure. Since these correspond to a transfer of energy between the pulsation and convection, it can be assumed at first glance that the work integral scales dimensionally with the ratio L/M. As verified by [21], it follows that the relation

$$\eta I \propto \left(\frac{L}{M}\right)^{2.7} \tag{9.40}$$

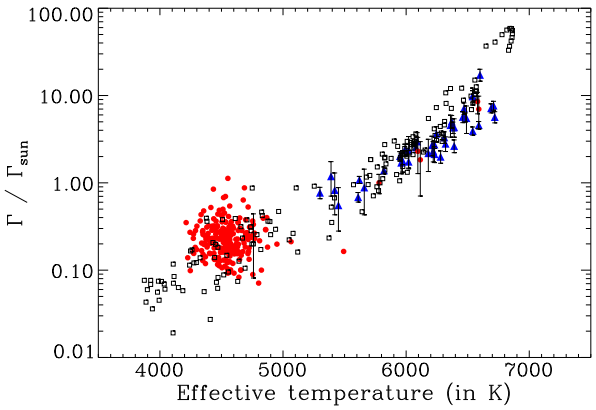

Fig. 9.4 Mode linewidths (normalised by the solar value, $\Gamma_{\rm sun} = 0.95$ μHz) versus effective temperature. The *squared symbols* represent theoretical calculations computed as explained in [21]. The *triangles* correspond to the observations of main-sequence stars derived by [4] from the Kepler data (with their 3-σ error-bars). The *dots* correspond to the observations of red giants (with $T_{\rm eff} < 5200$ K) and main-sequence (with $T_{\rm eff} > 5200$ K, with their 3-σ error-bars) stars as derived by [10, 11] from the CoRoT data

holds. In contrast, mode inertia (I) does not depend on mode energy leakage but rather on the star's static structure and, more precisely, on the properties of its uppermost layers. Hence, one can expect mode inertia to scale with the surface gravity.[4] More precisely, it has been shown in [21] that

$$I \propto g^{-2.4}. \tag{9.41}$$

Using Eqs. (9.40) and (9.41), it turns out that

$$\eta \propto T_{\rm eff}^{10.8} g^{-0.3}. \tag{9.42}$$

Such a crude analysis is unable to reproduce the precise shape of the mode linewidth with effective temperature. However, it does allow us to explain qualitatively the strong dependence of mode damping rates on effective temperature.

9.3.2 Relation Between $\nu_{\rm max}$ and $\nu_{\rm c}$

It has been conjectured by [23] that the frequency of the maximum of the power spectrum ($\nu_{\rm max}$) scales as the cut-off frequency $\nu_{\rm c}$, because the latter corresponds to a typical time scale of the atmosphere. The recent discovery of many stars with solar-like oscillations has confirmed this relation (e.g., [12, 71]). This relation has been theoretically explained by [19].

[4] Note that mode inertia also scales with the dynamical time scale $\sqrt{(GM/R^3)}$ with almost the same dispersion as for the surface gravity.

9.3.2.1 Maximum of the Power Spectrum

As a first step towards an understanding, one must determine which of the damping rate and the excitation rate is mainly responsible for the maximum of power in the observed spectra. Thus, we introduce the height of the mode profile in the power spectrum, which is an observable, as [15, 25]

$$H = \frac{P}{2\eta^2 \mathscr{M}}, \tag{9.43}$$

where $\mathscr{M}$ is the mode mass defined as the ratio $I/|\xi|^2$.

It is useful to express H in a form that does not explicitly depend on the mode mass ($\mathscr{M}$). To this end, we note that both the excitation P and the damping rate η are inversely proportional to the mode mass. Hence, to separate the effect of the driving and damping from the effect of mode mass, we introduce the quantities $\Pi = \mathscr{P}\mathscr{M}$ and $\Theta = \eta\mathscr{M}$, both independent of mode masses. Then, using Eq. (9.43), the expression of the mode height becomes

$$H = \frac{\Pi}{2\Theta^2}. \tag{9.44}$$

From Eq. (9.44) it turns out that the maximum of H is determined by the minimum of Θ^2 and corresponds to the plateau of the line widths. In other words, the depression (also named plateau) of the damping rates η is responsible for the presence of a maximum in the power spectrum, in agreement with [26]. This result is confirmed for the Sun by the GOLF observations [19] and more recently for solar-like stars by Kepler observations [4].

Therefore, the pertinent issue is to determine the origin of the plateau of the damping rates in order to settle the physical origin of the maximum of H and so that of $\nu_{\max}$.

9.3.2.2 Depression of the Damping Rates

Reference [6] first mentioned that the depression of the solar damping rates originates in a destabilising effect in the super-adiabatic layer. He also stressed that the plateau of the damping rates occurs when there is a resonance between the thermal time scale and the modal frequency. This result has been confirmed by [19] using the formalism described in Sect. 9.2.2. The mechanism responsible for the destabilising effect is therefore the Lagrangian perturbation of entropy (δS) that exhibits a rapid variation mainly in the super-adiabatic layers and in the atmospheric layers.

Reference [19] also proposed a simplified model to *illustrate* the role played by the entropy fluctuations. In the limit of highly non-adiabatic solution, the perturbations of both radiative and convective luminosities are dominated by perturbations of entropy. This leads to a second-order equation for the entropy perturbations δS

that can further be reduced to one of first-order by considering $\mathrm{d}\delta L/\mathrm{d}r \approx \delta L/H_p$. It was found then that

$$\frac{\mathrm{d}}{\mathrm{d}\ln T}\left(\frac{\delta S}{c_v}\right) + \lambda\left(\frac{\delta S}{c_v}\right) = 0 \quad \text{with } \lambda = \mathscr{A} - i\mathscr{B}, \tag{9.45}$$

where $c_v = (\partial U/\partial T)_\rho$ with U the internal energy, $\mathscr{A}$ is given by Eq. (8) of [19], and $\mathscr{B}$ defined by

$$\mathscr{B} = \mathscr{Q}\left[1 + (\psi - 1)\frac{L_c}{L}\right]^{-1}, \tag{9.46}$$

where $\kappa_T = (\partial \ln \kappa/\partial \ln T)_\rho$, L_c, and L_R are the convective and radiative luminosity respectively, T the temperature, and ψ is defined by Eq. (A.8) of [19]. We defined the ratio $\mathscr{Q}$ such as

$$\mathscr{Q} = \omega_{\mathrm{osc}}\tau \quad \text{with } \tau^{-1} = \frac{L}{4\pi r^2 \rho c_v T H_p} = \tau_{\mathrm{conv}}^{-1} + \tau_{\mathrm{rad}}^{-1} \tag{9.47}$$

with τ a local thermal time scale and τ_{rad} and τ_{conv} the radiative and convective thermal time scales, respectively.

From Eq. (9.45), the oscillatory part of $(\delta S/c_v)$ is proportional to $\exp[-\mathrm{i}\int \mathscr{B}\,\mathrm{d}\ln T]$ in the super-adiabatic layers. Depending on the coefficient $\mathscr{Q}$, the contribution from the entropy fluctuations to the damping rates will compensate for the contribution from the turbulent pressure (see Eq. (9.34) and Fig. 9.2). As shown by [19], a minimal damping is then obtained for $\mathscr{Q} \simeq 1$, where the destabilising contribution (from δS) nearly, but not completely, compensates for the strong damping of those layers below the super adiabatic (from δP_{turb}).

9.3.2.3 Relation Between the Cut-Off Frequency and the Thermal Frequency

From the deliberations of the previous section we see that the maximum of H (consequently, $\nu_{\max}$) occurs at the resonance $\mathscr{Q} \simeq 1$. Hence, from Eq. (9.47) one derives the resonance condition

$$\nu_{\max} \simeq \frac{1}{2\pi\tau}. \tag{9.48}$$

Further, using the mixing-length formalism, it has been shown [19] that there is a linear relation between $1/\tau$ and the cut-off frequency (ν_{c}). From Fig. 9.5, the relation between the thermal frequency $(1/\tau)$ and the cut-off frequency (ν_{c}) is close to linear, but still shows a significant dispersion for main-sequence stars, related to the dependence of $1/\tau$ on the Mach number. Indeed, using the mixing-length formalism, it is possible to show that

$$\nu_{\max} \propto \frac{1}{\tau} \propto \left(\frac{\mathscr{M}_a^3}{\alpha}\right)\nu_{\mathrm{c}}, \tag{9.49}$$

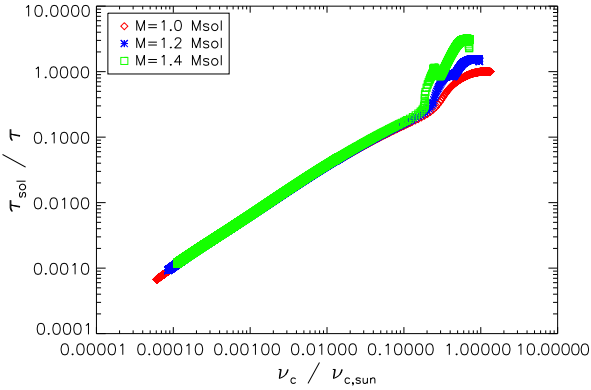

Fig. 9.5 Thermal frequency ($1/\tau$) versus the cut-off frequency (computed as the ratio $c_s/(2Hp)$), normalised to the solar values, for models with masses ranging from $M = 1.0M_\odot$, $M = 1.2M_\odot$, and $M = 1.4M_\odot$ from the ZAMS to the ascending vertical branch. The inputs physics of the models can be found in [19]

where $\mathscr{M}_a$ is the turbulent Mach number, and α the mixing-length parameter. From Eq. (9.49) we then conclude that the observed relation between $\nu_{\max}$ and ν_c is indeed the result of the resonance between $\nu_{\max}$ and $1/\tau$, as well as the relation between $1/\tau$ and ν_c.

9.3.3 Mode Amplitudes Across the HR Diagram

In this section, we consider the relations between mode amplitudes, in terms of both velocity and intensity fluctuations. These provide information on turbulent convection, mode physics, and stellar structure.

9.3.3.1 Theoretical Scaling Law in Terms of Mode Surface Velocity

On the basis of the theoretical calculations of [28, 45] have derived the first example of a scaling law given in terms of the maximum of the mode surface velocity (hereafter $V_{\max}$). This scaling law predicts that $V_{\max}$ varies as the ratio $(L/M)^s$ with a slope $s \simeq 1$. The theoretical calculations of [28] were based on the assumption that there is an *equipartition* between the energy carried by the most energetic eddies and the modes. As mentioned by [17] and [60], a necessary (but not sufficient) condition for having such equipartition is that turbulent viscosity is the dominant source of damping. However, there is currently no consensus as to the dominant physical processes contributing to the damping of p-modes, and, furthermore, this assumption is not supported by observations (see Sect. 9.2.2). Following the scaling proposed by [45], other theoretical scaling laws have been proposed and compared with ground-based Doppler measurements. We present here the latest such proposals by [64] and [68] and compare them with seismic data.

The mean-squared surface velocity of a mode is given by [60]

$$V^2(\nu_{\rm osc}, r) = \frac{\tau(\nu_{\rm osc})}{2} \frac{\mathscr{P}(\nu_{\rm osc})}{\mathscr{M}(\nu_{\rm osc,r})}, \tag{9.50}$$

where τ is the mode life-time (which is equal to the inverse of the mode damping rate η), r the radius in the atmosphere in which the mode velocity is measured, and $\mathscr{M}$ is the mode mass, which is defined for radial modes by the ratio $I/|\xi_r|^2$. Note that the mode mass must, in principle, be evaluated at the layer of the atmosphere where spectrographs dedicated to stellar seismology are the most sensitive. However, this layer is not well known [65]. Hence, for sake of simplicity, $\mathscr{M}$ is evaluated at the photosphere (i.e., $T = T_{\rm eff}$).

For the Sun, the frequency ($\nu_{\rm max}$) at which V reaches a maximum is shown to coincide with the frequency location of the plateau in the mode life-time τ (see [19] and Sect. 9.3.1). It was also found by [68] that $\mathscr{P}$, as well as the ratio $(\mathscr{P}/\mathscr{M})$, peak at this frequency. As a consequence, the existence of a scaling law for $V_{\rm max}$ simply relies on the existence of a scaling law for $\tau_{\rm max}$, $\mathscr{P}_{\rm max}$, and $\mathscr{M}_{\rm max}$ where $\tau_{\rm max}$, $\mathscr{P}_{\rm max}$, and $\mathscr{M}_{\rm max}$ are respectively the values of τ, $\mathscr{P}$, and $\mathscr{M}$ at $\nu = \nu_{\rm max}$. Scaling laws for $\tau_{\rm max}$ (i.e., $1/\eta$) have been presented and discussed in Sect. 9.3.1.

So, to derive a scaling relation for $V_{\rm max}$, the first step to make is to determine a relation between $\mathscr{P}_{\rm max}$ and $\mathscr{M}_{\rm max}$. Reference [64] have established, on the basis of a small set of 3D models of the surface layers of main-sequence (MS) stars, that $\mathscr{P}_{\rm max}$ scales as $(L/M)^s$, where the slope s is found to depend significantly on the adopted prescription for the frequency factor $\chi_k(\omega)$ (see the definition given in Sect. 9.2.1). A Lorentzian $\chi_k(\omega)$ is the more realistic choice [18, 62] and results in a slope $s = 2.6$. More recently, this study was extended by [68] to the case of sub- and red-giant stars. The authors found for $\mathscr{P}_{\rm max}$ the same scaling law as the one found for MS.

The dependence of $\mathscr{P}_{\rm max}$ on L and M can been explained on the basis of simple theoretical considerations [60]. We first point out that the ratio L/M is equivalent to the ratio $T_{\rm eff}^4/g$. In turn, the dependence on $T_{\rm eff}$ and g can be roughly explained as follows. We start from Eq. (9.21). Assuming a propagating wave, it is shown that $(d\xi_r/dr)^2 = \omega_{\rm osc}^2/c_s^2\xi_r^2$, where c_s is the sound speed. Accordingly, Eq. (9.21) simplifies to

$$\mathscr{P} \propto \frac{\nu_{\rm osc}^2}{I} \int \left(\frac{\xi_r}{c_s}\right)^2 F_{\rm kin} \Lambda^4 \, {\rm d}m, \tag{9.51}$$

where $\nu_{\rm osc} = \omega_{\rm osc}/(2\pi)$. The integrand of Eq. (9.51) is evaluated, for the sake of simplicity, at a single layer of the surface where mode driving is predominant. This layer being close to the photosphere, the term $\Lambda^4 F_{\rm kin}$ that appears in the integrand of Eq. (9.51) is evaluated at the photosphere (i.e., at $T = T_{\rm eff}$). This yields

$$\mathscr{P} \propto F_{\rm kin} \Lambda^4 \left(\frac{\nu_{\rm osc}}{c_s}\right)^2 \frac{1}{I} \int {\rm d}m \, \xi_r^2. \tag{9.52}$$

Finally, with the help of Eq. (9.52), the above reduces to

$$\mathscr{P} \propto F_{\rm kin} \Lambda^4 \left(\frac{\nu_{\rm osc}}{c_s}\right)^2. \tag{9.53}$$

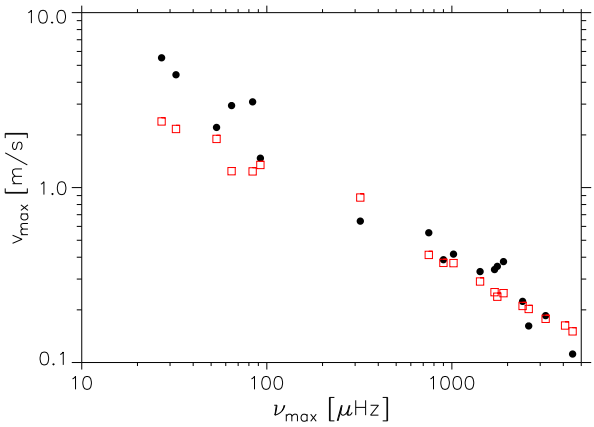

Fig. 9.6 Maximum of the mode velocity $V_{\max}$ as a function of $\nu_{\max}$. The *filled circles* correspond to observations, while the *red squares* correspond to the scaling law given by Eq. (9.55). For sub- and reg-giant ($\nu_{\max} \lesssim 200$ μHz), we have taken $p = 2.0$ and for MS ($\nu_{\max} \gtrsim 200$ μHz) $p = 1.3$

As already noticed in Sect. 9.2.2, $F_{\rm kin}$ scales approximately with the convective flux F_c, which is proportional to $T_{\rm eff}^4$ (in the upper part of the convective zone). We recall that $\nu_{\max}$ is shown to scale as $g/T_{\rm eff}^{1/2}$ and c_s as $T_{\rm eff}^{1/2}$ (see Sect. 9.3.2.1). Finally, the characteristic size Λ scales in turn as $T_{\rm eff}/g$. When we combine all of these scaling relations in Eq. (9.53), we establish that $\mathscr{P}_{\max}$ scales approximately as $T_{\rm eff}^6 g^{-2}$. This crude result then qualitatively explains the theoretical scaling laws found for $\mathscr{P}_{\max}$ by [64] and [68].

We now turn to $\mathscr{M}_{\max}$. In [68] it is found that for sub- and red-giant stars, $\mathscr{M}_{\max}$ scales as $(M/R^3)^{-p/2.}$ with $p = 2.0 \pm 0.1$. Accordingly, $\mathscr{M}_{\max}$ scales as the inverse of the star mean density, i.e., $\langle\rho\rangle \propto (M/R^3)$. For MS stars, the calculations performed by [64] yield a different slope, $p = 1.3 \pm 0.2$. These two different relations between $\mathscr{M}_{\max}$ and $\langle\rho\rangle$ are not yet understood and call for some theoretical support. When we combine the scaling laws for $\tau_{\max}$ (see Sect. 9.2.2), $\mathscr{P}_{\max}$ and $\mathscr{M}_{\max}$, into Eq. (9.50), we obtain for $V_{\max}$ the following law:

$$V_{\max} \propto T_{\rm eff}^{-5.4} g^{0.15} \left(\frac{L}{M}\right)^{1.3} \left(\frac{M}{R^3}\right)^{p/4}. \tag{9.54}$$

Given the fact that the large separation $\Delta\nu$ typically scales as $(M/R^3)^{1/2}$ (e.g., [74]), $\nu_{\max}$ scales as $g/T_{\rm eff}^{1/2}$ and that (L/M) is proportional to $T_{\rm eff}^{7/2}/\nu_{\max}$ [10, 11], Eq. (9.54) can be reformulated to include only the seismic indices $\nu_{\max}$ and $\Delta\nu$ and $T_{\rm eff}$:

$$V_{\max} \propto T_{\rm eff}^{-0.77} \nu_{\max}^{-1.15} \Delta\nu^{p/2}. \tag{9.55}$$

The scaling law given by Eq. (9.55) is compared in Fig. 9.6 with the ground-based Doppler velocity measurements obtained to the present. The amplitudes of the solar-like oscillations measured in MS are rather well reproduced by the theoretical scaling law. This is not the case for the sub- and red-giant stars for which the predictions are found to be systematically below the observations. We refer the reader to [68] for a detailed discussion about this discrepancy.

9.3.3.2 From Velocity to Bolometric Amplitudes

Current space-based missions (CoRoT and Kepler) detect and measure solar-like oscillations in numerous stars, using methods of high-precision photometry. Therefore, in order to compare predicted with measured mode amplitudes, it is necessary to convert mode-velocity amplitudes to intensity amplitudes.

The instantaneous bolometric mode amplitude is deduced at the photosphere according to [31, 58]

$$\frac{\delta L(t)}{L} = 4\frac{\delta T_{\rm eff}(t)}{T_{\rm eff}} + 2\frac{\delta R_*(t)}{R_*}, \tag{9.56}$$

where $\delta L(t)$ is the mode Lagrangian (bolometric) luminosity perturbation, $\delta T_{\rm eff}(t)$ the effective temperature fluctuation, and $\delta R_*(t)$ the variation of the stellar radius. The second term of Eq. (9.56) is negligible compared to $\delta T_{\rm eff}(t)$, so the rms bolometric amplitudes are given by

$$\left(\frac{\delta L}{L}\right)_{\rm rms} = 4\left(\frac{\delta T_{\rm eff}}{T_{\rm eff}}\right)_{\rm rms}, \tag{9.57}$$

where the subscript rms denotes the root mean-square.

We need the relationship between $(\delta T_{\rm eff}/T_{\rm eff})_{\rm rms}$ (or equivalently $(\frac{\delta L}{L})_{\rm rms}$) and the rms mode velocity $V_{\rm rms}$. To this end, we introduce the dimensionless coefficient ζ defined by

$$\left(\frac{\delta L}{L}\right)_{\rm rms} = 4\left(\frac{\delta T_{\rm eff}}{T_{\rm eff}}\right)_{\rm rms} = \zeta\left(\frac{\delta L}{L}\right)^{\odot}_{\rm rms}\left(\frac{V_{\rm rms}}{V_{\odot}}\right), \tag{9.58}$$

where $(\frac{\delta L}{L})^{\odot}_{\rm rms} = 2.53 \pm 0.11$ ppm is the maximum of the solar bolometric mode amplitude [53], $T^{\odot}_{\rm eff} = 5777$ K the effective temperature of the Sun, and $V^{\odot}_{\rm rms} = 18.5 \pm 1.5$ cm/s is the maximum of the solar mode (intrinsic) surface velocity evaluated at the photosphere as explained in [66].

Let us now define $(\delta L/L)_{\rm max}$ to be the maximum of $(\delta L/L)_{\rm rms}$. We want to establish a scaling for $(\delta L/L)_{\rm max}$. As seen in Eq. (9.58), we require a scaling law for ζ since that for $V_{\rm rms}$ is given by Eq. (9.54) (or equivalently by Eq. (9.55)). Consistent calculation of ζ requires us to take into account the energy lost by the pulsation. This can be estimated using a non-adiabatic pulsation code that takes into account coupling between oscillation, radiation, and turbulent convection (as described in Sect. 9.2.2). Due to the difficulties of consistently treating the underlying mechanisms, the use of the quasi-adiabatic relation has been proposed by [45] and is adopted for converting mode surface velocity into intensity amplitude. Indeed, adopting quasi-adiabatic pulsation and assuming an isothermal atmosphere,[5] one

[5] A more sophisticated quasi-adiabatic approach has been proposed by [69]. These authors go beyond the approximation of isothermal atmosphere by taking into account the temperature gradient and the fact that the intensity is measured at constant instantaneous optical depth. Both effects are taken into account by the non-adiabatic pulsation code MAD.

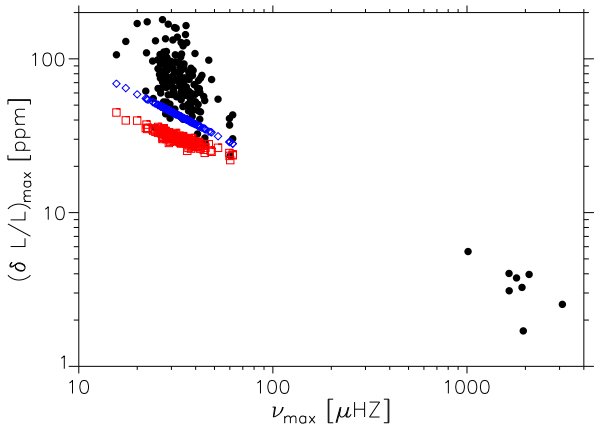

Fig. 9.7 Maximum of the mode intensity fluctuation $(\delta L/L)_{\max}$ as a function of $\nu_{\max}$. The *filled circles* located below $\nu_{\max} = 200$ μHz correspond to the seismic measures performed by [10, 11] on a large number of CoRoT red-giant stars, while those located above $\nu_{\max} = 200$ μHz correspond to the MS stars observed so far by CoRoT [10, 11]. The *red squares* are the theoretical amplitudes obtained with the adiabatic scaling law of Eq. (9.60), while the *blue diamonds* to those computed on the basis of the non-adiabatic scaling law given by Eq. (9.62)

can easily relate mode surface velocity to intensity perturbations (e.g., [45]). These approximations yield the following simple expression for ζ [45]:

$$\zeta_{\rm K95} = \sqrt{\frac{T_{\rm eff}^{\odot}}{T_{\rm eff}}}. \tag{9.59}$$

Derivation of Eq. (9.59) supposes that the modes propagate at the surface where they are measured. However, the acoustic modes are evanescent at the surface. Combining Eqs. (9.59) and (9.58) gives for $(\delta L/L)_{\max}$ the (quasi)-adiabatic scaling law:

$$(\delta L/L)_{\max} \propto T_{\rm eff}^{-0.5} V_{\max}, \tag{9.60}$$

where the scaling law of $V_{\max}$ is given by Eq. (9.55).

Bolometric mode amplitudes computed on the basis of Eq. (9.60) are compared with the bolometric mode amplitudes measured by [10, 11] on a set of CoRoT red-giant stars in Fig. 9.7. The adiabatic relation of Eq. (9.60) results, for red-giant stars, in a significant under-estimation compared to the CoRoT seismic data.

Reference [68] have computed the coefficient ζ (see Eq. (9.58)) using the MAD non-adiabatic pulsation code [42] and established that, for sub- and red-giants, ζ scales as

$$\zeta_{\rm nad} = \zeta_0 \left(\frac{L}{L_{\odot}} \frac{M_{\odot}}{M} \right)^{0.25}, \tag{9.61}$$

where $\zeta_0 = 0.59$. The increase of ζ with the ratio L/M is not surprising. Indeed, energy losses scale dimensionally as L/M. Red-giants stars are characterised by high

luminosities. As a consequence, we expect, for red-giants, large differences between $\zeta_{\rm nad}$ and ζ_{K95}. We recall that L/M is proportional to $T_{\rm eff}^{7/2}/\nu_{\rm max}$. Accordingly, substituting Eq. (9.61) into Eq. (9.58) yields, for $(\delta L/L)_{\rm max}$, the non-adiabatic scaling law[6]

$$(\delta L/L)_{\rm max} \propto T_{\rm eff}^{0.875}\, \nu_{\rm max}^{-0.25}\, V_{\rm max}\,, \tag{9.62}$$

where $V_{\rm max}$ is given by Eq. (9.55) with $p = 2$. This scaling law is compared in Fig. 9.7 with CoRoT observations. As seen in the figure, the differences that were found between the adiabatic scaling law and the CoRoT observations are reduced using the non-adiabatic scaling law. However, the remaining differences are still important. Their possible origins are discussed in [68].

9.4 Concluding Remarks

We have presented the state-of-the-art in the modelling of the physical processes of both driving and damping of solar-like modes with particular emphasis on the connections between pulsation and convection. We have shown that most of the observed scaling relations between asteroseismic quantities and stellar parameters are related to these connections.

This era of asteroseismology (also named ensemble asteroseismology) is only beginning, but has already shown great promise in providing information on turbulent convection properties. As a result, one can expect to be able to infer from studying mode amplitudes (including both driving and damping processes) these properties in stars from the main-sequence to red-giant phase.

Last, but not least, scaling relations are expected to provide us a *model-independent* and *accurate* determination of stellar parameters for a large set of stars, up to now impossible using classical methods. Actually, combining the scaling laws established for η, $\nu_{\rm max}$, and $\Delta\nu$ gives us access, at least in principle, to the mass, the radius, and the effective temperature of a star using only seismic data, i.e., without the help of spectroscopic measurements or stellar models. Although the scaling relations associated with $\nu_{\rm max}$ and $\Delta\nu$ are now rather well established and accepted, those for η still require investigations. Furthermore, all of these scaling laws ignore the influence of the abundance of surface metal, which has, for instance, been shown to have an important influence on mode amplitude [44, 66, 67]. As shown by [19], the relation between $\nu_{\rm max}$ and ν_c involves the turbulent Mach number, which is expected to depend on surface metal abundance [67]. Therefore, most of the dispersion seen in the observational data may well have a physical origin such as metal abundances.

Thus, a major effort towards a full understanding of the physical mechanisms governing mode physics is required. This is the keystone of an accurate determination of stellar parameters across a wide range of stars, a prospect anticipated keenly in large domains of astrophysics ranging from cosmology to investigations of galactic structure and evolution.

[6] This scaling is only valid for sub- and red-giant stars.

References

1. Ando, H., Osaki, Y.: Nonadiabatic nonradial oscillations: an application to the five-minute oscillation of the Sun. Publ. Astron. Soc. Jpn. **27**, 581–603 (1975)
2. Antia, H.M., Chitre, S.M., Narasimha, D.: Overstability of acoustic modes and the solar five-minute oscillations. Sol. Phys. **77**, 303–327 (1982)
3. Appourchaux, T., Michel, E., Auvergne, M., Baglin, A., Toutain, T., Baudin, F., Benomar, O., Chaplin, W.J., Deheuvels, S., Samadi, R., Verner, G.A., Boumier, P., García, R.A., Mosser, B., Hulot, J.C., Ballot, J., Barban, C., Elsworth, Y., Jiménez-Reyes, S.J., Kjeldsen, H., Régulo, C., Roxburgh, I.W.: CoRoT sounds the stars: p-mode parameters of sun-like oscillations on HD 49933. Astron. Astrophys. **488**, 705–714 (2008)
4. Appourchaux, T., Benomar, O., Gruberbauer, M., Chaplin, W.J., García, R.A., Handberg, R., Verner, G.A., Antia, H.M., Campante, T.L., Davies, G.R., Deheuvels, S., Hekker, S., Howe, R., Salabert, D., Bedding, T.R., White, T.R., Houdek, G., Silva Aguirre, V., Elsworth, Y.P., van Cleve, J., Clarke, B.D., Hall, J.R., Kjeldsen, H.: Oscillation mode linewidths of main-sequence and subgiant stars observed by Kepler. Astron. Astrophys. **537**, A134 (2012)
5. Balmforth, N.J.: Solar pulsational stability—III. Acoustical excitation by turbulent convection. Mon. Not. R. Astron. Soc. **255**, 639 (1992)
6. Balmforth, N.J.: Solar pulsational stability—I. Pulsation-mode thermodynamics. Mon. Not. R. Astron. Soc. **255**, 603–649 (1992)
7. Basu, S., Chaplin, W.J., Elsworth, Y.: Determining stellar radii using large separations: an error analysis. Astrophys. Space Sci. **328**, 79–82 (2010)
8. Batchelor, G.K.: The Theory of Homogeneous Turbulence. Cambridge University Press, Cambridge (1970)
9. Baudin, F., Samadi, R., Goupil, M.J., Appourchaux, T., Barban, C., Boumier, P., Chaplin, W.J., Gouttebroze, P.: Inferred acoustic rates of solar p modes from several helioseismic instruments. Astron. Astrophys. **433**, 349–356 (2005)
10. Baudin, F., Barban, C., Belkacem, K., Hekker, S., Morel, T., Samadi, R., Benomar, O., Goupil, M.J., Carrier, F., Ballot, J., Deheuvels, S., De Ridder, J., Hatzes, A.P., Kallinger, T., Weiss, W.W.: Amplitudes and lifetimes of solar-like oscillations observed by CoRoT. Red-giant versus main-sequence stars. Astron. Astrophys. **529**, A84 (2011)
11. Baudin, F., Barban, C., Belkacem, K., Hekker, S., Morel, T., Samadi, R., Benomar, O., Goupil, M.J., Carrier, F., Ballot, J., Deheuvels, S., De Ridder, J., Hatzes, A.P., Kallinger, T., Weiss, W.W.: Amplitudes and lifetimes of solar-like oscillations observed by CoRoT. Red-giant versus main-sequence stars. Astron. Astrophys. **535**, C1 (2011)
12. Bedding, T.R., Kjeldsen, H.: Solar-like oscillations. Publ. Astron. Soc. Aust. **20**, 203–212 (2003)
13. Belkacem, K.: Amplitudes of solar gravity modes. In: Rozelot, J.P., Neiner, C. (eds.) Pulsation of the Sun and Stars. Lecture Notes in Physics, vol. 832, p. 139 (2011)
14. Belkacem, K., Samadi, R., Goupil, M.J., Kupka, F.: A closure model with plumes. I. The solar convection. Astron. Astrophys. **460**, 173–182 (2006)
15. Belkacem, K., Samadi, R., Goupil, M.J., Kupka, F., Baudin, F.: A closure model with plumes. II. Application to the stochastic excitation of solar p modes. Astron. Astrophys. **460**, 183–190 (2006)
16. Belkacem, K., Samadi, R., Goupil, M.J., Dupret, M.A.: Stochastic excitation of non-radial modes. I. High-angular-degree p modes. Astron. Astrophys. **478**, 163–174 (2008)
17. Belkacem, K., Samadi, R., Goupil, M.J., Dupret, M.A., Brun, A.S., Baudin, F.: Stochastic excitation of nonradial modes. II. Are solar asymptotic gravity modes detectable? Astron. Astrophys. **494**, 191–204 (2009)
18. Belkacem, K., Samadi, R., Goupil, M.J., Baudin, F., Salabert, D., Appourchaux, T.: Turbulent eddy-time-correlation in the solar convective zone. Astron. Astrophys. **522**, L2 (2010)
19. Belkacem, K., Goupil, M.J., Dupret, M.A., Samadi, R., Baudin, F., Noels, A., Mosser, B.: The underlying physical meaning of the $\nu_{\max} - \nu_c$ relation. Astron. Astrophys. **530**, A142 (2011)

20. Belkacem, K., Samadi, R., Goupil, M.: Amplitudes of solar p modes: modelling of the eddy time-correlation function. J. Phys. Conf. Ser. **271**(1), 012047 (2011)
21. Belkacem, K., Dupret, M.A., Baudin, F., Appourchaux, T., Marques, J.P., Samadi, R.: Damping rates of solar-like oscillations across the HR diagram. Theoretical calculations confronted to CoRoT and Kepler observations. Astron. Astrophys. **540**, L7 (2012)
22. Bohm-Vitense, E.: Introduction to Stellar Astrophysics vol. 3. Cambridge University Press, Cambridge (1989)
23. Brown, T.M., Gilliland, R.L., Noyes, R.W., Ramsey, L.W.: Detection of possible p-mode oscillations on Procyon. Astrophys. J. **368**, 599–609 (1991)
24. Canuto, V.M.: Turbulent convection with overshooting—Reynolds stress approach. Astrophys. J. **392**, 218–232 (1992)
25. Chaplin, W.J., Houdek, G., Elsworth, Y., Gough, D.O., Isaak, G.R., New, R.: On model predictions of the power spectral density of radial solar p modes. Mon. Not. R. Astron. Soc. **360**, 859–868 (2005)
26. Chaplin, W.J., Houdek, G., Appourchaux, T., Elsworth, Y., New, R., Toutain, T.: Challenges for asteroseismic analysis of Sun-like stars. Astron. Astrophys. **485**, 813–822 (2008)
27. Chaplin, W.J., Houdek, G., Karoff, C., Elsworth, Y., New, R.: Mode lifetimes of stellar oscillations. Implications for asteroseismology. Astron. Astrophys. **500**, L21–L24 (2009)
28. Christensen-Dalsgaard, J., Frandsen, S.: Stellar 5 min oscillations. Sol. Phys. **82**, 469–486 (1983)
29. Dolginov, A., Muslimov, A.: Nonradial stellar oscillations excited by turbulent convection. Astrophys. Space Sci. **98**, 15–36 (1984)
30. Dupret, M.A., Barban, C., Goupil, M.J., Samadi, R., Grigahcène, A., Gabriel, M.: Theoretical damping rates and phase-lags for solar-like oscillations. In: Proceedings of SOHO 18/GONG 2006/HELAS I, Beyond the Spherical Sun. ESA Special Publication, vol. 624 (2006)
31. Dziemblowski, W.: Oscillations of giants and supergiants. Acta Astron. **27**, 95–126 (1977)
32. Evans, J.W., Michard, R.: Observational study of macroscopic inhomogeneities in the solar atmosphere. III. Vertical oscillatory motions in the solar photosphere. Astrophys. J. **136**, 493 (1962)
33. Freytag, B., Holweger, H., Steffen, M., Ludwig, H.G.: On the scale of photospheric convection. In: Paresce, F. (ed.) Science with the VLT Interferometer, p. 316 (1997)
34. Gabriel, A.H., Grec, G., Charra, J., Robillot, J.M., Roca Cortés, T., Turck-Chièze, S., Bocchia, R., Boumier, P., Cantin, M., Cespédes, E., Cougrand, B., Crétolle, J., Damé, L., Decaudin, M., Delache, P., Denis, N., Duc, R., Dzitko, H., Fossat, E., Fourmond, J.J., García, R.A., Gough, D., Grivel, C., Herreros, J.M., Lagardère, H., Moalic, J.P., Pallé, P.L., Pétrou, N., Sanchez, M., Ulrich, R., van der Raay, H.B.: Global oscillations at low frequency from the SOHO mission (GOLF). Sol. Phys. **162**, 61–99 (1995)
35. Gautschy, A., Saio, H.: Stellar pulsations across the HR diagram: Part 1. Annu. Rev. Astron. Astrophys. **33**, 75–114 (1995)
36. Gautschy, A., Saio, H.: Stellar pulsations across the HR diagram: Part 2. Annu. Rev. Astron. Astrophys. **34**, 551–606 (1996)
37. Goldreich, P., Keeley, D.A.: Solar seismology. I. The stability of the solar p-modes. Astrophys. J. **211**, 934–942 (1977)
38. Goldreich, P., Keeley, D.A.: Solar seismology. II. The stochastic excitation of the solar p-modes by turbulent convection. Astrophys. J. **212**, 243–251 (1977)
39. Goldreich, P., Kumar, P.: Thermal and mechanical damping of solar p-modes. Astrophys. J. **374**, 366–368 (1991)
40. Goldreich, P., Murray, N., Kumar, P.: Excitation of solar p-modes. Astrophys. J. **424**, 466–479 (1994)
41. Gough, D.: Some theoretical remarks on solar oscillations. In: Hill, H.A., Dziembowski, W.A. (eds.) Nonradial and Nonlinear Stellar Pulsation. Lecture Notes in Physics, vol. 125, pp. 273–299 (1980)
42. Grigahcène, A., Dupret, M.A., Gabriel, M., Garrido, R., Scuflaire, R.: Convection-pulsation coupling. I. A mixing-length perturbative theory. Astron. Astrophys. **434**, 1055–1062 (2005)

43. Houdek, G.: The effect of convection on pulsational stability. Commun. Asteroseismol. **157**, 137–143 (2008)
44. Houdek, G., Balmforth, N.J., Christensen-Dalsgaard, J., Gough, D.O.: Amplitudes of stochastically excited oscillations in main-sequence stars. Astron. Astrophys. **351**, 582–596 (1999)
45. Kjeldsen, H., Bedding, T.R.: Amplitudes of stellar oscillations: the implications for asteroseismology. Astron. Astrophys. **293**, 87–106 (1995)
46. Ledoux, P., Walraven, T.: Variable stars. Handb. Phys. **51**, 353–604 (1958)
47. Leibacher, J.W., Stein, R.F.: A new description of the solar five-minute oscillation. Astrophys. J. Lett. **7**, 191–192 (1971)
48. Leighton, R.B., Noyes, R.W., Simon, G.W.: Velocity fields in the solar atmosphere. I. Preliminary report. Astrophys. J. **135**, 474 (1962)
49. Lesieur, M.: Turbulence in Fluids, 3rd edn. Kluwer Academic, Dordrecht (1997)
50. Lighthill, M.: On sound generated aerodynamically. I. General theory. Proc. R. Soc. Lond. Ser. A **211**, 564–587 (1952)
51. Lighthill, J.: Waves in Fluids. Cambridge University Press, Cambridge (1978)
52. Michel, E., Baglin, A., Auvergne, M., Catala, C., Samadi, R., Baudin, F., Appourchaux, T., Barban, C., Weiss, W.W., Berthomieu, G., Boumier, P., Dupret, M.A., Garcia, R.A., Fridlund, M., Garrido, R., Goupil, M.J., Kjeldsen, H., Lebreton, Y., Mosser, B., Grotsch-Noels, A., Janot-Pacheco, E., Provost, J., Roxburgh, I.W., Thoul, A., Toutain, T., Tiphène, D., Turck-Chieze, S., Vauclair, S.D., Vauclair, G.P., Aerts, C., Alecian, G., Ballot, J., Charpinet, S., Hubert, A.M., Lignières, F., Mathias, P., Monteiro, M.J.P.F.G., Neiner, C., Poretti, E., Renan de Medeiros, J., Ribas, I., Rieutord, M.L., Cortés, T.R., Zwintz, K.: CoRoT measures solar-like oscillations and granulation in stars hotter than the Sun. Science **322**, 558 (2008)
53. Michel, E., Samadi, R., Baudin, F., Barban, C., Appourchaux, T., Auvergne, M.: Intrinsic photometric characterisation of stellar oscillations and granulation. Solar reference values and CoRoT response functions. Astron. Astrophys. **495**, 979–987 (2009)
54. Miglio, A., Montalbán, J., Baudin, F., Eggenberger, P., Noels, A., Hekker, S., de Ridder, J., Weiss, W., Baglin, A.: Probing populations of red giants in the galactic disk with CoRoT. Astron. Astrophys. **503**, L21–L24 (2009)
55. Mosser, B., Belkacem, K., Goupil, M., Miglio, A., Morel, T., Barban, C., Baudin, F., Hekker, S., Samadi, R., De Ridder, J., Weiss, W., Auvergne, M., Baglin, A.: Red-giant seismic properties analyzed with CoRoT. Astron. Astrophys. **517**, A22 (2010)
56. Osaki, Y.: Excitation mechanisms of solar oscillations. In: Osaki, Y., Shibahashi, H. (eds.) Lecture Notes in Physics: Progress of Seismology of the Sun and Stars, p. 75. Springer, Berlin (1990)
57. Pamyatnykh, A.A.: Pulsational instability domains in the upper main sequence. Acta Astron. **49**, 119–148 (1999)
58. Pesnell, W.D.: Nonradial, nonadiabatic stellar pulsations. Astrophys. J. **363**, 227–233 (1990)
59. Salabert, D., Leibacher, J., Appourchaux, T., Hill, F.: Measurement of low signal-to-noise ratio solar p-modes in spatially resolved helioseismic data. Astrophys. J. **696**, 653–667 (2009)
60. Samadi, R.: Stochastic excitation of acoustic modes in stars. In: Rozelot, J.P., Neiner, C. (eds.) Pulsation of the Sun and Stars. Lecture Notes in Physics, vol. 832, p. 305. Springer, Berlin (2011)
61. Samadi, R., Goupil, M.: Excitation of stellar p-modes by turbulent convection. I. Theoretical formulation. Astron. Astrophys. **370**, 136–146 (2001)
62. Samadi, R., Nordlund, Å., Stein, R.F., Goupil, M.J., Roxburgh, I.: Numerical 3D constraints on convective eddy time-correlations: consequences for stochastic excitation of solar p modes. Astron. Astrophys. **404**, 1129–1137 (2003)
63. Samadi, R., Nordlund, Å., Stein, R.F., Goupil, M.J., Roxburgh, I.: Numerical constraints on the model of stochastic excitation of solar-type oscillations. Astron. Astrophys. **403**, 303–312 (2003)
64. Samadi, R., Georgobiani, D., Trampedach, R., Goupil, M.J., Stein, R.F., Nordlund, Å.: Excitation of solar-like oscillations across the HR diagram. Astron. Astrophys. **463**, 297–308 (2007)

65. Samadi, R., Belkacem, K., Goupil, M.J., Dupret, M.A., Kupka, F.: Modeling the excitation of acoustic modes in α Centauri A. Astron. Astrophys. **489**, 291–299 (2008)
66. Samadi, R., Ludwig, H.G., Belkacem, K., Goupil, M.J., Benomar, O., Mosser, B., Dupret, M.A., Baudin, F., Appourchaux, T., Michel, E.: The CoRoT target HD 49933. II. Comparison of theoretical mode amplitudes with observations. Astron. Astrophys. **509**, A16 (2010)
67. Samadi, R., Ludwig, H.G., Belkacem, K., Goupil, M.J., Dupret, M.A.: The CoRoT target HD 49933. I. Effect of the metal abundance on the mode excitation rates. Astron. Astrophys. **509**, A15 (2010)
68. Samadi, R., Belkacem, K., Dupret, M.A., Ludwig, H.G., Baudin, F., Caffau, E., Goupil, M.J., Barban, C.: Amplitudes of solar-like oscillations in red-giant stars. Evidence for non-adiabatic effects using CoRoT observations. Astron. Astrophys. **543**, A120 (2012)
69. Severino, G., Straus, T., Steffen, M.: Velocity and intensity power and cross spectra in numerical simulations of solar convection. Sol. Phys. **251**, 549–562 (2008)
70. Stein, R.F.: Generation of acoustic and gravity waves by turbulence in an isothermal stratified atmosphere. Sol. Phys. **2**, 385–432 (1967)
71. Stello, D., Chaplin, W.J., Basu, S., Elsworth, Y., Bedding, T.R.: The relation between $\Delta\nu$ and $\nu_{\max}$ for solar-like oscillations. Mon. Not. R. Astron. Soc. **400**, L80–L84 (2009)
72. Ulrich, R.K.: The five-minute oscillations on the solar surface. Astrophys. J. **162**, 993 (1970)
73. Unno, W., Kato, S.: On the generation of acoustic noise from the turbulent atmosphere, I. Publ. Astron. Soc. Jpn. **14**, 417 (1962)
74. White, T.R., Bedding, T.R., Stello, D., Christensen-Dalsgaard, J., Huber, D., Kjeldsen, H.: Calculating asteroseismic diagrams for solar-like oscillations. Astrophys. J. **743**, 161 (2011)
75. Xiong, D.R., Cheng, Q.L., Deng, L.: Turbulent convection and pulsational stability of variable stars: non-adiabatic oscillations of the solar p-modes. Mon. Not. R. Astron. Soc. **319**, 1079–1093 (2000)

Chapter 10
Semi-convection: What Is the Underlying Physical Context?

A. Noels

Abstract Stellar conditions leading to a possible semi-convective mixing are discussed in three relevant cases: (1) low-mass MS stars in which the CNO cycle takes progressively the lead over the PP chain due to the increase in temperature as core hydrogen burning proceeds, (2) massive MS stars which experience a large contribution of the radiation pressure to the total pressure, and (3) core-helium-burning stars for which the production of carbon in the core increases the opacity. A short discussion of semi-convection in terms of instability of non-radial modes follows.

10.1 Introduction

In main sequence stars massive enough to burn hydrogen through the CNO cycle, a convective core is already present at the ZAMS. In most cases, its mass extension is maximum at the ZAMS, and then it shrinks with time due to the decrease in opacity resulting from the transformation of hydrogen into helium, which rather drastically reduces the density of free electrons. In such a case, the opacity is larger outside the convective core in layers which are richer in hydrogen, but as a result of the progressive decrease in mass extension of the convective core, there is neither chemical nor opacity discontinuity at the convective border. In some cases however the convective core mass tends to grow as the star evolves, and this leads to the formation of a hydrogen discontinuity at the border, the outer border being hydrogen richer and thus more opaque than the inner border. The layers affected by this, although outside the convective core, are unstable towards convection if the Schwarzschild criterion [13] is used to define the convective neutrality, i.e.

$$\nabla_{\rm rad} = \left(\frac{{\rm d}\ln T}{{\rm d}\ln P}\right)_{\rm rad} > \nabla_{\rm ad} = \frac{\Gamma_2 - 1}{\Gamma_2} \tag{10.1}$$

A. Noels (✉)
Institut d'Astrophysique et de Géophysique, University of Liège, Allée du 6 Août, 17, Liège, Belgium
e-mail: Arlette.Noels@ulg.ac.be

M. Goupil et al. (eds.), *Studying Stellar Rotation and Convection*,
Lecture Notes in Physics 865, DOI 10.1007/978-3-642-33380-4_10,

where the $\nabla_{\rm rad}$ and $\nabla_{\rm ad}$ refer to radiative and adiabatic temperature gradients, and Γ_2 is the second adiabatic coefficient. They however are stable when applying the Ledoux criterion [9] since

$$\nabla_{\rm rad} < \nabla_{\rm ad} + \frac{\beta}{4-3\beta}\frac{{\rm d}\ln\mu}{{\rm d}\ln P} \tag{10.2}$$

where β is the ratio of the gas pressure to the total pressure, and μ is the mean molecular weight. In a pioneering analysis, Schwarzschild and Härm [14] solved this problem by adding a partial chemical mixing in the so-called semi-convective layers in order to ensure their convective neutrality. The helium abundance in these layers was enriched to just the precise amount required to satisfy the Schwarzschild criterion. A similar partial mixing was adopted by Sakashita and Hayashi [12] but with the Ledoux criterion instead.

After recalling a few basic points of stellar structure in Sect. 10.2, I shall discuss the physical conditions leading to such an increase with time of the convective core mass, first in low mass stars (Sect. 10.3) and then in massive stars (Sect. 10.4). In Sect. 10.5, I shall briefly address the problem of semi-convection in helium-burning stars. Section 10.6 will be devoted to a short discussion in terms of vibrational stability. My aim is here to emphasize the physical conditions under which semi-convection may develop, not to describe the modern ways of tackling the problem nor to present an exhaustive review of the theoretical works done since the 1960s. These are presented and discussed by Zaussinger, Kupka, and Muthsam in Chap. 11, to which this constitutes a sort of preamble.

10.2 A Few Basic Points

Let us recall here a few basic points affecting the stellar structure:

Radiative temperature gradient In a simplified way the radiative temperature gradient can be written

$$\nabla_{\rm rad} \sim \frac{L}{m}\kappa \tag{10.3}$$

where L is the luminosity, and κ the opacity. This means that

- a large L/m value typical of nuclear burning cores is favorable to convection. The larger the temperature sensitivity of the nuclear energy production rate, the larger the L/m value;
- a large opacity mostly found in ionization zones located in the outer layers leads to the presence of a convective envelope.

Temperature sensitivity of a nuclear reaction The temperature sensitivity of a non-resonant nuclear reaction involving the fusion of two nucleons A_A and A_a (see for instance [3]) is given by

$$\nu = \left(\frac{{\rm d}\log\varepsilon}{{\rm d}\log T}\right)_\rho \tag{10.4}$$

where ε is the nuclear energy production rate, T is the temperature, and ϱ the density. Its value strongly depends on the Gamow factor b,

$$b = Z_A Z_a A_\mu^{1/2} \quad \text{with } A_\mu = \frac{A_A A_a}{A_A + A_a}. \tag{10.5}$$

The ν value is then easily estimated from the relations

$$\nu = \frac{\tau - 2}{3} \quad \text{with } \tau = \frac{3E_G}{kT} \quad \text{and} \quad E_G = \left(\frac{bkT}{2}\right)^{2/3} \tag{10.6}$$

where k is the Boltzmann constant, and E_G is the Gamow energy, i.e. the *most effective energy* for the nuclear reaction to take place.

Temperature sensitivity of the PP chain reactions From the relations above it is evident that the smallest ν value will be obtained for the $({}^1_1\mathrm{H}, {}^1_1\mathrm{H})$ reaction. At a temperature of about 10^7 K ($kT \sim 1$ keV), ν_{11} is of the order of 4. As soon as the charge of the nucleons increases as in $({}^3_2\mathrm{He}, {}^3_2\mathrm{He})$, the Gamow factor b drastically increases, and so does the temperature sensitivity. For kT equal to 1 keV, ν_{33} reaches a value of about 17.

PP chain operating out of equilibrium Near the end of the pre-main sequence phase when the temperature at the center reaches a value of about 10^7 K, the hydrogen-burning nuclear reactions start. In low-mass stars hydrogen burning is largely dominated by the PP chain. The abundances of the nucleons involved in the PP chain, essentially that of ${}^3_2\mathrm{He}$, are however still different from their equilibrium (or more precisely *stationary*) abundances. This means that ${}^3_2\mathrm{He}$ is accumulating up to the point where its destruction rate will equal its formation rate. The temperature sensitivity is given by

$$\nu_{\mathrm{PP}} = \nu_{11}\frac{\varepsilon_{11}}{\varepsilon} + \nu_{33}\frac{\varepsilon_{33}}{\varepsilon}. \tag{10.7}$$

Due to the high value of ν_{33}, the resulting sensitivity is large, and a convective core appears and remains during the whole process of reaching the equilibrium abundances.

PP chain operating at equilibrium When ${}^2_1\mathrm{H}$ and ${}^3_2\mathrm{He}$ reach their equilibrium abundances, i.e. when they are produced and destroyed at exactly the same rate, the whole PP chain is governed by the $({}^1_1\mathrm{H}, {}^1_1\mathrm{H})$ reaction (or *pp reaction*). This means that the ν value is low and the L/m ratio is not high enough to allow the presence of a convective core.

PP chain operating with overshooting If a certain amount of overshooting, or any other extra mixing, is taken into account above the convective core boundary, the convective core present before ZAMS can be maintained during the whole main sequence phase. This is due to the fact that this extra mixing prevents ${}^3_2\mathrm{He}$ from reaching its equilibrium abundance whatever the elapsed time since fresh ${}^3_2\mathrm{He}$ is continuously brought into the core.

Temperature sensitivity of the CNO cycle reactions Whatever the proton capture reaction involved in the CNO cycle, its sensitivity is high due to the large value of the Gamow factor. A convective core is present during the whole core hydrogen-burning phase.

Temperature sensitivity of the 3α helium-burning reaction The 3α reaction is a resonant reaction. Its temperature sensitivity (see [3]) is given by

$$\nu_{3\alpha} = \frac{42.9}{T_8} - 3 \tag{10.8}$$

where T_8 is the temperature in 10^8 K. Such large values of ν involve the presence of a convective helium-burning core in the whole stellar mass domain.

Central temperature of MS stars Assuming hydrostatic equilibrium, thermal equilibrium, and radiative transfer, a dimensional reasoning easily leads to (see for instance [8])

$$T \sim \frac{M}{R} \sim M^{1-\frac{\nu-1}{\nu+3}} \tag{10.9}$$

where M is the stellar mass, and R is the surface radius. Whatever the way of burning hydrogen, through PP chain or CNO cycle, the exponent of M is positive, which means that the central temperature increases with the stellar mass. This implies a progressive growth of the contribution of CNO in the nuclear reactions, from PP chain for low-mass stars to CNO cycle in intermediate and massive stars. Another important effect is the increase of the contribution of the radiation pressure to the total pressure as the stellar mass increases.

10.3 Semi-convection in Low-Mass Stars

In the mass range $1.0M_\odot$–$2.0M_\odot$ the small convective core, present while the PP chain elements are still reaching their equilibrium values, vanishes on the ZAMS. As the star evolves, however, the temperature at the center slowly increases, which leads to a growing contribution of the CNO cycle to the nuclear reactions. The temperature sensitivity increases from a value of about 5 to a larger value typical of CNO reactions (around 15). A convective core appears, and its mass extension increases as the CNO contribution increases. Figure 10.1 shows the evolution of the fractional core mass extension with the central hydrogen abundance. This growing tendency is enhanced when models are computed with overshooting since a convective core is already present at the ZAMS due to the non-equilibrium values of the $^3_2$He abundance in the mixed region (see Sect. 10.2).

When models are computed with the Ledoux criterion, such an evolution of the convective core leads to a well-defined and numerically stable discontinuity at the convective core boundary, as can be seen in the left panel in Fig. 10.2. This is not the case where the Schwarzschild criterion is used (see the right panel in Fig. 10.2) since small convective shells form in the region of varying mean molecular weight (μ-gradient region). The resulting effect is to create nearly neutral convective conditions in the whole μ-gradient region and to reproduce more or less the Schwarzschild and Härm solution of the problem of semi-convection (see Sect. 10.1). The number and the extent of these small convective shells are however

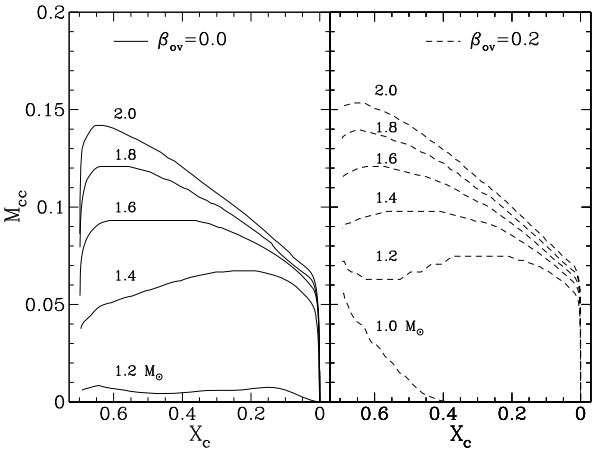

Fig. 10.1 Fractional convective core mass as a function of central hydrogen abundance X_c for models in the mass range $1.0M_\odot$–$2.0M_\odot$ computed without and with overshooting. The overshooting parameter β (ratio of the overshooting distance and the minimum between the convective core radius and the local pressure scale height) is indicated in each panel. (From [10])

dependent on the number of mesh points in the model in a somewhat erratic way. Although rather tempting, this solution is dangerous especially because of the potential numerical diffusion induced by these moving convective layers. The mass domain of stars affected by this semi-convective problem is limited to $1.0M_\odot$–$2.0M_\odot$, and the duration of the phase itself is only a small fraction of the main sequence lifetime since those intermediate convective zones appear mostly near the maximum extent of the convective core.

For intermediate-mass stars more massive than $2.0M_\odot$, the problem of semi-convection disappears since hydrogen burning is dominated by the CNO cycle already at the ZAMS, and as the evolution proceeds, the temperature sensitivity does not change significantly. Since the hydrogen abundance X decreases in the con-

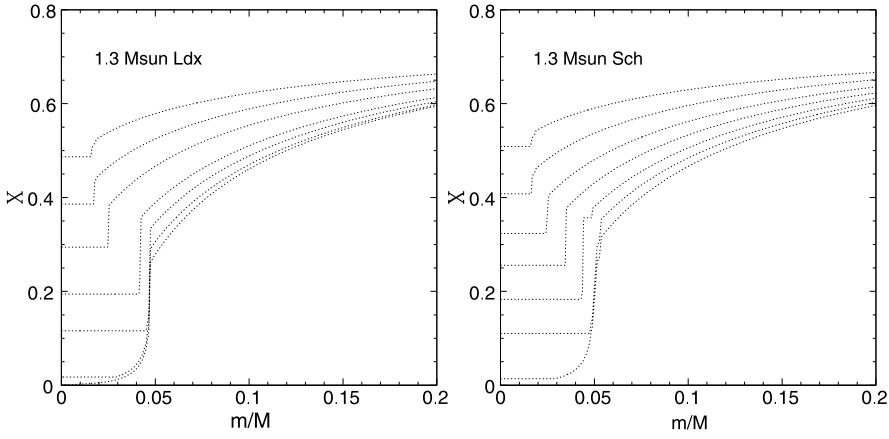

Fig. 10.2 Hydrogen profile in models of $1.3M_\odot$ ($X = 0.70$, $Z = 0.02$) computed with the Ledoux criterion (*left panel*) and with the Schwarzschild criterion (*right panel*) in the fractional mass interval $[0, 0.2]$

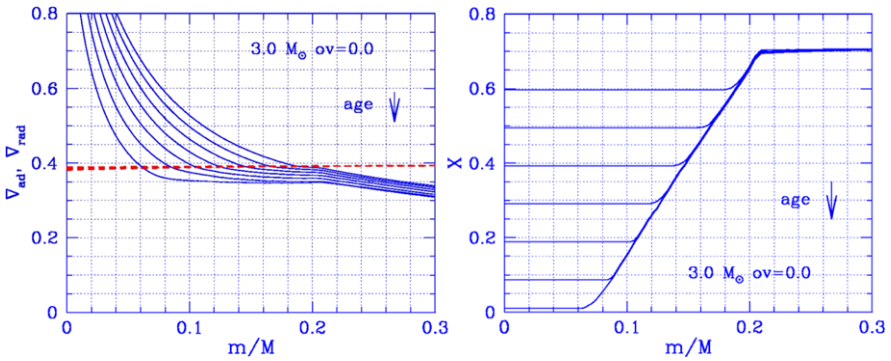

Fig. 10.3 Radiative and adiabatic temperature gradient distributions (*left panel*) and hydrogen profile (*right panel*) in models of $3M_\odot$ ($X = 0.70$, $Z = 0.02$) during MS. (From [11])

vective core, $\nabla_{\rm rad}$ decreases accordingly (see Fig. 10.3), and the μ-gradient region forms a smooth transition between the convective core and the homogeneous envelope.

10.4 Semi-convection in Massive Stars

Another problem arises for stellar masses larger than about $15M_\odot$. As recalled in Sect. 10.2, the radiation pressure becomes a larger and larger contributor to the total pressure as the stellar mass increases. The resulting effect is a decrease of the adiabatic temperature gradient due to a progressive decrease of Γ_2 from 5/3 to 4/3 as β (see Sect. 10.2) varies from 1 to 0. This effect favors convection and thus a larger mass extension of the convective core as M increases. As hydrogen burning proceeds, the core mass extension decreases, but $\nabla_{\rm rad}$ and $\nabla_{\rm ad}$ are extremely close to one another in the μ-gradient region. With the Ledoux criterion, the steepness of the μ-gradient is such that the layers remain stable toward convection. On the contrary, when adopting the Schwarzschild criterion, small convective shells appear in μ-gradient region. This is illustrated in Fig. 10.4 where the X profile, $\nabla_{\rm rad}$ and $\nabla_{\rm ad}$ are shown in the left and the right panels for a typical model ($X_c = 0.20$) of a MS $15M_\odot$ computed with the Ledoux and Schwarzschild criterions, respectively.

Near the end of core hydrogen burning, a small convective zone appears at the base of the homogeneous envelope in models computed with the Ledoux criterion. This does not affect the μ-gradient profile, which remains perfectly smooth with well-defined junctions with the convective core and the homogeneous envelope plateaus during the whole MS. In models computed with the Schwarzschild criterion, on the contrary, the somewhat erratic behavior of transient convective shells leads to a step behavior of the X profile, whose precise form depends on the adopted number of mesh points. The near equality of $\nabla_{\rm rad}$ and $\nabla_{\rm ad}$ in the μ-gradient region tends to mimic the treatment of semi-convection advocated by [14].

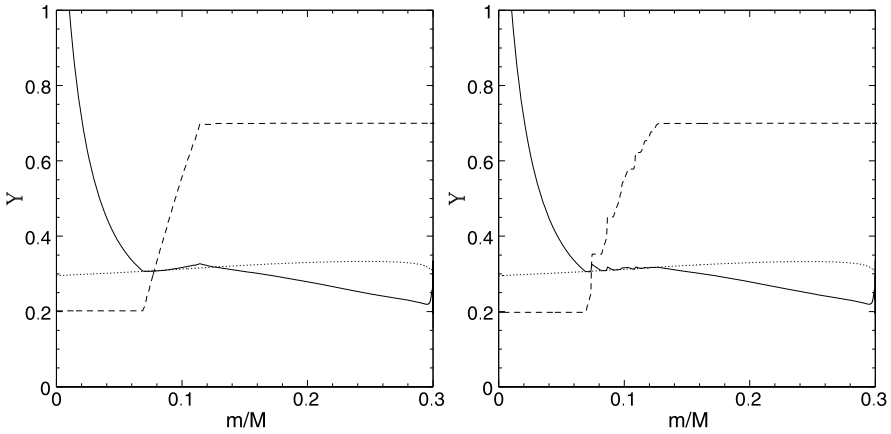

Fig. 10.4 Hydrogen profile (*dashed line*), $\nabla_{\rm rad}$ (*full line*) and $\nabla_{\rm ad}$ (*dotted line*) for an MS model with $X_c = 0.20$ computed with the Ledoux criterion (*left panel*) and with the Schwarzschild criterion (*right panel*) in a sequence of $15M_\odot$ MS ($X = 0.70$, $Z = 0.02$)

As the mass increases ($M \geq 30M_\odot$), the problem becomes more and more crucial since the mass extension of the convective cores even grows with time during the MS. The resulting discontinuity in X at the convective core boundary leads to a situation somewhat similar to that discussed in Sect. 10.3.

10.5 Semi-convection in Helium-Burning Stars

In models of core helium-burning massive stars the radiative opacity is dominated by electron scattering and is thus insensitive to the change in chemical composition produced by the transformation of helium into heavier α-elements. This is not the case however for models burning helium at lower temperature and higher density as it is found in intermediate- and low-mass stars. The opacity of free–free transitions depending on the charge of the ion is larger in carbon rich mixture than in helium richer ones. This is illustrated in the left panel of Fig. 10.6 taken from [2].

Core-helium-burning stars all have a convective core as discussed in Sect. 10.2. As a result of the transformation of helium into carbon leading to a larger opacity, the radiative temperature gradient increases in the convective core, while it remains nearly constant just outside the convective boundary since the chemical composition is there unchanged. A discontinuity in $\nabla_{\rm rad}$ tends to form at the core boundary as can be seen in Fig. 10.5, where $\nabla_{\rm rad}$, $\nabla_{\rm ad}$ and the helium profile as functions of the fractional mass $[0, 0.3]$ are given for a model of $4M_\odot$ (left panel) and $8M_\odot$ (right panel) in the core-helium-burning phase.

As discussed in [2], such a convective boundary is unstable since mixing a radiative layer close to the boundary with the homogeneous matter within the convective core enhances the carbon content in the layer and makes it unstable toward convection. A sort of overshooting called by [2] a *self driving mechanism* leads to the

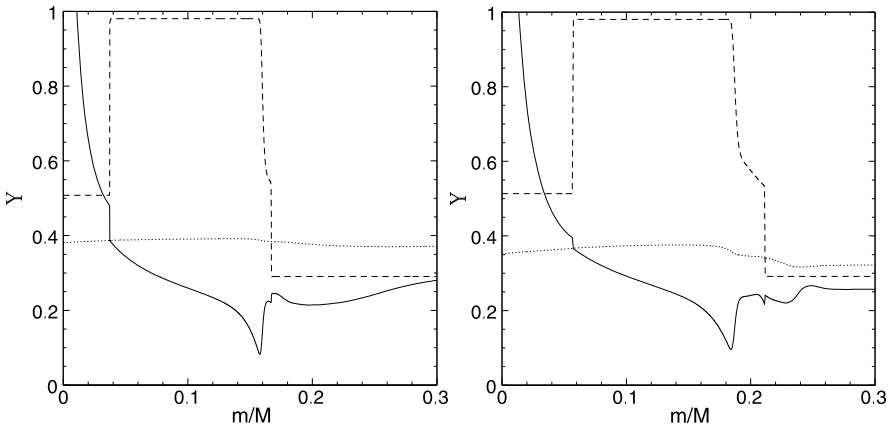

Fig. 10.5 Helium profile (*dashed line*), $\nabla_{\rm rad}$ (*full line*) and $\nabla_{\rm ad}$ (*dotted line*) as functions of the fractional mass $[0, 0.3]$ in models of $4M_\odot$ (*left panel*) and $8M_\odot$ (*right panel*) during core helium burning. A discontinuity in $\nabla_{\rm rad}$ is visible at the boundary of the convective core

extension of the core up to a layer for which the Schwarzschild criterion is satisfied with the chemical composition of the convective core. This progressive outward shift of the core boundary meets however a new difficulty which was first analyzed in [1]. The mass distribution of $\nabla_{\rm rad}$ indeed presents a minimum before reaching the boundary. Whether $\nabla_{\rm rad}$ increases or decreases with time, the existence of this minimum prevents a coherency in the determination of the convective boundary, as can be seen in the top and middle graphs in the right panel in Fig. 10.6. The bottom graph shows the resulting *induced semi-convection* as proposed in [1].

10.6 Discussion in Terms of Vibrational Stability

I very briefly discuss here some earlier works on the stability aspects relevant to semi-convection. Classical convection is due to a dynamical instability of g^- modes, while overstable convection present in layers of varying mean molecular weight results from a vibrational instability of dynamically stable g^+ modes trapped in the μ-gradient region [7]. The physical structures discussed in the above sections are generally favorable to the existence of such trapped g^+ modes. It is thus tempting to interpret a semi-convective mixing as a mixing resulting from the instability of these g^+ modes. The precise nature of the mixing is however far from straightforward. Since the destabilizing term tends to vanish when $\nabla_{\rm rad}$ and $\nabla_{\rm ad}$ are equal, it would be safe to say that a mixing tending to this equality would lead to a stable situation. Another mechanism acting in massive stars was proposed by [4], who showed that transient convective shells would progressively move across and partially mix the μ-gradient region until the Schwarzschild neutrality condition is met.

As already noted in Sect. 10.1, attempts have however been made by numerous stellar evolution scientists at forming semi-mixed regions either neutral toward the

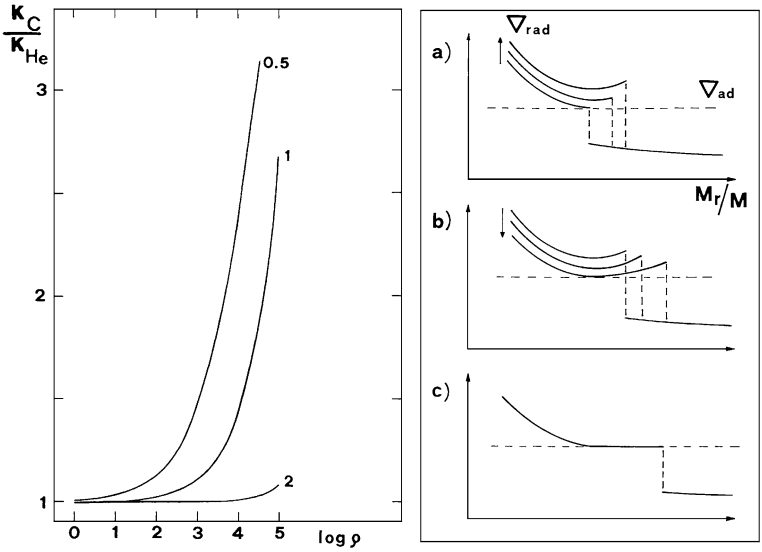

Fig. 10.6 Ratio of opacities in a pure carbon and a pure helium matter as a function of the logarithm of the density for labeled values of the temperature expressed in 10^8 K (*left panel*; from [2]). Mass distribution of ∇_{rad} and ∇_{ad} illustrating the problem of the minimum in ∇_{rad} during core helium burning (*right panel*; from [1]). In the *top* and *middle graphs*, ∇_{rad} increases and decreases with time, respectively. The induced semi-convective mixing is shown in the *bottom graph*

Schwarzschild or toward the Ledoux criterion. As pointed by Ledoux [9], adopting the Schwarzschild criterion as a neutrality condition in a semi-convective region has the advantage of leading to a dynamically stable situation, while the Ledoux criterion leads to marginally dynamically unstable conditions which would inevitably lead to a full convective mixing. *Ledoux was indeed the first to advocate in this context the use of the Schwarzschild criterion and* **not** *the Ledoux criterion as a neutrality condition in semi-convective zones*.

Even trapped modes must be checked through a full stability analysis. In the case of massive MS stars, [5] showed that low-order g^+ modes of high spherical harmonic degree could be trapped in the μ-gradient region. The timescales were found to be of the order of 10^3 to 10^4 years, which made them good candidates for a partial semi-convective mixing.

For low-mass MS stars, a similar analysis was performed [6] and unstable trapped low-order g^+ modes of high degree were also found. A very narrow mass range near $1.1 M_\odot$ was however affected by this instability. Moreover, unstable modes were only found during a short part of the main sequence phase near the maximum extent of the convective core.

Although it is impossible to draw a full picture of semi-convection from these stability analyses, it is interesting to point out that they seem to converge toward a partial chemical mixing of the semi-convective layers ensuring their being neutral with respect to the Schwarzschild criterion.

References

1. Castellani, V., Giannone, P., Renzini, A.: Induced semi-convection in Helium-burning horizontal-branch stars II. Astrophys. Space Sci. **10**, 355–362 (1971)
2. Castellani, V., Giannone, P., Renzini, A.: Overshooting of convective cores in Helium-burning horizontal-branch stars. Astrophys. Space Sci. **10**, 340–349 (1971)
3. Clayton, D.D.: Principles of Stellar Evolution and Nucleosynthesis. McGraw–Hill, New York (1968)
4. Gabriel, M.: On the mechanism of formation of semi-convective zone in stars. Astron. Astrophys. **6**, 124 (1970)
5. Gabriel, M., Noels, A.: Stability of a $30M_{\odot}$ star towards g^{+} modes of high spherical harmonic values. Astron. Astrophys. **53**, 149 (1976)
6. Gabriel, M., Noels, A.: Semiconvection in stars of about 1 solar mass. Astron. Astrophys. **54**, 631–634 (1977)
7. Kato, S.: Overstable convection in a medium stratified in mean molecular weight. Publ. Astron. Soc. Jpn. **18**, 374 (1966)
8. Kippenhahn, R., Weigert, A.: Stellar Structure and Evolution. Springer, Berlin (1994)
9. Ledoux, P.: On stellar models with convection and discontinuity of the mean molecular weight. Astron. J. **52**, 155 (1947)
10. Miglio, A., Montalbán, J., Noels, A., Eggenberger, P.: Probing the properties of convective cores through g modes: high-order g modes in SPB and γ Doradus stars. Mon. Not. R. Astron. Soc. **386**, 1487–1502 (2008)
11. Noels, A., Montalbán, J., Maceroni, C.: A-type stars: Evolution, rotation and binarity. In: Zverko, J., Ziznovsky, J., Adelman, S.J., Weiss, W.W. (eds.) The A-Star Puzzle. IAU Symposium, vol. 224, pp. 47–57 (2004)
12. Sakashita, S., Hayashi, C.: Internal structure of very massive stars. Prog. Theor. Phys. **26**, 942–946 (1961)
13. Schwarzschild, M.: Structure and Evolution of the Stars. Princeton University Press, Princeton (1958)
14. Schwarzschild, M., Härm, R.: Evolution of very massive stars. Astrophys. J. **128**, 348 (1958)

Chapter 11
Semi-convection

F. Zaussinger, F. Kupka, and H.J. Muthsam

Abstract Double-diffusive processes play an important role in various astrophysical and geophysical systems. Especially the case which considers a thermally unstable configuration stabilized by mean molecular weight and which is known as semi-convection has been studied for several decades. Whether a semi-convective region in a star should be treated layered or fully mixed has not yet been conclusively answered. However, in recent years numerical simulations have been used to investigate this fluid dynamical instability. With high resolution methods we can now develop a better understanding of this mixing process. For this review our intention is to present semi-convection from different points of view. At first, a summary of studies made during the last decades is used to demonstrate the continuous importance of semi- convection for stellar evolution. The physical process itself as well as linear stability criteria are explained subsequently. Finally, models, experiments, and the study through numerical simulations are discussed. Semi-convective mixing and related questions in stellar evolution and, recently, also in exoplanet science continue to be a vivid research field and have never ceased to surprise.

11.1 Introduction

The physical process known as *semi-convection*[1] was discovered in the early days of modelling of stellar structure and evolution, when in the 1950s it became fea-

[1] Both notations, *semi-convection* and *semiconvection*, are equivalent.

F. Zaussinger (✉)
BTU Cottbus, Siemens-Halske-Ring 14, 03046 Cottbus, Germany
e-mail: florian.zaussinger@tu-cottbus.de

F. Kupka · H.J. Muthsam
University of Vienna, Nordbergstrasse 15, 1090 Vienna, Austria

F. Kupka
e-mail: friedrich.kupka@univie.ac.at

H.J. Muthsam
e-mail: herbert.muthsam@univie.ac.at

M. Goupil et al. (eds.), *Studying Stellar Rotation and Convection*,
Lecture Notes in Physics 865, DOI 10.1007/978-3-642-33380-4_11,

sible to compute detailed stellar models, in particular for stars other than the Sun (see Schwarzschild and Härm [39]). Under conditions which are characterized by the term weak mixing, it can occur that neither thermal convection nor a strong shear flow are able to mix the fluid on short, hydrodynamical timescales. Despite this long history, the accurate physical modelling of semi-convection is still considered an unsolved problem. Many models for this process have been proposed, but for a long time, astrophysical tests thereof have been too indirect, and hydrodynamical simulations too expensive; thus, solid conclusions remained beyond reach. The situation is now changing with the increasing capabilities of asteroseismology and large, high-precision surveys on the one hand and advanced numerical techniques and ever more powerful supercomputers on the other. Semi-convection models are at last becoming subject to sufficiently thorough and direct tests to draw well-founded conclusions on their validity.

In this review, due to lack of space, we cannot give a complete survey of the entire literature on the subject, nor explain the differences between all of those models of semi-convection which have been proposed. We rather aim at explaining some of the major discoveries and conclusions valid beyond the limitations of specific models. In the following we hence begin with a discussion of the role semi-convection plays in stellar evolution, its discovery, the first attempts of modelling it, and attempts to verify, or rather falsify, those models with astrophysical data. A discussion of the undecided situation encountered in current modelling concludes the section on the meaning of semi-convection for stellar evolution. This section is followed by a discussion of the physics of semi-convection as a double-diffusive mixing process. We then explain some of the main physical quantities used in its modelling. In the next part we discuss some more advanced models and in particular some conclusions which can be drawn from them independently of the modelling details. Thereafter we turn to experiments and numerical hydrodynamical simulations which are now becoming an important tool in probing the physics and the quantitative predictions of semi-convection models. A final section presents some conclusions on the current evolution of the field, in particular with respect to the interest awakening in semi-convection in the neighbouring field of exoplanet science and with respect to the possibilities opened by the advancement of hydrodynamical simulations.

11.2 The Meaning of Semi-convection for Stellar Evolution

The first thorough analysis of the stability of the stratification inside a star under conditions such that a gradient in mean molecular weight μ competes with a gradient in temperature T was given by Ledoux [30]. From his analysis it followed that a sufficiently steep mean molecular weight gradient $\nabla_\mu = \mathrm{d}\ln\mu/\mathrm{d}\ln P$ could actually overpower the convective instability expected from the usual *Schwarzschild criterion* [38]. In modern notation the latter demands the logarithmic temperature gradient to be steeper than the adiabatic one, $\mathrm{d}\ln T/\mathrm{d}\ln P = \nabla > \nabla_{\mathrm{ad}} =$

$(\partial \ln T/\partial \ln P)_{\rm ad}$, in order for convection to occur. According to the *Ledoux criterion*, convection may still be suppressed if

$$\nabla_\mu > \nabla - \nabla_{\rm ad} > 0, \tag{11.1}$$

where $\nabla > \nabla_{\rm ad}$ implies unstable stratification with respect to $T(r)$ in the sense of [38] (r is taken to be the stellar radius), but $\nabla_\mu > 0$ implies stable stratification with respect to $\mu(r)$, whereas, most importantly, $\nabla_\mu > \nabla - \nabla_{\rm ad}$ holds as well. The notation used here assumes a perfect gas equation of state. In general, one has to consider $(\varphi/\delta)\nabla_\mu$ with $\varphi = (\partial \ln \rho/\partial \ln \mu)$ and $\delta = -(\partial \ln \rho/\partial \ln T)$ instead of ∇_μ in (11.1) (see, e.g., [21]). Ever since this result was published, the issue of whether to apply the Ledoux criterion or the Schwarzschild criterion of convective instability in models of stellar structure and evolution has been a topic of debate among astrophysicists. This is important because the Schwarzschild criterion predicts a larger region of the star to be *mixed*, and thus of homogeneous composition, than the Ledoux criterion. As a result, the two criteria can lead to different predictions for the evolution of a star during later stages.

The discussion became more complex with the work of Schwarzschild and Härm [39]. They found that for massive stars, convection could be so slow that it would transport only a small amount of energy, but nevertheless it could lead to a homogeneous composition in the intermediate layer between the convective core and the radiative envelope. This slow mixing process was termed 'semi-convection'. What made that scenario particularly difficult to model was the role of opacity and thus of radiative diffusivity in their models of massive stars along the main sequence. Both are functions of chemical composition. Since the dominating source of opacity in that physical regime is electron scattering and since hydrogen has a larger number of electrons per nucleon than helium, the hydrogen-rich material further outwards is actually more opaque than the helium-rich material further inwards. For that reason, the less well mixed material has a lower radiative conductivity, and the (radiative) diffusion process *counteracts* the stability implied by (11.1). The Ledoux criterion hence cannot be used on its own to determine if, or how well, a region is mixed: a more detailed model is needed.

Thus, in addition to the dimensionless gradients ∇_μ, ∇, and $\nabla_{\rm ad}$, the *diffusivities* play a key role in the stability of a stratification. In the case considered by [39], the thermal (radiative) diffusion $\kappa_{\rm T}$ is able to undermine the stability of the stratification expected according to (11.1) near the boundary of the convective core of a massive star because it operates on shorter time scales than the diffusion of concentration, or more precisely of helium, since $\kappa_{\rm T} \gg \kappa_{\rm He}$. For that reason, semi-convection is considered a *double-diffusive processes*, as the interplay between two diffusivities *and* their associated gradients determines whether and how rapidly a fluid is mixed and how efficiently heat is transported within it under such conditions.

During the same era, double-diffusive processes also began to gather attention in oceanography where $\kappa_{\rm T} \gg \kappa_{\rm salt}$ plays the same role as $\kappa_{\rm T} \gg \kappa_{\rm He}$ does in stars and where the gradients of temperature $\nabla_{\rm T}$ and salinity $\nabla_{\rm S}$ compete with each other. In oceanography semi-convection is usually termed diffusive convection (see Canuto [5] for further references). However, the opposite case of semi-convection,

where a mean molecular weight gradient destabilises a stratification which is stable with respect to its temperature gradient, i.e. $\nabla < \nabla_{\rm ad}$ but $\nabla_\mu < 0$, has traditionally attracted more attention in oceanography. It is known under the name thermohaline convection since the first theoretical analysis by Stern [42], although later on it has often been referred to by the name for a special case thereof, i.e. salt-fingers. The latter name is also commonly used in astrophysics irrespectively of the parameter region encountered as soon as $\nabla < \nabla_{\rm ad}$ and $\nabla_\mu < 0$. In stars, the 'fingers', of course, consist of a plasma which itself is a mixture of mostly hydrogen and helium or of helium and carbon, for example. A detailed linear stability analysis, which includes the diffusivities and local gradients and which can distinguish between different regimes of stability and instability, was developed in oceanography [1, 43, 56]. This analysis can also be applied to semi-convection and even to the case where a magnetic field is present as well [44]. Astrophysical scenarios where the equivalent of 'thermohaline convection' should occur where first identified in [51] for the case of late stages of off-centre (carbon) shell burning and for the case of accretion of heavier material onto a stellar surface [49], an idea revived after the discovery of very short period exoplanets (see also the discussion in [55]). After these initial discoveries only a few models were proposed which model this process under astrophysical conditions [22, 53] and which were actually applied in calculations of stellar structure and evolution (cf. also the recent work of [9, 26, 27]).

Progress on modelling semi-convection remained equally slow. In an early review, Stothers [46] concluded that only two out of ten schemes investigated by him were physically possible, consistent with astrophysical observations, and were not contradicted by contemporary laboratory data. One of those two turned out to be the model already proposed by Schwarzschild and Härm [39]. Among the models suggested more recently which have more commonly been applied to stellar evolution calculations are those of Langer et al. [28] and Spruit [41], to which we will return below, and the model by Castellani et al. [7].

Meanwhile, observational data combined with stellar evolution calculations was used to argue in favour of a very low mixing efficiency of semi-convection as postulated by the Ledoux criterion. Weiss [60] demonstrated that the red supergiant phase preceding the terminal stage of a blue progenitor of SN 1987A could be recovered if the Ledoux criterion were used for semi-convective regions in a star, while using the plain Schwarzschild criterion led to an evolutionary track in contradiction to observations. Stothers and Chin [47] investigated the distribution of red and blue supergiants in the metal-poor cluster NGC 330 in the Small Magellanic Cloud and concluded that the Ledoux criterion is strongly indicated by the available data. Stothers and Chin [48] then revisited the case of SN 1987A and considered a further dozen tests based on galactic stars. While they considered the case of SN 1987A as too uncertain due to the complexity of the physics describing the progenitor phase, and another seven of their tests to be indeterminate, five tests favoured the Ledoux criterion, and three of those five even very strongly, while not a single case favoured the plain Schwarzschild criterion.

In spite of this, there is no clear preference in the literature in favour of either criterion or of any of the more detailed models. Heger et al. [14] used the model of

layered semi-convection by Langer et al. [28] and, for comparison, also the model by Weaver et al. [58, 59] to produce their evolutionary tracks of supernova progenitor models. In turn, the model of Spruit [41] was used by Umeda and Nomoto [54] in their study of the ^{56}Ni production in core-collapse supernovae. On the other hand, Hirschi et al. [15] produced supernova progenitor models based on the plain Schwarzschild criterion with core overshooting for the hydrogen and helium burning phases of stars. They also provided some comparisons with models from the literature which treat semi-convection in different ways. However, since other input physics also varied in these models, strong conclusions on semi-convection cannot be drawn from their work. Likewise, Bertelli et al. [2] continued to use the model by Castellani et al. [7] emphasizing that semi-convection was of greater importance for the He burning phase than for the H burning phase.

Reducing these modelling uncertainties requires progress both with respect to observational data and to the way semi-convection is modelled. Asteroseismology now has reached a state where its results can be considered for constraining semi-convection even in stars of lower mass (Silva Aguirre et al. [40]). At the same time, physically more complete models are needed, and these have to be supplemented by numerical simulations, since laboratory experiments can only reach a limited parameter space.

11.3 The Double-Diffusive Mixing Process

We now discuss the physics of semi-convective mixing in more detail. As already mentioned, semi-convection is an example of double-diffusive convection. It is a multi-component fluid mixing process, and geophysical examples have been studied as long as have astrophysical ones, for example, the layering observed in salt lakes. Quite a few cases are known on earth where layering is taking place as part of double-diffusive convection. For instance, the East African rift Lake Kivu is characterized by steep staircases in dissolved gases like CO_2 and CH_4, with an average height of the mixed layers of $h = 48$ cm. See Schmidt et al. [37] for further information on the layering process in this lake. In the 1970s and 1980s of the last century Huppert and Turner [17] first investigated double-diffusive convection with laboratory experiments. Hereupon a broad range of experiments in different research fields followed. An interesting application of laboratory experiments are saline solar ponds, which are still used as energy source in coastal regions [50]. A typical solar pond consists of three layers, namely a mixed fresh water upper layer, a stably stratified salty middle layer and a semi-convective salt rich lower layer. The solar radiation, mainly in the infrared band, is absorbed in the lower semi-convective zone. The stably stratified middle layer inhibits the energy transport which achieves temperatures of up to 70 °C in the lower layer. Heat exchangers can be used to utilise the thermal energy source. A ‘do it yourself’ laboratory experiment is the coffee cup. Full-fat milk poured gently into a cup of hot coffee leads to a typical semi-convective layer formation after some minutes. However, the often mentioned Latte Macchiato

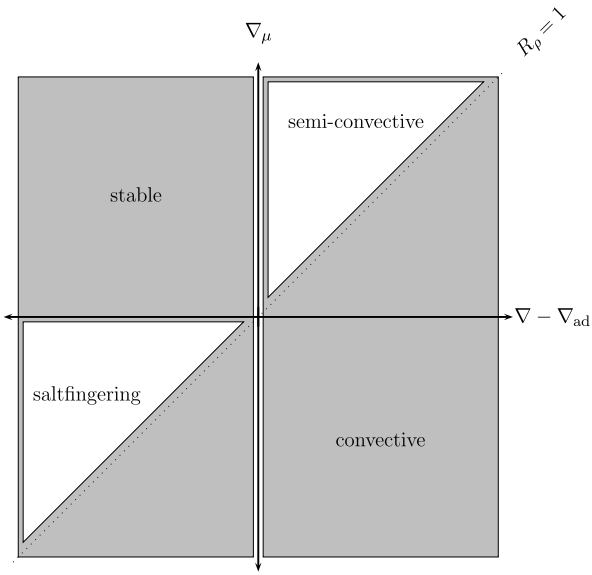

Fig. 11.1 Stability map in terms of the super adiabatic gradient $\nabla - \nabla_{\mathrm{ad}}$ and the mean molecular gradient ∇_μ. Semi-convective mixing is located in convectively unstable regions with $R_\rho > 1$

layers form due to a stable density ratio, but this configuration is thermally stable too. Indeed, their mixing process is double-diffusive but not convectively unstable.

Let us now turn to a more detailed description of the underlying physics of this process. In the following we define the dimensionless ratio[2] $R_\rho = \nabla_\mu/(\nabla - \nabla_{\mathrm{ad}})$ to measure the stabilising effect of the solute. In the geophysical and incompressible context the stability ratio is defined by $R_\rho = (\beta \Delta S)/(\alpha \Delta T)$, where α and β are thermal and solute expansion coefficients, respectively. Considering a convectively unstable stratification in terms of the Schwarzschild criterion, $\nabla > \nabla_{\mathrm{ad}}$, one finds two stability regions in the presence of a mean molecular gradient, $R_\rho < 1$ and $R_\rho > 1$. Regions where the superadiabatic gradient is steeper than the mean molecular weight gradient are not considered here, since in that case the stabilising influence of the solute is too weak to counteract the convective motion. The remaining parameter space $R_\rho > 1$ can be rewritten in terms of the Ledoux criterion (11.1). Figure 11.1 shows the stability map spanned in terms of the gradients ∇, ∇_{ad}, and ∇_μ. Obviously, the semi-convective and thermohaline parameter space is limited to a narrow range, which might lead to the assumption that both mixing processes are rather exceptional cases in nature.

In their compressible form, the hydrodynamic equations, which describe the double-diffusive mixing process in stars on the main sequence, are based on conservation of the mass ρ, the partial helium density $Y\rho$, the momentum density $\rho\mathbf{u}$ and the total energy density ρE. Hereafter, we neglect heavier elements since they do not contribute much to the stellar element mixture during the hydrogen core burning phase. The governing equations hence read

[2]Some authors use the inverse definition of the stability parameter R_ρ^{-1} but refer to the same ratio.

$$\frac{\partial \rho}{\partial t} = -\nabla \cdot [\rho \mathbf{u}], \tag{11.2}$$

$$\frac{\partial (Y\rho)}{\partial t} = -\nabla \cdot [\rho \mathbf{u} \cdot Y - \rho \kappa_{\mathrm{He}} \nabla Y], \tag{11.3}$$

$$\frac{\partial (\rho \mathbf{u})}{\partial t} = -\nabla \cdot \left[\rho (\mathbf{u} \otimes \mathbf{u}) + \Pi\right] - \rho \nabla \phi, \tag{11.4}$$

$$\frac{\partial (\rho E)}{\partial t} = -\nabla \cdot \left[\mathbf{u}(\rho E + P) - k_{\mathrm{h}} \nabla T - \nabla (\pi \mathbf{u})\right] - \rho \mathbf{u} g_z. \tag{11.5}$$

As usual, the pressure tensor is written as $\Pi = P\mathbb{1} - \pi$, while π denotes the viscosity tensor,

$$\pi_{ik} = \eta \left(\frac{\partial u_i}{\partial x_k} + \frac{\partial u_k}{\partial x_i} - \frac{2}{3} \delta_{ik} \nabla \cdot \mathbf{u} \right) + \zeta \delta_{ik} \nabla \cdot \mathbf{u}, \tag{11.6}$$

where δ_{ik} denotes the Kronecker delta, η the dynamic viscosity, ζ the bulk or second viscosity, and $k_{\mathrm{h}} = \kappa_{\mathrm{T}} \rho c_{\mathrm{p}}$ the thermal conductivity. The gravitational potential is denoted by ϕ, and g_z is the vertical component of gravitational acceleration. Of course, the thermodynamic closure changes according to the fluid we consider, but since our main focus here is on semi-convection in massive stars, the equation of state for a perfect gas with radiation is a valid approximation [32],

$$P = \frac{\mathscr{R} \rho T}{\mu} + \frac{1}{3} a T^4. \tag{11.7}$$

Under the assumption of fully ionized matter, the mean molecular weight becomes $\mu = 4(2 + 6X + Y)^{-1}$, where the hydrogen mass fraction $X = 1 - Y$ (see [61]).

In particular, the very low values of the Lewis number $Le = \kappa_{\mathrm{He}}/\kappa_{\mathrm{T}} < 10^{-9}$ and the Prandtl number[3] $Pr = \nu/\kappa_{\mathrm{T}} < 10^{-7}$ make solving the equations numerically so as to resolve all relevant scales a challenging task. We will give a detailed view on the numerical treatment of the equations in Sect. 11.4. In spite of the compressible formulation of the fluid flow, the Boussinesq approximation is still relevant for small layer heights. In that context, one has to take into account that the buoyancy depends on the temperature and the solute, respectively, $\rho = \rho_0(1 - \alpha(T - T_0) + \beta(S - S_0))$. Boundary conditions and initial conditions close the set of equations. They depend mainly on the specific problem and will be discussed in the Sect. 11.4 in more detail. Closed vertical boundaries in temperature and concentration are commonly implemented for single-layer simulations, while open or periodic conditions are chosen for layer formation experiments. The influence of the initial stratification of the temperature and the solute on the long-time behaviour is still an unsolved problem. In fact, for the same input model, the outcome differs significantly for linear, periodic, or steplike initial stratifications.

Semi-convection belongs to the hydrodynamical class of vibrational instabilities with growth rates on the thermal diffusion time scale. Pictorially, one might think of an upwardly displaced fluid blob in a Schwarzschild unstable, but Ledoux stable, fluid column. The convective unstable situation lets the blob rise, while the

[3] The Prandtl number Pr is often denoted with σ.

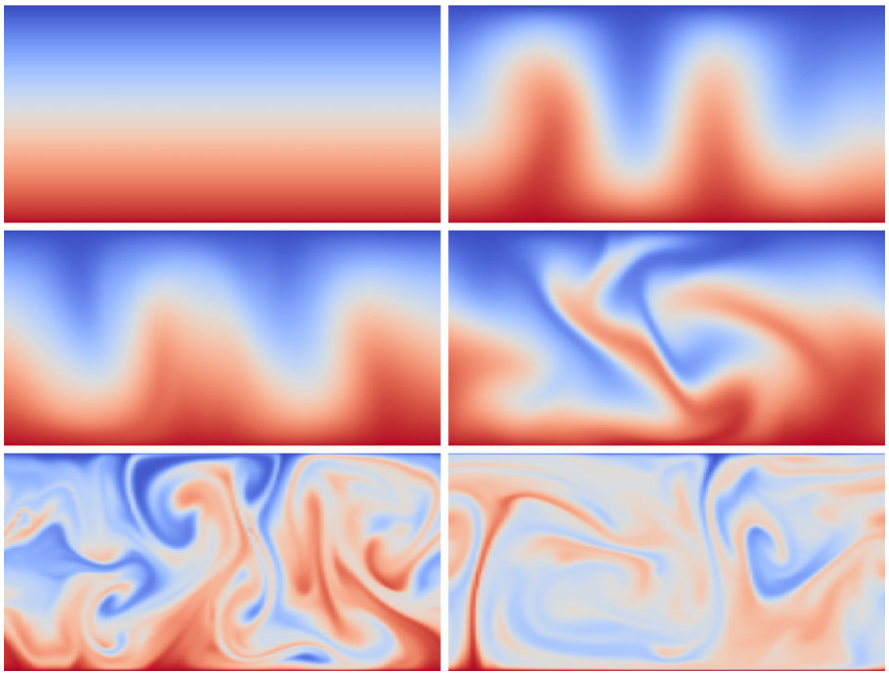

Fig. 11.2 Vibrational instability for $Pr = 0.1$, $Le = 0.01$, and $R_\rho = 1.15$ visualized for the helium concentration: the growing vibrational instability induces wave braking and the formation of a convectively mixed zone. Image sequence showing the evolution of the fluid as a function of time from *left* to *right* in consecutive rows

concurrent downward force of the mean molecular weight gradient counteracts this movement. For $R_\rho > 1$, the downward acceleration generates a force which is larger than the force due to thermal convection, which results in a net restoring force. Consequently, the fluid element starts to oscillate around the equilibrium state. As long as the displacement is non-adiabatic, the amplitude of the growth rate rises. Hence, the thermal diffusion plays a key role in this process. The much lower solute diffusion affects mainly the helium flux, whereupon cross correlations could be important too. A series of pictures, showing the onset of convection, the oscillatory phase and the fully evolved convective layer is depicted in Fig. 11.2. This vibrational movement is well observed for an initially linearly stratified temperature and solute profile. From linear stability analysis, for instance [36, 44, 57], one can obtain that $1 < R_\rho < (1 + Pr)/(Le + Pr)$ for the fluid to be dynamically stable, but vibrationally unstable. Thus, semi-convection occurs if $R_\rho > 1$ and $\kappa_\mathrm{T} > \kappa_\mathrm{He}$ (i.e. $Le < 1$), but in addition, viscosity puts an upper limit on R_ρ beyond which only pure diffusion processes occur (because of vibrational and dynamical stability).

Besides the qualitative description of semi-convection, the effective mixing rates and the time scales as functions of the Rayleigh, Prandtl, and Lewis numbers and the stability parameter R_ρ are important, and a lot of still-open questions relate to them.

There are several approaches to deal with those. We consider a semi-convective stack formed by thin layers.[4] The heat and mass transfer through the interfaces is by diffusion only but additionally depends on the local behaviour of the convectively mixed intermediate zone. Two methods have been particularly popular to model the efficient diffusion coefficient $D_{\rm sc}$ for stellar evolution. Commonly used stellar evolution codes revert to the models given by an extended mixing length theory (MLT), for instance, by Langer et al. [28],

$$D_{\rm sc} = \frac{\alpha_{\rm sc}}{6} \frac{4caT^3}{3\kappa_{\rm T}\rho c_{\rm p}} \frac{\nabla - \nabla_{\rm ad}}{\nabla_{\rm ad} + \nabla_\mu - \nabla}, \tag{11.8}$$

where the parameter $\alpha_{\rm sc}$ is adjusted to match observations. This diffusion coefficient can easily be rewritten in terms of the stability parameter R_ρ, namely $D_{\rm sc} = D(R_\rho - 1)^{-1}$, where D is mainly a function of $\alpha_{\rm sc}$. This leads to the conclusion that $\alpha_{\rm sc}$ adjusts the overall semi-convective stability in the considered zone.

In addition to such heuristic kinds of reasoning, numerical simulations have provided theoretical models since the early 1990s. Two-dimensional simulations of single and double layers were first performed first by Merryfield [32] in 1995 with focus on the vibrational instability and the stability of double layers. Recent three-dimensional semi-convection simulations are characterized by small Pr and Le, but are still far away from the relevant stellar parameter space. Even with the next generation of super computers, it will not be possible to reach Lewis numbers lower than 10^{-4}. Although the hunt for very high-resolution direct numerical simulations has commenced, one might ask whether such simulations are really necessary, since extrapolations into the relevant parameter space can be done that are based on 'cheap' simulations with higher Pr and Le.

Let us outline this in more detail here. Mixing rates are commonly measured in terms of the total flux $F_{\rm tot}$ over the diffusive flux $F_{\rm diff}$, i.e. the Nusselt number. Subsequently, the effective diffusivities $\kappa_{\rm T,eff} = \kappa_{\rm T} Nu_{\rm T}$ and $\kappa_{\rm S,eff} = \kappa_{\rm S} Nu_{\rm S}$ are obtained. It would be easy to estimate the diffusion timescales by $\tau_{\rm S} = D^2/\kappa_{\rm S,eff}$ and $\tau_{\rm T} = D^2/\kappa_{\rm T,eff}$. However, the Nusselt numbers are the relevant quantities to describe transport and mixing. From linear stability analysis (see [16]) we obtain

$$Nu_{\rm S} = Le^{-1/2} Nu_{\rm T} \tag{11.9}$$

for $Nu_{\rm S}, Nu_{\rm T} \gg 1$, which is in good agreement with numerical simulations and experiments. Thus, in the astrophysical limit we expect an *effective* helium diffusivity about four magnitudes higher than the thermal one. There is still disagreement about how to describe the heat flux in terms of a power law for the semi-convection case, $Nu_{\rm T} = \alpha Ra_{\rm T}^{\beta}$. Whether α is a function of R_ρ, Le, Pr or a constant is still unknown and a recent field of research. Knowing the values for the exponent β and the role of α would help us to estimate time scales and mixing efficiencies in semi-convective zones. The problem of properly choosing these exponents might lead us eventually to revert to very high-resolution numerical simulations to answer this question.

[4] This assumption depends on the model and is not general at all.

11.4 Models, Experiments and Numerical Simulations

We now discuss some of the tools used to facilitate a better physical understanding of semi-convection. At this point a few remarks on the meaning of 'models' as used in the following are in order. Astrophysicists usually understand the term model relating to a simplified description of a very complex system. For this purpose, specific sets of equations are derived either from more fundamental equations, which are too complex to solve for the given problem, or by heuristic reasoning, or by a mixture thereof. In the subsection below we deal with models in this sense. On the other hand, particularly in the community performing detailed hydrodynamical numerical simulations, the term 'model' is used to describe a specific scenario for which a simulation is performed. This second meaning is usually evident from its context.

11.4.1 Models

The majority of models of semi-convection which have actively been used in astrophysics are either derived by heuristic reasoning or inspired by laboratory experiments and field data obtained in oceanography and adopted to the scenario expected to hold for stars (cf. [7, 8, 28, 39, 41, 46, 58, 59]). While these models have their merits for very specific applications such as a stellar structure calculation, they cannot be used to answer physical questions on semi-convection interacting with other active fields such as a mean flow or a magnetic field.

The one-point closure approach used in Reynolds stress models of turbulent flows can be used to derive such more general, dynamical equations which describe the development of statistical parameters, for instance, mean concentration, mean temperature, or root mean square fluctuations of these quantities. This approach was first applied to stellar astrophysics by Xiong [62, 63], who calculated stellar structure models of massive stars with a non-local turbulence model based on the downgradient assumption (in this case the fluxes of the fluctuations of kinetic energy around its mean value are approximated, e.g., by a gradient model). The model in [63] contained dynamical equations for the development of the mean and root mean square fluctuations of concentration of hydrogen. A similar approach had been the theoretical basis of a model used in Grossman and Taam [12] to study semi-convection for stellar conditions. In spite of that, these models were essentially only ever used by the groups in which they were invented.

The most elaborated model of this type was published by Canuto [4], who avoided the introduction of a master length scale, which limited the previous non-local models (of semi-convection). Instead, he resorted to results from a renormalisation group approach developed for modelling turbulent flows to close his system of equations. A more easily applicable variant of this model was given in Canuto [6]. However, the models of [4, 6] have so far been used only in theoretical discussions such as the comparison of the model of [28] in [4] with the new model presented in that publication. Interestingly, it was stressed in [4, 6] that the correct

stability criterion which should replace (11.1) not only has to take into account the *molecular diffusivities* κ_c, κ_T (and the kinematic viscosity ν), but the *turbulent* or *effective diffusivities* K_c and K_h. These quantities express the combined action of molecular transport and advective (turbulent) transport and thus require a detailed convection model. In the end, the stability criterion (11.1) was argued to be replaced by

$$\frac{K_h}{K_c}(\nabla - \nabla_{ad}) > \nabla_\mu > \nabla - \nabla_{ad} \tag{11.10}$$

for the case $K_h/K_c > R_\rho > 1$ (this implies $\nabla - \nabla_{ad} > 0$). Note that in (11.10) the turbulent (advective) mixing, present through the ratio K_h/K_c, sets an upper limit for ∇_μ, a feature absent in (11.1). The Ledoux unstable case is expressed through

$$(\nabla - \nabla_{ad}) > \frac{K_c}{K_h}\nabla_\mu, \tag{11.11}$$

where $1 > R_\rho > 0$ (and thus also $\nabla - \nabla_{ad} > 0$ and $\nabla_\mu > 0$). With this framework the problem of 'choosing' between the Schwarzschild and Ledoux criteria in models of semi-convection was identified to be a problem of modelling K_c and K_h, and thus the turbulent fluxes, or, alternatively, the Nusselt numbers Nu_c (i.e. Nu_S) and Nu_T, rather than one of 'choosing the right linear stability criterion' (using the Schwarzschild criterion in this case implicitly assumes that $K_h/K_c \to \infty$). Another, important point discussed in Canuto [4–6] is the possibility that linear stability analysis might be misleading when used to model convection in the stably stratified regime (stability defined here with respect to the temperature gradient). In [5] the problem of a stable temperature gradient competing with a gradient of shear is discussed. For that case, the strength of both is commonly described by the Richardson number Ri, the ratio of the squares of buoyancy rate to shear rate. Classical, linear analysis predicts the production of turbulence be suppressed as soon as $Ri > Ri_{crit} = 1/4$. However, this linear analysis has been falsified by experiment, as was demonstrated for the ocean by Martin [31], where the surface layer of the ocean was found to be well mixed and turbulent despite $Ri \approx 4Ri_{crit} \approx O(1)$. Models that successfully reproduce this experimental result have been constructed (see [5] for further explanations and references), and naturally these models are not exclusively based, nor do they explicitly enforce the stability criterion obtained from linear analysis. This result should give a warning when constructing models of semi-convection which assume the results of linear stability analysis to strictly hold in the parameter ranges of astrophysical interest. Kimura et al. [20] have recently published direct numerical simulations of salt-fingers under the presence of a weak shear flow ($Ri \geq 1/2 > Ri_{crit} = 1/4$) in saltwater. They find pronounced differences of many relevant quantities (root mean square derivatives of velocities and effective diffusivities of heat and salt) for $Ri = 1/2$ when compared to cases of negligibly weak shear (which in their simulations occurs for about $Ri \gtrsim 6$). No similar work has yet been done for the case of semi-convection or low Prandtl numbers which occur in astrophysics.

To make further progress, models need both the challenge and the inspiration provided by experiments. Structural properties are a typical example. For models of semi-convection, the formation and existence of layers is often a crucial ingredient, for instance, for the model of Spruit [41] or in the analysis of Stevenson [44], while in other models the physics peculiar to such layers such as interfaces in-between them, and thus a variable gradient through a stack of layers tends to be neglected (for example, in the models of [4, 6, 63]). Clearly, to be answered these questions require experiments, whether they are made in the laboratory, in the field, or numerically.

11.4.2 Experiments

Already in the 1970s a series of laboratory experiments were carried out to investigate the formation of layers in double-diffusive processes. Huppert and Turner [17] performed a set of ice melting experiments in saltwater basins and predicted layer formation in this peculiar situation. The laboratory results could be confirmed at the Erebus Glacier in the Antarctic by Jacobs et al. [18]. He observed mean step heights of 20 m in salinity and temperature beneath the tip of the glacier tongue. Sidewall effects are found to form layers rapidly under certain conditions, e.g. when heat is generated by photographic supply. This process was studied in details by Thorpe, Hutt and Soulsby [52] using a strong lamp shining on the vertical wall of the fluid column, in particular to model oceanography-related boundary conditions. Another important work was published by Fernando [10] in 1987, who extensively studied the layer growth and the entrainment rate with a saltwater experiment. Especially, a critical layer height was predicted, at which a second convecting layer formed. Recent developments by Koetter [23] lead to the assumption that shear stress causes a significant structural modification. This process is relevant for semi-convective mixing in a rotating reference frame.

All the previously discussed experimental results are essentially limited to water as a fluid and thus to a different regime with respect to the Prandtl number, i.e. for $Pr > 1$ instead of $Pr \ll 1$, as would be appropriate for stellar plasma. Numerical simulations, however, can help to bridge this gap.

11.4.3 Numerical Simulations

Before turning to multidimensional simulations proper, let us briefly address a method which is computationally one-dimensional. The one-dimensional turbulence (ODT) approach (for a description, see [19], [11]) treats the advective and diffusive processes in different ways. The time-evolution due to diffusive processes is treated in the standard way. Advective processes are modelled via specific stochastic mappings. Basically, the approach can also be used in the sense of a subgrid model in multidimensional simulation.

In [11], however, it is applied as a stand-alone tool and, as a consequence, is computationally 1D (plus the time variable). This allows for fine gridding barely or not at all achievable in multidimensional simulations. In addition, in the specific implementation to which we refer care is taken about adaptive gridding. The method allows also the inclusion of horizontal shear flows.

Of course, there exist basic limitations to such an approach. The most elementary one is that quite generally any one-dimensional approach cannot faithfully represent structures in the other (horizontal) directions beyond yielding averages of the physical quantities (and possibly some spatial correlations, depending on details of what is actually being done). In the case of layered semi-convection with stairs forming, this amounts, in particular, to the inability to treat effects of waves of the interface. This refers not only to the efficiency of transport of material and heat through the interface, but, perhaps more importantly, to questions of stability of the interfaces against these wave motions.

However, some multidimensional models of semi-convection show the occurrence of interfaces even in parameter regions of astrophysical interest (low Prandtl number), see below. While these staircases do not necessarily last forever, there is a time span during which they may exist and for which these considerations are of interest.

Applying this methodology adopting the Boussinesq approximation, [11] study properties of interfaces both with the absence or presence of shear. The parameter domain spans Prandtl numbers from $Pr = 0.01$ to $Pr = 300$. A number of power-laws between parameters such as Pr, Le, Ra, R_ρ etc. are given. In sheared flow, this time for $Pr = 7$, three regimes for interface behaviour are identified. Not surprisingly, when increasing shear, i.e. decreasing Richardson number Ri, there firstly is but little difference to the unsheared case. Increasing shear then leads to a sharpening of the density jump due to enhanced entrainment. In the third regime with highest shear, the interface is broken and flattened out and ultimately destroyed.

First, truly multidimensional simulations in a regime attempting to approach astrophysically relevant cases (small Prandtl and Lewis numbers as compared to unity) commenced no earlier than in the 1990s with Merryfield's investigation [32]. In the setting of this paper, the physics applicable to the interior of a star of $30M_\odot$ is adopted. In the stellar model, the semi-convection zone has a vertical extension of about 3×10^5 km. Linear stability analysis including the change in molecular weight from top to bottom shows that the fastest growing gravity waves have a typical wavelength of $\sim$500 km for this star. A reasonable multiple of that size was chosen for the extension of the domain allowing the representation of several of such waves. A two-dimensional setting was adopted.

The numerics consists of Fourier collocation for temperature and velocity in the horizontal direction and of fourth-order central differences or tenth-order compact differentiation in the vertical. Some extra smoothing was applied to T because the chosen time-step was larger than stability considerations for the explicit time integration method would allow. The composition field with its finer features was treated by the flux corrected transport method.

The physical setting involved the anelastic approximation. Although aimed towards realistic stellar conditions, parameters used deviated from the physical values

for the stars. Naturally, the diffusion coefficients had to be chosen larger. In addition, however, it was necessary to impose a steeper temperature gradient because the growth times for the realistic one would have been too slow for computations to be feasible. Indeed, it is primarily a variation of the parameter $\nabla - \nabla_{\mathrm{ad}}$ which was used. A main result is that the character of the motions changes with decreasing driving. For strong driving, the waves originating from the vibrational instability grow, break, and ultimately the whole domain is convectively mixed. For cases of less driving, a step reminiscent of the staircase as in the model of Spruit [41] formed. In a case with still less driving, the final outcome resembles solitary waves.

The next major paper on semi-convection modelling in 2D was Biello's PhD-thesis (the easiest reference to results is [3]). Numerically, the work is not quite dissimilar to the paper just described: pseudo-spectral in the horizontal, compact finite differencing in the vertical direction. The code sets out from compressible hydrodynamics. Both high and fairly low Prandtl number cases are investigated (down to $Pr = 0.25$). With respect to the low Prandtl number regime, the issue whether one convective layer, extending from top to bottom, will form or whether layering will spontaneously cease, the outcome is pessimistic with respect to the latter scenario.

Recently, a group mainly from the United States and Germany has commenced working on modelling semi-convection numerically.[5] In [35] and [33] these investigators address questions of direct astrophysical interest. There, they consider the Boussinesq approximation for the case of low Prandtl and Lewis numbers. Numerically, their approach is based on spectral methods in all three dimensions, even the vertical, plus periodic boundary conditions (to temperature perturbation, etc.), again in the vertical as well. They identify two-parameter regimes which result from the simulations. In one, there ensues a sort of essentially homogeneous turbulence. It leads to a mass transport which surpasses case two, to be discussed immediately, by orders of magnitude. It is, however, still lower than in the case of ordinary convection. In case two, semi-convective layers with temperature and composition jumps develop. As time proceeds, they merge, leaving behind again a sort of turbulent state. Adopting methodology originally developed with thermohaline convection in mind, these authors derive a criterion that can be used to figure out which case to expect as a function of R_ρ.

At the same time, Zaussinger [64] investigated semi-convection with the fully compressible formulation and with the Boussinesq approximation using a (W)ENO-based staggered grid method. The parameter space covered three magnitudes in each relevant dimensionless number and, for the case of the compressible formulation, up to one pressure scale height. He showed a low dependence on the Prandtl number, which coincides with earlier theoretical assumptions. Furthermore, no significant

[5]Note that 'semi-convection' discussed in the present article is dubbed 'double-diffusive convection' in their work (which should be kept well separated from 'fingering convection' which refers to the specific case where the stably stratified component has a larger diffusion coefficient than the other, unstably stratified one). To avoid misunderstandings in the present paper, we use the terminology and notation more commonly found in astrophysics and introduced further above also for describing their work.

differences in the fluxes were observed in either method, even for the largest relevant scale heights. Therefore, the incompressible formulation was concluded to represent an appropriate and valid approximation describing thin semi-convective layers. The influence of R_ρ on the fluxes was found to scale with the power law exponent β.

For his work, Zaussinger [64] extended the ANTARES code, [34], which had been designed from the very beginning to operate in 1D, 2D and 3D. ANTARES is capable to also operate in spherical geometry, which, when tackling semi-convective zones as a whole, may be of interest. More recently, its developer team has extended the range of applicability of Kwatra's method [25] to the case of multicomponent flows, typically hydrogen and helium, and by enhancing its stability which was wanting in long-time runs (see [13]). This method solves the full Navier–Stokes equations without any approximations as are required by the Boussinesq or the anelastic formulation. Consequently, it can tackle at the same time flows of very low and high Mach number, including discontinuities. Still, its Courant–Friedrichs–Lewy condition involves the fluid velocity only (and not the sound speed), and it therefore enjoys the same favourable time-step properties as those more approximate formulations. This may be important for modelling entire semi-convective zones as opposed to thin layers only. Further developments concern numerical issues: new Runge–Kutta methods have been developed with the particular requirements of the time-advancement of Navier–Stokes equations and here, again, of semi-convection in mind. The most successful of these methods have been shown to yield a substantial gain in efficiency when compared to traditional Runge–Kutta time integrators that will translate into increased returns of computer runs. First results on these developments have been published in [24].

11.5 Conclusions

Summarizing the present state and future developments, let us remark first that semi-convection for the structure and evolution of gaseous giant planets has recently been revived by Chabrier and Baraffe [8], who argued that the radius excess found in some exoplanets could be explained by reduced heat conduction efficiency of a semi-convective zone. Indeed, the possibility of semi-convection in gaseous giant planets had already been proposed by Stevenson [45] two decades earlier, but the process never gained much attention as long as the planets of our own Solar System remained the only ones for which this process could be studied. Extending the perspectives discussed in [8, 45], very recently Leconte and Chabrier [29] argued that semi-convection has to be considered a key physical process also in gaseous giant planets and thus in most exoplanets found thus far and should hence be included in more complete planet structure and evolution models. The reason for this is that even if semi-convection may not be sufficient on its own to explain all current data on exoplanet radii and luminosities, its presence affects the heavy material content in giant planets, which is an important diagnostic for models of planet formation.

Obviously, such investigations will need basically the same knowledge and physical insight as is true for research in stellar physics. The question therefore must be: what has been achieved and what can be expected?

The time span between the seminal paper by Ledoux [30] and the present year happens to comprise two thirds of a century. This time span has witnessed an increase of analytic models for semi-convection of such a form that they can more or less easily (some of them definitely less easily) be incorporated into codes for stellar structure or evolution. To be sure, the very fact that models based on rather different physical premises are in concurrent use till today demonstrates that no unique conclusion has been reached regarding which model is possibly correct. A number of incorrect models have, however, been rejected. Having to choose among the different available models for a particular application, the most important requirement on any of them is certainly that they should take into account the physical fact that the fluxes of heat and mean molecular weight (helium, salt, etc.) are interlinked. Models which do not take that property into account can hardly be expected to yield reliable results. From the viewpoint of astrophysical observations, it may be that the advent of high-precision asteroseismology allows some further conclusions.

The most promising path for understanding and progress, however, is, in the authors' opinion, modelling based on the essentially complete equations of the problem in multidimensions. After all, this approach allows the close investigation of a number of relevant hydrodynamical processes, which otherwise could at most be guessed. This is true even when the parameter range relevant for stellar physics is elusive. The very same difficulty regarding parameters has not hindered investigations of ordinary stellar convection to make tremendous progress over the last decades. Admitting that semi-convection seems to be more difficult, hints from experiments that scaling laws hold over a pleasantly large range for a number of parameters are reassuring with regard to extrapolation.

The very least which can be expected from numerical simulations, in addition to elucidate basic physical effects, is that simplified models can be checked. For example, it is absolutely feasible to compare the predictions of ODT with the outcome of numerical experiments for nontrivial Prandtl numbers such as $Pr = 0.01$ and to get insight to the faithfulness of this approximation or others.

It is also encouraging that now two groups are working on multidimensional modelling of semi-convection, namely the group as exemplified in [33, 35] and the group as exemplified in [13, 24, 64]. It will be rewarding to compare the outcome of the codes using different numerics. At the same time, the influence of boundary conditions can be studied: the simulation code used by the first group assumes vertically periodic boundary conditions for the disturbances, while the code used by the latter group has no specific restrictions on the boundary conditions and thus can also apply, for instance, fixed plates.

Overall, it seems that isolated efforts, which dominated numerical modelling of semi-convection since it commenced in 1995, are increasingly giving way to a broader attack as appropriate for a problem of such complexity.

Acknowledgements The authors acknowledge support through grants P20973 and P21742 by the Austrian Science Fund (FWF) and by grants KU 1954/3-1 and KU 1954/3-2 within SPP 1276/1

and SPP 1276/2 MetStröm of the Deutsche Forschungsgemeinschaft (DFG). Numerical simulations used in this presentation have been performed at the Heraklit Cluster, Brandenburg University of Technology (BTU) Cottbus, Germany. We are thankful to V.M. Canuto for pointing out the work of Kimura et al. to us and for comments which improved the readability of the paper. We are also thankful to J. Ballot for carefully reading this manuscript.

References

1. Baines, P.G., Gill, A.E.: On thermohaline convection with linear gradients. J. Fluid Mech. **37**, 289–306 (1969)
2. Bertelli, G., Nasi, E., Girardi, L., Marigo, P.: Scaled solar tracks and isochrones in a large region of the Z–Y plane. II. From 2.5 to 20$M_{\odot}$ stars. Astron. Astrophys. **508**, 355–369 (2009)
3. Biello, L.: Layer formation in semiconvection. Ph.D. thesis, Department of Astronomy and Astrophysics, The University of Chicago (2001)
4. Canuto, V.M.: Turbulence in stars. III. Unified treatment of diffusion, convection, semiconvection, salt fingers, and differential rotation. Astrophys. J. **524**, 311–340 (1999)
5. Canuto, V.M.: Turbulence in astrophysical and geophysical flows. In: Hillebrandt, W., Kupka, F. (eds.) Interdisciplinary Aspects of Turbulence. Lecture Notes in Physics, vol. 756, p. 107. Springer, Berlin (2009)
6. Canuto, V.M.: Stellar mixing. II. Double diffusion processes. Astron. Astrophys. **528**, A77 (2011)
7. Castellani, V., Chieffi, A., Tornambe, A., Pulone, L.: Helium-burning evolutionary phases in population II stars. I Breathing pulses in horizontal branch stars. Astrophys. J. **296**, 204–212 (1985)
8. Chabrier, G., Baraffe, I.: Heat transport in giant (exo)planets: a new perspective. Astrophys. J. Lett. **661**, L81–L84 (2007)
9. Charbonnel, C., Lagarde, N.: Thermohaline instability and rotation-induced mixing. I. Low- and intermediate-mass solar metallicity stars up to the end of the AGB. Astron. Astrophys. **522**, A10 (2010)
10. Fernando, H.J.S.: The formation of a layered structure when a stable salinity gradient is heated from below. J. Fluid Mech. **182**, 525–541 (1987)
11. Gonzalez-Juez, E., Kerstein, A.R., Lignell, D.O.: Fluxes across double-diffusive interfaces: a one-dimensional-turbulence study. J. Fluid Mech. **677**, 218–254 (2011)
12. Grossman, S.A., Taam, R.E.: Double-diffusive mixing-length theory, semiconvection and massive star evolution. Mon. Not. R. Astron. Soc. **283**, 1165–1178 (1996)
13. Happenhofer, N., Grimm-Strele, H., Kupka, F., Löw-Baselli, B., Muthsam, H.: A low Mach number solver: enhancing stability and applicability. arXiv:1112.3507 [physics.comp-ph]
14. Heger, A., Langer, N., Woosley, S.E.: Presupernova evolution of rotating massive stars. I. Numerical method and evolution of the internal stellar structure. Astrophys. J. **528**, 368–396 (2000)
15. Hirschi, R., Meynet, G., Maeder, A.: Stellar evolution with rotation. XII. Pre-supernova models. Astron. Astrophys. **425**, 649–670 (2004)
16. Huppert, H.E., Moore, D.R.: Nonlinear double-diffusive convection. J. Fluid Mech. **78**, 821–854 (1976)
17. Huppert, H.E., Turner, J.S.: Double-diffusive convection. J. Fluid Mech. **106**, 299–329 (1981)
18. Jacobs, S.S., Huppert, H.E., Holdsworth, G., Drewry, D.J.: Thermohaline steps induced by melting of the Erebus Glacier Tongue. J. Geophys. Res. **86**, 6547–6555 (1981)
19. Kerstein, A.R.: One-dimensional turbulence stochastic simulation of multi-scale dynamics. In: Hillebrandt, W., Kupka, F. (eds.) Interdisciplinary Aspects of Turbulence. Lecture Notes in Physics, vol. 756, p. 291. Springer, Berlin (2009)
20. Kimura, S., Smyth, W., Kunze, E.: Turbulence in a sheared, salt-fingering-favorable environment: anisotropy and effective diffusivities. J. Phys. Oceanogr. **41**, 1144–1159 (2011)

21. Kippenhahn, R., Weigert, A.: Stellar Structure and Evolution. Springer, Berlin (1994)
22. Kippenhahn, R., Ruschenplatt, G., Thomas, H.C.: The time scale of thermohaline mixing in stars. Astron. Astrophys. **91**, 175–180 (1980)
23. Kötter, K.: Instabilität durch doppel-diffusive Konvektion: Strukturbildung in Experiment und Simulation. Ph.D. thesis, Universität Dortmund (2001)
24. Kupka, F., Happenhofer, N., Higueras, I., Koch, O.: Total-variation-diminishing implicit-explicit Runge–Kutta methods for the simulation of double-diffusive convection in astrophysics. J. Comput. Phys. **231**, 3561–3586 (2012)
25. Kwatra, N., Su, J., Grétarsson, J.T., Fedkiw, R.: A method for avoiding the acoustic time step restriction in compressible flow. J. Comput. Phys. **228**, 4146–4161 (2009)
26. Lagarde, N., Charbonnel, C., Decressin, T., Hagelberg, J.: Thermohaline instability and rotation-induced mixing. II. Yields of ^{3}He for low- and intermediate-mass stars. Astron. Astrophys. **536**, A28 (2011)
27. Lagarde, N., Romano, D., Charbonnel, C., Tosi, M., Chiappini, C., Matteucci, F.: Effects of thermohaline instability and rotation-induced mixing on the evolution of light elements in the galaxy: D, ^{3}He and ^{4}He. Astron. Astrophys. **542**, A62 (2012)
28. Langer, N., Fricke, K.J., Sugimoto, D.: Semiconvective diffusion and energy transport. Astron. Astrophys. **126**, 207 (1983)
29. Leconte, J., Chabrier, G.: A new vision of giant planet interiors: impact of double diffusive convection. Astron. Astrophys. **540**, A20 (2012)
30. Ledoux, P.: On stellar models with convection and discontinuity of the mean molecular weight. Astron. J. **52**, 155 (1947)
31. Martin, P.J.: Simulation of the mixed layer at OWS November and Papa with several models. J. Geophys. Res. **90**, 903–916 (1985)
32. Merryfield, W.J.: Hydrodynamics of semiconvection. Astrophys. J. **444**, 318–337 (1995)
33. Mirouh, G.M., Garaud, P., Stellmach, S., Traxler, A.L., Wood, T.S.: A new model for mixing by double-diffusive convection (semi-convection). I. The conditions for layer formation. Astrophys. J. **750**, 61 (2012)
34. Muthsam, H.J., Kupka, F., Löw-Baselli, B., Obertscheider, C., Langer, M., Lenz, P.: ANTARES—A Numerical Tool for Astrophysical RESearch with applications to solar granulation. New Astron. **15**, 460–475 (2010)
35. Rosenblum, E., Garaud, P., Traxler, A., Stellmach, S.: Turbulent mixing and layer formation in double-diffusive convection: three-dimensional numerical simulations and theory. Astrophys. J. **731**, 66 (2011)
36. Sani, R.: On finite amplitude roll cell disturbances in a fluid layer subjected to heat and mass transfer. Am. Inst. Chem. Eng. J. **11**(6), 971–980 (1965)
37. Schmidt, M.: Double-diffusive convection in Lake Kivu. Limnol. Oceanogr. **55**(1), 225–238 (2010)
38. Schwarzschild, K.: On the equilibrium of the sun's atmosphere. Nachr. K. Ges. Wiss. Gött. **195**, 41–53 (1906)
39. Schwarzschild, M., Härm, R.: Evolution of very massive stars. Astrophys. J. **128**, 348 (1958)
40. Silva Aguirre, V., Ballot, J., Serenelli, A.M., Weiss, A.: Constraining mixing processes in stellar cores using asteroseismology. Impact of semiconvection in low-mass stars. Astron. Astrophys. **529**, A63 (2011)
41. Spruit, H.C.: The rate of mixing in semiconvective zones. Astron. Astrophys. **253**, 131–138 (1992)
42. Stern, M.E.: The salt-fountain and thermohaline convection. Tellus **12**, 172 (1960)
43. Stern, M.E.: Collective instability of salt fingers. J. Fluid Mech. **35**, 209–218 (1969)
44. Stevenson, D.J.: Semiconvection as the occasional breaking of weakly amplified internal waves. Mon. Not. R. Astron. Soc. **187**, 129–144 (1979)
45. Stevenson, D.J.: Cosmochemistry and structure of the giant planets and their satellites. Icarus **62**, 4–15 (1985)
46. Stothers, R.: Internal structure of upper main-sequence stars. Mon. Not. R. Astron. Soc. **151**, 65 (1970)

47. Stothers, R.B., Chin, C.W.: Criterion for convection in an inhomogeneous star. Astrophys. J. Lett. **390**, L33–L35 (1992)
48. Stothers, R.B., Chin, C.W.: Galactic stars applied to tests of the criterion for convection and semiconvection in an inhomogeneous star. Astrophys. J. **431**, 797–805 (1994)
49. Stothers, R., Simon, N.R.: An explanation for the blue sequence of variable stars. Astrophys. J. **157**, 673 (1969)
50. Suarez, F.: A fully coupled, transient double-diffusive convective model for salt-gradient solar ponds. Int. J. Heat Mass Transf. **53**, 1718–1730 (2010)
51. Thomas, H.C.: Sternentwicklung VIII. Der Helium-Flash bei einem Stern von 1. 3 Sonnenmassen. Z. Astrophys. **67**, 420 (1967)
52. Thorpe, S.A., Hutt, P.K., Soulsby, R.: The effect of horizontal gradients on thermohaline convection. J. Fluid Mech. **38**, 375–400 (1969)
53. Ulrich, R.K.: Thermohaline convection in stellar interiors. Astrophys. J. **172**, 165 (1972)
54. Umeda, H., Nomoto, K.: How much ^{56}Ni can be produced in core-collapse supernovae? Evolution and explosions of 30–100$M_{\odot}$ stars. Astrophys. J. **673**, 1014–1022 (2008)
55. Vauclair, S.: Thermohaline convection and metallic fingers in polluted stars. In: Zverko, J., Ziznovsky, J., Adelman, S.J., Weiss, W.W. (eds.) The A-Star Puzzle. IAU Symposium, vol. 224, pp. 161–166. Cambridge University Press, Cambridge (2004)
56. Veronis, F.: On finite amplitude instability in thermohaline convection. J. Mar. Res. **23**, 1–17 (1965)
57. Veronis, G.: Effect of a stabilizing gradient of solute on thermal convection. J. Fluid Mech. **34**, 315–336 (1968)
58. Weaver, T.A., Woosley, S.E.: Nucleosynthesis in massive stars and the $^{12}C(\alpha, \gamma)^{16}O$ reaction rate. Phys. Rep. **227**, 65–96 (1993)
59. Weaver, T.A., Zimmerman, G.B., Woosley, S.E.: Presupernova evolution of massive stars. Astrophys. J. **225**, 1021–1029 (1978)
60. Weiss, A.: The progenitor of SN 1987A—Uncertain evolution of a 20 solar mass star. Astrophys. J. **339**, 365–381 (1989)
61. Weiss, A., Hillebrandt, W., Thomas, H.C., Ritter, H.: Cox and Giuli's Principles of Stellar Structure. Cambridge Scientific, Cambridge (2004)
62. Xiong, D.R.: Convective overshooting in stellar internal models. Astron. Astrophys. **150**, 133–138 (1985)
63. Xiong, D.R.: The evolution of massive stars using a non-local theory of convection. Astron. Astrophys. **167**, 239–246 (1986)
64. Zaussinger, F.: Numerical simulation of double-diffusive convection. Ph.D. thesis, MPI for Astrophysics, Max Planck Society (2011)

Chapter 12
Experimental and Numerical Investigation of Internal Gravity Waves Excited by Turbulent Penetrative Convection in Water Around Its Density Maximum

Stéphane Perrard, Michaël Le Bars, and Patrice Le Gal

Abstract This study is devoted to the experimental and numerical analysis of the excitation of gravity waves by turbulent convection. This situation is representative of many geophysical or astrophysical systems such as the convective bottom layer of the atmosphere that radiates internal waves in the stratosphere, or the interaction between the convective and the radiative zones in stars. In our experiments, we use water as a working fluid as it possesses the remarkable property of having a maximum density at 4 °C. Therefore, when establishing on a water layer a temperature gradient between 0 °C at the bottom and room temperature at the top, a turbulent convective region appears spontaneously under a stably stratified zone. In these conditions, gravity waves are excited by the convective fluid motions penetrating the stratified layer. Although this type of flow, called penetrative convection, has already been described, we present here the first velocity field measurement of wave emission and propagation. We show in particular that an intermediate layer that we call the buffer layer emerges between the convective and the stratified zones. In this buffer layer, the angle of propagation of the waves varies with the altitude since it is slaved to the Brunt–Väisälä frequency which evolves rapidly between the convective and the stratified layer. A minimum angle is reached at the end of the buffer layer. Then we observe that an angle of propagation is selected when the waves travel through the stratified layer. We expect this process of wave selection to take place in natural situations.

S. Perrard (✉)
Laboratoire Matière et Systèmes Complexes, UMR 7057, CNRS/Université Paris Diderot, Bâtiment Condorcet, 10 rue Alice Domon et Léonie Duquet, 75013 Paris, France
e-mail: perrard@clipper.ens.fr

M. Le Bars · P. Le Gal
Institut de Recherche sur les Phénomènes Hors Equilibre, UMR 7342, CNRS/Aix-Marseille Université, 49 rue F. Joliot Curie, 13384 Marseille Cédex 13, France

M. Le Bars
e-mail: lebars@irphe.univ-mrs.fr

M. Goupil et al. (eds.), *Studying Stellar Rotation and Convection*,
Lecture Notes in Physics 865, DOI 10.1007/978-3-642-33380-4_12,

12.1 Introduction

In most of geo- and astrophysical systems, turbulent convective fluid layers are contiguous with stably stratified zones. Examples include the oceanic upper mixed layer and underlying pycnocline, the atmospheric convective layer and overlying stratosphere, the convective and radiative zones in stars, etc. In classical models of planetary and stellar fluid mechanics, stratified zones are often postulated to be without proper motion. They can nevertheless support oscillatory motions called gravity or internal waves, where the restoring force is due to buoyancy. It has been recognized some 40 years ago in geophysics [3] and more recently in astrophysics [24] that gravity waves can be excited by turbulent convective motions at the interface separating the convective to the stratified fluid domain. This mechanism could be of fundamental importance regarding the transport of momentum and energy through the stratified layer, with important consequences for the system's global organization and evolution. For instance, it has been suggested that in the Earth's atmosphere, the momentum transported by convectively generated gravity waves could drive the quasi-biennial oscillation, i.e. the measured quasi-periodic oscillation of the equatorial zonal wind between easterlies and westerlies in the tropical stratosphere with a mean period of 28 to 29 months [10]. Gravity waves are also known to affect the global momentum budget in the middle and upper atmosphere as well as in the troposphere through wave drag [2]. In stars, convectively generated internal waves constitute an efficient process for angular momentum transport over large distances: they are now seen as an important ingredient in the evolution of rotation within stars [12]. Gravity waves are also invoked as a source of mixing for chemical elements and could help to resolve the enigma of the Lithium dip, forming a coherent picture of mixing in all main sequence stars [21].

Despite a significant number of studies, the current treatment of convectively generated gravity waves still presents major weaknesses. Indeed, the precise mechanism for the generation of such waves, since their typical amplitude as well as their time and space frequency spectra still remain largely unknown. This is mostly due to the difficulties encountered in rigorously describing, in theoretical and numerical models, the transition layer between the convective and the stratified zones, and to simultaneously address a very large range of time and length scales. Two types of approaches can be imagined from a theoretical or a numerical point of view. The first consists in describing the whole system with a single set of equations and methods; but this remains up to now out of reach of theoretical models and of precise numerical simulations (see however the very interesting works in 2D in [18] and [19], and the most recent simulations in 3D by [4], but with a moderate resolution). The second, more widely applied, is to describe separately the convective and stratified zones, which allows one to solve each of them with relevant methods and scales but necessitates that one follows the location of the interface and imposes ad hoc interface conditions that control part of the physical mechanisms. For instance, when considering a fixed interface, coupling is only induced by stresses at the boundary, and the possible effects of interface deformations by overshooting plumes are neglected [21]. In this context, an experimental approach based on relatively simple

laboratory arrangements using water as a working fluid is of great interest, since it allows one to get a global picture of this complex system including all of its interactions and nonlinearities.

Internal waves correspond to periodic density fluctuations in time and space in a stably stratified layer, i.e. where the density decreases with the altitude. In the case of a temperature stratification the Rayleigh number is negative and convective motions will never appear. On the other hand, a small displacement of a fluid particle induces a buoyancy force due to the local difference of density. Writing the classical set of equations for fluid mechanics with a perfect fluid in the Boussinesq approximation and looking for plane wave solutions, the dispersion relation for internal waves can be deduced analytically:

$$\omega^2 = N^2 \sin^2 \theta \tag{12.1}$$

where ω is the frequency of the waves, and θ the angle between the wave vector and the vertical axis. Note that the wavelength does not appear explicitly in this dispersion relation. N is the Brunt–Väisälä frequency given by

$$N(z) = \frac{1}{2\pi}\sqrt{g\alpha(T)\frac{dT}{dz}} \tag{12.2}$$

where $\alpha(T)$ corresponds to the thermal dilatation coefficient and g to the acceleration of gravity. In the case of a constant temperature gradient and no variation of α with temperature (for instance far from the maximum density of water), the Brunt–Väisälä frequency N remains constant.

Several experimental studies published in the 1960s and 1970s and mostly dedicated to geophysical applications, focus on this internal waves generation by convective motions. Some of them focus on non-stationary situations where an initially thermally stratified layer of water is suddenly heated from below [6]: a convective mixed zone then forms from the bottom of the tank and progressively invades the whole layer of fluid. Others studies benefit from the unusual property of water that its density has a maximum value near 4 °C. Consequently, in a tank filled with water with a horizontal bottom at about 0 °C and a warmer top at room temperature or more, the density stratification is stable in the higher part of the tank and unstable below the 4 °C isotherm. With sufficient separation between the top and bottom plates, the bottom layer is convectively unstable, whereas the upper layer remains stably stratified, allowing one to study stationary configurations once steady-state heat fluxes are established [23]. As expected, in both transient and stationary experiments, the presence of inertial waves in the stratified zone have been observed, based mostly on local temperature measurements. But such local measurements do not allow one to build a global description of the flows, and in particular the coupling between the stable and the unstable layers is still puzzling. To the best of our knowledge, only one recent study by [16] has reinvestigated these questions using modern techniques of non-intrusive global flow measurements, but only for the non-stationary case. Interesting results regarding the excited spectra of internal waves in space and time and the strong two-way coupling between convection and internal waves have, however, been reported. These results now demand confirmation and

generalization in the stationary configuration, which is the purpose of the present study.

In the seventies, McLaren et al. [13] and later Cerasoli [5] investigated the nature and the energy transfer of internal gravity waves generated by a thermal (i.e. an instantaneous release of a buoyant volume of fluid), using respectively particle tracking method and local conduction measurements complemented by dye line visualization. More recently, Ansong and Sutherland [2] have presented experimental results of the generation of internal gravity waves by a turbulent buoyant plume (i.e. a continuous release of buoyant fluid) impinging upon the interface between a uniform density layer of fluid and a linearly stratified layer (all made of salty water). Using non-intrusive schlieren measurements, they determined the fraction of the energy flux associated with the plume at the neutral buoyancy level that is extracted by the waves, and quantified the maximum vertical displacement amplitude. In this case, the frequency of the waves was found to lie in a narrow range relative to the buoyancy frequency, contrary to the numerical results by Rogers and Glatzmaier [18], who predicted a rather extended range for the frequency of waves emitted from a mixing layer. This point will also be discussed here.

12.2 Experimental Setup and Measurement Techniques for Penetrative Convection in Water Around 4 °C

To simplify the fluid motions and their measurements, we choose to confine the layer of water between two vertical walls (x and z being respectively the horizontal and vertical coordinates) separated by a short lateral distance equal to 4 cm along the y direction. We have used two different experimental cells that both almost reproduce the Hele–Shaw geometry. The first was built using two Plexiglas plates of dimensions 20 cm × 20 cm in the (x, z) plane and thick enough (2 cm) to reduce horizontal outward heat fluxes as the conductivity of Plexiglas is three times lower than the conductivity of water. A second container has been also used. It is taller, allowing a better analysis of the propagation of the internal waves in the stratified layer. It was built by two "vacuumed" glass slabs with a very low thermal conductivity $\lambda_v = 8.4 \times 10^{-2}$ W/K/m, i.e. a hundred times smaller than water conductivity. The x and z dimensions of these windows are 18 cm × 35 cm. The two other lateral vertical walls of both containers were made in Plexiglas with an additional layer of polystyrene foam of thickness 6 cm. The experimental containers were closed by bottom ($z = 0$) and top ($z = 35$ cm or 20 cm) copper plates whose temperatures were regulated by two thermal baths with an accuracy of 0.01 °C. We have checked by visual inspection that as desired, mainly two-dimensional fluid motions take place in the water layers, greatly simplifying the measurements of the velocity field. This narrow geometry also allows us to determine the free position of the separation zone between the convective and the stratified layer which depends on the heat transport. To avoid long thermal transients, we have used the double-bucket technique [17] to prepare a temperature stratified layer of water above a homogeneous layer at 4 °C.

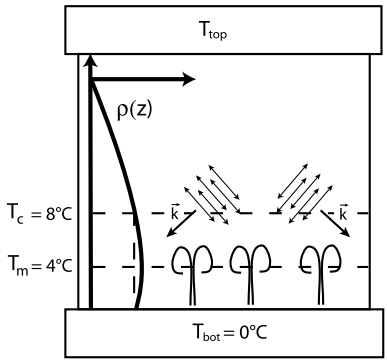

Fig. 12.1 Schematic representation of our experiment. The non-monotonic water density profile allows us to observe two different layers in a stationary state. The lower one is a turbulent convective layer, whereas the upper layer is stratified where internal waves can propagate

The bottom copper plate temperature is then regulated at $T_{\text{bot}} = 0$ °C and the upper at a temperature T_{top} ranging from 18 °C to 35 °C depending on the experimental run. As the density of water increases with the temperature between $T_{\text{bot}} = 0$ °C and $T_m = 4$ °C, natural convective motions appear in the bottom layer. This convective layer grows and finally reaches a steady state where its height does not evolve any more. This position is around $z_m \sim 25$ cm from the bottom, which gives a height of 10 cm for the stable stratification in the case where the tall vacuumed-glass container is used. Figure 12.1 gives a schematic representation of the experimental arrangement and of the physical mechanisms of penetrative convection.

Two kinds of measurements were taken in order to characterize both layers. The simplest used local temperature probes. A set of four temperature-type K sensors were positioned at different heights in the middle part of the experimental cell. Another temperature probe was also used to measure vertical temperature profiles. This direct and simple technique was already used (with platinum probes (Pt 100)) by Townsend [23], who reported the first observation of internal waves in water around 4 °C by measuring the temperature fluctuations in the stratified layer. The typical amplitude of temperature fluctuations is $\delta T \sim 0.01$ K, which corresponds to a relative variation of density of $\delta\rho/\rho \sim 10^{-6}$. Note that this amplitude is hundred times smaller than the fluctuation of density usually observed in experiments on internal waves using salt water. An important consequence of this small density gradient is the impossibility to use the now-popular synthetic schlieren method [20]. This technique is based on the variation of the optical refraction index which is undetectable in our case. Therefore, we use the more sensitive Particle Image Velocimetry method (PIV) [1] to directly measure the velocity field associated to the fluid motions. Small particles with a diameter $d = 30$ µm and a density close to the water density (at the temperatures considered here) are used as tracers. Fortunately, the convective motions are turbulent enough to mix these particles in the whole flow within a few days. A laser beam illuminates these particles on a vertical section of thickness 1 mm and 4500×2500 resolution images are recorded with a numerical photographic camera. A PIV measurement algorithm [15] is then used to extract the velocity fields from the data. Our analysis was performed using typically 128×32 boxes of 128×32 pixels with a distance between the centers of two neighboring vertical boxes of

$\Delta Z = 0.15$ mm and $\Delta X = 0.6$ mm between two horizontal boxes. Finally, the time step between two images is chosen between $\Delta t = 5$ s and 20 s. This technique produces velocity maps of 100×80 vectors as functions of time. The range of velocity values which can be measured with an accuracy better than 5 % depends on the value of ΔX, ΔZ and Δt. Owing to the high variation of the velocity along the vertical direction z in the region between the two layers, the PIV parameters are adapted to each measurement, that is why we have used several different time increments. We have chosen rectangular boxes to increase the accuracy along the horizontal direction and the number of measurement points along the vertical direction. After the extraction of the measured velocity field $V(x, z, t)$, we perform a signal analysis in the three-dimensional Fourier space (f, k_x, k_z) for respectively time, x direction and z direction. To separate the weak wave signals from the background noise, we use the singular property of internal waves to propagate in a direction making an angle θ relative to the vertical direction independent of the wavelength. There are four directions of propagation for each Fourier component (f, k_x, k_z) of the velocity field $V(\mathbf{r}, t)$, making the traditional St. Andrew's cross whose branches are perpendicular to the wave vectors. In our case, as we will see, internal waves may contain a wide range of frequencies, and we need to separate both the Fourier components in time (different values of f) and the Fourier components associated to different directions of propagation given by the sign of k_x and k_z. To perform this analysis, the velocity field has been studied with the help of the Hilbert transform, a useful tool first used on internal wave observations in [14]. This technic uses the central symmetry of the Fourier transform of a real signal, here $V(x, z, t)$. The wave beam of frequency f propagating along the (k_x, k_z) direction is the sum of two symmetrical Fourier components (f, k_x, k_z) and $(-f, -k_x, -k_z)$. In the spatial Fourier domain, the components of waves propagating along two opposite directions are combined in (k_x, k_z) and $(-k_x, -k_z)$. We separate these components by keeping only the positive frequency in the three-dimensional Fourier space. After performing an inverse Fourier transform in time, each quarter of the (k_x, k_z) space corresponds now to the wave propagating along the chosen direction. We can thus filter and keep only one quarter of the (k_x, k_z) plane and perform the inverse Fourier transform in space to obtain the space-time velocity field $V(x, z, t)$ associated to one of the four beams of the St. Andrew's cross. Additional band-pass filtering in time and space has been also occasionally performed and will be mentioned when used.

12.3 Turbulent Penetrative Convection

12.3.1 Classical Rayleigh Bénard Convection Between Two Horizontal Plates

A layer of liquid subjected to a negative vertical gradient of temperature between a bottom and a top solid plate is set into motion if the buoyancy force due to the thermal dilatation of the fluid is large enough to compensate for the diffusion of

both temperature and momentum. The associated nondimensional number, called the Rayleigh number, measures the ratio of these destabilizing to stabilizing effects:

$$Ra = \frac{g\alpha \Delta T H^3}{\kappa \nu}, \tag{12.3}$$

where α is the thermal dilatation coefficient, ΔT the temperature difference between the top and the bottom of the layer, H the height of the fluid layer, and κ and ν respectively the thermal diffusion coefficient and kinematic viscosity. We can note that this Rayleigh number is negative if the temperature gradient has the opposite sign of α. For solid boundary conditions, the critical Rayleigh number value is $Ra_c = 1708$ and 1101 for mixed solid/fluid boundary conditions. Far from this threshold, turbulent convection invades the whole fluid layer except for two thin thermal boundary layers of thickness δ_c, confined close to the solid top and bottom plates. The mean temperature in the turbulent bulk is constant equal to $T_m = T_{\text{bot}} + \Delta T/2$, in contrast with the temperature in the two boundary layers, which varies linearly with the altitude. δ_c corresponds to the thickness of these boundary layers for which the local Rayleigh number is equal to the critical value calculated with $\Delta T/2$, i.e.,

$$Ra(\delta_c) = Ra_c, \tag{12.4}$$

where $Ra_c = 1101$. This characteristic length was first introduced by Malkus [11], and the picture of two thin boundary layers of thickness δ_c separated by a homogeneous bulk at a temperature T_m is now the classical image associated with turbulent Rayleigh–Bénard convection for Rayleigh numbers higher than 10^6.

12.3.2 Penetrative Convection in Water Around 4 °C

For water, the sign of α changes at 4 °C. Thus the lower layer where $0\ ^\circ\text{C} < T < T_{\max} = 4\ ^\circ\text{C}$ can be unstable if thick enough ($Ra > Ra_c$) contrary to the upper stratified zone corresponding to $T > 4\ ^\circ\text{C}$ which will be always stable ($Ra < 0$). Using the physical parameters of water, we estimate the value for the Rayleigh number to be around $Ra = 10^7$ for a convective layer of height $H = 15$ cm. This large value for the Rayleigh number justifies to use the approach of Malkus [11] to evaluate the thickness of the bottom diffusive thermal boundary layer in our penetrative convection experiment:

$$\delta_c = \left(\frac{Ra_c \kappa \nu}{g} \frac{\rho_0}{\Delta \rho} \right)^{1/3}, \tag{12.5}$$

where $\Delta\rho/\rho_0$ corresponds to the relative variation of water density between $T_{\text{bot}} = 0\ ^\circ\text{C}$ and $T_{\max} = 4\ ^\circ\text{C}$. As can be seen, δ_c depends only on the physical properties of water and is equal here to $\delta_c = 0.6$ cm. This value is confirmed by measuring the vertical temperature profile at the bottom of the convective layer, for several values of the temperature at the top ($T_{\text{top}} = 8, 15, 20, 35\ ^\circ\text{C}$), and for both, the Plexiglas and the vacuumed glass tanks ($H = 20$ mm and $H = 35$ mm, respectively).

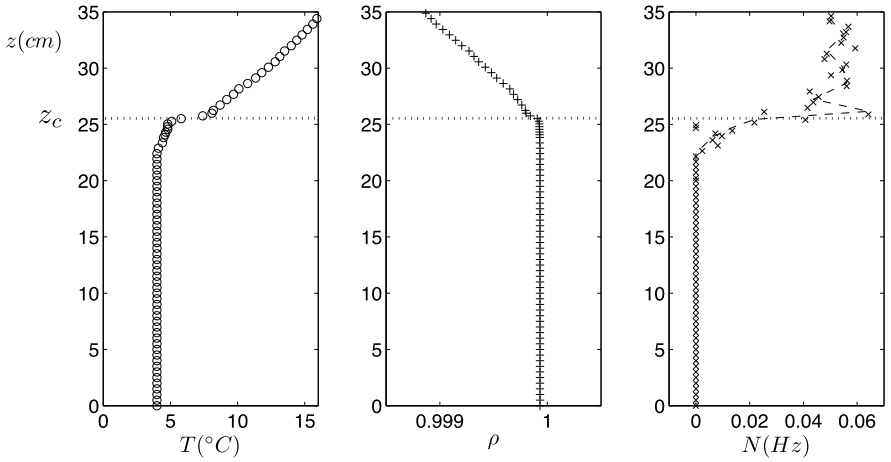

Fig. 12.2 (**a**) Vertical temperature profile showing the constant temperature in the turbulent convective layer ($0 < z < 23$ cm). (**b**) Vertical density profile calculated from the temperature profile. (**c**) Vertical Brunt–Väisälä frequency $N(z)$. The *dotted line* represents the mean position z_m of the $T_c = 8$ °C isotherm

As presented in Fig. 12.2(a), we measure in the whole convective layer a constant mean temperature T_m equal to $T_{\max} = 4$ °C with a typical variation of 0.1 °C. This layer corresponds to a well-mixed zone of water. Close to the density maximum at $T_{\max} = 4$ °C, $\rho(T)$ is a symmetric function of $T - T_{\max}$, so a fluid particle at 0 °C will have a density equal to one at 8 °C and thus, even in the limit of adiabatic motion, cannot penetrate beyond the 8 °C isotherm. The vertical density profile has been computed using our temperature measurements and the physical properties of water. It is shown in Fig. 12.2(b). The well-mixed layer extends from $z = \delta_c \sim 0.6$ cm to $z = 23$ cm. For $z > 25$ cm, the density gradient is almost constant, which gives a constant value of $N = 0.05 \pm 0.01$ Hz (see Fig. 12.2(c)). In this region, we expect the propagation of waves to be along straight lines forming different angles θ with the vertical axis depending on the wave frequency. The vertical position of the limit between the convective and the stratified layers can be determined using the heat flux Q_d through the lower diffusive boundary layer. As the system reaches a stationary state, there is a thermal equilibrium between each layer, and the vertical heat flux $Q(z)$ has to be conserved for all value of z. We define this limit by the position z_c of the $T_c = 8$ °C isotherm. In the following, z_c is measured to be around 25 cm. The heat flux verifies the implicit equation

$$Q_d = Q_s, \tag{12.6}$$

where Q_s is the thermal diffusive flux through a stratified layer of thickness $z_{\text{up}} - z_c$ subjected to a difference in temperature of $\Delta T = T_{\text{up}} - T_c$. Using Fourier's law, we can deduce the value for z_c:

$$z_c = \delta_c \frac{T_{\text{up}} - T_c}{T_m - T_{\text{bot}}}, \tag{12.7}$$

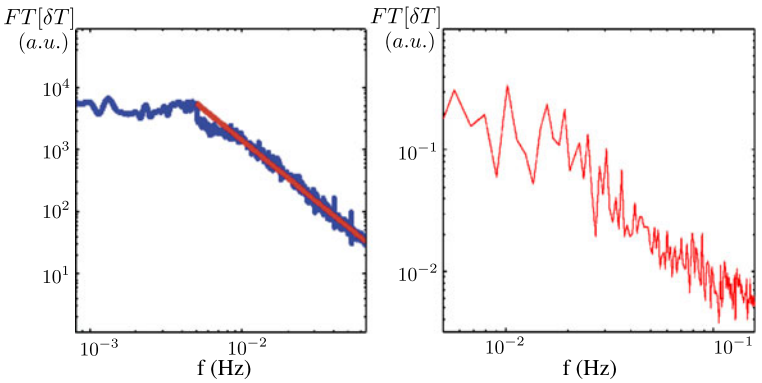

Fig. 12.3 (**a**) Temporal temperature spectrum in the convective layer. The measurement has been performed by two type K probes. We find a direct energy cascade from small to higher frequencies for $f > f_c \sim 5 \times 10^{-3}$ Hz. (**b**) Temporal temperature spectrum in the stratified layer. Due to their small amplitude, gravity waves are not detected, and the spectrum is typical of a f^{-1} noise spectrum (f^{-2} for the energy spectrum)

where δ_c corresponds to the thickness of the lower thermal boundary layer (see Eq. (12.5)). As the thickness of the boundary layer δ_c and the difference of temperature $T_m - T_{\text{bot}}$ are fixed by the maximum density of water at 4 °C, the height of the stratified layer depends only on the temperature imposed at the top of the tank. We remark that between the convective and the stratified zones, we observe an intermediate layer of thickness around two centimeters where the temperature and the density gradients vary with z, first slowly, then very rapidly. This zone is in fact delimited by the 4 °C and 8 °C isotherms. This intermediate zone plays an important role in the transmission of both momentum and energy from the convective motions of the internal waves, as we will see below.

Before studying the generation of internal waves and their interaction with convection, we will first describe our natural wave maker, the turbulent convective layer. For this purpose, we perform two point temperature measurements at $z_1 = 5$ cm and $z_2 = 12$ cm (in the container 1) and compute the Fourier transform of $\delta T = T(z_2) - T(z_1)$. This method eliminates the thermal fluctuations of the reference junction. The resulting temperature spectrum ranges from $f = 2 \times 10^{-6}$ Hz to $f = 3$ Hz (see Fig. 12.3(a)). Figure 12.3(b) presents the same spectrum but measured in the stratified layer. As can be seen, no coherent temperature fluctuations are detectable in this zone as the gravity waves amplitude is very small; thus, this spectrum corresponds to thermal noise with a classical power-law proportional to f^{-2}. The temperature fluctuations in the convective zone flat part of the spectrum in Fig. 12.3(a) is observed in a large range of frequencies starting from very low frequency (certainly associated to large circulation in the whole container) up to a characteristic frequency $f_c \sim 5 \times 10^{-3}$ Hz. The existence of this characteristic low frequency f_c suggests a production mechanism that forbids the generation of fluctuations at frequencies higher than f_c. This effect is in fact also observed in classical turbulent convective systems with top and bottom solid boundaries conditions.

Any temperature fluctuation grows from small perturbations at the solid plate that diffuse in the boundary layer of thickness δ_c (see Eq. (12.5)) and forms ascendant plumes in the bulk. The rising of one of these convective plumes causes the fluid in the boundary layer to be carried away, and the thin thermal layer has to be rebuilt before another plume could appear. The reconstruction time corresponds to the diffusion time τ_c for a perturbation to diffuse through this layer. This duration has been evaluated by Howard [8]:

$$\tau_c = \frac{{\delta_c}^2}{\kappa}. \tag{12.8}$$

Using the values corresponding to our experiments (κ is equal to 1.36×10^{-7} m^2/s at 4 °C), we find $\tau_c \sim 250$ s whose inverse has indeed the same order of magnitude as the experimental observed frequency f_c observed on the spectrum (see Fig. 12.3(a)).

As observed in the spectrum of Fig. 12.3(a), an energy cascade takes place for frequencies higher than f_c. In the frequency range larger than f_c where the signal-to-noise ratio is larger than 1, we observe an energy cascade on more than 1 decade. The corresponding exponent is equal to -4 ± 0.01 for the energy spectrum. This value is larger (in absolute value) than the typical value around -2.8 found in turbulent Rayleigh–Bénard convection [7]. This difference of slope in the spectrum can have two origins. The first reason is the lateral confinement of the flow and the quasi-bidimensional motions of the fluid between the two vertical walls that increases the dissipation at every scale larger than the thickness of the tank. The second reason comes from the main feature of penetrative convection. As there is no longer fixed boundary condition at the top of the convective layer a part of the energy can be transmitted to waves that propagate in the stratified layer. This mechanism induces the radiation of energy by waves that will be damped by viscosity, far from the convective layer. Therefore, the traditional energy cascade is modified by the energy flux which is transmitted to the waves, and can also increases the spectrum exponent. The relative importance of these two processes will be analyzed by the numerical simulations (see Sect. 12.6).

This completes the picture of penetrative convection sketched in Fig. 12.1: a turbulent convective layer with plumes emerging from thermal fluctuations in the bottom diffusive thermal layer at a typical rate around f_c. Theses plumes rise through the turbulent convective layer before they excite internal gravity waves when penetrating a buffer zone at the bottom of the stratified layer. One of the possible consequences of this energy release mechanism is that the turbulent spectrum of penetrative convection is steeper than the classical turbulent convection spectrum.

12.4 The Buffer Zone Between the Convective and Stratified Layers

After a few days, the convection zone reaches an equilibrium height with two asymmetric boundary layers: the thin lower one and the upper one for which the height is proportional to the imposed temperature difference $T_{\text{up}} - T_c$. By simple visual inspection of tracers, we observe large amplitude motions in the horizontal direction

at a very low frequency in the intermediate buffer zone. At the bottom of the buffer zone, the position of the isotherm 4 °C fluctuates in time when a convective plume goes through the interface. These plumes excite internal waves, their wavelengths being selected by the sizes of the wave makers that generate them. Typically the plumes have a size of δ_c. However, there is also the scale of the whole container as there is always large convective cells, even in the Rayleigh–Bénard turbulent regimes ($R_a > 10^6$) [7]. Thus, we do not expect a sharp length selection, but rather a wave generation on a large range of wavelengths between 0.6 cm and 20 cm.

Using PIV measurement, we observe fluctuations of velocity in space and time. As expected, these fluctuations possess a large range of frequencies around $f_c = 0.02$ Hz but smaller than the Brunt–Väisälä frequency and a large range of wavelengths varying from the size of the box (20 cm) to 1 cm. We observe only waves propagating from the bottom to the top in both horizontal directions ($k_x > 0$ and $k_x < 0$).

The next step in our analysis is to prove that the angle θ and the associated frequency f of waves follow the dispersion relation given by Eq. (12.1). As these waves are produced by turbulent motions, there is no coherence between successive generated wave packets. Moreover, the duration of propagation through the buffer zone for a wave of typical wavelength of 5 cm will only be a few periods. So the time of coherence has the same order of magnitude as the period of the waves. For such small scale separation, a classical Fourier filtering is not efficient enough to analyze the velocity signal. Thus, we have developed a special data analysis technique, which preserves the signal information localized both in space and time. This technique does not need any supposition on the time of coherence of the generated waves and permits one to determine accurately the mean time-average phase velocity of the waves. To do so, we compute local correlation functions at each point of coordinate $\mathbf{r}$, between $V(\mathbf{r}, t)$ and $V(\mathbf{r} + \delta\mathbf{r}, t + \tau)$:

$$C(\tau, \delta\mathbf{r}) = \frac{1}{T} \int_0^T V(\mathbf{r}, t) V(\mathbf{r} + \delta\mathbf{r}, t + \tau)\, dt. \tag{12.9}$$

For a periodic signal propagating along an arbitrary direction $\mathbf{s}$, the associated correlation function will be periodic in time. The value of the first maximum for a positive time $\tau > 0$ will give the phase shift between $\mathbf{r}$ and $\mathbf{r} + \mathbf{s}$. Along the direction orthogonal to the propagation, the phase shift will vanish. Therefore, we can measure both the phase velocity and its direction as a local function of space and time.

Applying our technique to the measured velocity field in the buffer zone, we can deduce the local mean direction of propagation of internal waves. This angle of mean direction of propagation does not depend on x, but as shown in Fig. 12.4, we observe a strong dependence on the altitude z. In this buffer zone, the waves do not propagate along a straight line. This result can be linked to the vertical Brunt–Väisälä profile $N(z)$ shown in Fig. 12.2. Indeed, close to the maximum density of water, $N(z)$ scales as

$$N(z) = N_0 \sqrt{\frac{z - z_0}{l_0}} \tag{12.10}$$

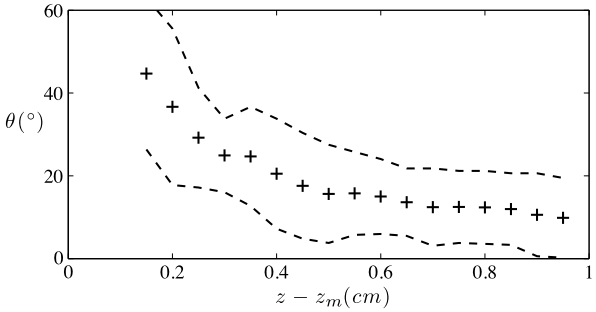

Fig. 12.4 The direction of propagation θ of the waves in the buffer zone, obtained by autocorrelation of the velocity fields measured by PIV technique. The *solid line* is the theoretical value of θ, computed with the dispersion relation and the experimental measured values of $N(z)$ plotted on Fig. 12.2. *Dashed lines* represent the bandwidth of θ of the internal wave packet

where $N_0 = 0.024$ and $l_0 = 1$ cm has been computed using the measured vertical density profile $\rho(z)$ (see Fig. 12.3). The corresponding theoretical curves have been added to Fig. 12.4 (solid lines). It agrees closely with the experimental data with no adjustable parameter. We insist here that this graph represents the mean direction of propagation of wave packets with a large variability around this average value. The dashed line shown on Fig. 12.4 correspond to the uncertainty on θ due to the large bandwidth of the observed internal waves. Even if we can measure a mean direction of propagation, in the buffer zone there is no narrow selection of the propagation angle of internal waves.

12.5 The Stratified Layer

In the buffer layer we have seen that the direction of propagation changes drastically with z. As soon as the waves travel out of this layer, the density gradient becomes independent of z, and the direction of propagation for each wave will no longer evolve. So in the stratified layer we expect to observe waves propagating straightway in all possible directions with a range of frequencies a priori between 0 and N.

With our PIV technique we have measured the velocity field associated with these waves. As before, the spectrum is filtered to keep only the waves propagating along $k_x > 0$ and for all of the frequencies between $0.1N$ and N. A PIV snapshot of this field is shown in Fig. 12.5. Contrary to the buffer zone, the wave propagated straightway on a longer distance, more than 10 cm. At this range of propagation, we observe that the waves are damped by viscosity before reaching the top of the tank. It justified a posteriori that there is no significant reflection of waves on the upper copper plate. This feature allows us to evaluate the dissipation along the vertical axis. For this purpose, we compute in the stratified layer the vertical kinetic energy profile E_c given by

$$\langle E_c(z) \rangle = \frac{1}{L} \int_0^L V(z,x)^2 \, dx, \tag{12.11}$$

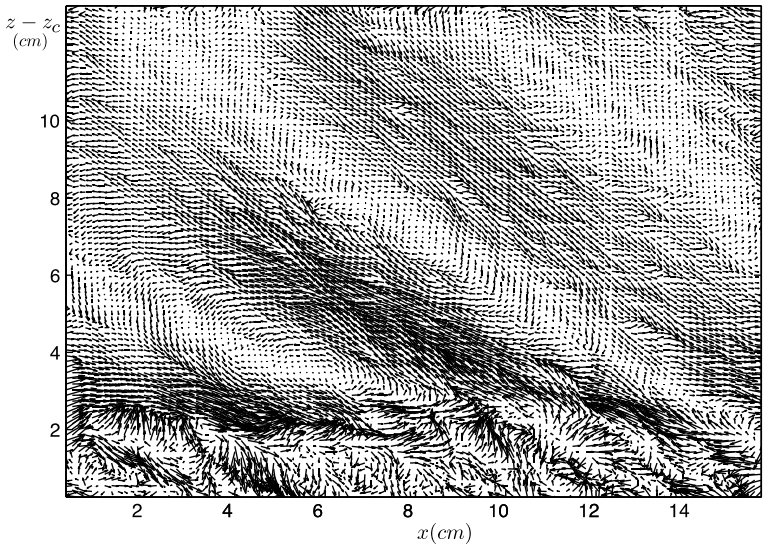

Fig. 12.5 Instantaneous velocity field in the stratified layer. Only waves propagating toward the right have been kept by our filtering process

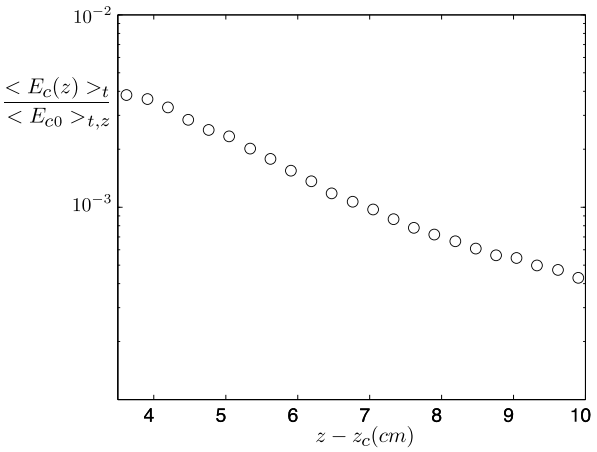

Fig. 12.6 Mean kinetic energy of the gravity waves in the stratified layer as a function of the altitude z

where L corresponds to the horizontal width of the tank. The experimental value of E_c as a function of z is shown in Fig. 12.6. We observe an exponential decay of E_c with the altitude. In the derivation of the internal wave equation it is possible to add the viscous term at the first order [9]. So the viscous damping in amplitude of a wave characterized by its frequency ω and wavenumber k can be written as

$$A(z) = e^{-\alpha(k)\xi/2}, \quad \text{where } \alpha(k) = \frac{\nu k^3}{\omega\sqrt{(\frac{N}{\omega})^2 - 1}}, \tag{12.12}$$

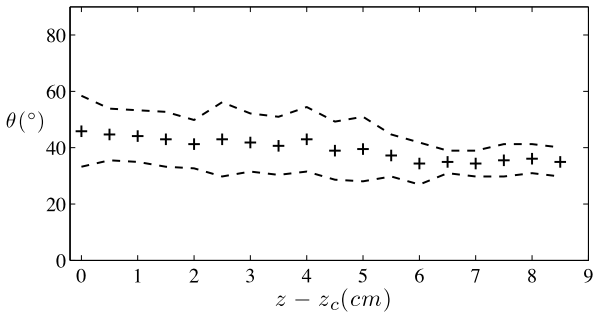

Fig. 12.7 The direction of propagation of the waves in the stratified zone, obtained from the velocity fields measured by PIV. In contrast to the buffer zone, here a selection of frequencies and angles is observed. The *dashed lines* represent the bandwidth of θ of the internal wave packet

and where ξ corresponds to the coordinate orthogonal to the wave vector. This relation has been verified experimentally [14]. We find an experimental value of $\alpha = 0.21\ \text{cm}^{-1}$, which corresponds to a typical damping length of 3 cm along the vertical axis, which is smaller than the height of the stratified layer. The ratio between the incoming energy from the convective layer and the outgoing energy to the stratified layer being about 20 [23], we can construct an effective damping length for the buffer zone. This length is five times smaller than the one measured in the stratified layer attesting to the fact that the buffer layer avoids the propagation of energy upward.

As we see in Fig. 12.5, the internal waves seem to propagate along a selected direction. To accurately measure the angle of propagation θ, we use the algorithm developed previously for the buffer zone analysis (see Sect. 12.4). We observe in Fig. 12.7 that a narrow range of θ, between 30° and 50°, is selected. This range corresponds to a frequency between $0.4N$ and $0.8N$. For this stratified layer, the dispersion around the mean value is smaller than for the buffer zone. This selection of angle in a stratified layer has also been observed in previous experiments, where internal waves were generated by a turbulent layer [6] or by a single plume [2]. These last authors note, in particular, that an angle of 30° corresponds to the maximum of energy transport by the waves and an angle of 45° to the maximum of momentum transport.

In a closely related study, Taylor and Sarkar [22] suggest a viscous damping mechanism occurring during wave propagation to explain the progressive selection process. Although our study shows an intense damping of the waves in the intermediate buffer layer, together with a selection of the propagation angle of these waves when traveling through and exiting this layer, this explanation is still debated, and more work should be dedicated to definitively answer this question.

12.6 Numerical Simulation: To Go Further into the Analysis

To complement this experimental study, a two-dimensional numerical simulation has been performed using the commercial software COMSOL Multiphysics, which is based on the finite-element method. Coupled Navier–Stokes and temperature equations are solved in a square tank of height 35 cm and width 20 cm.

Velocity/temperature boundary conditions are respectively no slip/imposed 0 °C temperature at the bottom, slip/imposed 50 °C temperature at the top, and no slip/imposed heat flux on both sides, mimicking the heat loss by conduction through the 3-cm-thick Plexiglas plates in the experimental setup. Chosen physical parameters are typical for water around 4 °C, with a thermal diffusion coefficient $\kappa = 1.3 \times 10^{-7}$ m^2/s, a viscosity $\nu = 1.8 \times 10^{-6}$ m^2/s, and an equation of state $\rho = 1 - 8.1 \times 10^{-6}(T - 3.98)^2$. The numerical grid is refined near the boundaries and especially near the lower one to correctly resolve the small-scale dynamics of turbulent plumes. Elements are of standard Lagrange P_2–P_3 type for solving Navier–Stokes equations (i.e., quadratic for the pressure field and cubic for the velocity field) and are quadratic for solving the temperature field. At each time step the system is solved with the sparse direct linear solver PARDISO.[1] The number of degrees of freedom (DoF) used in the simulations is 125,866. The total duration of the simulation corresponds to a 27.8-hour experiment, starting from a fluid at rest with a uniform temperature of 3 °C in the convective zone $z < 25$ cm and a linear temperature profile from 3 °C to 50 °C in the stratified zone $z > 25$ cm.

Figure 12.8 illustrates the typical state of the convective zone once the turbulent convection is established. As described in the above notes on the experiment, the temperature profile is mostly constant in the bulk with a mean value of about 3 °C and with a thin thermal boundary layer at the bottom. Convective flows correspond to small-scale chaotic plumes growing from the lower boundary, superimposed on a large-scale cellular motion. Typical vertical temperature and velocity vertical profiles extracted at $x = 10$ cm are shown in Fig. 12.9.

The profiles of Fig. 12.9 illustrate the main difficulty of this study: temperature fluctuations above the established linear profile and velocity fluctuations associated with the wave field in the stratified zone are 1 to 2 orders of magnitude smaller than temperature and velocity fluctuations associated with convective motions. This makes them difficult to compute and to observe. Nevertheless, a good way to visualize the wave field is to compute the time derivative of the temperature, as shown in Fig. 12.8; we then notice that the amplitude of the wave pattern rapidly decreases from the interface, as noticed in the experiment.

In order to better investigate the temporal characteristics of the flow, we have analyzed by Fourier transform the temperature at two locations, one in the convective zone and one in the stratified zone. Results are shown in Fig. 12.10(a). For comparison, the same spectra for a simulation with the same parameters but where gravity waves propagation has been artificially prevented by setting the velocity field to zero for $z > 25$ cm is shown in Fig. 12.10(b). We clearly recover the results found in the experiment. The convective spectrum is flat up to the typical cut-off frequency corresponding to τ_c (see Eq. (12.8)). It then decreases rapidly with a typical exponent -4. We do not see significant difference between the convective spectra in the presence and absence of gravity wave, which suggests that this relatively high exponent is mostly due to the two-dimensionality of our study. The spectrum associated with gravity waves clearly shows frequency selection between 3×10^{-3} Hz

[1] www.pardiso-project.org.

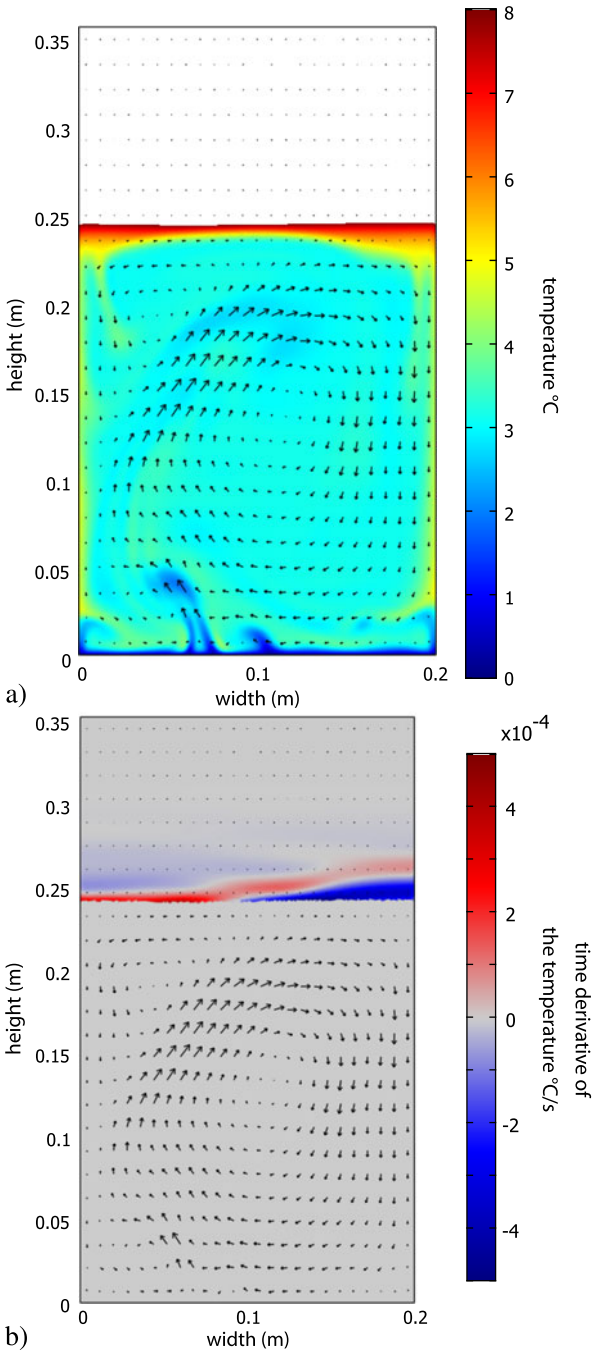

Fig. 12.8 (**a**) Time derivative of the temperature field for locations where $T > 8$ °C (i.e. in the stratified zone) obtained at time $t = 27.8$ hours. Also shown is the velocity field (*black arrows*); (**b**) temperature field (in *color*, between 0 °C and 8 °C in order to focus on the convective zone) and velocity field (*black arrows*) obtained at time $t = 27.8$ hours

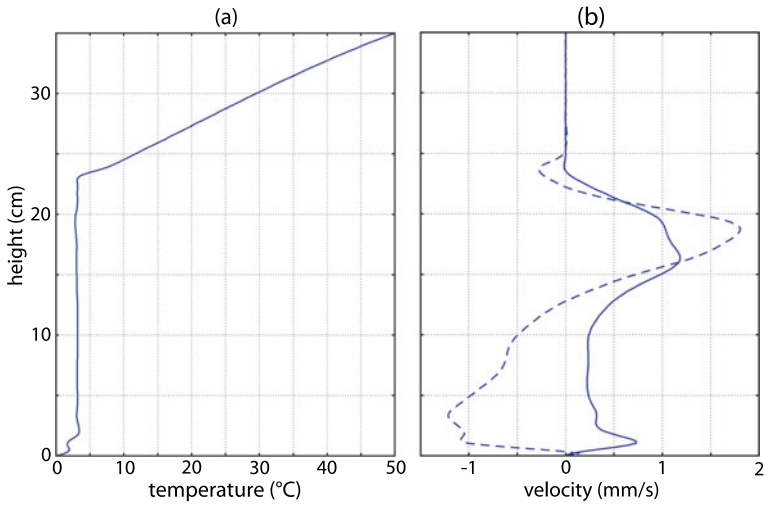

Fig. 12.9 Vertical profiles for (**a**) the temperature and (**b**) the vertical (*solid*) and horizontal (*dashed*) velocity at time $t = 27.8$ hours in the middle of the tank ($x = 10$ cm)

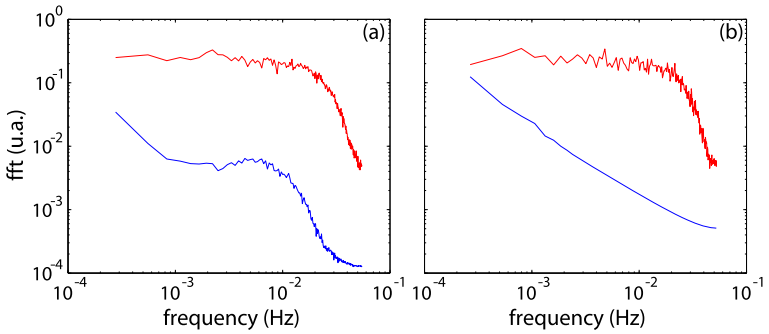

Fig. 12.10 Temporal temperature spectrum in the convective layer (*upper curve*, signal measured at $x = 17$ cm and $z = 10$ cm) and in the stratified layer (*lower curve*, signal measured at $x = 17$ cm and $z = 28$ cm): (**a**) for the standard simulation and (**b**) for a simulation with the same parameters but where gravity waves propagation has been artificially prevented by setting the velocity field to zero for $z > 25$ cm. Each curve corresponds to the mean value of the Fourier transforms over a sliding window of 1 hour of the signal corrected by a degree 1 polynomial fit (to suppress the long term drift), from time $t = 1.5$ hour to time $t = 27.8$ hours

and 7×10^{-3} Hz, corresponding to propagation angles between 25° and 60°, the favorite angle being around 40°. By comparison, the corresponding spectrum in the absence of waves propagation (the waves have been artificially prevented) is typical of an f^{-2} noise spectrum, highlighting the good resolution of the wave field by our method.

12.7 Conclusion

In this study, we have used the very peculiar property of water of having a maximum density at a temperature of 4 °C. This property has permitted the experimental investigation of penetrative convection in a stationary regime. Turbulent convection that sets in the lower part of a water layer cooled by its bottom plate at a temperature lower than 4 °C can generate gravity waves in the upper stably stratified layer. These waves are excited by the rising of turbulent plumes impinging the bottom of the stratified layer. Although dealing with the small values of the involved density gradients is a challenging task, this difficulty has been circumvented using a very sensitive PIV technique, which is then combined with a dedicated data analysis. Our experimental study is then completed by a 2D numerical direct simulation. In both experimental and numerical investigations, we recover the known selection of propagation angles of the waves in the stratified layer. We have however identified a third layer squeezed between the convective and the stratified layers that we have called the buffer layer and where the Brunt–Väisälä frequency varies with the altitude. In this zone there is no angle selection and a strong damping in the vertical direction. We expect the different properties of penetrative convection that we studied here to apply in natural situations such as the generation and the propagation of g-waves in star radiative zones or internal waves excitation in the stratosphere or in the oceans.

References

1. Adrian, R.J.: Particle-imaging techniques for experimental fluid-mechanics. Annu. Rev. Fluid Mech. **23**, 261–304 (1991)
2. Ansong, J.K., Sutherland, B.R.: Internal gravity waves generated by convective plumes. J. Fluid Mech. **648**, 405 (2010)
3. Bretherton, F.P.: On the mean motion induced by internal gravity waves. J. Fluid Mech. **36**, 785–803 (1969)
4. Brun, A.S., Strugarek, A.: Understanding the solar inner magnetism and dynamics. In: Sekii, T., Watanabe, T., Sakurai, T. (eds.) Proceedings of the 3rd Hinode Science Meeting, 1–4 December 2009. ASP Conf. Ser., vol. 454 (2012)
5. Cerasoli, C.P.: Experiments on buoyant-parcel motion and the generation of internal gravity waves. J. Fluid Mech. **86**, 247–271 (1978)
6. Deardorff, J.W., Willis, G.E., Lilly, D.K.: Laboratory investigation of non-steady penetrative convection. J. Fluid Mech. **35**, 7–31 (1969)
7. Heslot, F., Castaing, B., Libchaber, A.: Transitions to turbulence in Helium gas. Phys. Rev. A **36**, 5870–5873 (1987)
8. Howard, L.N.: Convection at high Rayleigh number. In: Proc. 11. Int. Congr. Appl. Mech., pp. 1109–1115 (1964)
9. Hurley, D.G., Keady, G.: The generation of internal waves by vibrating elliptic cylinders. Part 2. Approximate viscous solution. J. Fluid Mech. **351**, 119–138 (1997)
10. Lindzen, R.S., Holton, J.R.: A theory of the quasi-biennial oscillation. J. Atmos. Sci. **25**, 1095–1107 (1968)
11. Malkus, W.V.R.: The heat transport and spectrum of thermal turbulence. Proc. R. Soc. Lond., Ser. A **225**, 196–212 (1954)
12. Mathis, S., Talon, S., Pantillon, F.P., Charbonnel, C., Zahn, J.P.: Wave transport in stellar radiation zone influenced by the Coriolis acceleration. J. Phys. Conf. Ser. **118**(1), 012025 (2008)

13. McLaren, T.I., Pierce, A.D., Fohl, T., Murphy, B.L.: An investigation of internal gravity waves generated by a buoyantly rising fluid in a stratified medium. J. Fluid Mech. **57**, 229–240 (1973)
14. Mercier, M.J., Garnier, N.B., Dauxois, T.: Reflection and diffraction of internal waves analyzed with the Hilbert transform. Phys. Fluids **20**(8), 086601 (2008)
15. Meunier, P., Leweke, T.: Analysis and treatment of errors due to high velocity gradients in particle image velocimetry. Exp. Fluids **35**, 408–421 (2003)
16. Michaelian, M.: The coupling between turbulent, penetrative convection and internal waves. Eur. J. Mech. B, Fluids **21**, 1–28 (2002)
17. Oster, G.: Density gradients. Sci. Am. **213**, 70–76 (1965)
18. Rogers, T.M., Glatzmaier, G.A.: Penetrative convection within the anelastic approximation. Astrophys. J. **620**, 432–441 (2005)
19. Rogers, T.M., MacGregor, K.B.: On the interaction of internal gravity waves with a magnetic field—II. Convective forcing. Mon. Not. R. Astron. Soc. **410**, 946–962 (2011)
20. Sutherland, B.R., Dalziel, S.B., Hughes, G.O., Linden, P.F.: Visualization and measurement of internal waves by synthetic schlieren. Part 1. Vertically oscillating cylinder. J. Fluid Mech. **390**, 93–126 (1999)
21. Talon, S., Charbonnel, C.: Angular momentum transport by internal gravity waves. I—Pop I main sequence stars. Astron. Astrophys. **405**, 1025–1032 (2003)
22. Taylor, J.R., Sarkar, S.: Internal gravity waves generated by a turbulent bottom Ekman layer. J. Fluid Mech. **590**, 331–354 (2007)
23. Townsend, A.A.: Natural convection in water over an ice surface. Q. J. R. Meteorol. Soc. **91**, 243–245 (1965)
24. Zahn, J.P., Talon, S., Matias, J.: Angular momentum transport by internal waves in the solar interior. Astron. Astrophys. **322**, 320–328 (1997)

Index

Symbols
2D models, 51
β Cephei stars, 159
D_{eff}, 5, 6, 10, 11, 18, 19
D_{h}, 4–6, 11, 14, 18–20
D_{shear}, 5, 6, 11, 14, 15, 18, 20
λ Eri variables, 173
μ-gradient, 6, 10, 14, 18, 212
μ-gradient region, 212, 214, 216, 217

A
Accretion, 81, 82
Acoustic rays, 116, 119, 120
Acoustic waves, 116
Alfvén radius, 79
Anelastic approximation, 231
Angular momentum, 3, 6, 7, 15, 16, 20
Angular momentum transport, 240
Arnoldi–Chebyshev, 96
Ascendant plumes, 248
Asteroseismology, 234
Asymptotic theory, 115

B
Baroclinic flows, 64
Be stars, 161, 170, 172
Birthline, 81, 82, 87
Blue loop, 3, 7, 15, 20
Blue-to-red supergiant ratio, 14, 15, 20
Boussinesq approximation, 225, 231, 232
Brunt–Väisälä, 249
Brunt–Väisälä frequency, 66, 239, 241, 246, 249, 256
Buffer layer, 239, 250, 252, 256
Buffer zone, 248, 249, 252

C
Cepheids, 15
Chandrasekhar–Milne expansion, 144, 154
Chaotic mode, 121–123, 128, 129
Chaotic plumes, 253
Chaotic systems, 118
Chemical composition evolution, 78
Convection, 23, 24, 26–31, 37, 38, 41, 179–182, 188–190, 192, 194, 198, 201, 203
Convection waves, 241
Convective layer, 239, 240, 242, 243, 245–248, 255, 256
Convective overshoot, 85
Convective penetration, 11
Convective plumes, 248, 249
Convective zone, 239, 253
Core He-burning lifetime, 7
Core helium lifetime, 3, 7
Coriolis force, 163, 164

D
Density maximum, 239
Differential rotation, 64, 76, 77, 87
Differentiation matrix, 61
Direct numerical simulations, 229
Disk locking, 82, 83
Double-diffusive processes, 221
Dynamo, 24, 26, 30, 31, 34, 35, 41
Dynamo operates, 79

E
Effective diffusion coefficient, 5
Energy test, 64
ESTER code, 49
ESTER project, 51
Evolutionary models, 83

M. Goupil et al. (eds.), *Studying Stellar Rotation and Convection*,
Lecture Notes in Physics 865, DOI 10.1007/978-3-642-33380-4,

Evolutionary tracks, 3, 4, 7, 20
Exoplanets, 233

F
Fast rotating metal poor massive stars, 7
Fast-rotating, 17
Fast-rotating metal-poor massive stars, 3
Fossil magnetic field, 31, 32, 34–38, 41
Frequency regularities, 124
Fully compressible formulation, 232

G
g-waves, 256
Gravity darkening, 67
Gravity or internal waves, 240
Gravity waves, 75, 239, 240, 247, 251, 253, 255, 256

H
Hamiltonian systems, 116–118
Heat conductivity, 54
Horizontal shear diffusion, 5
Horizontal shear diffusion coefficient, 4
Horizontal turbulence, 77
Hough function, 137, 139
Husimi distributions, 120, 121

I
Induced semi-convection, 216
Inertial modes, 133, 135, 136
Inertial waves, 241
Integrable systems, 117, 118
Internal gravity waves, 86, 239, 242, 248
Internal transport of angular momentum, 75, 83, 84
Internal waves, 31, 32, 34, 37, 40, 41, 239–241, 243, 244, 247, 249, 250, 252, 256
Invariant tori, 118
Island mode, 121–124, 126, 127

K
Kwatra's method, 233

L
Laboratory experiments, 230
Laplace tidal equation, 137, 153
Ledoux and Schwarzschild criterions, 214
Ledoux criterion, 210, 212, 214, 217, 221
Lewis number, 225
Lifetimes, 3, 4, 7, 11, 20
Lithium, 85, 86
Lithium abundance, 85, 86
Loss of angular momentum, 79

M
Magnetic field, 79, 80, 86
Mapping of coordinates, 57
Maximum density at a temperature of 4 °C, 256
Maximum density of water, 241, 249
Mean molecular weight gradient, 220
Meridional circulation, 24, 25, 29–34, 36, 39, 41, 65, 75–78, 88
Meridional currents, 5, 6, 15
Metal-poor massive stars, 17
Metallicity, 7, 11, 20
Mixed systems, 118
Mixing length theory, 227
MLT, 83
Mode amplitudes, 179, 181, 182, 198, 201–203
Mode damping, 180–182, 188, 189, 191–195, 199
Mode driving, 179, 180, 182–184, 187, 199
Mode visibility, 122, 123
Modes
  chaotic modes, 101, 104
  island modes, 101, 104, 105
  whispering gallery modes, 101, 104
  rosette modes, 106–108
Multidimensional modelling, 234
Multidimensional simulations, 230

N
Natural basis, 58
Newton's method, 62

O
Overshoot, 11
Overshooting, 160, 162, 170
Overshooting plumes, 240

P
Parametric instability, 151, 152, 154
Penetrative convection, 239, 242, 243, 245, 248, 256
Perturbative methods, 92, 101
  domains of validity, 102, 103
Phase space, 116, 120
Plumes, 242, 248, 249, 252
PMS, 81–83, 85, 86
Poincaré surface of section, 117, 119, 120
PP chain operating at equilibrium, 211
PP chain operating out of equilibrium, 211
PP chain operating with overshooting, 211
Prandtl number, 225
Pre-main sequence, 81
Primary nitrogen, 3, 7, 17–20
Protostar, 81
PSS, 117, 118

Q
Quantum chaos, 120

R
r-modes, 133, 135, 136, 138, 140, 146, 147, 149, 150, 153, 154, 165
Radiative zone, 239
Random matrix theory, 129
Ray dynamics, 119
Reynolds number, 78
Reynolds stress, 180, 181, 184, 190
Reynolds stress models, 228
Richardson number, 79
Rotational mixing, 18
Runge–Kutta methods, 233

S
Salt-fingers, 222
Scaling laws, 192, 198–200, 203
Schwarzschild, 217
Schwarzschild criterion, 209, 210, 212, 214, 216, 217, 220
Secondary nitrogen, 17
Self driving mechanism, 215
Self-consistent field method, 51
Semi-convection, 219
Shear diffusion, 7
Shear-induced turbulence, 32, 34, 38, 39
Shellular rotation, 4, 76, 77
Short wavelength limit, 116
Solar-like oscillations, 179, 181, 183, 192, 195, 201
SPB stars, 159
Spectral methods, 60
Spheroidal coordinates, 57
Stable islands, 119, 122
Stellar wind, 79
Stewartson layer, 65
Stratified layer, 239–243, 246–248, 250–252, 256
Stratified zone, 241, 253
Stress-free conditions, 54
Subinertial domain, 103, 106, 108
Supergiants, 13
Superinertial domain, 106
Surface abundances, 4
Surface composition, 3, 7, 11
Surface enrichments, 20
Surface velocities, 7, 20

T
Temperature boundary conditions, 55
Temperature gradient, 241
Temperature sensitivity, 213
Temperature sensitivity of a nuclear reaction, 210
Temperature sensitivity of the 3α helium-burning reaction, 212
Temperature sensitivity of the CNO cycle reactions, 211
Temperature sensitivity of the PP chain reactions, 211
Temperature stratification, 241
The heat flux, 53
Thermohaline convection, 222
Traditional approximation, 92, 105–108, 138–140, 149, 152–154, 166
Transport of angular momentum, 76, 81, 83–85, 88
Turbulence, 76, 180, 184, 185
Turbulent buoyant plume, 242
Turbulent convection, 239, 245, 256
Turbulent convective fluid layers, 240
Turbulent convective layer, 243, 246–248
Turbulent convective systems, 247
Turbulent diffusivity, 79
Turbulent penetrative convection, 239, 244
Turbulent plumes, 253, 256
Turbulent pressure, 180, 181, 188, 190, 191
Turbulent Rayleigh–Bénard convection, 245, 248
Turbulent viscosity, 77, 78, 88

V
Velocities, 3, 4
Vertical shear diffusion coefficient, 4, 5
Vibrational instabilities, 225
Vibrational stability, 216
Virial test, 62
Von Zeipel, 66

W
Water around 4 °C, 242, 243, 245, 253
Water that its density has a maximum value near 4 °C, 241
Whispering gallery mode, 121–123